Estimation of the CO2 and CH4 fluxes in France using atmospheric concentrations from ICOS network and data-assimilation techniques

Abdelhadi El Yazidi

NNT : 2018SACLV067

Estimation of the CO_2 and CH_4 fluxes in France using atmospheric concentrations from ICOS network and data-assimilation techniques.

Thèse de doctorat de l'Université Paris-Saclay
préparée à Université de Versailles Saint-Quentin-en-Yvelines

École doctorale n°129 Sciences de l'environnement Ile de France (SEIF)
Spécialité de doctorat: Météorologie, océanographie, physique de l'Environnement

Thèse soutenue au LSCE, le 1er octobre 2018, par

Abdelhadi El Yazidi

Composition du Jury :

M. Philippe Bousquet Professeur, LSCE	Président
M. Christoph Gerbig Chargé de recherche, MPBI	Rapporteur
Mme. Greet Janssen-Maenhout Chargé de recherche, JRC	Rapporteur
Mme. Christine Lac Chargé de recherche, CRNM	Examinateur
M. Vincent-Henri Peuch Chargé de recherche, ECMWF	Examinateur
M. Philippe Ciais Directeur de recherche, LSCE	Directeur de thèse
M. Michel Ramonet Chargé de recherche, LSCE	Co-Directeur de thèse

Thèse de doctorat

université PARIS-SACLAY | ÉCOLE DOCTORALE Sciences de l'environnement d'île-de-France (SEIF)

Titre : Estimation des flux de CO_2 et de CH_4 en France en utilisant les concentrations atmosphérique du réseau ICOS et les techniques d'assimilation de données

Mots clés : Gaz à effet de serre, CO_2, CH_4, France, inversion

Depuis la révolution industrielle, les croissances économique et démographique ont augmenté de manière exponentielle induisant la hausse de la combustion d'énergies fossiles, telles que le charbon, le pétrole, et le gaz naturel. La combustion de ces sources d'énergie conduit à l'émission de gaz à effet de serre (GES), principalement le dioxyde de carbone (CO_2) et le méthane (CH_4), qui par leur accumulation dans l'atmosphère entraînent une accentuation de l'effet de serre.

Selon le GIEC (Groupe d'experts Intergouvernemental sur l'Évolution du Climat), l'implication des émissions anthropiques dans l'augmentation de l'effet de serre est extrêmement probable avec un pourcentage de certitude qui dépasse 95%. Toutefois, l'estimation des bilans régionaux d'émissions de GES reste très incertaine. L'objectif de cette thèse est de contribuer à l'amélioration des estimations des bilans régionaux de GES en France, en utilisant les techniques de la modélisation inverse et les mesures atmosphériques du CO_2 et de CH_4 fournis par le réseau ICOS (Integrated Carbon Observation System).

Dans un premier temps, on s'est focalisé sur l'étude des concentrations mesurées de CO_2, CH_4 et CO (monoxyde de carbone). Cette étude a pour objectif, l'identification des mesures atmosphériques contaminées par les émissions locales (quelques kilomètres au tour de la station) et qui provoque ce qu'on appelle « les pics de concentrations ». Trois méthodes ont été appliquées sur des séries temporelles fournies par quatre stations du réseau ICOS, afin de déterminer leur degré de contamination. Ainsi, les résultats des différentes méthodes ont été comparés à un inventaire de données contaminées fourni par les gestionnaires des stations. À l'issue de ce travail, une méthode a été proposée pour effectuer un nettoyage automatique des séries de mesure du réseau ICOS.

Dans un deuxième temps, le modèle régional de chimie-transport CHIMERE est utilisé pour simuler les concentrations atmosphériques du CO_2 et du CH_4 de l'année 2014 sur un domaine centré sur la France. L'objet de cette étude est d'évaluer la sensibilité des concentrations simulées en utilisant différentes données d'entrées (sensibilité aux transports météorologiques et sensibilité aux flux de surface). Cette analyse a permis de quantifier à la fois les erreurs liées aux transports et les erreurs liées aux flux de surface. Ainsi, la meilleure combinaison des données d'entrée a été sélectionnée pour l'étape d'inversion des flux.

Dans un dernier plan, les mesures atmosphériques des concentrations de CO_2 et du CH_4 sont utilisées par le système d'inversion PYMAI (Berchet et coll., 2013 et 2015) afin d'estimer les bilans régionaux d'émission de CO_2 et CH_4 en France. L'inversion est réalisée pour un mois d'hiver (janvier) et un mois d'été (juillet) en utilisant le modèle de transport CHIMERE. Le résultat de ce travail a permis la quantification les émissions de CO_2 et de CH_4 à l'échelle nationale et régionale, ainsi qu'une réduction d'incertitude bilans nationaux à hauteur de 35 %.

Title : Estimation of the CO_2 and CH_4, fluxes in France using atmospheric concentrations from ICOS network and data-assimilation techniques

Keywords : Greenhouse gas, CO_2, CH_4, France, inversion

Since the industrial revolution, the economic and the demographic growths have increased exponentially, leading to an enhancement of the fossil fuels combustion, such as coal, oil, and natural gas. Consuming these source of energy amplifies the greenhouse gas emissions, mainly carbon dioxide (CO_2) and methane (CH_4), whose accumulation in the atmosphere lead to the increase of the greenhouse effect. According to the 5th assessment report of the Intergovernmental Panel on Climate Change (IPCC), it is extremely likely (95-100% of certainty) that the observed increase in the greenhouse effect is related to the increase of the anthropogenic emissions. However, the estimations of the GHG budget at the regional and the national scales remains highly uncertain. The aim of this thesis is to improve the estimation of the CO_2 and CH_4 fluxes in France, using data assimilation techniques and atmospheric measurements provided by the Integrated Carbon Observation System (ICOS) network.

The first phase focuses on analyzing the measured CO_2, CH_4, and CO (Carbon monoxide) atmospheric concentrations provided by surface monitoring stations. This study is concerned with the problem of identifying atmospheric data influenced by local emissions that can result in spikes in the GHG time series. Three methods are implemented on continuous measurements of four contrasted atmospheric sites. The aim of this analysis is to evaluate the performance of the used methods for the correctly detect the contaminated data. This work allows us to select the most reliable method that was proposed to perform daily spike detection in the ICOS Atmospheric Thematic Centre Quality Control (ATC-QC) software.

Secondly, we simulate the atmospheric concentrations of CO_2 and CH_4 using the chemistry transport model CHIMERE in a domain centered over France for the year 2014. The objective of this study is to evaluate the sensitivity of simulated concentrations using different input data (sensitivity to the meteorological transport and sensitivity to the surface fluxes). This work led to the quantification of both the transport and surface fluxes errors based on the combination of different simulations. Thus, the most reliable combination of the best input data was selected for the flux inversion study.

Lastly, the measured CO_2 and CH_4 concentrations are used by the PYMAI inversion system (Berchet et al., 2013 and 2015) in order to estimate the CO_2 and CH_4 fluxes in France. The Inversion is performed for one month in winter (January) and one month in summer (July), using the transport model CHIMERE. The inversion results have provided very interesting results for the regional estimation of the CO_2 and CH_4 surface fluxes in France with an uncertainty reduction that may attain 35% of the national totals.

Acknowledgments

First of all, I would like to express my special appreciation and gratitude to Philippe Ciais, Michel Ramonet, Isabelle Pison and Grégoire Broquet for supervising my Ph.D. You have been a tremendous mentors for me. Thank you, Philippe, for encouraging my research and guiding my scientific learning. Philippe, your advice has inspired and helped me to grow as a research scientist. Thank you, Michel, for your endless support and the time you spent helping me with this thesis. Michel, the joy and the enthusiasm you have for science were catching and motivational for me, even during hard times. Thank you, Isabelle and Grégoire, for your advice, for having pursued my thesis, and for all the time you spent explaining re-explaining me some concepts that were abstract to me.

I would like to thank Christoph Gerbig and Greet Maenhoult for their acceptance to review this thesis. Christine Lac and Vincent-Henri Peuch, thank you for accepting the be part of my Ph.D. jury. I would like to thank also Dominik Brunner and Martina Schmidt for the inspiring discussions and for the time they spent during the thesis committee meeting. Your advice and constructive remarks allowed me to advance the Ph.D. works.

I would like to thank the Climate-Kic for financing this thesis. I am also grateful to CEA for all the financial support and the traveling grants provided for the participation in different summer schools and conferences.

I am also grateful to all of the ICOS team members at LSCE for supporting me and being with me during the past three years. Special thanks in particular to the persons in charge of the monitoring programs and to all the people working for maintenance and data quality control of the stations. LSCE administration would not be that efficient without Catherine Huguen and Elsa Cortijo. Thanks to them for their continuous support in administrative procedures.

My special thanks to Antoine Berchet who helped me to get familiar with the PYMAI inversion system. Thank you, Antoine, for being patient with my questions. My warm thanks to my best friends Ettouhami El Yazidi, Mohamed Bouzidi and Tareq Soubai, thank you for all the good and the bad times we spent together, thank you for your endless support and encouragement during the whole Ph.D. Also many thanks to my family, friends, and everyone I met at LSCE: Oussama Rahimi, Amina, Khadija, Radouane, Amouna, Sabina, Ayché, Sébastien, Sarah, Luis, Céline, Julie, Xin, Lamia, Hamza, …

Lastly, and more importantly, A very warm thanks to my parents. Words can not express how grateful I am to my beloved mother Bouchra Naciri and my dearest father Abdelmajid El Yazidi. Thank you for pushing me towards my goals. Thank you for always being there for me and always welcoming me with open arms.

Contents

Figures

Tables

Chapter I: Introduction

I.1 Global radiative balance:

The Earth receives an energy of 340 $W.m^{-2}$ from shortwave solar radiation (Figure I.1). 30% of this energy is directly reflected back to space by clouds, aerosols, and the earth surface. The remaining part of the incident shortwave radiation (185 $W.m^{-2}$) is absorbed by the atmosphere and earth's surface. This energy will be reemitted afterward by the earth system in longwave radiation (e.g., sensible and latent heat, and thermal energy). The latent heat (around 84 $W.m^{-2}$) is associated to the evaporation of water at the Earth surface, whereas the sensible heat (around 20 $W.m^{-2}$) stands for the heat transfer by conduction between the Earth surface and the atmosphere. In addition to these fluxes, the Earth emits infrared radiation (398 $W.m^{-2}$), in the form of thermal energy. 60% of the total infrared flux (239 $W.m^{-2}$) is re-emitted directly to space, while the remaining part is absorbed by greenhouse gases (H_2O, CO_2, and CH_4). This later contribution (342 $W.m^{-2}$) of infrared radiations to the Earth system (Figure I.1), known as the greenhouse effect, leads to the increase in global temperature.

Without the natural greenhouse effect, the mean temperature at the Earth surface would be -18° Celsius (C) instead of +15° C. This indicates that the natural greenhouse effect ensures a warming of 33°C, making life possible on Earth. In order to maintain this natural warming, the total of energy absorbed and emitted by the Earth system must be zero. However, the emission of additional greenhouse gases in the atmosphere by the human activities, causes an energy imbalance of 0.8±0.2 $W.m^{-2}$ (Trenberth et al, 2009), which leads to the global warming of the atmosphere.

Since 1990 the Intergovernmental Panel on Climate Change (IPCC) demonstrated that human activities have modified significantly the Earth temperature compared to the pre-industrial period (5th Assessment Report of the IPCC 2013). In fact, the enhancement of the earth radiative energy imbalance contributes to the increase in Earth temperature, impacting the oceans, the atmosphere, the continental surfaces. The fast changes in the recent temperature threaten the most fragile ecosystems and could potentially impact the current civilization (Hatfield et al., 2015).

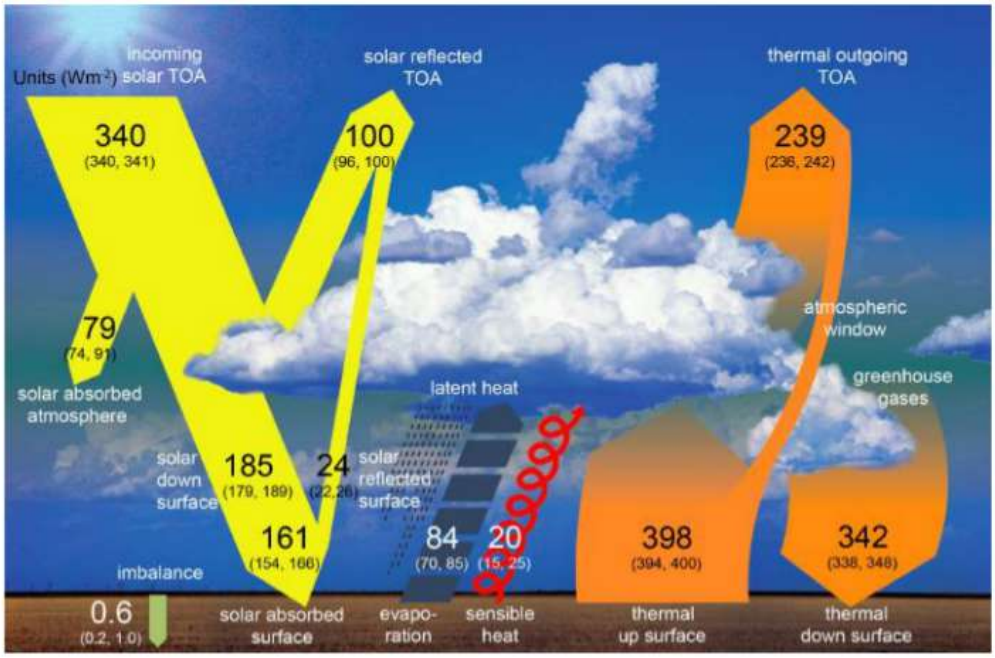

Figure I.1 : Global radiative balance in the current climate. The numbers in bold correspond to the estimate of each energy flux in W.m^{-2} (5th Assessment Report of the Intergovernmental Panel on Climate Change 2013)

I.2 Role of the greenhouse gases in global warming

Since the industrial revolution, human activities have been injecting into the atmosphere important quantity of carbon dioxide (36183 $MtCO_2$ in 2016, according to Global Carbon Atlas, www.globalcarbonatlas.org/) and other greenhouse gases such as methane (CH_4) and nitrous oxide (N2O). The CO_2 emissions are mainly related to fossil fuel combustion for industrial, domestic and transport energy needs. CH_4 is mostly linked to agricultural practices (e.g., rice growing and enteric fermentation), waste decomposition, as well as oil and gas production. Whereas, N2O is emitted mostly from agricultural activities, with the use of mineral and animal fertilizers. Other new substances such as the Chlorofluorocarbons (CFC), hydrochlorofluorocarbons (HCFC), whose origin is totally anthropogenic, are characterized by a greenhouse gas effect that may exceed thousands of times the one of CO_2 (Flanner et al., 2018). All these gases alter the global energy balance leading to the additional energy trapping near the surface. Other atmospheric components, such as aerosols, have a negative radiative forcing, which may lead to the atmospheric cooling (Figure I.2)

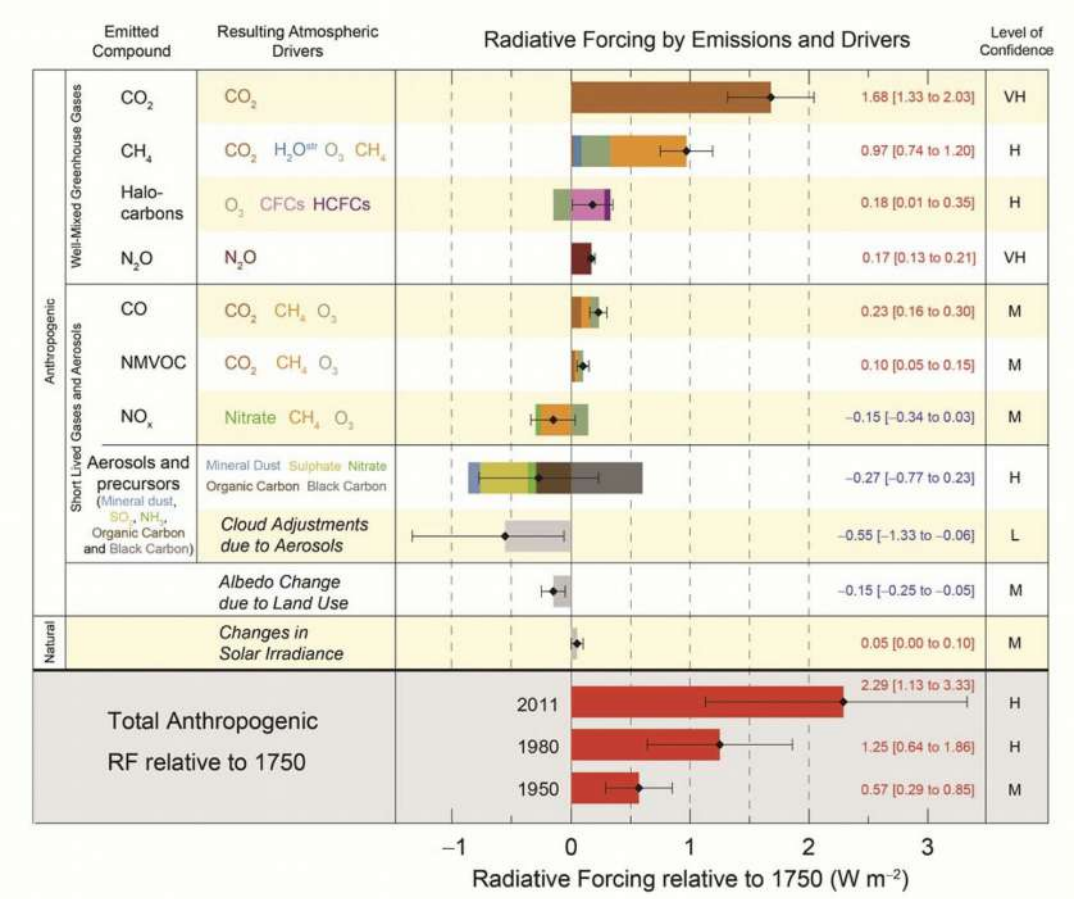

Figure I.2: Radiative forcing of the main anthropogenic (greenhouse gases, aerosol, short-lived gas) and natural (solar radiation) factors impacting the climate in 2011 compared to 1750 (5th Assessment Report of the IPCC 2013)

The contribution of the main greenhouse gases to the radiative forcing is presented in figure I.2. Since the beginning of the pre-industrial era, the additional radiative forcing caused by the anthropogenic activities is estimated to 2.3 $W.m^{-2}$ (between 1.1 to -3.0 $W.m^{-2}$, Myhre et al., 2013). According to the 5th Assessment Report of the IPCC (IPCC 2013), the CO_2 is responsible for the highest radiative forcing that exceeds 1.5 $W.m^{-2}$ (Figure I.2). CO_2 contributes by more than 50% to the additional radiative forcing produced by the greenhouse gases, whereas the CH_4 contribution is about 20%. The impact of the other atmospheric components and short-lived particles is limited (e.g. ozone, carbon monoxide, and the volatile organic compound). Each greenhouse gas has a different impact on the global warming, which depends on its own atmospheric residence time and its radiative forcing. In order to compare the relative contributions of these

gases, we use the Global Warming Potential index (GWP). This index has been developed by Houghton and Jenkins (1990) in order to quantify the greenhouse effect of each gas compared to CO_2. Greenhouse gas emissions are often calculated based on the amount of CO_2 that would be required to produce a similar warming effect over a given time period. This is calculated by multiplying the amount of the emitted gas by its corresponding GWP index. The CO_2 represents the reference value with a GWP index equal 1. For CH_4, Etminan et al., (2016) estimated a GWP index 32 times higher than CO_2 over a 100 year time period. The GWP index of N_2O is estimated to 260 for the same period (Etminan et al., 2016).

I.3 Carbon budget

I.3.1 Carbon dioxide cycle

CO_2 is the subject of many exchanges between land, ocean, and atmosphere. Figure I.3 represents the main carbon fluxes between the different reservoirs constituting the global carbon cycle.

The atmospheric concentrations of CO_2, which was 280 ppm (parts per million by volume) during the pre-industrial era, increased to 380 ppm in 2011 (IPCC, 2013), and exceeded an average of 410 ppm across the entire month for the first time at Mauna Loa in last April. The rise of atmospheric CO_2 concentrations is mainly related to the emissions by fossil fuel combustion estimated to 9.4 ± 0.5 GtC/yr (Le Quéré et al., 2017). The second largest anthropogenic source results from the land use changes, in particular, the deforestation estimated to 1.3 ± 0.7 GtC/yr (Le Quéré et al., 2017).

As shown in figure I.3, the global carbon cycle links together the atmosphere, the oceans, the land, and the fossil fuel reservoirs. The carbon fluxes are distributed, between these reservoirs, in different proportions. For example, the carbon fluxes between the atmosphere and the land are exchanged in both directions. The carbon is absorbed by the biomass due to the photosynthesis processes (123 PgC/year), and returns back to the atmosphere by surface emissions, fires, as well as plant, animal and microorganism respirations.

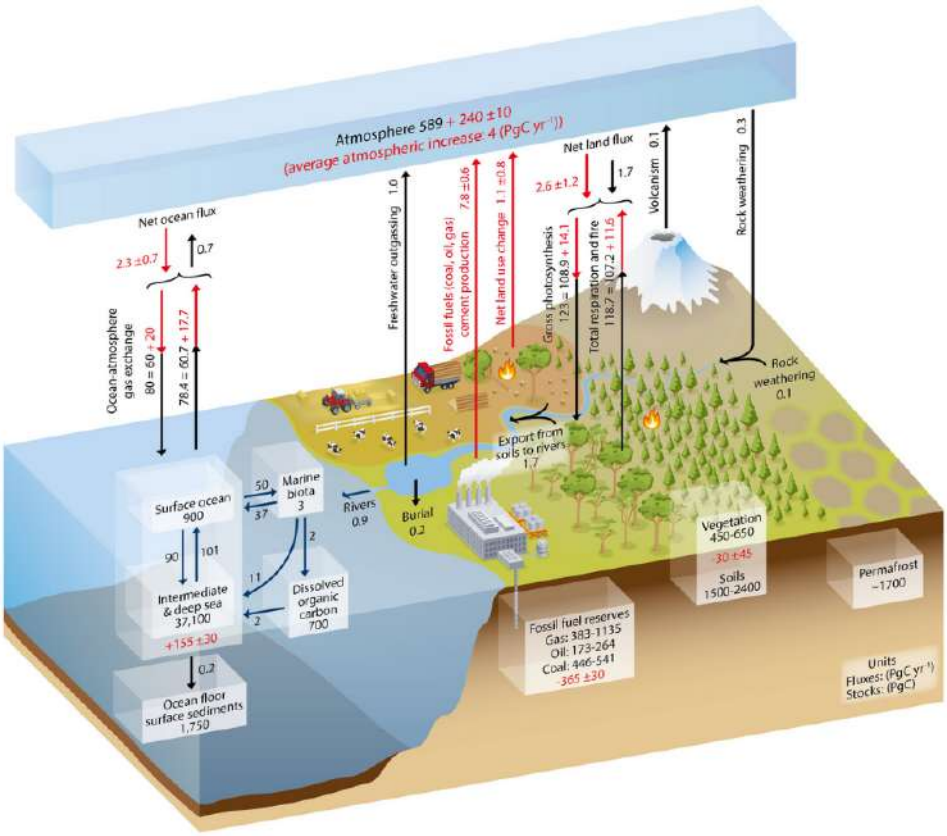

Figure I.3: Representation of the carbon cycle. The annual fluxes are estimated in PgC/year and averaged over the period 2000-2009. The amount of CO_2 stored in the three reservoirs is expressed in PgC. The figure is taken from the 5th assessment report of the intergovernmental panel for the Climate Change (IPCC 2013)

The fluxes represented by black arrows on the figure I.3 show the net fluxes estimated for the pre-industrial era. The red arrows represent the additional fluxes emitted on average in the decade 2000-2009 by the human activities, including fossil fuel burning, land use changes and cement production. The additional anthropogenic carbon fluxes are estimated to 9 PgC/year. Of these 9 PgC/year, about 5 are absorbed by land and oceans, and 4 remain in the atmosphere, leading to the increase of the CO_2 atmospheric concentrations which is precisely monitored at background observatories (Prather et al., 2012). If the magnitude of the oceanic and terrestrial sources and sinks are relatively well known on a global scale, their contributions at the sub-continental scale remain largely uncertain.

I.3.2 Methane cycle

During the pre-industrial era, the methane atmospheric concentration was about 700 ppb (parts per billion by volume), with a total emission of 215 $TgCH_4$/year (Lelieveld et al., 2002). Since 1750, CH_4 atmospheric concentrations increased by 150% (from 700 ppb) to a global mean value of 1853±2 ppb in 2016 (WMO Greenhouse Gas Bulletin N.13). The methane emissions can be separated into three types: natural, pyrogenic, leakages:

- Natural emissions are the result of fermentation reactions and methanogenesis processes of some microbes, produced from organic matter under low oxygen conditions. This category includes emissions from wetlands (e.g., peatlands, swamps, rice fields), termites, animals, landfill sites, wastewater, ruminants.

- Pyrogenic sources result from incomplete combustions, from biomass fires or fossil fuels such as domestic biofuels.

- Leakage emissions are caused by fossil fuel extraction and use (e.g., coal, natural gas, and oil industry).

The relative proportions of the different CH_4 sources were estimated by Dlugokencky et al (2011) as presented in figure I.4, and recently revised by Saunois et al., (2016). The methane natural emissions were estimated to 218±47 $TgCH_4$/year, whereas the anthropogenic emissions were estimated to 335±68 $TgCH_4$/year. The anthropogenic activities include emissions from agriculture, waste treatment, biomass fires, transportation and fossil fuels combustion. At the global scale, the highest contribution was determined for wetlands with a total ranging between 177 and 284 $TgCH_4$/year. The contributions of the geological sources, termites, hydrates and freshwater emissions are estimated respectively to 54±21, 12±10, 5±3, and 40±23 $TgCH_4$/year. For the anthropogenic emissions, the most important contributions come from fossil fuels, waste management, rice and farming estimated to 95±10, 78±12, 37±3, 90±4 $TgCH_4$/year respectively. The comparison between these sources showed the significant impact at the global scale of the wetlands, followed by the anthropogenic emissions. However, over the regional domain studied in this thesis (metropolitan France) some emissions, like the wetlands, biomass burning, rice cultivation, are much less important and can be neglected (Champeaux et al., 2005).

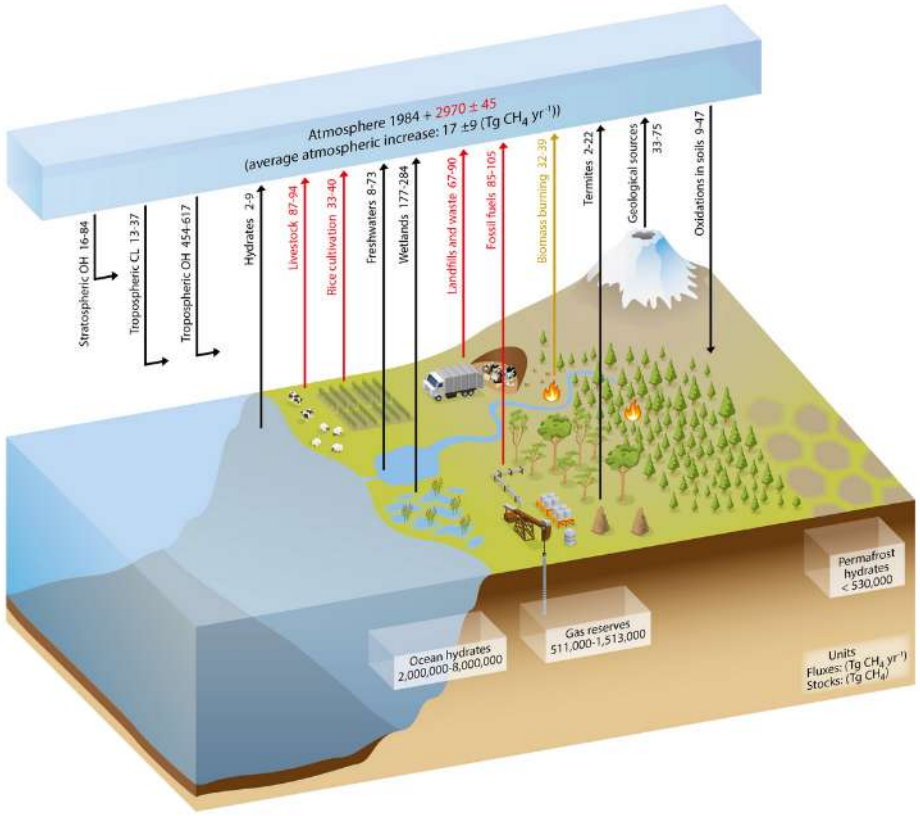

Figure I.4: Representation of the methane cycle. The annual fluxes are estimated in TgCH 4/year and averaged over the period 2000-2009. The amount of CH_4 stored in the three reservoirs is expressed in $TgCH_4$. This figure is taken from the 5th assessment report of the intergovernmental panel for the Climate Change (IPCC 2013)

I.4 CO_2 and CH_4 atmospheric measurerments

Direct measurement of the greenhouse gases has begun in 1958 by the sampling of the atmospheric concentrations of CO_2 at Mauna Loa (Hawai, USA) with the initiative of C. D. Keeling (Keeling, 1960). Measurement networks have been gradually expanded around the world and extended to other greenhouse gases, including the methane since 1978 (Blake et al., 1982, Dlugokencky et al., 1994), with the objective to follow the evolution of the atmospheric concentrations of the principal GHG, and to monitor their long-term trends. Nowadays, both CO_2 and CH_4 concentrations are regularly measured in the atmosphere by several

networks distributed around the world (Figure I.5). Two types of approaches are commonly adopted for the atmospheric sampling of the greenhouse gas concentrations:

- Continuous measurements by in-situ instruments: this approach is based on direct measurements using instruments at surface sites or on mobile platforms (aircraft, ships). The main advantage of the continuous measurements relays on the ability to investigate the atmospheric variations at short term scales. The development of laser-based optical measuring instruments has allowed a strong development of measurement sites over the last 10 years.

- Flask sampling coupled with in-lab analysis: such monitoring programs are generally developed at a frequency of few samples per month, which allows the characterization of long term trends and seasonal variations at background sites. The main advantage of the flask sampling is the possibility to perform multi-species measurements with limited infrastructure in the field.

Figure I.5 distinguishes several measurement networks. Panels a) and b), retrieved from the Earth System Research Laboratory website (https://www.esrl.noaa.gov/gmd/ccgg/globalview/), show the collaborative monitoring network led by NOAA/ESRL (USA). AGAGE (Advanced Global Atmosphere Gases Experiment) is also one of the oldest networks, providing measurements of different greenhouse gases (but not CO_2) since the beginning of the 1980s (Prinn et al., 2000; Cunnold et al. 2002). More recently, regional networks have also been developed, such as the RAMCES network in France presented in panel c) (Yver et al., 2011). The European Research Infrastructure network ICOS (Integrated Carbon Observation System, https://www.icos-ri.eu/icos-national-networks) aims to develop a dense and standardized monitoring network in Europe. Several data retrieved from the RAMCES and ICOS networks are used in this thesis.

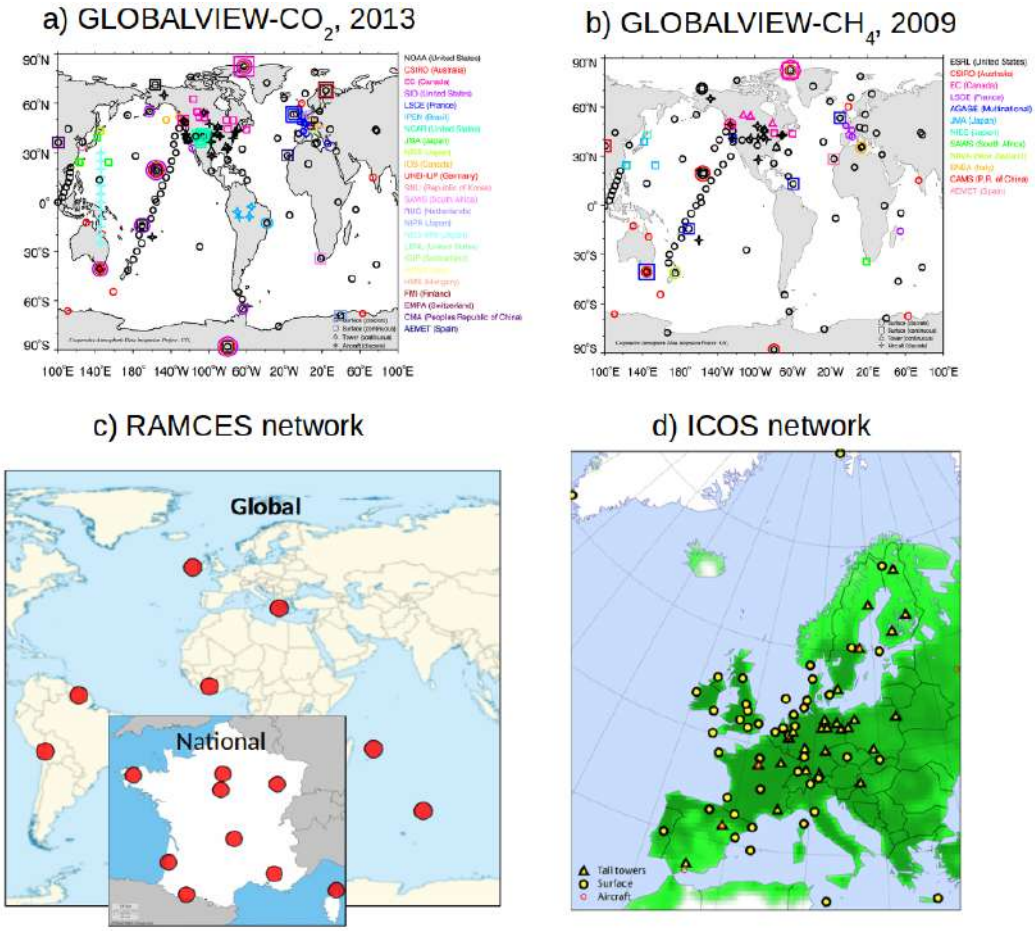

Figure I.5: maps of the GLOBALVIEW, ICOS and RAMCES atmospheric station networks

The increasing number of measurement sites has made possible the development of methods dedicated to the estimation of the CO_2 and CH_4 surface fluxes at increasingly finer spatial scales (Bergamaschi et al., 2018, Kountouris et al., 2018).

I.5 Flux estimation approaches :

I.5.1 Bottom-up approach:

The greenhouse gas emissions from anthropogenic sectors can be estimated at different administrative scales (city, region, country) for policy makers, or on regular gridded scales for scientists, by using geo-referenced fields of socio-economic data and source-specific emission factors. For example, national emission

inventories are reported every year by the countries to the United Nations Framework Convention on Climate Change (UNFCCC) and form the official data for international climate policies. In France, this activity is compiled by the *Centre Interprofessionnel Technique d'Etudes de la Pollution Atmosphérique* (CITEPA). Emissions are classified into different sectors (agriculture, transport, energy industries, residential, manufacturing combustion, industrial processes, waste, etc…), and their estimates must follow the guidelines established by the Intergovernmental Panel on Climate Change (IPCC). Similar activities are performed more and more frequently at regional and city scales. The bottom-up approach has significant uncertainties due to the incomplete accounting of all emitting sectors, and by the large uncertainties in the emission factors and activity statistics for many source sectors.

The greenhouse gases inventories currently reported by UNFCCC do not provide a complete picture of the global emissions since not all countries report their emissions every year. For this reason, comprehensive and consistent inventories are developed in addition to the national inventories reported to UNFCCC. This is for example the case of the Emissions Database for Global Atmospheric Research (EDGAR) (Janssens-Maenhout et al., 2017), which estimate anthropogenic emissions for all world countries (e.g. EDGARv4.3.2 FT2012 inventory available at http://edgar.jrc.ec.europa.eu/), or the European inventory provided by Institute for Energy Economics and the Rational Use of Energy (IER), University Stuttgart. Such inventories also have the advantage of providing information on regular spatial grids, which can be used as an input to the atmospheric simulations.

The inventories, like EDGAR or IER, generally do not cover all natural emission processes, like for example the CO_2 exchange with the terrestrial ecosystems due to the plant and soil respiration, or the carbon uptake due to the photosynthesis. For those sectors, we may use biogeochemical models which often used remote sensing observations of the state of the vegetation and the weather. Such models are themselves validated by using direct measurement of atmospheric fluxes, which are very local and representative of an area less than 1 km^2 (Schmid et al., 1994). Due to the strong spatio-temporal heterogeneities of the fluxes, the extrapolation of such measurements using biogeochemical models still faces significant uncertainties.

I.5.2 Top-down approach

The top-down approach provides an estimation of the surface fluxes using measured atmospheric concentrations, atmospheric models, and prior information of the surface fluxes. In this thesis, the

quantification of the CO_2 and CH_4 fluxes over France will be performed using the Bayesian top-down approach (Tarantola et al. 2005) called hereafter by the inverse modelling. The robustness of this approach depends on the quality of the transport model that mix and transport the surface fluxes to be comparable with the measured concentration. The atmospheric concentration of a given gas represents the amount of fluxes transported in the atmosphere through different processes (e.g. horizontal and vertical mixing). As shown by Peylin et al (2002), the estimation of the CO_2 fluxes at the regional scale can be uncertain in case of important transport errors. Consequently, the first step before the development of any inverse modelling framework should be the evaluation of the quality of the transport model used to build our inverse system.

The top-down approaches represent thus a powerful tool to evaluate and verify the emission inventories provided by the bottom-up approach (Marquis et al., 2008). Previous studies showed significant differences between the top-down and the bottom-up GHG estimates (Bergamaschi et al., 2018, Kountouris et al., 2018, Le Quéré et al., 2015, Saunois et al., 2016). For example, the long term atmospheric measurements of sulfur hexafluoride (SF6), an industrial gas with an atmospheric lifetime of about 850 years, suggested an under-estimation of the SF6 emissions reported by countries to UNFCC by a factor of two (Levin et al., 2010). Several studies have demonstrated in recent years that atmospheric measurements of CO_2 and CH_4 can be used to quantify top-down continental emissions in Europe and the United States, where the monitoring networks are the densest. This was the case for example for Bergamaschi et al (2018) who estimates higher CH_4 emissions for the European countries compared to the bottom-up inventories.

I.6 Estimation of the regional fluxes

I.6.1 Some techniques for flux optimization

During the last two decades, the top-down approaches, known also by flux inversion, have been largely used for the estimation of the GHG surface fluxes at the global (e.g. Enting et al., 1995; Kaminski et al., 1999a; Gurney et al., 2003; Locatelli et al., 2013), and the regional scale (e.g. Gerbig et al., 2003; Peylin et al., 2005; Lauvaux et al., 2012; Broquet et al., 2013, Berchet et al., 2014, Bergamaschi et al., 2018, and Pison et al., 2018). Several techniques have been developed with the aim to estimate the surface flux patterns at a relatively high spatio-temporal resolution. One approach consists of dividing the domain into several regions based on prior information such as the vegetation type or climate area. Panareda et al (2016) used this approach to optimize the surface fluxes by applying a factor to rescale the CO_2 biogenic fluxes for each vegetation type. A different approach was used by Lauvaux et al. (2012) to optimize the regional fluxes at a

weekly time scale by separating between daytime and night-time data. Lauvaux et al (2012) resolved the problem using the Bayesian inversion approach for matrice solution based on an analytical framework (Tarantola, 2005). Using the same Bayesian approach, Bréon et al (2015) and Staufer et al (2016) performed a flux inversion in order to estimate the anthropogenic CO_2 emissions using the atmospheric measurements at a sub-national scale in France. For this thesis, we have used a similar Bayesian approach applied to the national inventory of CO_2 and CH_4 emissions over France, where we are benefiting from the recent development of the atmospheric monitoring network as part of the Europeans research infrastructure ICOS.

I.6.2 Estimation of CO_2 fluxes

Using the Bayesian inversion framework, a compilation of three mesoscale and two global transport models, was performed in order to estimate the European CO_2 fluxes from three atmospheric inversion frameworks (Rivier et al., 2010). In this work, the authors demonstrate that the European continent could be split in a CO_2 sink for all western and southern European countries, and a CO_2 source for the central and Eastern Europe (Figure I.6). In this study, the five inversion systems were in good agreement to estimate a sink of about -1 GtC/year for western and southern Europe, a CO_2 source of less than 0.8 GtC/year for Central Europe, and less than 0.2 GtC/year for Eastern Europe (Figure I.6). In a more recent study, Kountouris et al., (2018) estimate the biogenic carbon fluxes for Europe using seven high-resolution regional inversion systems. The result of this study confirms the CO_2 sink over Europe with a value that may reach -0.71 GtC/year as presented in figure I.7. The two studies estimated the annual CO_2 budget in Europe with significant uncertainties, which may reach more than 50%. This indicates that our knowledge of the biospheric CO_2 flux estimate in Europe remains uncertain.

The comparison between the regional inversion results of Kountouris et al (2018) and earlier studies (Ciais et al., 2000, Gurney et al., 2004, Rivier et al., 2010, Peylin et al,. 2013, Reuter et al,. 2014) confirms the high uncertainty of the European CO_2 surface fluxes (Figure I.7). The estimated fluxes from Kountouris et al., (2018) range between -0.23±0.13 GtC/year and -0.38±0.17 GtC/year, and reach -0.55±0.2 GtC/year for the TransCom European region as defined in Gurney et al (2002). For the earlier studies the estimated fluxes vary between -0.3±0.8 GtC/year for the period 1985-1995 (Ciais et al., 2000) and -1.1±0.3 GtC/year for the year 2007 (Reuter et al., 2014). The significant differences between the different studies can be related to the high interannual variability of the surface fluxes as demonstrated by Broquet et al (2013). The first inverse modelling of CO_2 have focused on the natural CO_2 fluxes, which have much larger uncertainties than the anthropogenic CO_2 emissions. In thoses studies it is commonly assumed that the uncertainty of fossil fuel

CO_2 emissions is negligible (Peylin et al., 2011). In order to increase our understanding about temporal and the spatial variabilities of the CO_2 fluxes in France (biogenic and anthropogenic), we have developed in this thesis a high-resolution inversion framework dedicated to optimize the estimated CO_2 surface fluxes at a fine resolution over France.

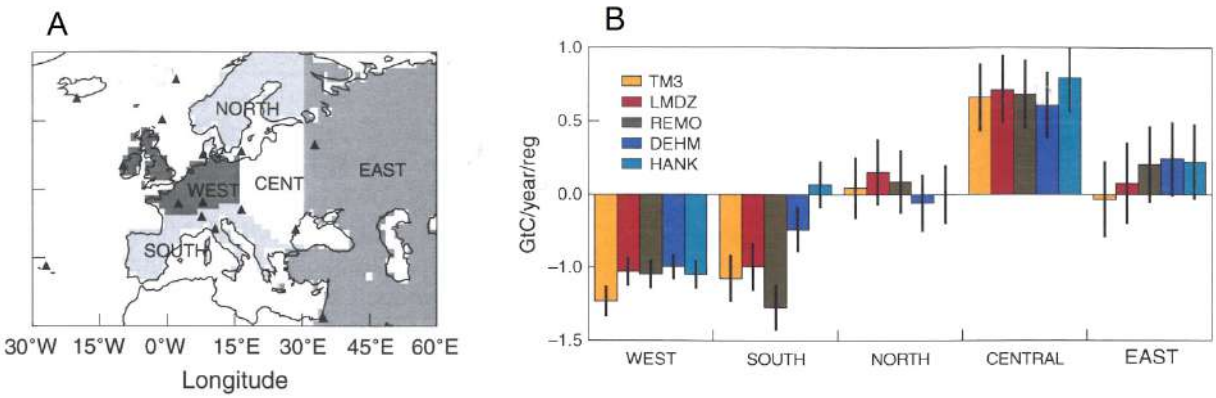

Figure I.6: Panel (A) displays the regions on which the estimated fluxes are aggregated. Panel (B) represents the estimated net carbon flux and the corresponding uncertainties for the sub-continental European regions presented in panel (A). The inversion was performed using five atmospheric transport models as described in Rivier et al., (2010). The figure is taken from Rivier et al., (2010).

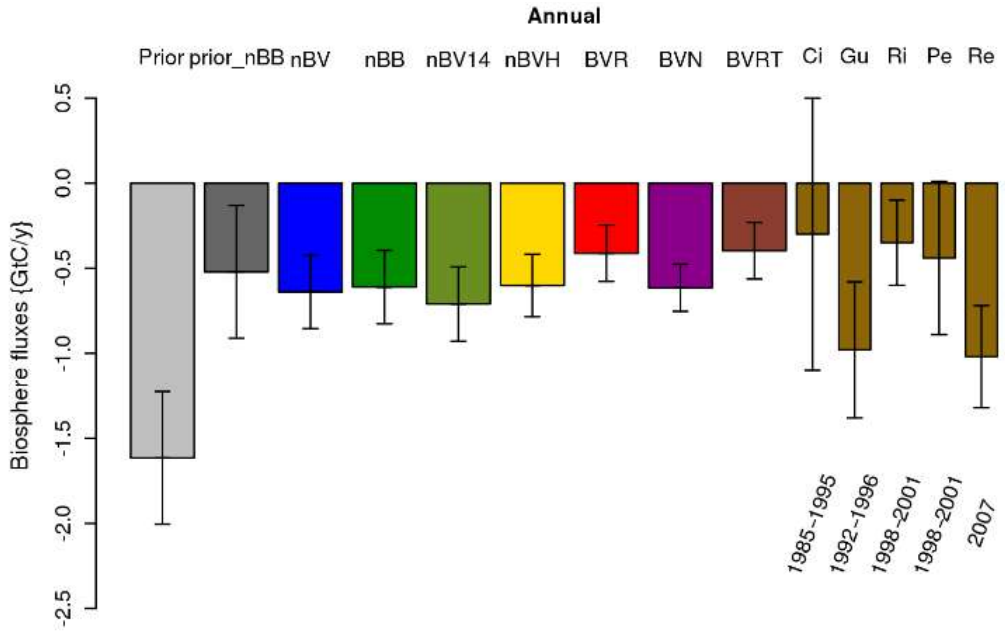

Figure I.7: Annual biogenic CO_2 budget (GtC/yr) in Europe retrieved from the inversion results using seven different scenarios (nBV, nBB, nBV14, nBVH, BVR, BVN, and BVRT) as described by Kountouris et al., (2018). The inversion results are compared to previous studies labeled by Ci (Ciais et al., 2000), Gu (Gurney et al., 2004), Ri (Rivier et al., 2010), Pe (Peylin et al,. 2013), Re (Reuter et al,. 2014). Periods for the inverted fluxes are given below the estimated fluxes. The figure is taken from Kountouris et al., (2018).

I.6.1 Estimation of CH_4 fluxes

For the CH_4 flux inversion, a recent study was carried out by Bergamaschi et al., (2018) for the estimation of the European methane emissions using seven inverse models for the years 2006-2012. The used inverse models estimate a CH_4 emission that ranges between 20.2 and 29.7 $TgCH_4$/year for the EU-28 countries, with a significant seasonal cycle (Bergamaschi et al., 2018). These estimates are different from the total emission reported by the United Nations Framework Convention on Climate Change (UNFCCC). For the EU-28, the UNFCCC emissions based on bottom-up approaches provided a total of 21.3 $TgCH_4$/year for 2006, and 18.8 $TgCH_4$/year for 2012 (Figure I.8). The difference between the UNFCCC estimates and the inversion results was assumed to be linked to the contribution of the natural emissions (e.g. wetlands, peatlands, swamps, and rice fields). The later emissions are quantified for the EU-28 by a range of 2.3-8.2 $TgCH_4$/year from the WETland CH_4 Inter-comparison of Models Project (WETCHIMP, Kaplan et al ., 2018). Similar conclusions were found by Pison et al., (2018) about the impact of the CH_4 natural emission on the flux estimation over

France during the year 2012. The inversion system developed by Pison et al (2018) increases the total CH_4 emission fluxes over France by a value ranging between 25 % and 50 % compared to fluxes reported by the UNFCCC and displayed a significant seasonal cycle which was absent in bottom-up estimates. Similar to CO_2, the same inversion system is applied to CH_4 in order the to decrease the uncertainties associated with current estimates and to increase our understanding of the small-scale patterns responsible for the CH_4 variations.

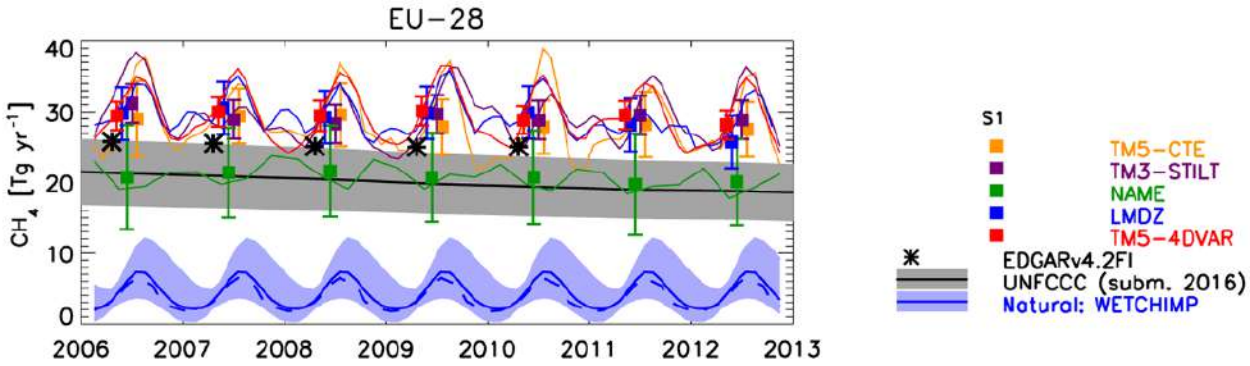

Figure I.8: The annual variations of the total CH_4 emissions for the EU-28 countries derived from five inversion systems (colored symbols) as described by Bergamaschi et al (2018). For comparison, the CH_4 anthropogenic emissions reported to United Nations Framework Convention on Climate Change (UNFCCC, blackline, the grey range for the corresponding uncertainties), and from EDGARv4.2FT-InGOS (black stars) are presented. The blue lines (resp. light-blue range) show wetland CH_4 emissions (resp. minimum-maximum range) retrieved from the WETCHIMP ensemble of seven models. The figure is taken from Bergamaschi et al (2018)

I.7 Objective and structure of this thesis

In line with earlier studies, the present work in this thesis aims at improving the knowledge of the CO_2 and CH_4 sources and sinks over France using the top-down atmospheric approach. This work is motivated by the increasing number of the measurement stations during the last decade over Europe, which provides valuable information to feed the inversion system dedicated to estimate the greenhouse gas surface fluxes. The availability of high-resolution atmospheric transport models (Menut et al., 2013), which improve the representation of the simulated concentrations at a high frequency, has also contributed to have made possible the objectives of this study. The advances of the last two aspects represent the principal ingredient to

improve our understanding of the national and regional budget of the principal greenhouse gases using the atmospheric measurements and inverse techniques, which are described in the following chapters.

Chapter II represents an analysis of the long-lived trace gas concentrations in the atmosphere from continuous measurement at four contrasting sites from a tall-tower station in France (OPE site), a high-mountain station in France (Pic Du Midi), a regional marine background site in Crete (Finokalia) and a marine clean-air site in the Southern Hemisphere (Amsterdam Island). Continuous measurement of CO_2, CH_4, and CO are investigated in order to identify the atmospheric data influenced by local emissions (within few kilometers) that can result in high spikes in time series of greenhouse gases (GHG) and long-lived tracer measurements. These spikes due to local emissions are very difficult, or even impossible, to simulate by the transport models and need to be separated from the regional and the large-scale atmospheric signals. We have considered three spike detection methods known as Coefficient Of Variation (COV), Robust Extraction of Baseline Signal (REBS) and Standard Deviation of the background (SD) to detect and filter out positive spikes in continuous time series. The results of the different methods are compared to each other and against manual detections performed by station managers. This study provides the information required to better evaluate the influence of the local contamination on the continuous time series and to quantify their impact on the hourly measurements used by the atmospheric transport models.

Chapter III involves simulations of the CO_2 and CH_4 atmospheric concentrations during the year 2014 using the regional chemistry-transport model CHIMERE (Menut et al., 2013) over France with a horizontal resolution of 0.1°x0.1°. A set of 8 forward simulations has been performed with two meteorological fields (AROME and ECMWF), two biogenic models (CTESSEL and VPRM), and two anthropogenic inventories (IER and EDGARv4.2). The simulated concentrations of CO_2 and CH_4 are compared to the atmospheric measurements provided by 16 observation sites from national and European networks (8 stations in France, and 8 in the neighbouring countries). The model performance is evaluated in order to assess the sensitivity of simulated concentration to various input data at the national and the sub-national scales. The multiscale evaluation and the comparison between the different input data have implications for the enhancement of the simulated concentration and consequently for setting up an appropriate inverse system. The best couple of input data (transport and surfaces fluxes) is, thus, selected as prior information for the inversion of CO_2 and CH_4 fluxes in France.

Chapter IV focuses on estimating the CO_2 and the CH_4 fluxes over France for two months: one month in winter (January) and one month in summer (July), in order to estimate the optimized fluxes for two

contrasted periods. The flux estimation is carried out using the analytical inversion framework PYMAI developed by Berchet et al., (2013, and 2015) and the atmospheric surface stations. The inversion is performed using the best prior information selected based on the analysis of the bottom-up estimates (Chapter 3). To account for the inversion errors, the used system is completed by a statistical calculation, implemented by Berchet et al., (2013), that quantify the objectively the inversion errors. These errors are evaluated and compared to an analytical uncertainty estimation provided by the analysis of the difference between the different surface fluxes and transport models used in Chapter 3. We conclude the study by a comparison between the retrieved fluxes and the prior estimates, in addition to a comparison with results from earlier studies in order to quantify the impact of our inversion system on the uncertainties of the surface fluxes.

Chapter II: Identification of spikes associated with local sources in continuous time series of atmospheric CO, CO_2 and CH_4

Abdelhadi El Yazidi[1]. Michel Ramonet[1]. Philippe Ciais[1]. Gregoire Broquet[1]. Isabelle Pison[1]. Amara Abbaris[1]. Dominik Brunner[2]. Sebastien Conil[3]. Marc Delmotte[1]. Francois Gheusi[4]. Frederic Guerin[5]. Lynn Hazan[1]. Nesrine Kachroudi[1]. Giorgos Kouvarakis[6]. Nikolaos Mihalopoulos[6]. Leonard Rivier[1]. Dominique Serça[5]

[1]Laboratoire des sciences du climate et de l'environnement, LSCE/IPSL, CEA-CNRS-UVSQ, Université Paris-Saclay, 91191 Gif-sur-Yvette,France
[2]Laboratory for Air Pollution/Environmental Technology, Swiss Federal Laboratories For Materials Science and Technology, EMPA, Duebendorf, Switzerland
[3]Direction Recherche & Développement, Andra, CMHM, RD960, 55290 Bure France
[4]Laboratoire d'Aérologie, Université de Toulouse, CNRS, UPS, UMR5560, 14 Av. Edouard Belin, 31400 Toulouse,
[5]Geosciences Environnement Toulouse UMR 5563 & UR 234 IRD, Université Paul-Sabatier, Avenue Edouard Belin 14, F-31400 Toulouse, France
[6]Environmental Chemical Processes Laboratory, Department of Chemistry, University of Crete, 71003, Heraklion, Greece

The full article of El Yazidi et al. 2018 was published in the journal of Atmospheric Measurement Techniques, 11, 1599-1614, (Copernicus Publications) on March 22th, 2018, date of submission, July 17th, 2017.

II.1 Summary

II.1.1 Context of the study

The greenhouse gases (GHG) estimations are carried out based on atmospheric inverse models that use the measurement of the atmospheric concentrations of long-lived GHG provided by ground-based sampling sites. These inverse systems are based on atmospheric transport models that use as input estimates of the surface fluxes to reproduce the atmospheric concentrations of the GHG. Due to the limited spatial resolution of the transport models and the uncertain surface emissions, the simulated concentrations may exhibit some atmospheric variations that do not fit correctly to the observed variations. Especially, local emissions located nearby the atmospheric station, within a couple of kilometers, may lead to significant impacts on the atmospheric concentrations. In such case we expect the contaminated data to show intense and sharp positive

perturbations, which cannot be captured by the transport models. Thus, it is essential to separate the data which are strongly influenced by local emissions, from those influenced by regional and large-scale fluxes. To avoid an error of allocation of the local emission to larger scales by the inversion, the influence of these local contaminations must be filtered out from the time series.

II.1.2 Material and methods

We have developed an analysis of greenhouse gases atmospheric time series in order to provide a method of identifying atmospheric data influenced by local emissions that can result in short term spikes. In order to detect and filter out the spikes from the continuous greenhouse gas time series we have implemented three spike detection methods known as coefficient of variation (COV, Brantley et al., 2014), robust extraction of baseline signal (REBS, Ruckstuhl et al., 2012) and standard deviation of the background (SD, Drewnick et al., 2012). The methods are applied on two years of CO_2, CH_4, and CO measurements provided by four atmospheric sites from stations representative of the European ICOS (Integrated Carbon Observation System) Research Infrastructure network and more remote sites. We use a continental rural tower of 100 m height in eastern France (OPE), a high-mountain observatory in the south-west of France (PDM), a regional marine background site in Crete (FKL) and a marine clean-air background site in the Southern Hemisphere on Amsterdam Island (AMS). This selection allows us to address spike detection problems in time series characterized by different variabilities.

II.1.3 Selection and the optimization of the spike detection methods

All methods were found to be able to detect short-term spikes (lasting from a few seconds to a few minutes) in the time series. The spikes detected by the three methods are compared to each other, and when available against manual detection performed by station managers and recorded in their logbooks. For PDM site, the analysis of the GHG time series is completed by a field campaign data analysis that involves two sampling instruments measuring simultaneously CH_4 and CO_2 molar fractions 200 m away from each other, one being very close from a waste water treatment plant causing CH_4 spikes. The comparison of the two time series was used as a test of the efficiency of different methods to filter out the local spikes in order to retrieve the uncontaminated background signal. The evaluation of the results of the three methods leads us to exclude the COV method due to the requirement to arbitrarily specify an a priori percentage of rejected data in the time series. This a-priori determination of the percentage of spikes may over or underestimate the actual number of spikes. The two other methods freely determine the number of spikes for a given set of internal

parameters. These parameters are calibrated to provide the best match with spikes known to reflect local emissions episodes that are well documented by the station managers. The calibration of the SD and the REBS methods is performed based on the existing dataset, and sensitivity tests are done to evaluate the impact of each parameter. Based on the different sensitivity tests for the SD and REBS parameters, and the prior estimation of the percentages of spikes manually detected by site managers, we have proposed an optimal configuration of the two methods used to detect the local contaminations at the four stations.

II.1.4 Principal results

The application of the automatic methods on the time series showed a good performance of SD and REBS to correctly detect spikes associated with local contaminations. At PDM, the measurements made by the two analyzers located 200 m from each other confirmed that the CH_4 spikes observed at one site, corresponding to a local source from a sewage treatment facility close to the observatory buildings. From this experiment, we also found that the REBS method underestimates the number of positive anomalies in the CH_4 data caused by local sewage emissions. When the percentage of spikes is high, the calculation of the REBS method baseline is biased toward higher concentrations. This lead to the underestimation of spike anomalies since the difference between the baseline and the measured concentrations is lower than the threshold value. For the same situations, the SD method correctly detects most of the contaminated data.

The comparison between the two automatic methods and the manual flagging showed a good agreement with 70 % of successful spike data detection for SD and 60 % for REBS for sites where local contaminations were initially identified in the station logbook. The analysis shows substantial differences between the manual and the automatic spike detection method for the measurements which are at the lower part of the spikes. These data are very difficult to detect since they are close to the reference values to which the spikes are compared.

Running the spike detection method on 1-minute time series allows the quantification of the impact of the contaminated data on the hourly averages used by the atmospheric inversion systems. This analysis confirms that the impact of the short-duration spikes on hourly data at the background sites remain less than 0.5 ppm for CO_2 and less than 5 ppb for CH_4 and CO. At stations located in areas surrounded by more local sources (e.g. rural areas in Europe) this offset by local sources may impact the hourly averages by a value up to 10 ppb for CH_4 and CO, and 1 ppm for CO_2.

II.1.5 Conclusions and implications

As a conclusion from this analysis from a limited number of atmospheric stations, we recommend the use of the SD method, which appears to provide the better results, and is also the easiest one to implement in the automatic data processing set up for the ICOS network. Consequently, after presenting the results of this work to the ICOS atmospheric community, the SD method was proposed for implementation in the ICOS data processing handled by the Atmospheric Thematic Centre to automatically process the raw data from the ICOS stations on a daily basis (Hazan et al., 2016). This method has been recently applied to the 1 minutes GHG time series of 15 ICOS stations for the year 2017 (Figure II.1). At most stations, the monthly mean percentages of 1 min data identified as spikes are generally lower than 5%, with few exceptions which may reach percentages up to 10 to 15% (Figure II.2). For each hour when minute averaged data are identified as spike and consequently filtered out, it results in a decrease of the corresponding hourly concentration. The differences between the hourly means calculated with and without the 1 min spike data have been averaged on a monthly basis for the year 2017 (Figure II.3). The results for the 15 ICOS stations show that differences are generally lower than 0.2 ppm for CO_2, 1 ppb for CH_4 and 0.4 ppb for CO. There are few exceptions, with a monthly mean difference up to 0.8 ppm CO_2 in Puijo (February 2017), and 3 ppb CH_4 in Ispra (December 2017). Those results are currently investigated by the different station managers in order to associate the identified spike using the method we have developed, with processes associated with local pollutant emissions and local atmospheric transport.

Figure_II. 1: ICOS Stations used to evaluate the spike detection algorithm

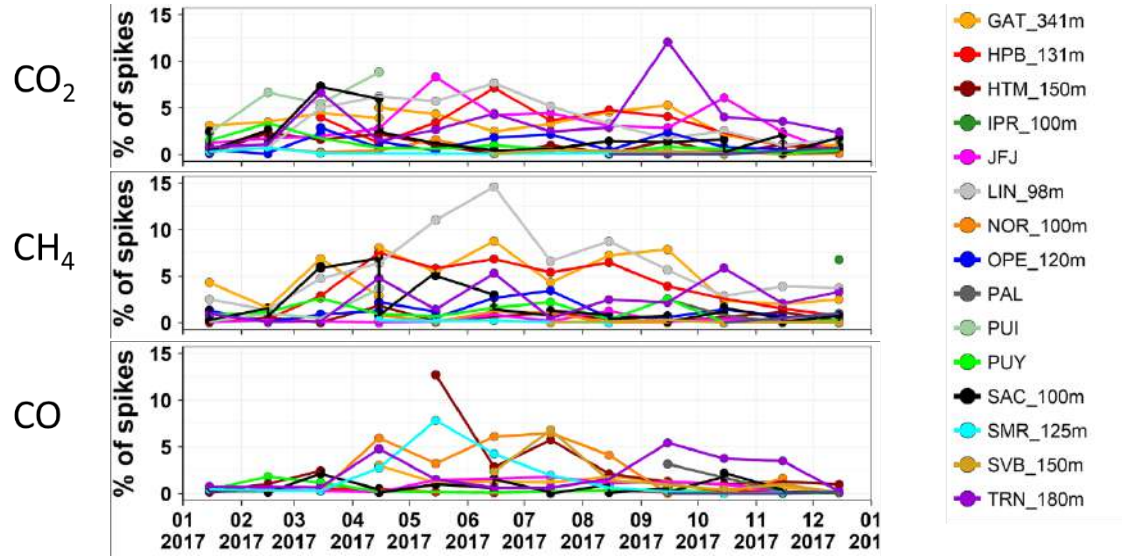

Figure_II. 2: Percentages of minute data detected as spikes for CO_2, CH_4 and CO, every month in 2017 at 15 ICOS stations

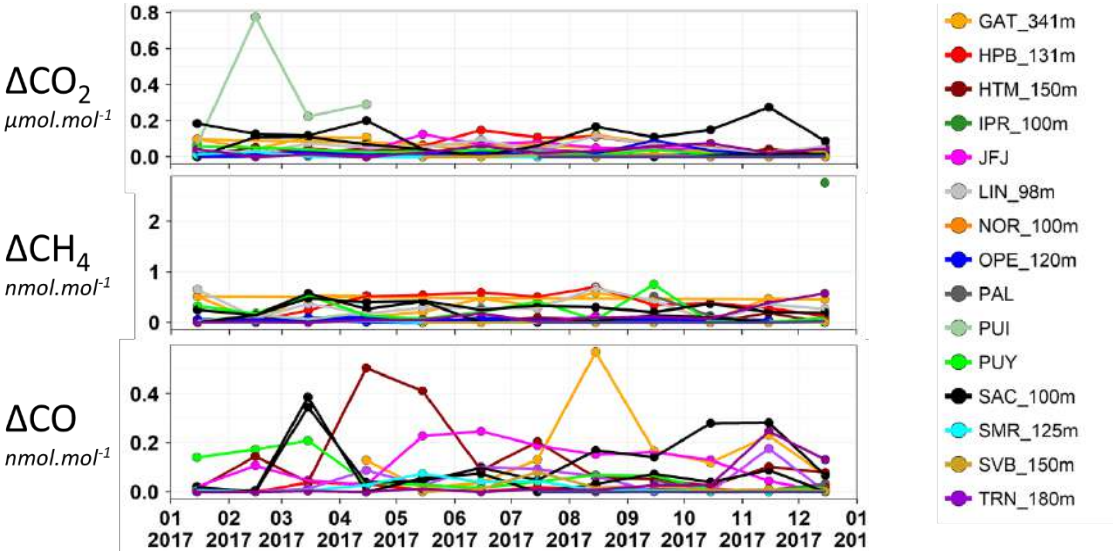

Figure_II. 3: Monthly means of the CO_2, CH_4 and CO hourly concentration differences with and without spikes at15 ICOS stations

II.2 Introduction

Continuous measurements of long-lived greenhouse gases (GHG) such as carbon dioxide (CO_2) and methane (CH_4) at ground-based monitoring stations are commonly used in atmospheric inversions for the estimation of surface fluxes. The variability of GHG continuous time series reflects atmospheric transport processes and surface fluxes. One difficulty in matching these measurements with atmospheric transport model simulations

is that they exhibit variability at a wide range of timescales, which is imperfectly captured by transport models due to their limited spatial resolution and to uncertain surface emission inventories. In particular, local emissions in the vicinity of stations can have a major influence on concentrations, generating brief but intense positive perturbations, hereafter referred to as "spikes". Every measurement has a specific spatial representativeness, and knowledge of this information allows for a much finer interpretation of the observation. It is desirable, in continuous GHG time series, to separate those data strongly influenced by local emissions (fluxes within less than few kilometres) from those influenced by regional (few tens of kilometres) and large-scale (hundreds or thousands of kilometers) fluxes and transport. The influence of local fluxes, in particular of nearby point sources of emissions, should be filtered out prior to the use of the time series in inversion models if the models do not have the ability to represent it. For instance, a road near a station can emit CO_2, causing spikes in the time series, because this road is not accounted for in the emission inventory used in an inversion.

Having empirical information on the representativeness of continuous GHG time series, e.g. a logbook available for each station, allows for more precise interpretation of the atmospheric measurements in terms of the processes involved in the observed variability. It is interesting, for example, to assign the contribution of specific sources (e.g. point sources of fossil CO_2 emissions or biomass burning events) within the local vicinity of the station. Several methods have been proposed to account from local to regional influences in greenhouse gas observations according to other observables, such as wind speed and direction (Perez et al., 2012a) and tracers like radon-222 or black carbon (Biraud et al., 2002; Fang et al., 2015; Williams et al., 2016). Air-mass trajectory information is also frequently used (Ramonet and Monfray, 1996; Ferrarese et al., 2003; Maione et al., 2008; Fleming et al., 2011; Perez et al., 2012; Gerbig et al., 2006). Other methods based on a statistical treatment of time series (Giostra et al., 2011; Ruckstuhl et al., 2012) are easier to generalize because they require no additional observable. A commonly used strategy by modelers, using transport models of a typical resolution from 10 to 50 km, consists of systematically removing some periods of the day (e.g. nighttime for surface stations or daytime for mountain sites) in order to filter the influence of non-resolved mesoscale circulations or vertical transport processes poorly represented by models (e.g. sporadic turbulence in stable or neutral nighttime boundary layers).

The development of regional networks for monitoring GHG and related tracer concentrations leads to an increasing number of continuous measurement stations, especially in continental areas. For example, the European ICOS (Integrated Carbon Observation System) Research Infrastructure is developing a network of

tall towers for very precise GHG measurements across the European continent. It is thus important to characterize the representativeness of each individual measurement in order to separate spikes from local emissions that should not be used in studies aiming at constraining regional fluxes. In this study, our objective is to compare methods that could be used operationally to remove the contaminations from local sources at continuous measurement stations. Local contamination may be due, for example, to fossil-fuel-based power generation at the station facility and local traffic. The short-term variations (few seconds to minutes) of GHG associated with those of local sources have rarely been analysed, and they have generally been time averaged with consecutive data. Some studies, however, have been focusing on local emissions on the basis of the detection of short-term "spikes" (Monster et al., 2015). Here, "local" refers to emissions at less than a few kilometers from the station causing positive short-term spikes of a few seconds to a few minutes superimposed on the signal resulting from boundary layer mixing, synoptic transport regional fluxes. Other methods such as the Fourier transform filters (Savitkzy Golay, 1964) and the wavelet transforms (e.g. Wee et al., 2008) have been considered at the beginning of this study, but these methods require continuous time series and smooth signals. Considering that the measurements are regularly interrupted due to different reasons (e.g. calibration, flushing time after switching from sampling level to another, power or internet outage), we had to select a method that handles time series with data gaps. Moreover, applying a Fourier transform method on continuous measurements provides a signal composed by frequencies only, and all information that varies with time will be lost. In other words, we can analyse what happens (spikes to be filtered out) without knowing when this happens, which is essential information to better understand the sources of contaminations. We compare here spike detection algorithms for local sources in greenhouse gases (CO_2 and CH_4) and long-lived tracer time series (CO). The algorithms chosen in this study have been applied to air pollution data (e.g. ultrafine particles, particulate matter and nitrogen dioxide NO2) which have shorter lifetimes than CO_2, CH_4, and CO (Brantley et al., 2014). In the case of GHG, spikes can be caused by local sources but also by the fast transport of remote emissions. Compared to short lifetime species, spikes in GHG are not always larger than the variability associated with synoptic scales. For CO_2, uptake by local vegetation may occasionally lead to negative spikes, which will not be evaluated in this study (only positive spikes are considered).

The three spike detection algorithms – coefficient of variation (COV), robust extraction of baseline signal (REBS) and standard deviation of the background (SD) – are described in section II.3.2, then applied to 2 years of continuous measurements of CO_2, CH_4, and CO at four stations representative of the European network of GHG monitoring stations. The study will focus more on the SD and the REBS since they are fully

automatic and they do not require any a priori information for the implementation. The results are discussed in section II.4. Wherever possible, the ability of an algorithm to successfully detect and remove the effects of local sources and transport is verified using independent information about the presence and position of known local emissions.

II.3 Methodology

We selected four contrasting atmospheric GHG measurement sites operated by LSCE (Laboratoire des Sciences du Climat et de l'Environnement): a tall-tower station in France, a high-mountain station in France, a regional marine background site in Crete and a marine clean-air site in the Southern Hemisphere, which provided continuous data from 2013 to December of 2015 (Table II.1). Continuous measurements used in this study are averages with 1 min time resolution and are processed in near real-time (NRT) by the ICOS Atmospheric Thematic Centre (Hazan et al., 2016). The four stations have been used in regional and global atmospheric inversions to estimate GHG surface fluxes at regional and global scales (e.g. Bergamaschi et al., 2018; Le Quéré et al., 2007; Saunois et al., 2016).

II.3.1 Measurement sites and methods

II.3.1.1 Measurement sites

Amsterdam Island (AMS; 37°48'S, 77°32'E). This marine background station is operated since 1980 to monitor trends of trace gases in the southern hemispheric mid-latitude clean-air atmosphere. The observatory is located on the coast of a small island (55 km2) covered by short grasslands, in the middle of the Indian Ocean 3000 km south-east of Madagascar. Measurements are performed at the Pointe Bénédicte site located north of the island, on the edge of a 55 m cliff above sea level. The air is sampled at the top of a 20 m high tower. The station contributes to the Global Atmospheric Watch program (WMO/GAW). The data used to feed the WMO/GAW database and estimate the long-term trends are filtered according to local wind measurements to avoid the influence of CO_2 emissions from the island itself (Ramonet and Monfray, 1996).

Finokalia (FKL; 35°20'N, 25°40'E). This coastal station is located on the northern coast of Crete, 350 km south of mainland Greece. The nearest city is Heraklion with a population of about 150 000 inhabitants, 50 km west of the station. There are no significant anthropogenic emissions within a circle of 15 km around the station (Kouvarakis et al., 2000). The station is on the top of a 230 m hill above sea level, and the air is

sampled at the top of a 15 m mast. The dry season from April to September is associated with strong winds from north and north-west (central Europe and Balkans), and the wet season from October to March is associated with air masses from North Africa (south and south-west winds) in addition to the dominant north-westerly winds. The station is operated by the Environmental Chemical Processes Laboratory (ECPL) at the University of Crete, which also collects aerosol and reactive gases (Hildebrandt et al., 2010; Pikridas et al., 2010; Bossioli et al., 2016; Kopanakis et al., 2016).

Pic du Midi (PDM; 42°56'N, 0°08'E). This high mountain site is located at 2877 m a.s.l. on the north westside of the Pyrenees range in south-west France, 150 km east of the Atlantic Ocean and 200 km west of the Mediterranean Sea. Due to its high elevation, the station often samples tropospheric air from the Atlantic Ocean, as well as air masses from continental Europe during high-pressure conditions over France (north-easterly winds) or from the Iberian Peninsula under southerly winds. Upslope winds and mesoscale circulations are frequent especially in summer and early autumn, bringing boundary layer air mostly from south west France (covered by intensive croplands and forests; Gheusi et al., 2011; Tsamalis et al., 2014; Fu et al., 2016).

Observatoire Pérenne de l'Environnement (OPE; 48°33'N, 5°30'E). This 120 m tall tower is located in a rural area at 395 m a.s.l. in the north-east of France (250 km east of Paris). It is located in a transition zone between oceanic westerly regimes and easterly winds advecting air from eastern Europe. The station continuously measures air quality and greenhouse gases since September 2011 as part of the European ICOS network. Every hour, ambient air is sampled for 20 min alternatively at heights of 10, 50 and 120 m on the tower (Table II.1).

II.3.1.2 Measurement methods

The gas analyzers used at the four stations are cavity ringdown spectroscopy instruments (CRDS; O'Keefe and Deacon, 1988), namely Picarro/G2401 analyzers at FKL, OPE and PDM with CO_2, CH_4 and CO and Picarro/G2301 at AMS with CO_2 and CH_4 (Table II.1). The measurement protocols used at the four stations are similar and based on ICOS specifications (https://www.icos-ri.eu/documents/ATCPublic). A calibration using four reference gases is performed every 3 to 4 weeks. Two more reference gases are analysed regularly for quality control purposes. The raw data (0.2 to 0.5 Hz) are transferred once per day to a central server and NRT datasets are available within 24 h. The NRT data processing (Hazan et al., 2016) includes automatic filtering of raw data based on the physical parameters of the analyzers (e.g. cavity temperature and pressure)

and threshold values for rejection of outliers. This last filter aims to reject aberrant values from the NRT dataset. It may happen that it rejects an extreme but real event, for instance due to an urban pollution plume. In such cases, the data will be validated afterwards by the station manager. After the automatic processing, the station managers are invited to validate or invalidate data manually using a specific software developed by the ICOS Atmospheric Thematic Centre. For data manually flagged as invalid, a reason must be provided (e.g. leakage, maintenance, local traffic). This procedure does not ensure the systematic rejection of spikes in the data from local or regional processes.

Meteorological measurements are also performed at the four stations with barometric pressure, temperature, wind speed, wind direction and relative humidity. Wind speed and direction are measured using 2-D or 3-D ultrasonic sensors installed at the same height of the greenhouse gas measurements. The sensors are adapted to the local weather; for instance at PDM (2877 m a.s.l.) the sensor is heated to avoid icing.

Site	Measured spices	Instrument	Longitude	Latitude	Ground level (m asl)	Sampling hight (m agl)	Starting date	End date
Pic du Midi (PDM)	CO, CO_2, and CH_4	Picarro / G2401	0°08'E	42°56'N	2877	10	2014-05-07	2015-12-31
Observatoire Pérenne de l'Environnement (OPE)	CO, CO_2, and CH_4		5°5'E	48°55'N	395	10, 50 and 120	2013-03-07	
Finokalia (FKL)	CO, CO_2, and CH_4		35°20' E	25°40' N	230	15	2014-06-05	
Amsterdam (AMS)	CO_2, and CH_4	Picarro / G2301	37°48' E	77°32' S	55	20	2013-01-01	

Table II.1: Measurement sites characteristics

II.3.2 Spike detection algorithms

Three algorithms were tested to detect positive short-duration GHG spikes lasting from a few seconds to a few minutes, using time series of 1 min averaged mole fractions of CO_2 (as illustrated in the appendix, Figure SII.1), CH_4 and CO. The three methods presented in this section are commonly based on the calculation of the local standard deviations of measurements. A spike is detected when the difference between a previously determined background and the current data value is above a defined threshold. We will present in this

section the corresponding threshold for the three methods. CO_2, CH_4, and CO 1 min data were processed using R version 3.1.3 (R Core Team, 2015) together with packages openair (Ropkins and Carslaw, 2015), IDPmisc (Locher et al., 2012) and ggplot2 (Wickham et al., 2016) using the three spike detection algorithms.

II.3.2.1 Coefficient of variation (COV) method

The COV method (Brantley et al., 2014) is a modified version of the method presented by Hagler et al. (2010). It was developed to analyse data from a mobile laboratory measuring ultrafine particle concentrations near a road transect (Brantley et al., 2014) for peak detection of carbon monoxide, which was used as an indicator of the passage of vehicles. In our application, we calculate the COV coefficients for CO_2, CH_4 and CO time series following two steps. First, the standard deviation of a moving 5 min time window (with one window for each 1 min data point) is calculated (2 min before and after each 1 min data point). Second, the standard deviation of each time window is divided by the mean value of the complete time series. The 99th percentile of the COV coefficients is used as a threshold above which 1 min data are considered to be part of a spike. We also identified as contaminated data all data recorded 2 min before and after each contaminated data. The COV method is sensitive to the choice of threshold percentile. In the Figure SII.2-A we illustrate an example of spike detection using the COV method during a CO contamination episode known to be affected by a local fire. One important feature of the COV algorithm, compared to the other methods, is the a priori definition of the percentage of data to be filtered (threshold percentile), meaning that the number of spike data is not automatically detected.

II.3.2.2 Standard deviation of the background (SD)

The SD method (Drewnick et al., 2012) considers that a time series is a combination of a smooth signal superimposed with a fast variable signal. The variable signal component in our case is related to local emissions causing spikes. To determine the variability of background concentration levels we calculated the standard deviation (σ) of data falling between the first and the third quartile of the entire dataset. A sensitivity test with various quantile ranges is presented in section II.4.1.1. We then select the first available data point, called C_{unf} (unflagged data, example in the Supplement Figure SII.2-B), assuming that it is not in a spike. The next data point in the time series C_i is evaluated with respect to C_{unf}, spikes are defined by data values higher than a threshold defined as C_{unf} plus an additive value: $\alpha * \sigma + \sqrt{n} * \sigma$ (e.g. the red data point in Figure SII.2-B), where α is a parameter to control the selection threshold, and n is the number of points between C_{unf} and C_i. The value of α depends on the time series variability. A sensitivity analysis on the influence of α is

presented in section II.4.1.1. We set a default value of $\alpha = 1$ for CO_2 and CH_4 and $\alpha = 3$ for CO (Drewnick et al., 2012). The lower value for CO_2 and CH_4 is justified in section II.4.1.1. The integer n contains a temporal information about the evolution of the time series. Indeed, while identifying a spike C_i, the next data point is evaluated against C_{unf} using an increased threshold to take in consideration the variability of the baseline during the spike event. If C_i is lower than the threshold from eqation II.1, it is considered as "non-spike" and becomes the new reference value C_{unf}. The following data will then be compared to this updated C_{unf}.

$$C_i \geq C_{unf} + \alpha * \sigma + \sqrt{n} * \sigma \quad \text{(II.1)}$$

The SD method was applied over one-week time windows, i.e. the standard deviation over σ a week is used for threshold calculation. Using a longer period (e.g. one year) would give more weight to the seasonal and long-term variabilities which are not relevant to identify short-term spikes using the one-year standard deviation.

II.3.2.3 Robust extraction of baseline signal (REBS)

The REBS method (Ruckstuhl et al., 2012) is a statistical method based on a local linear regression of the time series over a moving time window (characterized by a duration called the "bandwidth"), to account for the slow variability of the baseline signal, while outliers lying too far from the modelled baseline are iteratively discarded. The bandwidth h must be wide enough to allow for a sufficiently low fraction of outliers within h. The REBS code used here is based on the rfbaseline application developed in the IDPmisc package (Locher, et al., 2012) in R software. It is a modified version of the robust baseline estimation method developed to delete baseline from chemical analytical spectra (Ruckstuhl et al., 2001). The REBS method was applied at the high-Alpine Jungfraujoch site (Switzerland, 3580 m a.s.l.) and has been proven robust to estimate the background measurements of GHG (Ruckstuhl et al., 2012). The REBS method considers that greenhouse gas time series are composed of a background signal plus a regional contribution which may also include local effects (spikes) and measurement errors. The main difficulty is to correctly define the baseline signal of the measured time series. To achieve this goal, the choice of the bandwidth value is important. In the Jungfraujoch study, the baseline signal was defined as the smooth curve retrieved from REBS technique (Ruckstuhl et al., 2012) using a band width of 90 days, in order to distinguish the contribution of regional emissions that add to the slow seasonal variability. Since, in our study, the targeted spikes last a few seconds to a few minutes, we chose to calculate the baseline using a bandwidth of 60 min to detect spikes of a few minutes (maximum 5 min). The threshold for spike detection in REBS is based on the calculation of a scale

parameter β, which represents the standard deviation of data below the baseline curve, called $\hat{g}(t_i)$. All measurements $Y(t_i)$ that satisfy $Y(t_i) > \hat{g}(t_i) + \beta * \gamma$ are classified as locally contaminated (illustration in Figure SII.2-C). β is a parameter to adjust the filtering strength. Ruckstuhl et al. (2012) set β = 3 for the detection of polluted data. For our purpose, a sensitivity test with different values of β is carried out in section II.4.1.2.

II.4 Results

II.4.1 Optimization of the SD and REBS methods

II.4.1.1 Sensitivity to the parameters of the SD method

We conducted sensitivity tests in order to evaluate the influence of the two parameters α and σ used in the SD method. For α we tested values ranging from 1 to 3. Here, we present only the results for $\alpha = 1$ and $\alpha = 3$. For σ we compared the results calculated with σ based on 50% of 1-week data, data between the first and third quartile (scenario σ_b) and for all the data of the week (scenario σ_t). We studied four configurations (two values of α with σ_b or σ_t) on 1 min data every week at the four stations. Figure II.4 shows an example of spikes detected by SD at FKL on 16 December 2014, corresponding to a known waste-burning episode reported by the station manager. The station logbook mentions waste-burning occurring nearby the station between 06:30 and 08:30, shown by a purple bar in Figure II.4. The blue area in Figure II.4 shows the CO data between the first and third quartiles, leading to a $\sigma_b = 3.6$ ppb. Considering all the data, we obtain a 3 times higher standard deviation: $\sigma_t = 12.5$ ppb. The SD method with $\alpha = 3$ and $\sigma_b = 3.6$ ppb selects two 1 min data points as spike as illustrated by the orange dots falling within the observed fire episode in Figure II.4. With $\alpha = 3$ and $\sigma_t = 12.5$ ppb, the method fails to detect any spike, indicating that the threshold value was too high. With $\alpha = 1$ and σ_b the SD method selects 44 additional 1 min spikes compared to $\alpha = 3$ (data not reported as contaminated by the station manager). In both cases ($\alpha = 1$ or $\alpha = 3$) and σ_t lead to a very high threshold and an underestimation of the number of spikes detected, since σ_t includes the spike variabilities. Based on this sensitivity test against a known local emission episode, we definitively rejected the use of σ_t scenario.

Table II.2 represents the percentage of contaminated data detected over 1 year at the four sites, in the four tested configurations. As can be seen, using all 1 min data to calculate σ_t leads to a higher threshold and consequently to less data detected as contaminated. On average over the four stations and the three species, switching from σ_b to σ_t decreases the percentage of spikes by a factor of 15 ± 16 (Table II.2). Setting $\alpha = 3$ increases the threshold and also decreases the number of spikes by on average a factor of 5 ± 7 (Table II.2).

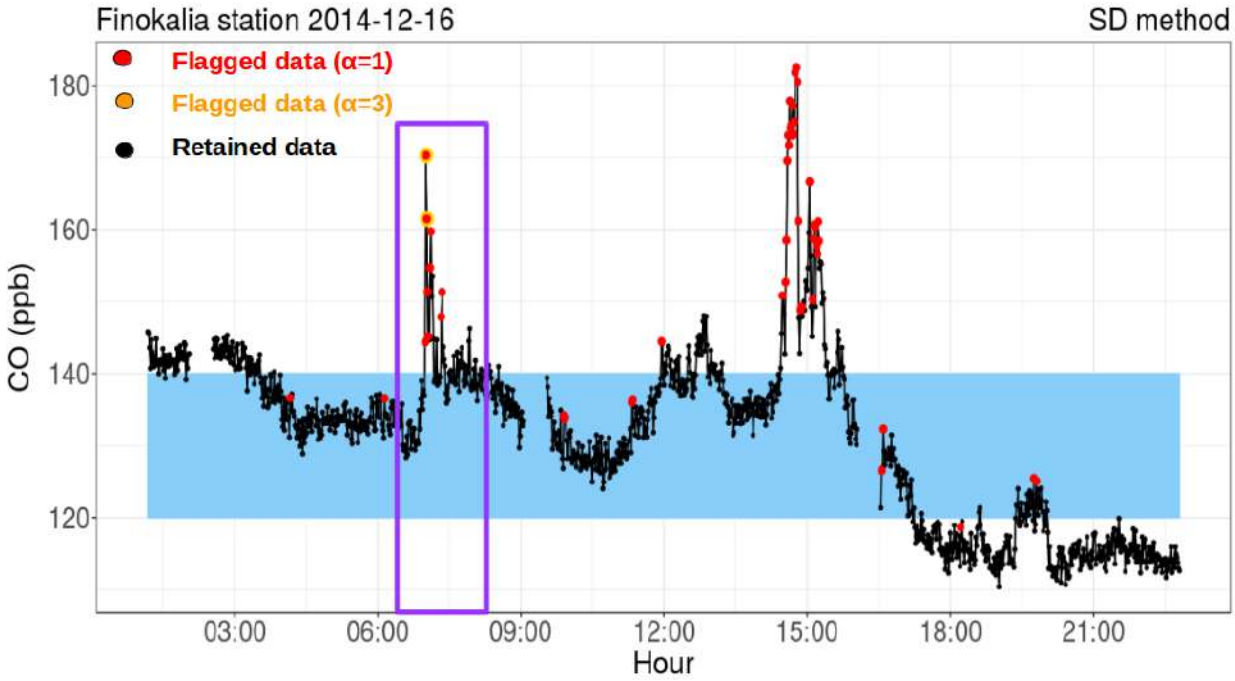

Figure II.4: comparison between two sets of α parameter for SD method. Red color represents detected spikes for α=1, orange data are the detected spikes for α=3. The blue area shows the data between the first and the third quartile (q1=0.25, and q2=0.75).

Site	Spices	Contaminated data percentages (%)			
		σ_b scenario		σ_t scenario	
		α =1	α =3	α =1	α =3
AMS	CH_4	0.03	0.01	0.006	0.003
	CO_2	0.07	0.03	0.01	0.006
FKL	CH_4	0.2	0.02	0.02	0.002
	CO_2	0.1	0.04	0.01	0.002
	CO	3	0.4	0.3	0.07
OPE	CH_4	0.7	0.3	0.06	0.01
	CO_2	0.8	0.04	0.02	0.01
	CO	0.9	0.4	0.1	0.02
PDM	CH_4	6	2	1	0.1
	CO_2	0.2	0.05	0.02	0.005
	CO	3	0.1	0.04	0.004

Table II.2: Sensitivity of SD method spike detection for two sets of α (α=1 and α=3), and for two range of background data interval (σb and σt scenario) for the four stations and all species.

The parameter α is related to the variability of the time series. Since our study aims to provide recommendations for automatic data processing of a monitoring network like ICOS in Europe, we would ideally keep the same set of parameters for all the stations of the network for each species. However, all the tests conducted in the present study have shown that it was not optimal to use the same parameter for the CO time series as for the CO_2 and CH_4 time series. Setting a lower α for CO leads to the overestimation of the number of spikes in the time series. This must result from the different variabilities of those trace gases. For instance, the ratio between hourly and minute-scale variabilities (characterized by standard deviations) for the sites used in this study is on average 2 times smaller for CO compared to CO_2 and CH_4. As recommended in Brantley et al. (2014) and Drewnick et al. (2012), we decided to keep α = 3 for CO and set α = 1 for CH_4 and CO_2 because of their lower variability.

II.4.1.2 Sensitivity to the parameters of the REBS method

In order to evaluate the sensitivity of spikes to the parameter β, we tested values of β ranging from 1 to 10. In this study, we present the REBS method using the default value β = 3 as proposed by (Ruckstuhl et al., 2012) in Jungfraujoch, compared with the optimal value for our purpose, β = 8. The resulting spike selection at FKL (during a local fire episode) is shown in Figure II.5. By setting β = 3, the REBS method detects the spike during the episode but it also finds other events which do not appear to be associated with evident contaminations (Figure II.5). With β = 8, the REBS correctly detects spikes during the fire episode (orange points in Figure II.5). We further compared these two values of β at the four stations every week for the year 2015 (from January to December) and report spike detection statistics in Table II.3. About 10× more spikes for CO, and 5 to 7 times more for CH_4 and CO_2, were detected by the REBS method with β = 3 compared to β = 8. Using β = 3, we detected more than 2 % of spikes for all species and up to 7 % for CO_2 at AMS. Using β = 8 these percentages are reduced to 0.2 and 1.5 %, respectively (Table II.3). Indeed, β = 8 provides results in better agreement with spikes manually reported by site managers. Spike detection statistics for β ranging between 1 and 10 are presented in Table SII.1 in the Supplement, and additional illustrations for β = 1, 4, 8 and 10 are in Figure SII.3.

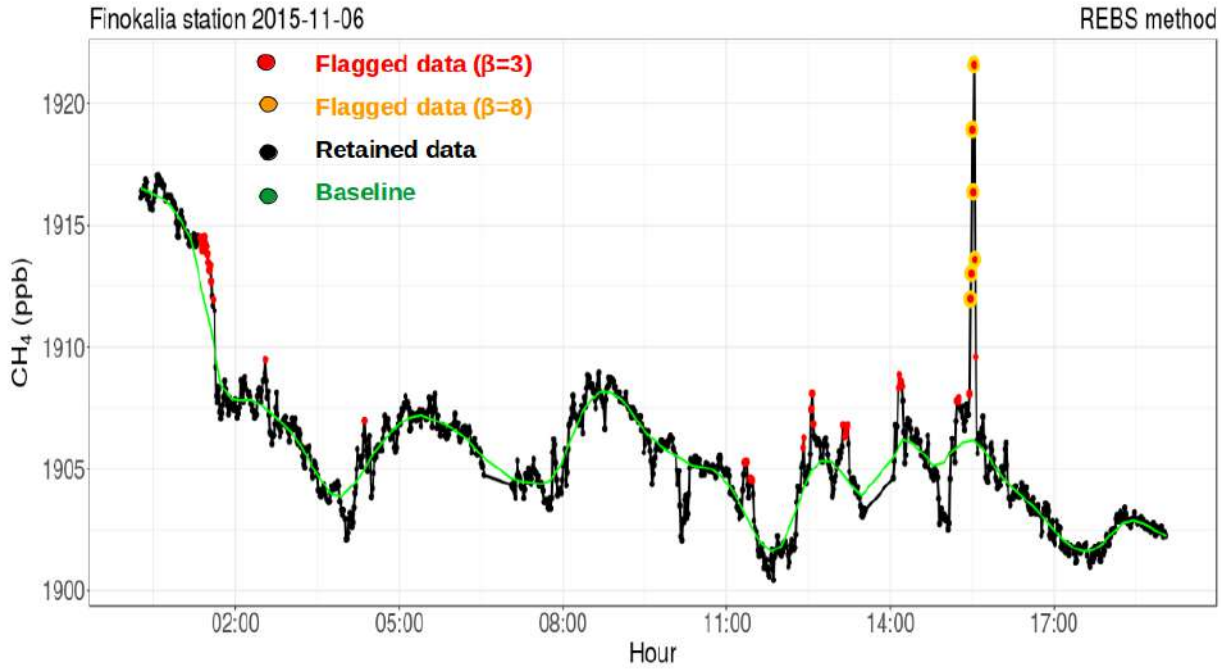

Figure II.5: comparison between two sets of β parameter for REBS method. Red represents detected data for β=3, orange are the detected data for β=8, applied on FKL measurement 6th of November 2014.

Sites	Species	Contaminated data percentages (%)	
		β = 3	β = 8
AMS	CH_4	2.3	0.2
	CO_2	6.9	1.5
FKL	CH_4	4.8	0.8
	CO_2	4.2	0.6
	CO	1.2	0.1
OPE	CH_4	1.8	0.5
	CO_2	1.6	0.5
	CO	1	0.3
PDM	CH_4	7.8	2.2
	CO_2	5.2	0.8
	CO	1.5	0.2

Table II.3: Sensitivity of REBS spike detection method for two sets of($\beta = 3$ and $\beta = 8$) for the four stations and all species for the year 2015.Based on these sensitivity tests for the SD and REBS parameters, and the a prior estimation of the percentages of spikes manually detected by site managers, we apply the SD method with σb and $\alpha = 3$ for CO and with σb and $\alpha = 1$ for CO_2 and CH_4. For the REBS method we use $\beta = 8$.

II.4.2 Statistics of the three spike detection methods

The statistics for local spike detection with the three methods are given in Table II.4. Due to the lack of completeness of the reports by the staff about potential local contaminations, we cannot compare those average statistics to the manual spike detection. With COV we detect an average of about 2 % of spikes with the 99th percentile threshold for all stations and species (section II.3.2.1). With the methods SD and REBS, more variable percentages of spikes are found depending on the trace gas variabilities at each station. The percentages of contaminated data range from 0.1 % for CO_2 at AMS to 7 % for CH_4 at PDM. The value of 7% detected for CH_4 at PDM is higher than at all other sites and species and reveals the influence of a source of methane on a site (see below and next paragraph). For OPE, we found a significant percentage of spikes (between 1 and 2 %) for all species, which may be explained by the higher number of local emission sources compared to other stations located in more pristine environments. At FKL and AMS we obtain different percentages of spikes between SD and REBS for CO_2. In fact, we assume that this difference can be related to the sea–land circulation when winds turn, leading to a fast change in atmospheric concentrations. For FKL, AMS and PDM, the percentage of spikes found with the SD and REBS methods vary by around 1 % except for CH_4 at PDM, where both SD and REBS detect high percentages of spikes (7% for SD method and 2.3% for REBS method). This is not expected for a high-mountain station. The results of a field campaign organized at PDM in 2015 (section II.4.1) revealed the influence of a local water treatment facility at the station, producing CH_4 (see section II.4.1).

Sites	species	SD		REBS		COV	
		Percentage (%)	Number of detected data	Percentage (%)	Number of detected data	Percentage (%)	Number of detected data
AMS	CH_4	0.6	8801	0.2	3318	2.1	29315
	CO_2	0.1	1454	1.7	24210	1.8	24672
FKL	CH_4	0.3	2096	1	7680	2	14657
	CO_2	0.1	1052	0.6	4831	1.9	14295
	CO	0.2	1618	0.1	1002	2.1	15617
OPE	CH_4	1.8	5473	1	2987	1.3	3864
	CO_2	1.1	3296	1	2749	1.5	4186
	CO	1.3	3777	1.1	3120	1.4	4118
PDM	CH_4	7	56548	2.3	19056	1.8	14243
	CO_2	0.3	2567	1	8757	1.9	15618
	CO	0.2	1970	0.2	1348	2	16603

Table II.4: percentage (rounded to one decimal) and number of contaminated data detected by SD, REBS, and COV method overall stations (AMS, FKL, OPE and PDM) and for the three species CO, CO_2 and CH_4.Generally, the methods SD and REBS automatically detect spikes. However, the COV method requires a prior knowledge of datasets and the approximate number of data to be filtered. Because of this limitation for automatic spike detection we have discarded the COV method from further tests for the selection of the most reliable method for spike detection.

II.4.1 Comparison of SD and REBS methods to detect CH_4 spikes at the PDM clean-air mountain station

In this section, we use field campaign data involving two instruments at PDM to study the efficiency of the SD and REBS methods. As noted above, the SD method detects 20× more spikes for CH_4 than for CO_2 at PDM ICOS site (Table II.4). Looking for all possible local methane emissions at the site, we identified a small sewage treatment facility located about 20 m below the air intake of the analyzer (called AN-1) to be responsible for local CH_4 production. A test campaign was then organized between July and August 2015 with a second analyzer (called AN-2) installed 200 m away from of AN-1 (Figure SII.4). The two analyzers were installed to measure simultaneously CH_4 and CO_2 molar fractions from 1 July to 31 August, as presented in Figures II.6 and II.7. We applied the SD and REBS methods to the CH_4 and CO_2 time series from both analyzers. For CH_4, analyzer AN-2 shows much fewer spikes than AN-1. For instance, between early July and late August 2015, there is more than 12 % of contaminated data with the SD method and 3 %

with the REBS method in the AN-1 record, compared to only 0.8 % with SD and 0.7 % with REBS for the AN-2 instrument (Table II.5). Considering that the two analyzers are measuring ambient air sampled 200 m apart, this large difference is clearly due to the local emission from the sewage facility. Interestingly, for CO_2 we detect more spikes in AN-2 than in AN-1 (Figure II.7). More than 1 % of CO_2 spikes were found in the AN-2 record compared to 0.5 % for AN-1 (Table II.5, Figure II.7). This is explained by the proximity of a diesel generator to AN-2, used for a few hours during electrical storms. Both SD and REBS detect the same CO_2 spikes in both AN-1 and AN-2 time series (Figure II.7). For CH_4, SD and REBS methods confirm the frequent contamination of the AN-1 time series since 2014 and show a good ability to detect the spikes, yet with significant differences regarding the percentage of data detected as contaminated. Considering that the AN-2 analyzer provides a less contaminated CH_4 time series, we have used this experiment to compare between the two methods and select which one performs better for CH_4 spikes at PDM.

		ICOS site		TDF site	
		SD	REBS	SD	REBS
CH_4	Percentage (%)	13	3	0.8	0.7
	Number of contaminated data	10244	2396	684	602
CO_2	Percentage (%)	0.2	0.5	1.1	1.4
	Number of contaminated data	158	390	849	1050

Table II.5: percentages and number of contaminated data detected by SD, REBS methods for CO_2 and CH_4 at PDM.

Figures II.8 and II.9 represent the CH_4 and CO_2 measurements of AN-1 and AN-2. For AN-2, CH_4 concentrations (black data point in Figure II.8) rarely exceed 1950 ppb, whereas for AN-1 it exceeds 2000 ppb (black data point) and occasionally reaches almost 2200 ppb. SD and REBS methods both detect all contaminated data that range between 1980 and 2200 ppb for AN-1. The differences between the two automatic methods are more important for data that are below 1980 ppb. Furthermore, the filtered data (green data point) using the SD method better fit the 1:1 correlation line with the less contaminated analyzer than the REBS method (Figure II.8). The REBS method underestimates the lower part (foot) of the spikes (contaminated data that range between 1900 and 1980 ppb; Figure II.6-A' AN-1). However, for CO_2 the two methods detect nearly the same spikes (Figure II.7) and provide a similar filtered time series (Figure II.9). How can we explain the insufficient performance of the REBS method to detect the lower part of the CH_4 spikes? This method defines spikes using the estimated baseline (Ruckstuhl et al., 2012). When the

population of contaminated data is high, the baseline is flawed due to the influence of spikes, and the baseline determination will be overestimated. In Figure II.8, we notice the missed detection of a number of contaminated data when using the REBS method due to the high values of the baseline. The SD method detects most of the local spikes at PDM, even if a slight underestimation of contaminated CH_4 data remains even after data filtering (Figure II.8).

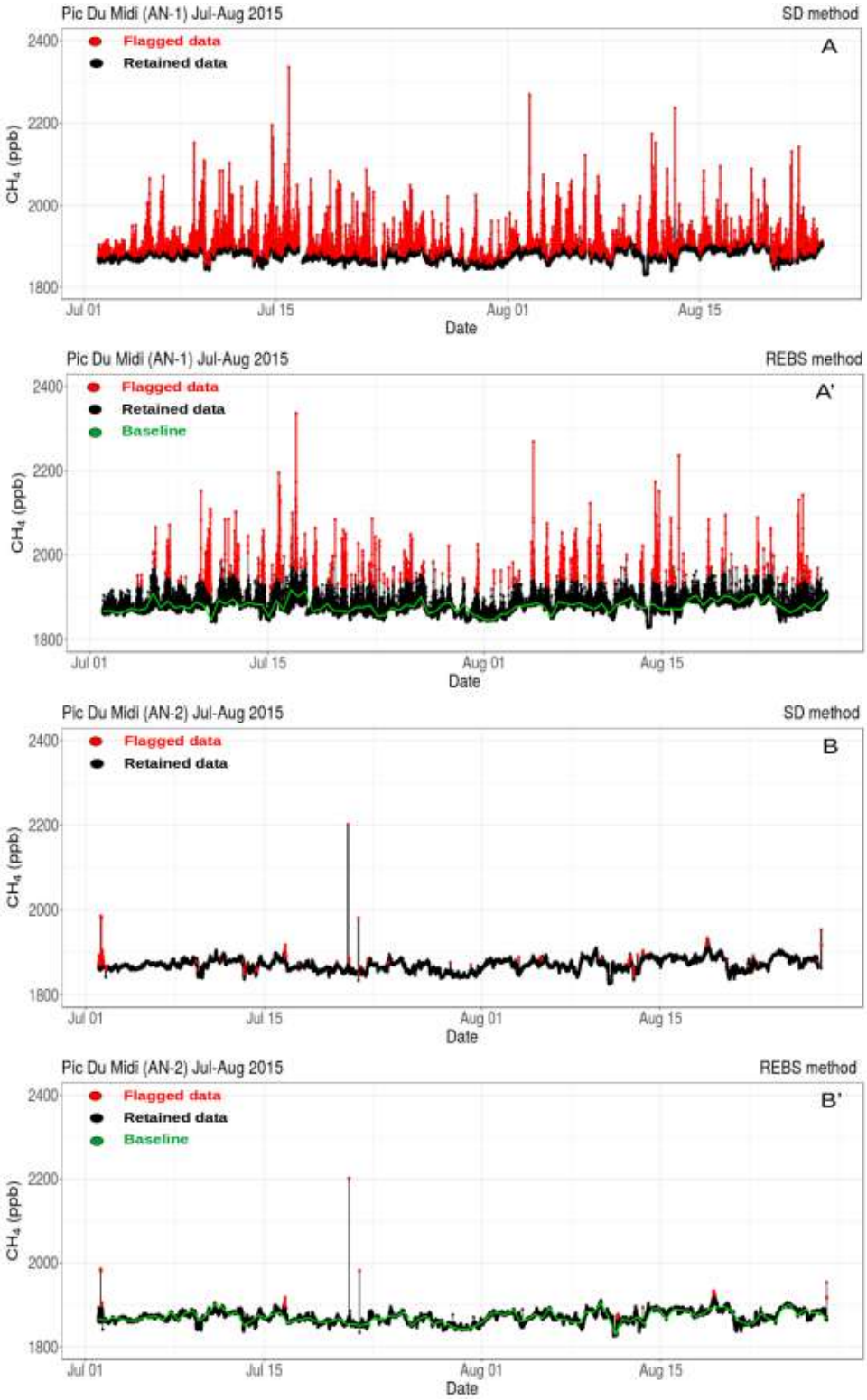

Figure II.6: AN-1 CH_4 measurement at T55 building for A and A', and AN-2 TDF building for B and B'. Black data points are the retained measurements, red points represent the flagged using SD method for A and B, and REBS method for A' and B'

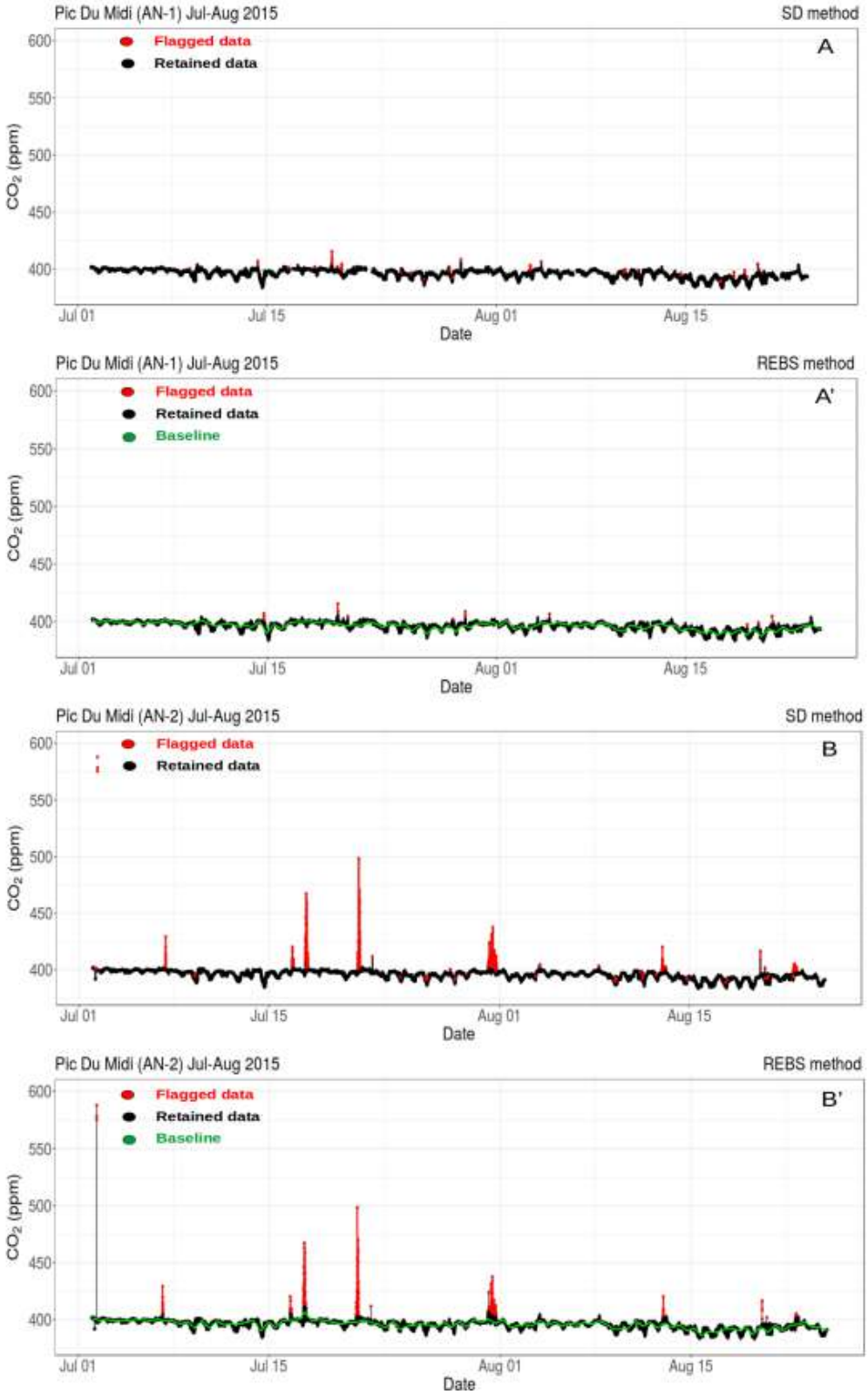

Figure II.7: AN-1 CO_2 measurement at T55 building for A and A', and AN-2 TDF building for B and B'. Black data points are the retained measurements, red points represent the flagged using SD method for A and B, and REBS method for A' and B'

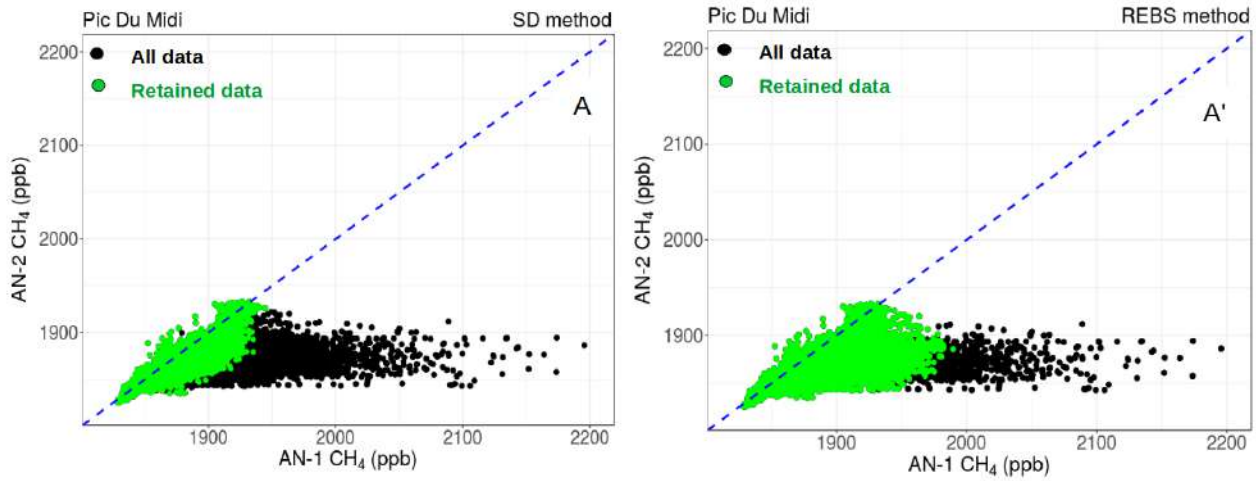

Figure II.8: plots of CH_4 measurements of AN-1 against AN-2. All data are in black, and the green points represent the retained data using SD method for A and REBS method for A'

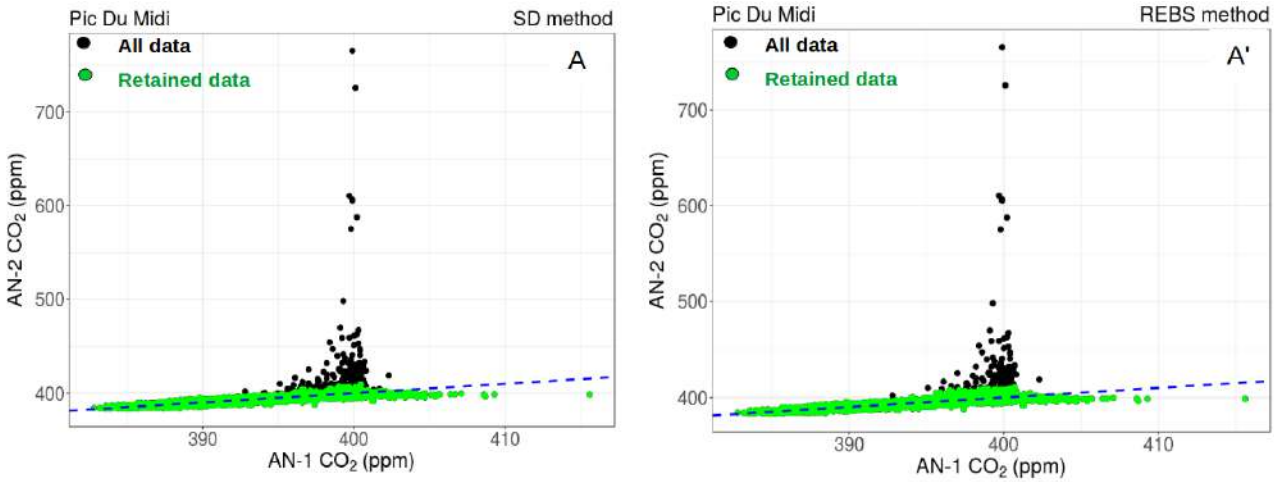

Figure II.9: plots of CO_2 measurements of AN-1 against AN-2. All data are in black, and the green points represent the retained data using SD method for A and REBS method for A'

II.4.2 Comparison between automatic and manual spike detection

In this section, we analyze how SD and REBS methods detect spikes of CO_2, CH_4, and CO that were independently identified by the station staff and related to a known local source of contamination at FKL and PDM.

At FKL the contamination events reported by the site manager are associated with local fires nearby the station. The technical staff recorded dates of burning which could lead to significant emissions of trace gases, especially CO and CO_2. It should be noted that this information is not exhaustive in the sense that the person in charge does not necessarily have information on all burning events. We have matched the trace gas time series with the logbook information showing 17 days with local burning events between 2014 and 2015. We applied the SD and the REBS methods over 1-week time windows containing each burning event. First, we run the algorithms separately on the three species (CH_4, CO_2, and CO). Then, if the algorithm detects a spike in at least one species, we consider data for all other species as spikes as well. Figure SII.5 shows an example of the SD method applied on a fire episode between 15:00 and 16:00 on 6 November 2014. The spike occurred for the three species CO, CO_2, and CH_4, with a similar pattern (spike also identified by the station manager).

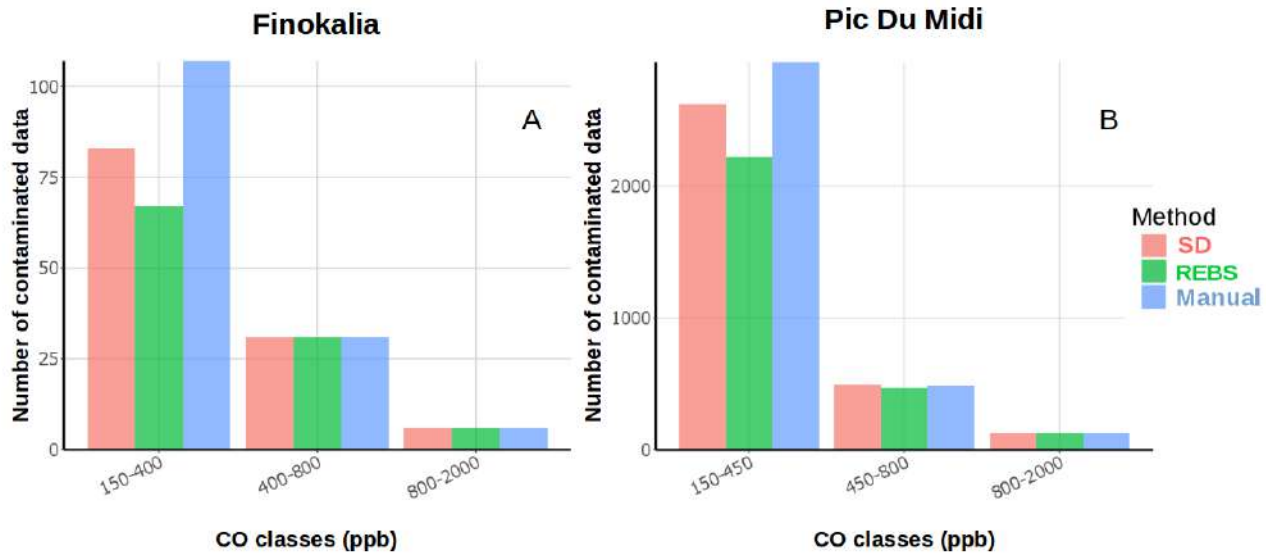

Figure II.10: Number of flagged CO measurements using manual method (blue), SD method (red), and REBS method (green) for Finokalia (A) and Pic Du Midi (B) .

Figure II.10-A represents the number of contaminated data detected by the automatic methods and manual flagging by the station staff at FKL. The numbers of selected data are split into three concentration ranges. The two automatic methods and the manual flagging detect the same number of contaminated data for CO classes higher than 400 ppb. We have an excellent agreement for the spikes with the highest concentrations. For the low-concentration spikes (< 400 ppb), the automatic methods are less selective than the manual flagging. In Figure II.11 we show an example of contaminated data detected by automatic and manual flagging methods at FKL. When the difference between uncontaminated (identified as reference) and spike data is not significant compared to a certain standard deviation threshold, the methods may thus fail. The data highlighted by the blue circle in Figure II.11 give an example of when spikes identified by automatic methods diverge from the manual identification. Such data are either close to the baseline REBS selection (Figure II.11-C) or close to the C_{unf} value for the SD method (Figure II.11-B). At this point it is important to note that the person in charge of data flagging selects spikes using a known period (from a starting to an ending time).

A second comparison study between automatic methods and manual detection has been performed at PDM using the CO time series from December 2014 to February 2015. During winter, the station experienced several snow fall episodes and snow was removed with a diesel-powered snow blower. This operation influenced the GHG concentrations and leads to sharp spikes easily observed in the CO time series (Figure SII.6). Most of the spikes are successfully detected by the SD and the REBS methods. Figure II.10-B represents the number of contaminated data detected by SD in red and REBS in green and data manually eliminated by the site manager in blue at PDM. Similar to the FKL local fires, the SD and the REBS methods detected the same number of spikes as the manual selection for high concentrations; 857 contaminated data points are detected by the SD method (same as the principal investigator, or PI) for concentrations higher than 400 ppb, and 828 data points are detected by the REBS method. The main difference between the automatic and the manual flagging methods are related to the lower part of the spikes. For 2861 data (CO < 400 ppb) flagged manually by the PI station, the SD method detects 2270 data points whereas the REBS method detects only 1799 data points. In fact, for moderate spikes the SD method selects 70 % of contaminated data according to the PI whereas the REBS method retrieves only 60 %. We have also calculated the number of events not considered by the manual flagging and considered by the automatic methods. For a total of 3402 data detected by the SD method, only 211 data were not considered by the PI, which represents 0.25 % on the whole period. For the REBS method, 133 data out of 2981 were not detected by the PI (nearly 0.15 %). However, these statements should be used with caution since the manual spike

detection information is not exhaustive, and the person in charge does not necessarily have information on all contaminated events.

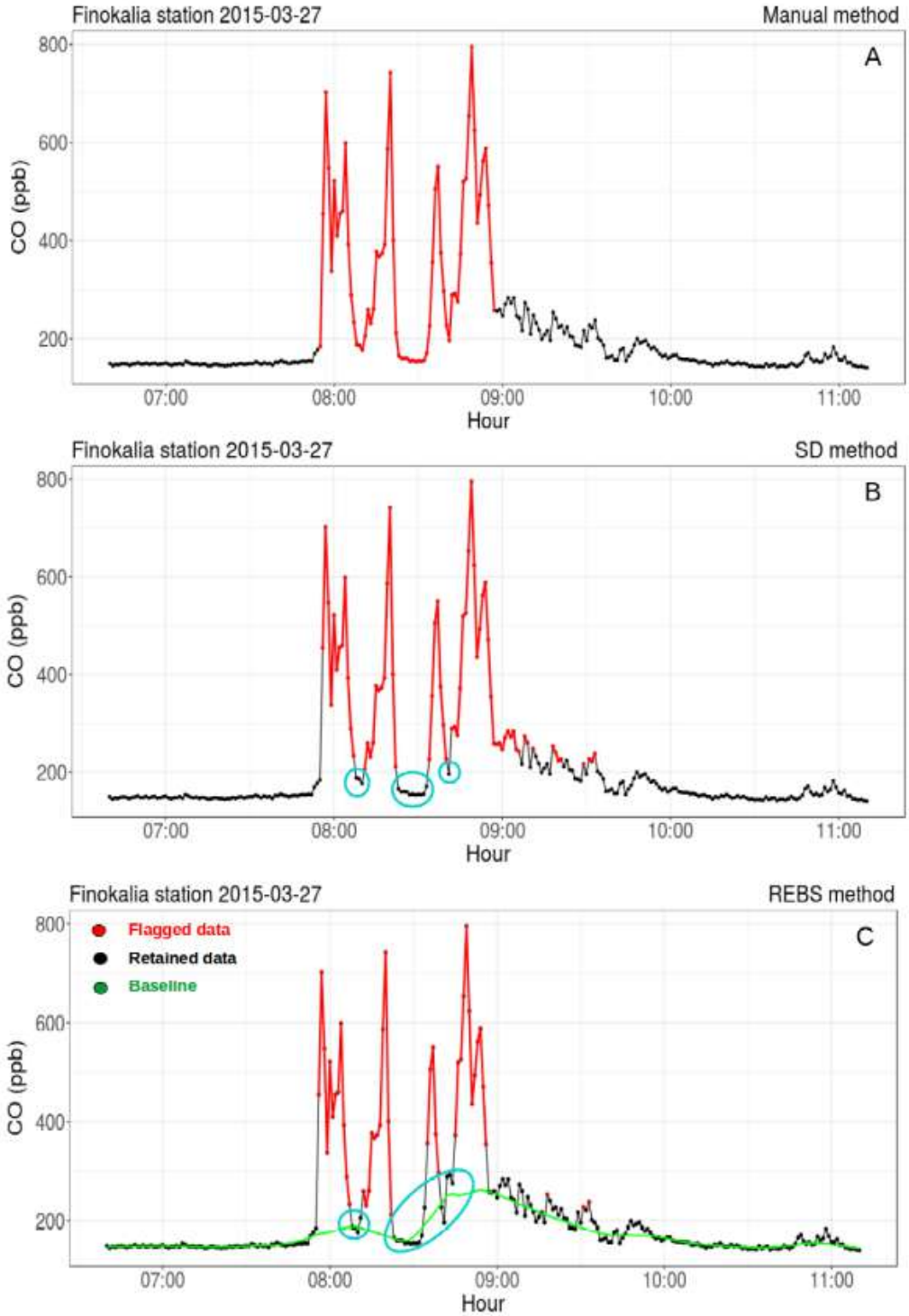

Figure II.11: Example of a spike detection using manual (A), SD (B), and REBS (C) methods during a known biomass burning event at Finokalia.

II.4.3 Influence of the spike detection on hourly averages:

In this section, we estimate the impact of the spike detection on data used for atmospheric inversions, which are typically hourly or half-hourly averages. For this purpose, we have calculated the differences between the hourly averages of the filtered and non-filtered time series. In table II.6, we present the number of hours in which at least 1 min data for each species was filtered. We classified the results into three intervals. For CO_2, the first interval represents the values lower than 0.5 ppm, the second interval is for differences between 0.5 and 1 ppm and the third stands for the higher differences (values more than 1 ppm). For CH_4 and CO we set the first interval for values lower than 5 ppb, the second interval represents the data between 5 and 10 ppb and the third for differences higher than 10 ppb.

Most of the differences between filtered and non-filtered hourly data vary between 0 and 0.5 ppm for CO_2 and between 0 and 5 ppb for CH_4 and CO. For CO_2 at the AMS station, the SD method detects 1454 1-min data points (Table II.4), which occur in 104 hours during the 3 years of measurements. Of those hours, 62 % are characterized by a difference up to 0.5 ppm, and 18 % show more than 1 ppm of difference. For CH_4 measurements in AMS, the 8801 contaminated data points detected by the SD method (Table II.4) occur during only 21 h, this modifies the hourly averages by 5 ppb as a maximum. For the four sites, we notice a similar effect on the hourly averages. Most of the impacted hours are characterized by a difference within the first interval (0.5 ppm for CO_2; 5 ppb for CH_4 and CO). However, for OPE we observe higher differences with 53, 36 and 47 % of the impacted hours in the highest interval, respectively, for CO_2, CH_4 and CO. This feature is probably related to the higher number of the nearby local emission sources nearby OPE site compared to the other stations, which are located in more pristine environments. Figure SII.7 shows a decrease of the number of impacted hours for higher intervals (the same pattern as the three other stations). Overall, the aggregation of filtered measurements at the hourly timescale showed a relatively weak impact of the filtered data for background sites, but more significant effect for stations located closer to local sources.

	CO_2 (ppm)			CH_4 (ppb)			CO (ppb)		
	]0-0.5[	[0.5-1[	>=1	]0-5[	[5-10[	>=10	]0-5[	[5-10[	>=10
AMS	64 (0.3‰)	21 (0.1‰)	19 (0.1‰)	21 (0.1‰)	0	0			
FKL	133 (1‰)	12 (0.1‰)	5 (0.04‰)	134 (1‰)	11 (0.1‰)	7 (0.05‰)	218 (1.7‰)	8 (0.06‰)	8 (0.06‰)
PDM	522 (3.7‰)	30 (0.2‰)	16 (0.1‰)	4696 (34‰)	741 (5.3‰)	623 (4.4‰)	518 (3.7‰)	4 (0.03‰)	1 (0.01‰)
OPE	36 (0.3‰)	24 (0.2‰)	69 (0.5‰)	53 (0.5‰)	10 (0.08‰)	36 (0.3‰)	107 (0.9‰)	20 (0.2‰)	111 (0.9‰)

Table II.6: Classification of the number of hours in which the SD method filtered at least one-minute data point for CO, CO_2, and CH_4 at the four sites. The intervals represent the differences between filtered and the non-filtered time-series averaged at a hourly scale in (ppm) for CO_2 and (ppb) for CO, and CH_4. The values in brackets represent the percentages of the impacted hours on the whole time-series.

II.5 Conclusion

The recent increase in the number of studies that have been applied to study the spatial representativeness of GHG observations demonstrates the need to define efficient and reliable methods for the identification of spikes related to local contamination sources. Three methods based on the standard deviation calculation were compared in order to provide an objective algorithm for the GHG data spike detection.

We addressed the problem of identifying concentration spikes of a few minutes duration in GHG continuous time series by applying automatic detection methods (COV, SD, and REBS) previously used for atmospheric pollution but not systematically for GHG time series. Stations with different regimes of variability where local emission sources are identified without ambiguity (engines/waste near the station buildings, or fires nearby) are chosen to evaluate the performance of the automatic methods against spikes manually identified by station managers. The COV algorithm can be considered as a semiautomatic method since it requires an a priori choice of a percentage of data rejected as spikes. We tested the COV method with a percentage of 1 % of spike data for all species and for all stations. This limitation made the COV method less flexible and informative for universal automatic spike detection across different sites. For the two fully automatic methods (SD and REBS) we performed several sensitivity tests in order to recommend the best set of parameters for our four chosen stations, which are considered to be representative of most ICOS stations (disregarding those located in suburban environments).

The application of the automatic methods on contaminated time series at the Pic du Midi observatory showed the ability of SD and REBS to detect real spikes on the CH_4 time series caused by the sewage treatment facility of the observatory. Nevertheless, significant differences regarding the rejection percentage were noticed between the methods. Both methods have a tendency to unduly keep a certain fraction of the spike base (lowest concentrations in spikes). REBS is worse than SD in this respect. In the REBS method, when the percentage of spikes is high, the baseline determination is biased toward high concentrations, leading to underestimate spike anomalies above this baseline. However, the SD method correctly detects most of the contaminated data. The comparison between SD, REBS and the manual flagging methods showed good agreement with an overall percentage of 70 % of successful spike data detection for SD and 60 % for REBS, at two stations (FKL and PDM) where local contaminations are well identified by the local staff. These two automatic algorithms detect short-term spikes, allowing for a more consistent and automatic filtering of the time series even if they identify less contaminated data than by manually flagging.

The estimation of the impact of the spike detection on data used for atmospheric inversions showed a relatively weak impact of the filtered data for background sites and a more significant effect for stations located closer to local sources. However, even if the implementation of an automatic algorithm can successfully identify short-term spikes due to local contaminations, it is important to note that the priority in the selection of a background site should be to avoid as much as possible the occurrence of such spikes. In the case where the spikes can not be totally avoided, it is then important to try to understand their cause and look for possible actions to minimize them. The modification of the air inlet at the Pic du Midi, described in this study, is a very good example of what can be done once the origin of spikes is understood.

The SD method is found to be efficient and reliable for the purpose of spike detection. It has been proposed for operational implementation in the ICOS Atmospheric Thematic Centre Quality Control (ATC-QC) software to perform daily spike detection of the near-real-time dataset of continuous ICOS stations. The first step will be to run the SD method in a test mode overall ICOS stations and compare with manual detection when available in order to set optimal values of parameters. This analysis can be complemented with wind speed and direction data in order to possibly attribute spikes to fixed local sources.

Chapter III: Evaluation of the sensitivity of the transport model CHIMERE using different meteorological fields and surface fluxes for simulating the CO_2 and the CH_4 concentrations

III.1 Introduction

The development of the regional atmospheric networks, such as the Integrated Carbon Observing System (ICOS), provide useful constraints for the estimation of the regional greenhouse gas fluxes (GHG). The atmospheric variability of the measured GHG concentrations depends on the changes of the transport processes and the variations of the surface fluxes. The measured GHG concentrations may display short-duration variabilities which can not be optimally reproduced by the transport models due to their limited spatial resolution and to impact of the surface emission errors. The sampling sites are distributed in a way to be regionally representative, but not too close to high emission hotspots characterized by important errors (Hogue et al., 2016). Such regional oriented network includes coastal sites (e.g. Ahmadov et al., 2009), Peri-urban stations (e.g. Ramonet et al., 2010), tall tower sampling sites (e.g. Schmidt et al., 2014), and high altitude mountain stations (e.g. Reimann et al., 2008). These measurements are used by the inversion system that combines them optimally with prior flux information and atmospheric transport models to estimate optimized fluxes assumed to be close to reality (Kountouris et al ., 2018, Pison et al., 2018, Bergamaschi et al., 2018, Berchet et al ., 2015). With the development of high-resolution transport model and the increasing number of the observation sites, the estimation of the optimized GHG fluxes can be performed at a fine spatial and temporal resolution. Before proceeding with the optimization of GHG fluxes, we need, first, to evaluate the capability of the atmospheric transport model to reproduce correctly the atmospheric variabilities of the GHG concentrations.

The accuracy of the simulated concentrations depends on the used atmospheric model and the quality of the surface fluxes. These fluxes are generally estimated using bottom-up approaches. The flux estimates must resolve the variations of the GHG concentrations at a fine spatial resolution and a time step of about 1 hour in order to be comparable with the atmospheric measurement. The distribution of the national inventories in

space and time may lead to significant uncertainties (Peylin et al., 2011). This uncertainty becomes larger with the increase of the spatiotemporal resolution (Hogue et al., 2016). The estimation of the uncertainties related to the GHG fluxes can be performed statistically using automatic methods (e.g. Saikawa et al., 2017), or analytically by comparing the fluxes provided by different products (e.g. Peylin et al., 2011). The quantification of the emission uncertainties represents a challenging task to better understand the linkages among emissions and the atmospheric concentrations simulated by the transport models. In this study, we will investigate the uncertainties of the surface CO_2 and CH_4 fluxes using a combination of different products, with the aim to quantify the magnitude of the difference between the used fluxes and their impact on the simulated concentrations from the hourly to the seasonal scale.

The second aspect responsible for the quality of the simulated GHG concentrations depends on the performance of the transport models to correctly represent the atmospheric processes such as the horizontal and vertical mixing. Several studies investigated the ability of the transport model to represent the variabilities of GHG atmospheric concentrations at the global scale with a resolution of a few hundreds of km (e.g., Feng et al., 2011; Patra et al., 2009b, 2009a), and at the regional scale with a resolution up to 100 km (e.g., Aalto et al., 2006; Chevillard et al., 2002; Pillai et al., 2011). In general, the synoptic variabilities are reasonably well described by a regional atmospheric transport model characterized by a finer spatiotemporal resolution (Geels et al., 2007). Most of the coarse global atmospheric transport models do not resolve explicitly the mesoscale circulation caused by the heterogeneity of the land used and the complexity of orography. For example, the orography driven flows that partly controls the GHG variabilities in the mountainous regions cannot be resolved adequately by global models (Geels et al., 2007). In these regions, the use of a high-resolution regional model reproduce more accurately the spatial and the temporal variabilities of the atmospheric concentrations compared to coarse global models (Pillai et al., 2011). Moreover, the errors associated to the localization of the station in the model, called hereafter by representativeness errors, can be significantly reduced by the high-resolution regional models (Geels et al., 2007, Law et al., 2008, Saeki et al., 2013). Indeed, a model evaluation seems essential in order to quantify the errors associated with the transport processes. This will be performed in this study based on the difference between two meteorological fields used to drive the simulated atmospheric concentrations.

This chapter aims at evaluating the sensitivity of a regional transport model regarding different input data. A set of 8 regional simulations are performed over France using the Eulerian off-line chemistry-transport model CHIMERE for the year 2014 with two meteorological fields, two models of the vegetation-atmosphere CO_2

fluxes, and two anthropogenic emission maps. The simulations are compared to each other and against the observed data in order to analyze the sensitivity of the modelled CO_2 and CH_4 concentrations regarding the different input data. The main objective of this analysis is to quantify the flux errors and the transport errors from the local to the sub-regional scale. We use 16 atmospheric sites distributed over a domain in Western Europe with 8 stations in France and 8 sites located in the neighbouring countries. In this study, we discuss the advantages of using a high resolution mesoscale meteorological model for simulating the CO_2 and CH_4 concentrations at different station categories (e.g. coastal, continental tall towers, and mountain stations). We also investigate the uncertainties related to the biogenic and anthropogenic fluxes at the national and the sub-national scales. In section III.2, we present in detail the observation and the simulation framework, in addition to the prescribed CO_2 and CH_4 surface fluxes used as an input for the transport model. In sections III.3.1 to III.3.4, we study the differences between the fluxes provided by the anthropogenic maps and the biogenic models. Section III.3.5 focuses on the sensitivity of the simulated concentrations regarding the transport data. In section III.3.7 we present the sensitivity of the simulated concentrations to the different surface fluxes (the anthropogenic and the biogenic fluxes). We finish the study by conclusions and implications in section III.4.

III.2 Methods

III.2.1 CHIMERE atmospheric transport model

CHIMERE is a three-dimensional Eulerian regional transport and chemistry numerical model developed to provide daily forecasts of several pollutants (e.g. ozone and aerosols) and to perform long-term simulations of the greenhouse emissions at the mesoscale (Menut et al., 2013). In this study, we use CHIMERE without chemistry, since CO_2 is an inert tracer and the lifetime of CH_4 with respect to its chemical destruction by OH radicals is much longer than the transit time between emissions and observations in the used domain (Figure III.3). CHIMERE requires some external forcing: 3-D meteorological fields, biogenic and anthropogenic surface fluxes, initial and boundary conditions. CHIMERE can be used to calculate atmospheric trace gases concentrations from urban to continental scales and from 1 km^2 to a few degrees of resolution. Figure III.1 shows the framework of CHIMERE transport configuration used in this thesis.

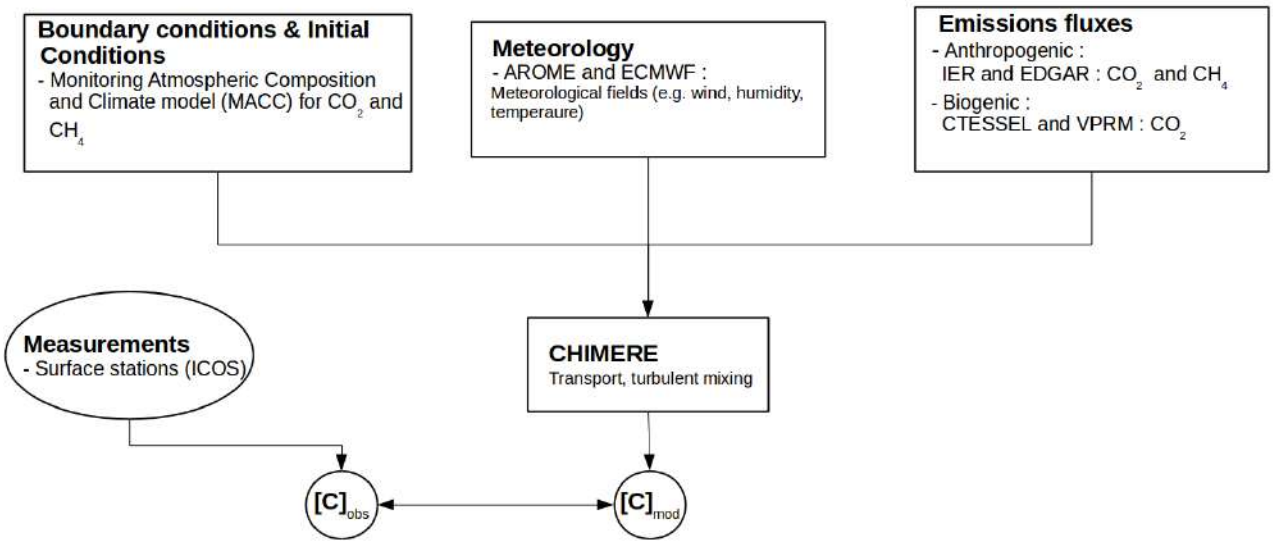

Figure III.1: Diagram of CHIMERE transport model. The boxes represent the different processes. Cmod and Cobs stand for the modeled and the observed atmospheric concentrations respectively.

To simulate atmospheric concentrations of CO_2 and CH_4, we integrate CHIMERE on a regular grid with a horizontal resolution of 0.1°x0.1° in latitude and longitude in a region going from -7.5° to 10.5° East and from 38.5° to 52.5° North centred over France (Figure III.3). In the vertical, the model has 18 sigma-pressure layers ranging from the surface up to 300 hPa (approximately 9000 magl). The vertical resolution varies between 50 m near the surface (the top of the first level is at 5 magl), 200 m in the mid altitude, and 1500 m at the troposphere top. The atmospheric transport is parameterized using two schemes. For the horizontal transport (advection), we use the Van Leer scheme (scheme of order 2 in space) which computes the concentrations of a grid cell using a linear slope relating the two adjacent grid cells (Van Leer, 1979). For the vertical mixing, we use the upwind scheme (Courant et al., 1952) which calculates the fluxes at the grid cells interface according to the sign of the wind speed. It assumes that the mass flux, for a given tracer, is the product of the wind by the tracer concentration in the upwind cell (Courant et al., 1952). CHIMERE offers the option to activate or not the deep convection. Due to the lack of the updraft and downdraft meteorological data provided for AROME (described in the next section), the deep convection was desactivated in this study. The boundary layer height is estimated as the altitude where the Richardson number equals R_{ic}=0.5 (Troen and Mahrt, 1986).

Initial and boundary conditions of the GHG concentrations are taken from the global transport model MACC (Monitoring Atmospheric Composition and Climate) described in detail in Marécal et al. (2015). The version

of MACC data used in this study is characterized by a horizontal resolution of 0.15°, 60 levels in the vertical, and a temporal resolution of three hours.

We have performed 8 simulations using CHIMERE with two meteorological fields from numerical weather analysis (AROME and ECMWF section III.2.2), two anthropogenic emission inventories based on energy use statistics (IER and EDGAR section III.2.3.1) for both CO_2 and CH_4, and two biogenic flux models for CO_2 (VPRM and CTESSEL section III.2.3.2). The set of simulations is compared to measurements at the atmospheric measurement sites shown in figure III.3 presented in section III.2.4. We have used 16 monitoring stations with 8 sites in France and 8 stations located in the neighbouring countries. We simulate CO_2 and CH_4 concentrations over the year 2014 every hour from January to December. The main characteristics of the performed simulations are described in table III.1.

Process	Methods	
	CO_2	CH_4
Meteorological data	AROME or ECMWF	
Domain	-7.5°W to 10.5°E / 38.5°N to 52.5°N	
Horizontal resolution	0.1° x 0.1°	
Vertical resolution	18 levels (surface to 300 hPa)	
Horizontal transport	Van Leer scheme (Van Leer, 1979)	
Vertical transport	Upwind scheme (Courant et al., 1952)	
Turbulence & boundary layer	Troen and Mahrt scheme (Troen and Mahrt, 1986)	
Anthropogenic emission inventories	IER or EDGAR	
Biogenic flux simulations	VPRM or CTESSEL	-
Initial and boundary conditions	MACC	

Table III.1: Main characteristics of the CHIMERE configuration used in this study. (-) means that no biogenic fluxes were used for CH_4

III.2.2 Meteorological fields

CHIMERE is supplied with pre-calculated meteorological fields from the meteorological analysis data of AROME and ECMWF. These two models have different spatial resolutions that are horizontally respectively higher and lower than that of our CHIMERE configuration (0.1°). These fields are linearly interpolated to

provide the meteorological data on the CHIMERE grid and at 1 hour temporal resolution using the CHIMERE pre-processing meteorological tools.

III.2.2.1 AROME

AROME is the mesoscale meteorological model used since 2008 for operational weather forecast at Meteo-France (http://www.meteofrance.com/accueil). The model is initialized by larger model such as ALADIN (Bubnova et al. 1995), or global fields from weather forecast models such as ARPEGE (Courtier et al. 1991). Most of the physical parameterizations of AROME is derived from the research Méso-NH model (Tulet et al., 2003), which has been used, previously in several studies, for modelling the atmospheric CO_2 concentration at a regional scale (Lac et al., 2013, Staufer et al., 2016). The dynamics of AROME come from the Non-Hydrostatic ALADIN model (Bubnova et al., 1995). We used AROME analysis fields at a 3 hours temporal resolution, a horizontal resolution of 0.025°, and 60 levels in the vertical.

III.2.2.2 ECMWF

The ECMWF (European Centre for Medium-Range Weather Forecasts https://www.ecmwf.int/) uses the IFS (Integrated Forcast System) model for meteorological forecasts at a global scale (ECMWF 2015a). In this study, we use analysis data provided by the deterministic model (ECMWF 2015a). This model was widely used for modelling the greenhouse gases on a global scale (e.g. Chevalier et al., 2010, Locatelli et al., 2013), and on a regional scales (e.g. Bréon et al., 2015, Kadygrov et al., 2015, and Pison et al., 2018). The ECMWF model is composed of 137 levels in the vertical, and a horizontal resolution of ~0.15° across the globe.

III.2.1 CO_2 and CH_4 surface fluxes

The anthropogenic emissions of CO_2 and CH_4 are generally described by models based on geo-referenced fields of socio-economic data and emission factors for different economic sectors. Administrative based inventories are developed on national, regional and city scales with the objective to report emissions aggregated according to the considered regions. Research oriented inventories are elaborated using a similar methodology, but provided on regular spatial grids, as required for the atmospheric simulations that we are developing. Some inventories also contain information on the temporal profile of emissions for each sector, generally based on periodic functions representing diurnal, weekly and seasonal changes of emissions from traffic, residential fuel use and energy production.

The natural CO_2 land fluxes can be calculated by vegetation models, which can be of variable complexity. Vegetation models all use climate input data, and some of them also use remote sensing information, as well as other input data such as flux tower measurements, soil and vegetation maps. For atmospheric transport simulation, we need maps of net CO_2 fluxes from all land use types on a time step of about 1 hour since the flux variations are strongly coupled with transport variations. We thus use simulations from vegetation models at such temporal resolution.

The CH_4 biogenic emissions, such as natural wetlands, were neglected due to the lack of accurate estimations and the low extension of these emission sources in our domain (Champeaux et al., 2005). The natural CO_2 and CH_4 oceanic fluxes were also neglected in this study since their contribution in the regional scale is expected to be very small compared to the vegetation and anthropogenic fluxes (Gerbig et al., 2003).

In the following paragraphs, we describe the anthropogenic emission maps used for CO_2 and CH_4 and the biogenic models used in this study for CO_2.

III.2.1.1 Anthropogenic emissions

III.2.3.1.1 EDGARv4.2 FT2010 database

The EDGAR (Emission Database for Global Atmospheric Research) data product provides maps of anthropogenic emissions of greenhouse gases (CO_2, CH_4, N2O), and air pollutants (CO, PFC, …) on a grid of 0.1°x0.1° resolution over the globe. We use the EDGARv4.2 FT2010 inventory available at http://edgar.jrc.ec.europa.eu/overview.php?v=42. Since no time profile is provided for the EDGAR emission maps, we have introduced temporal factors by matching different UNFCCC (United Nations Framework Convention on Climate Change) sectors of emissions with the temporal profiles used for the LOTOS EUROS project (Schaap et al., 2005).

UNFCCC category	**Description**	**species**	**Corresponding sectors for which Schaap et al (2005) defines temporal profiles**
1A1+1A2	Energy manufacturing transformation	CH_4	Industry
1A1a	Energy industry	CO_2	Power
1A1c+2G	Transformation non-energy use	CO_2	Processes
1A2	Combustion in manufacturing industry	CO_2	Industry
1A3b	Road transportation	CO_2, CH_4	Traffic
1A3a+1A3c+1A3d+1A3e	Non-road transportation	CO_2, CH_4	Traffic
1A3d	International and domestic shipping	CO_2	Traffic
1A4	Energy for buildings	CO_2, CH_4	Residential
1B1	Fugitive emissions from solid fuels	CH_4	Processes
1B2b	Gas production and distribution	CH_4	Power
1B2a	Oil production and refineries	CO_2, CH_4	Processes
2A	Non-metallic mineral processes including cement production	CO_2	Processes
2B+3	Chemical processes and solvents	CO_2	Processes
2C	Metal processes	CO_2	Processes
4A	Enteric fermentation	CH_4	Processes
6A+6C	Solid waste disposal	CO_2, CH_4	Processes
6B	Waste water	CH_4	Processes

Table III.2: Table linking the UNFCCC categories of emissions and the activity sectors for which the temporal profiles are defined in the LOTOS EUROS project http://www.eea.europa.eu/publications/EMEPCORIN-AIR5. For example the temporal factor of the industry sector is applied to the UNFCCC category 1A1+1A2 (Energy manufacturing transformation).

III.2.3.1.2 Temporal profiles applied to the EDGAR emissions:

The temporal profiles are implemented for cumulated UNFCCC emission categories. For example, the temporal profile of the CH_4 process sector is applied to the sum of emissions of the waste water, solid waste disposal, enteric fermentation and oil production and refineries UNFCCC categories (Table III.2). These profiles are based on the combination of, periodic cycles of the hourly emissions of the day, daily emissions of the week, and monthly emissions of the year. Figure III.2 represents these cycles for industrial, residential, traffic, power, and processes sectors. The traffic data includes the information about the rush hour peaks, the intensity of traffic, and weekends effect (Schaap et al,. 2005). Some sectors are characterised by an important amplitude of the cycles (at the 1-hour to 1 month resolution). At the seasonal scale, the residential sector is the most affected by the temporal variations. The maximum of the residential sector is reached during winter when an important amount of energy is used in houses for heating. A simlar bimodal temporal variation per day is observed for both sectors transport and residential sector. The latter should be connected to the local temperature or heating degree day variable, whereas the transport sector is much less sensitive to the ambient temperatures. The emissions for these two sectors are characterized by two maximums that correspond to the rush hours. This set of temporal profiles is primarily based on Western European data, and should fit well with the variations in France and in the neighbouring countries partially covered by the used modelling domain.

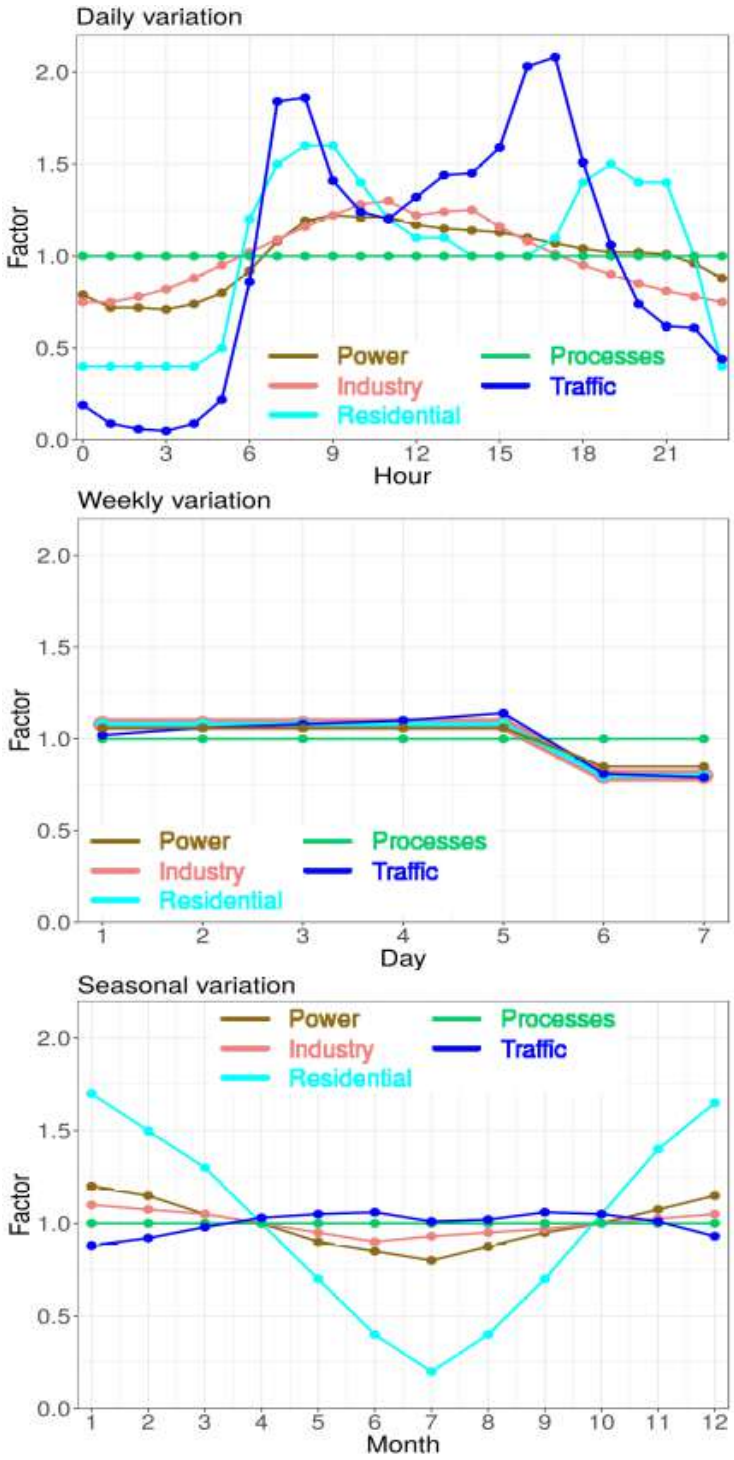

Figure III.2: Normalized temporal profiles of daily, weekly and seasonal variations, applied for power, industry,residential, processes, and traffic sectors for both CO_2 and CH_4. The daily variations are presented in localtime.

First, we have applied the time profiles to each sector of EDGAR emission annual totals using the correspondence table (Table III.2) for hours of the day, days of the week, and months of the year. Then, for each hour of the year, we calculated the sum of the EDGAR emissions of all sectors in the domain of the study (Figure III.3) in order to retrieve an estimation of the temporal variations of the anthropogenic emission maps at the hourly time resolution for CO_2 and CH_4. Note that for CH_4, a constant temporal factor (factor=1/(365*24)) that convert gCH_4/year to gCH_4/hour was applied for the principal sectors of emission, which represent more than 90% of the total CH_4 emissions (e.g., waste management, enteric fermentation, and oil production and refineries). All the time factors (the 24 hourly factors of the diurnal cycle, the 7 daily factors of the weekly cycle, and the 12 monthly factors of the annual cycle) have a mean value of 1//(365*24), which convert from yearly to hourly scale. The resulting hourly emission maps thus, conserve the annual emission budget of EDGAR in each grid point.

III.2.3.1.3 IER database

In this study, we use one of the IER inventories produced for Europe by the Institute for Energy Economics and the Rational Use of Energy, University Stuttgart (IER). The underlying model provides an estimate of the CO_2 and the CH_4 anthropogenic emissions at a high spatiotemporal resolution for the year 2005 by the disaggregation of the national total provided by the UNFCCC on a map that covers Europe.
The emissions in the IER inventories are decomposed into 10 sectors that follow the Selected Nomenclature of Air Pollutants (SNAP) representation of the EMEP/CORINAIR (http://www.eea.europa.eu/publications/EMEPCORINAIR5). The 10 SNAP emission sectors are distributed in space and time, using the spatial proxies and temporal functions described in the report “Spatial and temporal disaggregation of anthropogenic greenhouse gas emissions in Europe: Emission Inventory for Europe 2005 Institut fur Energiewirtschaft und Rationelle Energieanwendung. http://carboeurope.ier.uni stuttgart.de/”.

In this study, we used the IER inventory for CO_2 and CH_4 at 0.08° horizontal and 1-hour temporal resolutions. The temporal functions from IER were applied to the emission sectors as described by Vogel et al (2013). Similar to EDGAR emissions, the time varying factors were applied to the emission sectors known by significant temporal variations (e.g. residential, road transportation, energy industry, etc.). In practice, this means that the time varying functions were applied to emission sectors that represent respectively ~9% and ~80% of the CH_4 and CO_2 total emission.

III.2.1.2 Vegetation – atmosphere CO_2 fluxes

III.2.3.2.1 VPRM

The Vegetation Photosynthesis and Respiration Model (VPRM) is a diagnostic biosphere model that estimates the fluxes in coherence with the Eddy Covariance fluxes (Mahadevan et al., 2008). VRPM uses the temperature (T2m) and downward shortwave radiation meteorological data from the ECMWF model, the enhanced vegetation index (EVI) and the land surface water index (LSWI) from the MODIS satellite (Moderate Resolution Imaging Spectroradiometer). The later parameters are optimized against European measurement sites (described in Kountouris et al,. 2015) for 8 vegetation classes: the Evergreen, the Deciduous, and the Mixed Forest, the Shrubland, the Cropland, the Grassland, the Savanna, and one last group for snow, water, and urban areas derived from the Synergistic Land Cover Product model (SYNMAP, Jung et al., 2006). The use of the vegetation index and the urban classification allows VPRM to estimate the characteristics of the biogenic fluxes in the urban areas. The model estimates the respiration (R) and the Gross Ecosystem Exchange (GEE) (Mahadevan et al., (2008)) from which we can compute the Net ecosystem exchange, which represents their sum (NEE = - GEE + R). In this study, we use VPRM at 1-hour time step and 0.125°x0.08° (longitude x latitude) spatial resolution for the year 2014 for a domain covering Western Europe.

III.2.3.2.1.2 CTESSEL

The Carbon-TESSEL or CTESSEL model is the ECMWF land surface model describing energy and CO_2 fluxes between the surface and the atmosphere (Van den Hurk et al., 2000). It is based on Hydrology-Tiled ECMWF scheme for Surface Exchange over Land model (H-TESSEL) (Balsamo et al., 2009; van den Hurk et al., 2000). The model was developed to resolve the exchange of heat with the atmosphere and the water content of soil for weather forecast applications.

The NEE is the results of the ecosystem respiration (R) and the Gross Ecosystem Exchange (GEE), which are computed independently in the model. The respiration (R) is calculated using an empirical equation driven by snow cover, soil moisture, and soil temperature. The Gross Ecosystem Exchange (GEE) is computed using soil temperature, soil moisture, radiation, and a climatology (based on a 9-year averaging from 2000 to 2008) of the leaf area index (LAI) from MODIS satellite. The list of parameters used for the calculation of the NEE is described in detail in Boussetta et al. (2012). The land use change is not accounted for in the CTESSEL

model since the vegetation growth is represented by a 9 year LAI climatology. Moreover, the model does not include any urban schemes for the calculation of the NEE fluxes over the urban areas. As was demonstrated by Bréon et al (2015), the CTESSEL seems to assume that urban areas are covered by ecosystems. In this study, we use outputs from the CTESSEL simulations at ~0.15°x0.15° (longitude x latitude) spatial resolution and 3 hours temporal resolution to represent the Net Ecosystem Exchange for the CO_2 atmospheric modelling. Note that Panareda et al (2016) developed a recent version of the CTESSEL model using a biogenic flux adjustment scheme, but this version was not available for this study.

III.2.2 Atmospheric concentration measurements

We used hourly averages of the CO_2 and CH_4 continuous concentrations measurements at 16 surface stations (Table III.3) located in the domain (figure III.3). Five stations are currently in the process of labelling in the ICOS European infrastructure (CBW, JFJ, OPE, PUY, TRN), and consequently follow the ICOS measurement specifications (Laurent, 2016). Five more contribute to the French monitoring network (BIS, ERS, GIF, OHP, PDM) and also follow very closely the ICOS recommendations. Three stations are part of the ClimaDat Spanish project (DEC, GIC, VAC) available at http://www.climadat.es/. The UK station of Ridge Hill (RGL) was set up in 2012 through the UK-DECC project, in close collaboration with AGAGE (Advanced Global Atmospheric Gases, https://agage.mit.edu/) and ICOS networks (Stanley et al., 2017). In addition, we have downloaded from the World Data Center for Greenhouse Gases (WDCGG; https://ds.data.jma.go.jp/gmd/-wdcgg/) the CO_2 and CH_4 time series from Schauinsland (SCH, Germany), and Plateau Rosa (PRS, Italy). The measurement protocols used at the atmospheric sites are relatively similar, and all agree with WMO recommendations. The instruments are calibrated every 3 to 4 weeks using reference gases calibrated with WMO standards. All observations are respectively expressed in the WMO-X2007 and WMO-X2014A scales for CO_2 and CH_4. At most stations, one or two more reference gases are analyzed regularly for quality control purposes.

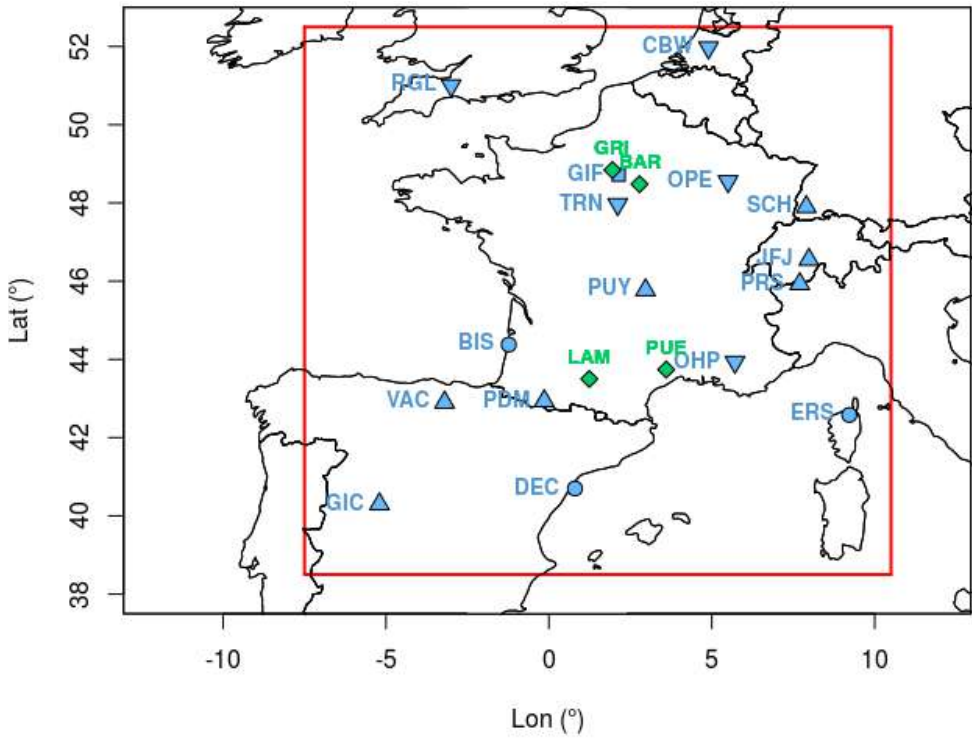

Figure III.3: Simulation domain (red box) and observation sites used in this study. The blue and green color stand for the atmospheric measurement site (https://icos-atc.lsce.ipsl.fr/) and the ecosystem measurement sites (https://icos-eco.fr/) respectively. Note that the atmospheric sites are grouped into four categories according to their characteristics (e.g. topography and environment): coastal (circle), mountain (triangle), peri-urban (square for GIF only), and tall tower (inversed triangle).

Station	Code	Lon (°)	Lat (°)	Altitude (m asl)	Inlet height (m)	Type	Institute	Reference
Biscarrosse	BIS	-1.2	44.3	120	47	Coastal	LSCE	Ahmadov et al, (2009)
Delta de l'Ebre	DEC	0.8	40.7	1	10	Coastal	IC3	-
Ersa	ERS	9.3	42.9	533	40	Coastal	LSCE	-
Gredos	GIC	-5.2	40.3	1436	20	Mountain	IC3	-
Jungfraujoch	JFJ	7.9	46.5	3580	5	Mountain	EMPA	Reimann et al, (2008)
Pic Du Midi	PDM	0.1	42.9	2877	10	Mountain	LSCE, OMP	Tsamalis et al., (2014)
Plateau Rosa	PRS	7.7	45.9	3480	10	Mountain	RSE	Ferrarese et al, (2015)
Puy de dôme	PUY	2.9	45.8	1465	10	Mountain	LSCE, OPGC	Lopez et al, (2015)
Schauinsland	SCH	7.9	47.9	1205	7	Mountain	UBA	Schmidt et al., (2003)
Valderejo	VAC	-3.2	42.9	1086	20	Mountain	IC3	-
Gif-sur-Yvette	GIF	2.1	48.7	160	7	Peri-urban	LSCE	Ramonet et al, (2010)
Cabauw	CBW	4.9	51.9	0	20, 60, 120, 200	Tall tower	ECN	Tolk et al, (2009)
Observatoire Haute Provence	OHP	5.7	43.9	650	10, 100	Tall tower	LSCE, PyTHEAS	Belviso et al., (2016)
Observatoire pérenne de l'environnement	OPE	5.5	48.6	390	10, 50, 120	Tall tower	LSCE, ANDRA	Ramonet et al, (2010)
Ridge Hill Observatory	RGL	-2.5	51.9	199	45, 90	Tall tower	Univ.Bristol	Stanley et al., (2017)
Trainou	TRN	2.1	47.9	131	50, 100, 180	Tall tower	LSCE	Schmidt et al, (2014)

Table III.3: Atmospheric stations characteristics. The altitude of the site represents the altitude of the ground above sea level at the site location, and the inlet height is the altitude of the inlet above ground level. The type of sites are classified according to the topography. (-) means that corresponding sites are recent and still not published.

III.2.3 Ecosystem measurements

In addition to the high precision measurements of CO_2 and CH_4 mixing ratios performed at the atmospheric sites, ICOS is also deploying stations dedicated to the direct measurements of carbon fluxes. Those stations, called ecosystem stations, are monitoring water vapour, heat and CO_2 fluxes in addition to several meteorological and ecosystem parameters like soil temperature and water content at different depths. All variables are measured in order to calculate the carbon and the water-energy balances of the ecosystems. The ecosystem network set up in France, aims to represent the major types of vegetation including grasslands, forests, and crops. The sites used in this study (figure III.3, and Table III.4), provide CO_2 fluxes at half-hourly resolution using the eddy covariance technique. This approach is considered as the main technique to estimate the flux exchanges between the soil and the atmosphere on the local scale (for ~1 ha to 1 km2 areas). It uses 3D wind measurements and other atmospheric parameters to estimate carbon dioxide, methane, water vapor, and heat fluxes based on statistical calculations. More information about the eddy covariance approach can be found in Aubinet et al., 2012. It is important to compare the ~1 ha to 1 km2 spatial representativeness of the eddy flux measurements with the spatial resolution of the biospheric models (≈ 8500 ha and 20000 ha respectively for VPRM and CTESSEL). The upscaling of these local scale measurements maybe problematic in case of large heterogeneity in the landscape surrounding the ecosystem sites. We have analyzed the measured CO_2 fluxes at four different ecosystems sites to evaluate the two biospheric models (CTESSEL and VPRM) used as an input for the atmospheric simulations.

Site	code	Longitude	Latitude	Land cover classification	Institute	Reference
Barbeau	BAR	2.8	48.5	Deciduous forest	CNRS	Delpierre et al. (2009)
Grignon	GRI	1.9	48.8	Crop	INRA	Stella et al. (2002)
Lamasquère	LAM	1.2	43.5	Crop	CNRS	Béziat et al. (2013)
Puechabon	PUE	3.6	43.7	Evergreen forest	CNRS	Allard et al. (2008)

Table III.4: Ecosystem stations used in this study.

III.3 results

III.3.1 Comparison of the national totals and temporal distribution of IER and EDGAR anthropogenic fluxes

In this section, we have compared the mean temporal features and the total emissions aggregated over France for the two inventories described previously (IER for the year 2005 and EDGARv4.2 for the year 2012). The two corresponding annual emission maps were rescaled for the year 2014 to fit the corresponding emission total of CITEPA (Centre Interprofessionnel Technique d'Etudes de la Pollution Atmosphérique, https://www.citepa.org/fr/activites/inventaires-des-emissions/secten) that is used for the National Communication to the UNFCCC. Recently, several studies indicated that the uncertainty in annual national totals from inventories is better than 10% for CO_2 (Peylin et al., 2011), and 20% for CH_4 (Peng et al., 2016). Table III.5 represents the comparison of the rescaled total of CO_2 and CH_4 anthropogenic emissions for the year 2014 over France for IER and EDGAR according to the inventory compiled by CITEPA.

Species	**IER (Mt)**	**EDGAR (Mt)**	**Relative difference (%)**	**CITEPA SECTEN[(1)]**	**Differences CITEPA IER / EDGAR**
CO_2	337	343	~ 2%	322	4.7 / 6.5%
CH_4	2.52	2.71	~ 7%	2.34	8 / 16%

Table III.5: Comparison of the rescaled annual anthropogenic emissions for metropolitan France from IER, EDGARv4.2 and CITEPA (SECTEN format) inventories for the year 2014. In order to make the CITEPA data easily understandable the anthropogenic emission are prepared using the SECTEN format (SECTeurs Economiques et éNergie). [(1)] means that emissions are separated according to Energy and the Economic sectors (SECTEN format).

The relative difference between IER and EDGAR is 7% for CH_4, whereas for CO_2 EDGAR and IER annual totals differ only by 2%. However, both inventories give higher total emissions than the national inventory compiled by CITEPA. The CO_2 total emission offset (2 to 7%) can be explained by the difference in the sectors taken considered by the different inventories. As shown by Ciais et al., 2010, one of the main reasons for the discrepancy between inventories is the definition of the sectors boundaries. For example, the consideration of the biofuels, and the bunker fuels, used for maritime and aircraft international transportation, may increase the CO_2 national budget by 5% to 10%. According to the UNFCCC definition, the emissions due to biomass combustion and to international maritime, river and airborne transport are not

considered in the national inventory compiled by CITEPA for France. Those emissions can be quantified separately, and if we add the 23Mt of CO_2 due to those contributions (extracted from https://www.citepa.org/en/air-and-climate/pollutants-and-ghg/ghg/co2), the CITEPA estimates fall within 2% of IER/EDGAR ones (Table III.5). For CH_4, adding the extra emission due to biomass and international transport (0.14Mt CH_4 extracted from https://www.citepa.org/en/air-and-climate/pollutants-and-ghg/ghg/ch4), the CITEPA estimates range within 10% from IER and EDGAR.

III.3.2 Spatial differences between IER and EDGAR totals

In order to investigate the spatial differences of the two emission maps at 0.1°x0.1° resolution, we represent in figures III.4-A and III.5-A the difference between EDGAR and IER totals for CO_2 and CH_4 respectively. For CO_2 the differences can reach more than 400 $KgCO_2/yr$, whereas For CH_4 it may attain 1000 gCH_4/yr. These high differences are located over big cities and industrial areas (e.g., Paris region). For CH_4 important differences can also occur over large area such as Brittany region, where the differences range between 50 and 200 gCH_4/yr (Figure III.5-A). These differences can be explained by possible inconsistencies in national totals resulting from unaccounted emissions in different sectors, differences for the localization of the point sources, and the errors related to the emission factors (Ciais et al., 2010).

Further, we calculate the percentage of the grid cells for several classes of the absolute difference between EDGAR and IER over the metropolitan France for CO_2 figure III.4-B and CH_4 figure III.5-B. In figure III.4-C and 5-C, we calculate the percentage of the total emission of the grid cells corresponding to the different classes used for figures III.4-B and III.5-B. In France, over 95% of the CO_2 emission grid cells are characterized by an absolute difference (EDGAR minus IER) less than 20 $kgCO_2/yr$ (Figure III.4-B). For CH_4, more than 95% of the emission grid cells are associated with an absolute difference less than 60 gCH_4/yr (Figure III.5-B). These percentages of the grid cells represent 84% and 80% of the total national EDGAR emissions for CO_2 and CH_4 respectively. As can be seen in figure III.4-C and III.5-C the grid cells that are characterized by a difference higher than 20 $kgCO_2/yr$ and 100 gCH_4/yr represent less than 20% of the national emission for CO_2 and CH_4 respectively. In fact, the important differences between EDGAR and IER (more than 100 $kgCO_2/yr$ and 700 gCH_4/yr) occur in a very limited area (hot spots), which does not exceed 1% of the grid cells, and represent up to 2% of national total emissions in France. For Germany and Benelux countries, the larger differences can be explained by the fact that IER uses more detailed data for the economic activities and the demography than EDGAR (Pregger et al.,2007).

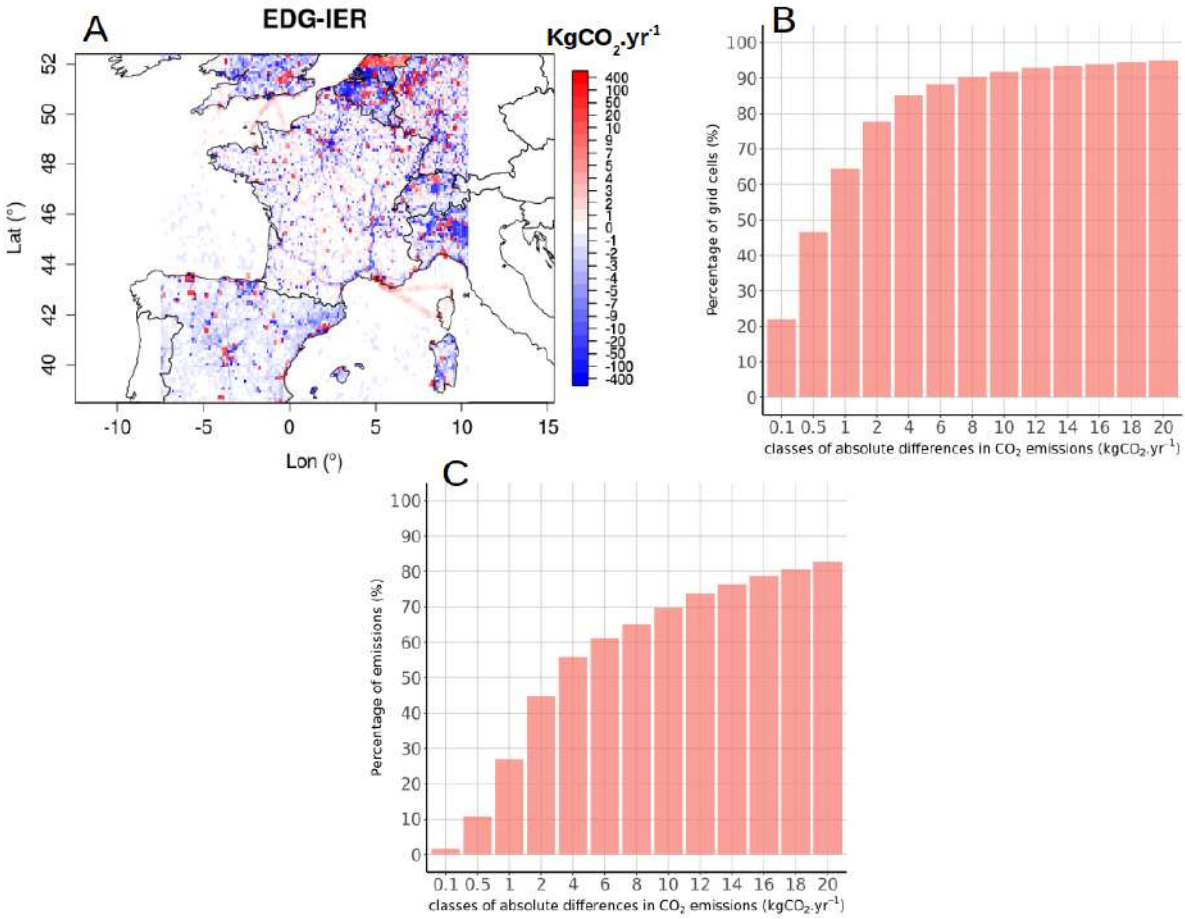

Figure III.4: Panel A, stand for the spatial distribution of the difference between EDGAR and IER inventories (EDGAR minus IER) for CO_2. Panel B (resp. C) represent the cumulated percentages of the grid cells (resp. national emissions) of the absolute difference between EDGAR and IER for the metropolitan France. The cumulated percentages are calculated for various classes of CO_2 emissions differences

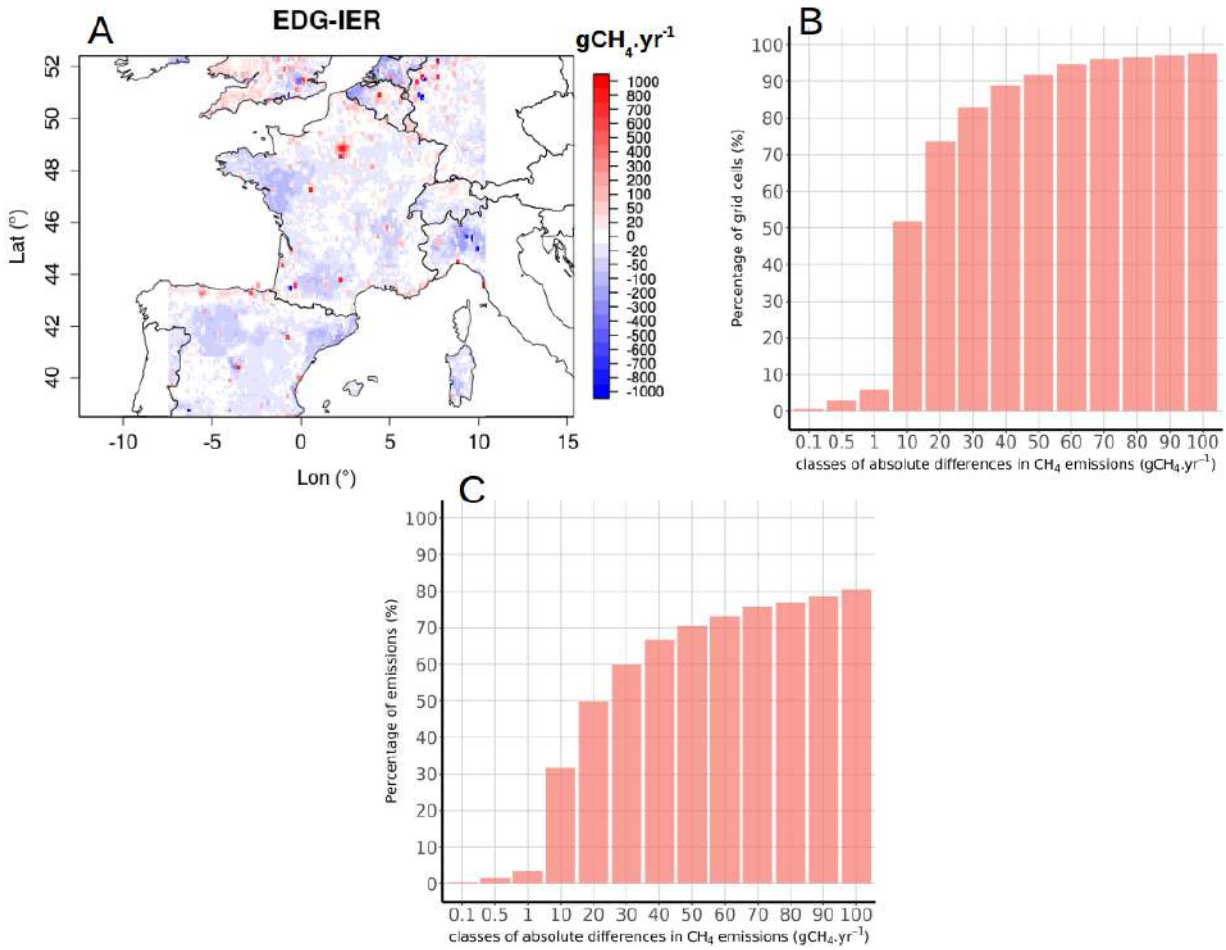

Figure III.5: Panel A, stand for the spatial distribution of the difference between EDGAR and IER inventories (EDGAR minus IER) for CH_4. Panel B (resp. C) represent the cumulated percentages of the grid cells (resp. national emissions) of the absolute difference between EDGAR and IER for the metropolitan France. The cumulated percentages are calculated for various classes of CH_4 emissions differences.

III.3.3 Temporal differences between IER and EDGAR

The emission inventories are generally produced at a yearly scale using statistics of economic activities at the country level. In order to evaluate the simulated atmospheric concentration, we need time-varying emission maps, ideally at the same temporal resolution than the mesoscale transport models (hourly resolution). As explained in the section III.2.3.1 the time varying emissions have been estimated for both IER and EDGAR inventories for the different sectors, using periodical functions (temporal profiles).

In Figure III.6, we represent the temporal variations of the CO_2 and the CH_4 anthropogenic emissions calculated for the two inventories at the level of France. For CH_4 (resp. CO_2) we represent the daily, weekly, and seasonal cycles respectively in panels A, B, and C (resp. D, E, and F) for January (solid line) and July (dashed line). We notice a much larger seasonal variation for IER emissions compared to EDGAR for both CO_2 and CH_4 (Figure. III.6 C-F). The CO_2 seasonal cycle of IER compared to EDGAR emissions (figure III.6-F) has emission higher in winter and lower in summer.

The comparison between the two inventories at a shorter time scale also shows significant differences. Note that the diurnal emission maximums in the morning and late in the afternoon are related to the traffic rush hours (section III.2.3.1). In January (figure III.6-D and III.6-E solid lines), the CO_2 emissions of IER are about 30% higher than EDGAR. The difference reaches a maximum during daytime (40%), but during the night, it decreases slightly to 20%. In July (figure III.6-D and III.6-E dashed line), the CO_2 EDGAR emissions are 30% larger then IER during the night and less than 5% during the day. In both inventories, the amplitude of the diurnal cycle is larger than the weekly and the seasonal cycle amplitudes.

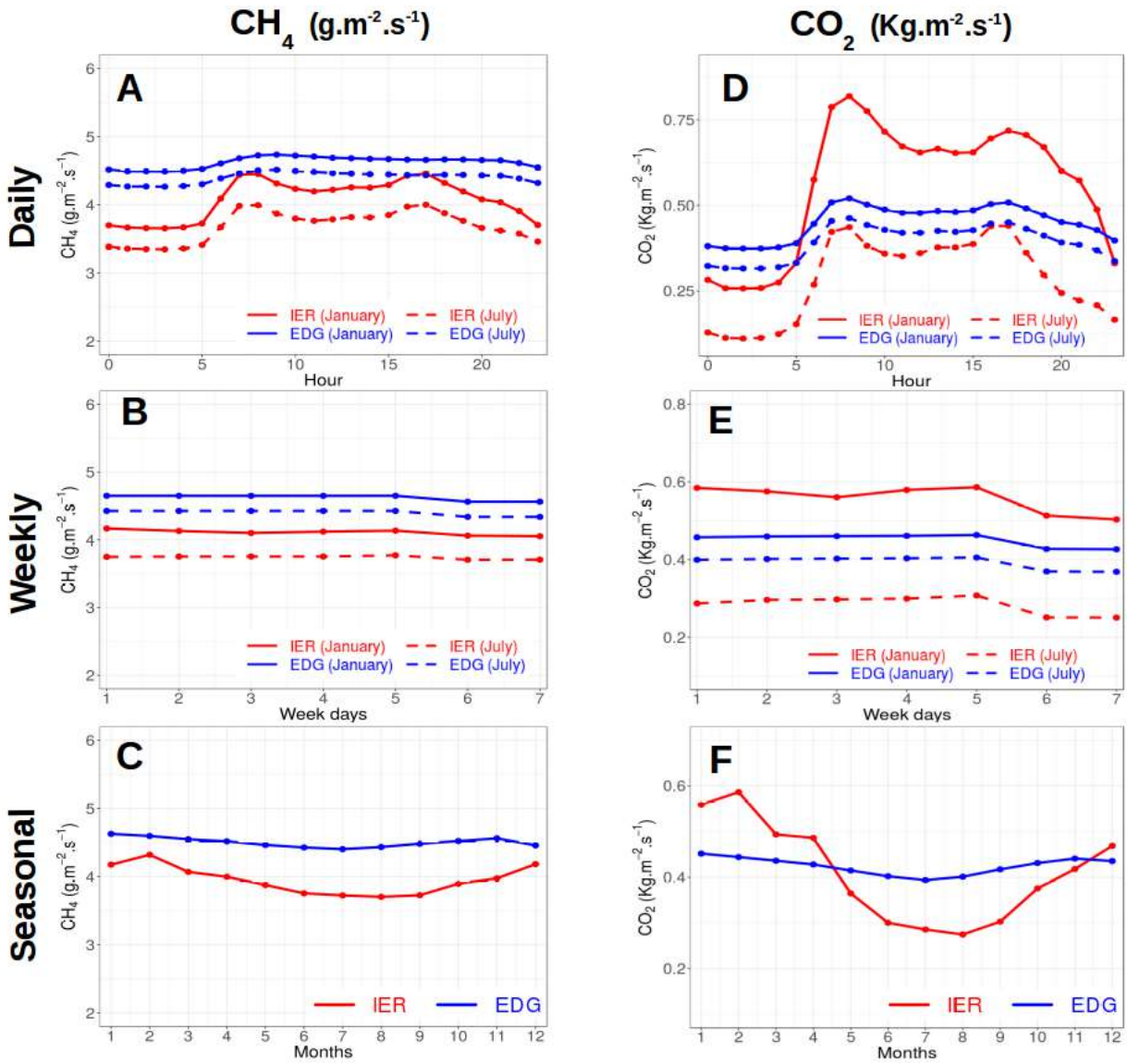

Figure III.6: Temporal variation of CH_4 and CO_2 total anthropogenic fluxes over France at a daily (A and D), weekly (B and E), and monthly scales (C and F). Solid and dashed line represent respectively the totals for January and July.

For CH_4, the emissions of IER are systematically lower than EDGAR (figure III.6-C), which corresponds to the 7% lower total emission in Table III.5. The temporal variations of the CH_4 emissions are relatively weak since we applied a constant factor (factor=1/365*24, see section III.2.3.1) to the principal CH_4 emission sectors (e.g. gas production and distribution, enteric fermentation and waste management). The temporal variation was applied only to the energy production, the industrial emission, and the road traffic sectors, which represent less than 10% of the national totals.

The two anthropogenic emission products displayed a significant difference in their temporal and spatial variation, especially for CO_2, although the annual totals showed a difference of 2% for CO_2 and less than 7%

for CH_4. Consequently, this comparison shows that more efforts are required to a develop better quality of the anthropogenic emissions maps at high spatio-temporal resolutions, which can be achieved for example by using city scale information to enhance the quality of the traffic emission maps, and the energy consumption in urban areas.

III.3.4 Comparison of the biogenic CO_2 fluxes between CTESSEL and VPRM

Similarly to the comparison of the anthropogenic emission maps, we have compared the time varying maps of biogenic CO_2 exchanges from the two vegetation models (CTESSEL Boussetta et al., 2012 and VPRM Mahadevan et al.,2008). Figure III.7 presents a comparison of the monthly totals of the net ecosystem CO_2 exchange (NEE) simulated over France by those two models. Note that NEE is the sum of two fluxes: the gross ecosystem exchange (GEE) and the ecosystem respiration (Mahadevan et al.,2008). Both fluxes are sensitive to temperature and the soil moisture, and GEE is particularly sensitive to photosynthetically-active shortwave radiation.

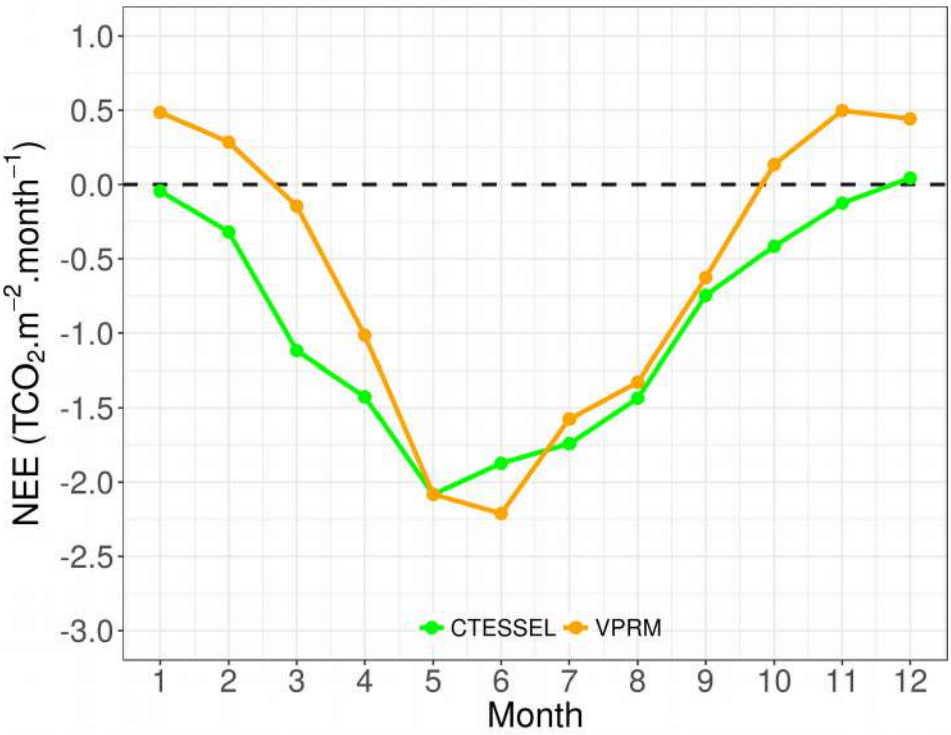

Figure III.7: Monthly totals of NEE fluxes for VPRM and CTESSEL over France.

Both VPRM and CTESSEL, show close high negative values of NEE (uptake from the atmosphere) between late spring and early summer (figure III.7). The two models have a similar maximum uptake, in June for

VPRM (-2.2 $tCO_2.m^2.month^{-1}$) and in May for CTESSEL (-2 $tCO_2.m^2.month^{-1}$). The difference is more important in winter. From October to February, VPRM is characterized by a positive NEE total over France explained by respiration exceeding gross ecosystem exchange, as expected for northern temperate regions, and consistent with flux tower measurements (Sampson et al., 2001). Except for December where the monthly flux is slightly positive (+0.05 $tCO_2.m^2.month^{-1}$), CTESSEL NEE remains always negative, indicating an uptake of CO_2 all year round, even in winter. This unexpected result may be related to the fact that CTESSEL calculates the GEE and the R separately, and rescales the two parameters to fit the net CO_2 uptake from flux measurements at the global scales only (Boussetta et ., 2012). Even if this calibration provides accurate results at the global scale (Boussetta et al., 2012), the calibration of the net ecosystem parameters may lead to significant errors at the subcontinental scale. Panareda et al., (2014) already indicated that the CO_2 fluxes retrieved from the used version of the CTESSEL model are characterized by a negative bias in Europe, especially during winter. This bias is related to the misrepresentation of the ecosystem respiration for some vegetation types (Panareda et al., 2016). In France, a large bias in the NEE was related to the respiration of the croplands. The evaluation of the CTESSEL model against atmospheric sites showed a significant underestimation of CO_2 from respiration during winter (Panareda et al., 2014). As a result of this evaluation, an effort was made to develop the Biogenic Fluxes Adjustment Scheme (BFAS) in order to correct the NEE bias of the CTESSEL model used for MACC atmospheric model (Panareda et al., 2016). This flux-adjusted version of CTESSEL was not available for this study.

III.3.4.1 Spatial distribution of the modeled fluxes for January and July

We present in figure III.8 the spatial distribution of simulated NEE fluxes for January and July in the domain of the study for each model. In July both models simulate negative value of NEE (uptake of more than -200 $gCO_2.m^{-2}.month^{-1}$) over a major part of the domain (except Spain). The NEE spatial distributions appear quite similar between the two models, but substantial differences can be observed in some regions (figure III.8-C and III.8-F). During July, important contrast between VPRM and CTESSEL occur in a large area in the north of the domain (North of France, Germany and Belgium), with a difference that may attain 200 $gCO_2.m^{-2}.month^{-1}$ (Figure III.8-F). In January the comparison of the two maps (Figure III.8 A-B) reflects the overestimation of the carbon uptake by CTESSEL. According to VPRM, the NEE is positive everywhere in France during January, except in Corsica (figure III.8-A), whereas for CTESSEL, the NEE is negative over a large part of France, with some exception in Les Landes Forest, Pyrénées, and Massif Central regions. In the

north part of France, CTESSEL simulates a source of CO_2 of around -40 $gCO_2.m^{-2}.month^{-1}$ (Figure III.8-B) when in VPRM this source exceeds 60 $gCO_2.m^{-2}.month^{-1}$ (Figure III.8-A).

From this comparison, we can conclude that both CTESSEL and VPRM are characterized by a peak CO_2 uptake during late spring. Even if the monthly totals of the two models do not diverge much during spring-summer, very large differences in the spatial distribution of NEE uptake are found in summer with much less uptake in VPRM than CTESSEL in the north of France, Benelux and Western Germany. These differences are expected to impact significantly the CO_2 atmospheric concentrations.

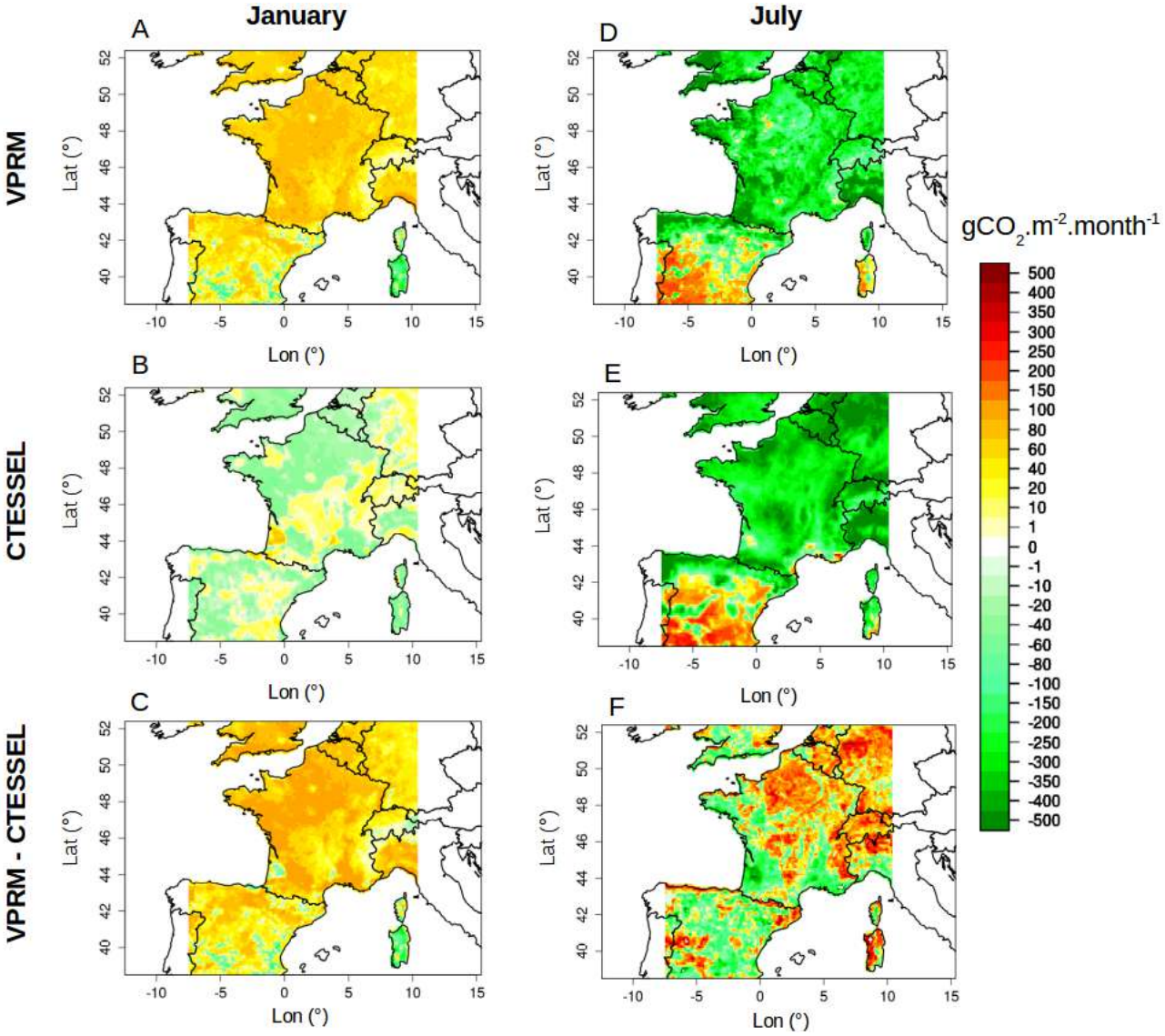

Figure III.8: Spatial distribution of the total Net Ecosystem Exchange (NEE) during January and July, for VPRM (panels A and D), CTESSEL (panels B and E), and VPRM minus CTESSEL (panels C and F). By convention, a positive sign is a source of CO_2 emitted to the atmosphere.

III.3.4.2 Comparison between the modeled and the simulated NEE

The eddy covariance method (EC) makes it possible to estimate the NEE fluxes at the local scale using 3D wind measurements and CO_2 concentration measurements on top of flux towers. In this section, we compare between observed fluxes at four EC sites in France and the modeled NEE of the CTESSEL and the VPRM extracted from the grid-cell containing each flux tower. Eddy covariance measurements are available in France at two forest sites (Barbeau and Puechabon,) and two crop sites (Grignon and Lamasquere). Barbeau and Grignon are located in the Ile de France region, and the other (Puechabon and Lamasquere) are in the South of France (Figure III.3). The comparison of the mean diurnal cycles of NEE is presented for January and July (Figure III.9), whereas the seasonal cycle comparison is presented in figure III.10.

III.3.4.2.1 Diurnal cycle analysis

In January we notice a very small diurnal cycle for both modeled and observed eddy covariance NEE at the four sites (Figure III.9-January). Contrary to the VPRM model, CTESSEL simulates a net uptake of CO_2 in midday at all sites, which is only observed at Grignon (winter wheat) and Puéchabon (green oak). This can be explained for EC data by the carbon uptake due to the early development of winter wheat in the Ile de France region (sowing in Octobre, germination in November) and by the evergreen phenology of green oak with wet conditions in winter ensuring CO_2 uptake at Puéchabon. During summer, a larger diurnal cycle is shown in observed and simulated NEE, with a stronger amplitude in Barbeau and Lamasquere sites (Figure III.9-July). The misrepresentation of the amplitude of the diurnal cycle at the cultivated sites (too low at Lamasquere and too high at Grignon) can be explained by the fact that wheat started to be senescent in June with the NEE reaching 0 at the beginning of July, and by the cultivation of a highly productive summer crop (maize) at Lamasquère with GEE probably under-estimated by the models. In fact, at Lamasquere, the strong observed amplitude corresponds to the flowering phase of the maize (started late June), with maximum leaf area and photosynthetic uptake, which is sown in April and harvested during August. Beziat (2009) works (Pierre Beziat thesis), confirms that the discrepancies between the observed and the simulated NEE at Lamasquère are associated to precocious harvesting of the maize which is not taking into account by the models.

The site to site variability in the EC measurements is not reproduced by the models showing a different phase and amplitude at the four sites, especially during July. Consequently, the simulated diurnal cycles are under-estimated by a factor of 2-3 respectively for Barbeau and Lamasquere and overestimated at Grignon and

Puechabon (Figure III.9-July). At Grignon, the observations show a flat diurnal cycle with a constant positive NEE through the whole day. The NEE peak in the simulated diurnal cycle occurs too early for VPRM (~2 hours earlier than observed) and too late for CTESSEL (2-3 hours later). This phase difference appears for all sites, especially during July. Several studies were carried out to evaluate the simulate NEE at the station level (e.g. Krinner et al., 2005, and Zhao et al., 2013). The later studies showed important differences between the simulated and the observed diurnal cycle especially at cropland sites, confirming the difficulty to correctly simulate the biogenic fluxes at the scale of the EC measurements.

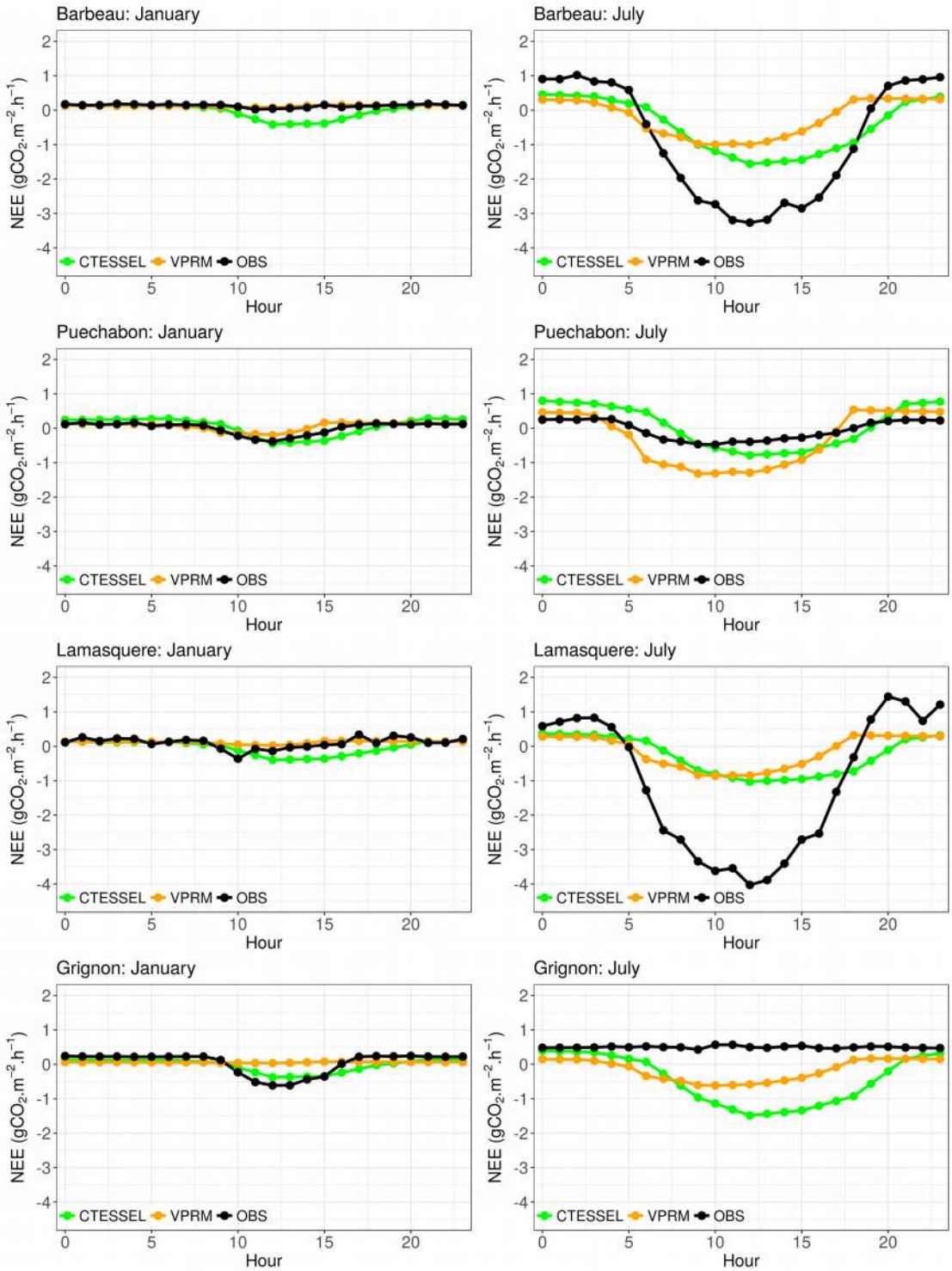

Figure III.9: Diurnal cycle of the simulated and the observed Net Ecosystem Exchange (NEE) for four different sites (Barbeau, Grignon, Lamasquere, Puechabon, Figure 3), during January (panel A) and July (B). The time is presented in UTC

III.3.4.2.2 Seasonal cycle analysis

The simulated seasonal cycle of NEE by CTESSEL and VPRM is compared to EC measurements in figure III.10. Note that the observed NEE seasonal variation at the cultivated sites is strongly dependent on the site management and on the phenology of the cultivated species grown that year. The site management is not included in CTESSEL and VPRM, and the phenology is included in both models through satellite greenness observations, but not at the point scale of the EC measurements. Therefore, the spring NEE uptake of winter wheat at Grignon followed by a CO_2 source after the harvesting in June; is not captured by the models. The large and short NEE peak uptake of maize at Lamasquère is also missed in both models. At Lamasquere the maize crop that was sown in April and harvested during late August, explains the maximum of the NEE during July and the decrease starting from August. Both Grignon and Lamasquere sites are irrigated and their phenology is controlled by the soil water content. Moreover, the cultivated sites follow a yearly crop rotation plan, and the models do not consider this rotation in the used surface scheme on the scale of EC measurements (rotations are implicitly included as well as vegetation heterogeneity in the greenness satellite index used in the models to define the phenology). This suggests that the development of biogenic models that include modules describing the grazing, the irrigation, the harvesting, and the plant rotation plan can improve the phase and amplitude of NEE

The phase of the seasonal NEE is better represented by the models at the two forest sites, especially during winter. However, the amplitude of the seasonal cycle is not well reproduced by the two models. For example, in Barbeau the two models simulated an amplitude of -0.6 $gCO_2.m^{-2}.h^{-1}$, where the EC data attain -1.4 $gCO_2.m^{-2}.h^{-1}$. The difficulties in modeling the NEE at the forest site during summer can be associated to a misrepresentation of the phenology (Szczypta et al., 2014). Especially, the inefficiency of the satellite data to correctly estimates the water stress during summer, which affects the simulation of the GEE and the R (Mahadevan et al., 2008). In fact, Szczypta et al., (2014) demonstrate that several environmental parameters, such as soil moisture and rain pulses, may significantly influence the seasonal cycle of the carbon fluxes in a during summer. Other reason that may explains the discrepancies between the modeled and the observed NEE is addressed to the uncertainties related to the land cover schemes used to define the vegetation types (Congalton et al., 2014). Both models used a vegetation classification which defines the type of plant in each grid-cell. However, these vegetation models are sometimes not suitable for the modeling of the CO_2 fluxes. For instance, the forest type that is composed mainly by high vegetation over low vegetation may lead to

important source of error in regions where the contribution of the low vegetation is underestimated by the models.

Overall the VPRM model performs better than CTESSEL in wintertime, but none of the models is clearly better to reproduce the observed seasonal phase and amplitude of NEE. Clearly much more EC sites would be needed to identify the processes responsible for misfit between observations and simulations. Comparison at EC sites is informative of biases of models, but the bias of a model at a point site observation of NEE does not relate evidently to the bias of this model over a region with different management plans and vegetation types.

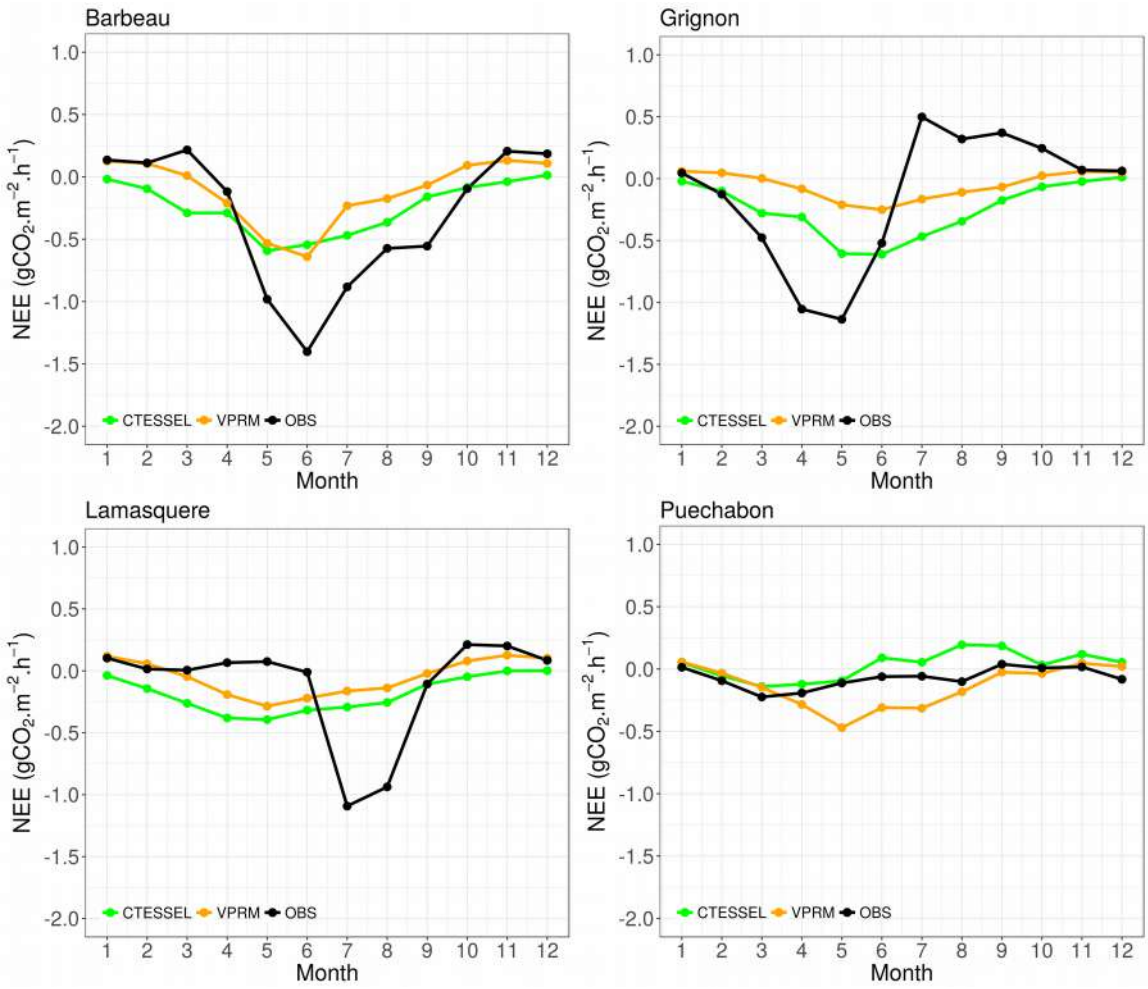

Figure III.10: Seasonal cycle of simulated and observed Net Ecosystem Exchange (NEE) at the four sites (Barbeau, Grignon, Lamasquere, Puechabon)

III.3.5 Sensitivity of the concentrations to the meteorological forcing

We have performed two simulations with the CHIMERE model driven by the meteorological fields provided by ECMWF and AROME. In this analysis, the two simulations are performed with the same CO_2 (EDGAR and VPRM) and CH_4 (EDGAR) surface fluxes, in order to study the sensitivity of the CO_2 and CH_4 concentrations to the meteorological fields that drive the atmospheric transport over the domain presented in figure III.3 (section III.2.4). We will first present the sensitivity of the diurnal and seasonal cycles at the atmospheric sites, before discussing the spatial distribution of the differences over the domain. We will also study the sensitivity of the simulated concentration to different diurnal time windows by comparing the daytime to the nighttime data.

Conducting the comparison between the two meteo-transport configurations using other emission maps may result in different results (different maps and time series of differences between the concentrations obtained with the 2 models). To simplify the analysis, we show results for one set of fluxes only, but we have checked that the general patterns of differences analyzed below are quite similar for different flux products. For brevity reason, the time series analysis is focused on the eight French atmospheric sites (BIS, OPE, TRN, PUY, PDM, OHP, ERS, and GIF). The sites outside of France are presented in the appendix (Figures SIII.5, SIII.6, SIII.7, and SIII.8).

III.3.5.1 Diurnal cycle

The comparison between the simulated and the observed concentrations at the French sites is performed using the mean diurnal cycle for January (Figures III.11 and III.12 for CO_2 and CH_4 respectively), and July (Figures III.13 and III.14 for CO_2 and CH_4 respectively). Note that the diurnal cycle analysis for PDM and OHP is not presented for January, since the measurements at these sites start in May and June 2014 respectively.

In January we observe in most sites higher concentrations of CO_2 and CH_4, when using ECMWF compared to AROME (Figures III.11 and III.12). At some sites, like ERS and OPE, this offset remains constant through the day, but generally, it is slightly more pronounced in the nighttime.

During the afternoon (from 12:00 to 18:00), the difference between AROME and ECMWF at low altitude sites remains lower than 1ppm for CO_2 and vary between 5 and 15 ppb for CH_4 for January (figures III.11 and 12). This difference increases during the night and may reach 2 ppm and 20 ppb of difference for CO_2 and

CH_4 respectively (e.g. GIF site in figure III.11, and BIS in figure III.12). This indicates that the simulated concentrations are more sensitive to the transport processes during the night for the low altitude sites. At the mountain sites the important differences are noticed during the day (e.g. PUY in figure III.11, the remaining mountain sites for January can be found in the appendix). These differences can be explained by the difficulty in the simulated upslope winds which bring the boundary layer air from lower elevations during the day at the site leading to significant bias between the atmospheric models (Chevalier et al., 2010, Patra et al., 2008). The difficulty in simulating the atmospheric concentrations at mountain sites are related to the horizontal (AROME at 0.025°, and ECMWF at 0.15°) and the vertical (60 levels for AROME, and 137 levels for ECMWF) resolution of the models, which influences the representation of the mesoscale driven flows, e.g. from thermic driven or at night gravitational flows.

As the low altitude sites, the higher CO_2 and CH_4 concentrations when using ECMWF compared to AROME can be explained by the differences between the simulated wind for the two models (Figure SIII.9). In fact, during January, the simulated wind speeds by AROME are higher by a factor between 1.5 and 2 compared to ECMWF. For example, at OPE we have a monthly wind speed of 9 m/s for AROME, where for ECMWF the wind speed does not exceed 6 m/s. This confirms that higher wind speed leads to an increase in the horizontal mixing (Geels et al., 2007), and consequently a decrease in the atmospheric concentrations.

There is no significant difference in the amplitudes of the diurnal cycles simulated for CH_4 by the two models in January, except at BIS. At this site, the AROME model simulates higher CH_4 concentration (up to 20 ppb) during the night. This signal represents an anomaly for two reasons: there are very few sites where AROME concentrations are higher than ECMWF, and there is no such difference for CO_2. The increase of CH_4 concentration during the night with AROME model, cannot be explained only by the PBL heights which are quite similar for the two models (Figure SIII.1). The difference could be due to the horizontal transport simulated with AROME and ECMWF wind fields, and the reason why we observe such a difference for CH_4 and not for CO_2 is due to the presence of a hotspot CH_4 emission east of the station (Figure III.15-C). Consequently, a higher percentage of wind from the east significantly increases the CH_4 concentrations during the night (Figure III.15-A). It should be noted that this nighttime CH_4 increase in the AROME simulation is overestimated compared to the observations.

In July the differences of CO_2 and CH_4 concentrations generated by the use of AROME and ECMWF meteorological fields are less systematic than in January. First of all, we observe in July opposite results for CO_2 and CH_4 at several sites. At most sites, the ECMWF simulation gives higher CH_4 concentration, whereas for CO_2 the concentrations are generally higher or equal than with AROME. Contrary to January when both CO_2 and CH_4 fluxes are positive, in July there is NEE surface CO_2 uptake. Consequently, it looks like the

ECMWF model tends to have a higher sensitivity to the surface emissions (positive for CH_4, negative for CO_2) than AROME. Moreover, the higher wind speed of ECMWF compared to AROME during July (Figure SIII.9), increases the advection of air masses, and leads to lower atmospheric concentrations. However, the opposite can be seen for CH_4 (e.g. BIS). In order to explain the higher CH_4 concentration using ECMWF compared to AROME during the afternoon, we represent in figure III.15-B the diurnal averages of CH_4 concentration (using data from 12:00 to 18:00). In Figure III.15-B we notice a lower CH_4 concentration using ECMWF compared to AROME between 5th and 15th of July (differences less than 5 ppb). But during some specific synoptic events (e.g. between 22th and 28th July), we observe a higher CH_4 concentration using ECMWF, leading to higher values compared to AROME. The difference between the two simulations is related to the change in the wind direction as presented on the top of figure III.15-B. In fact, during this period, ECMWF simulates east and north-east winds which advect higher CH_4 concentration from the emission point source located one grid-cell east of BIS (Figure III.15-C). Despite the higher ECMWF wind speed 5.5 m/s compared to AROME 4 m/s at BIS, the difference in the wind direction between the two transport fields impacts significantly the simulated concentration, and lead to higher CH_4 concentration using ECMWF compared to AROME.

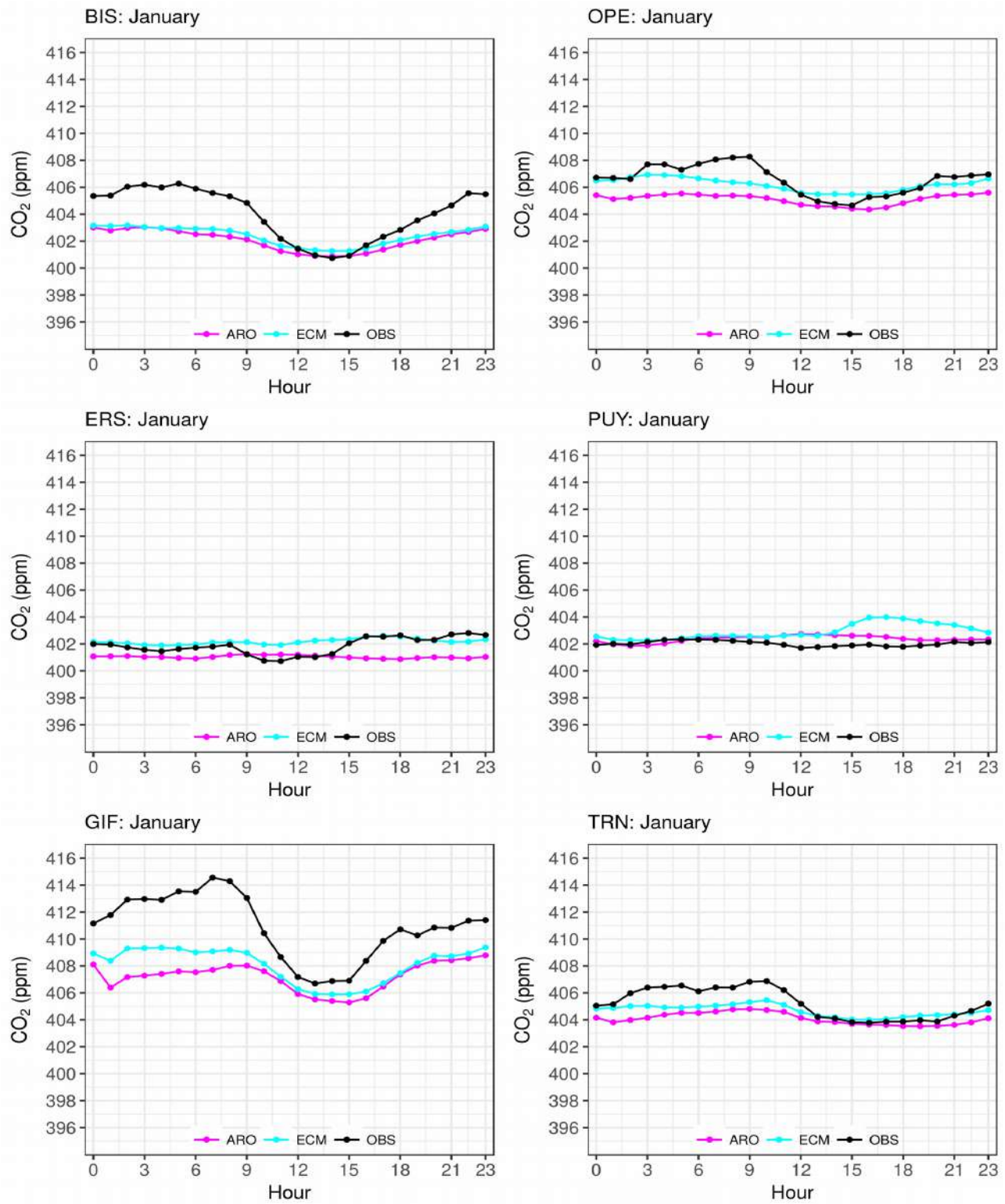

Figure III.11: CO_2 average diurnal cycle at BIS, OPE, PUY, TRN, ERS, and GIF, for the observed (black) and the simulated (red and blue for AROME and ECMWF respectivly) concentrations during January.

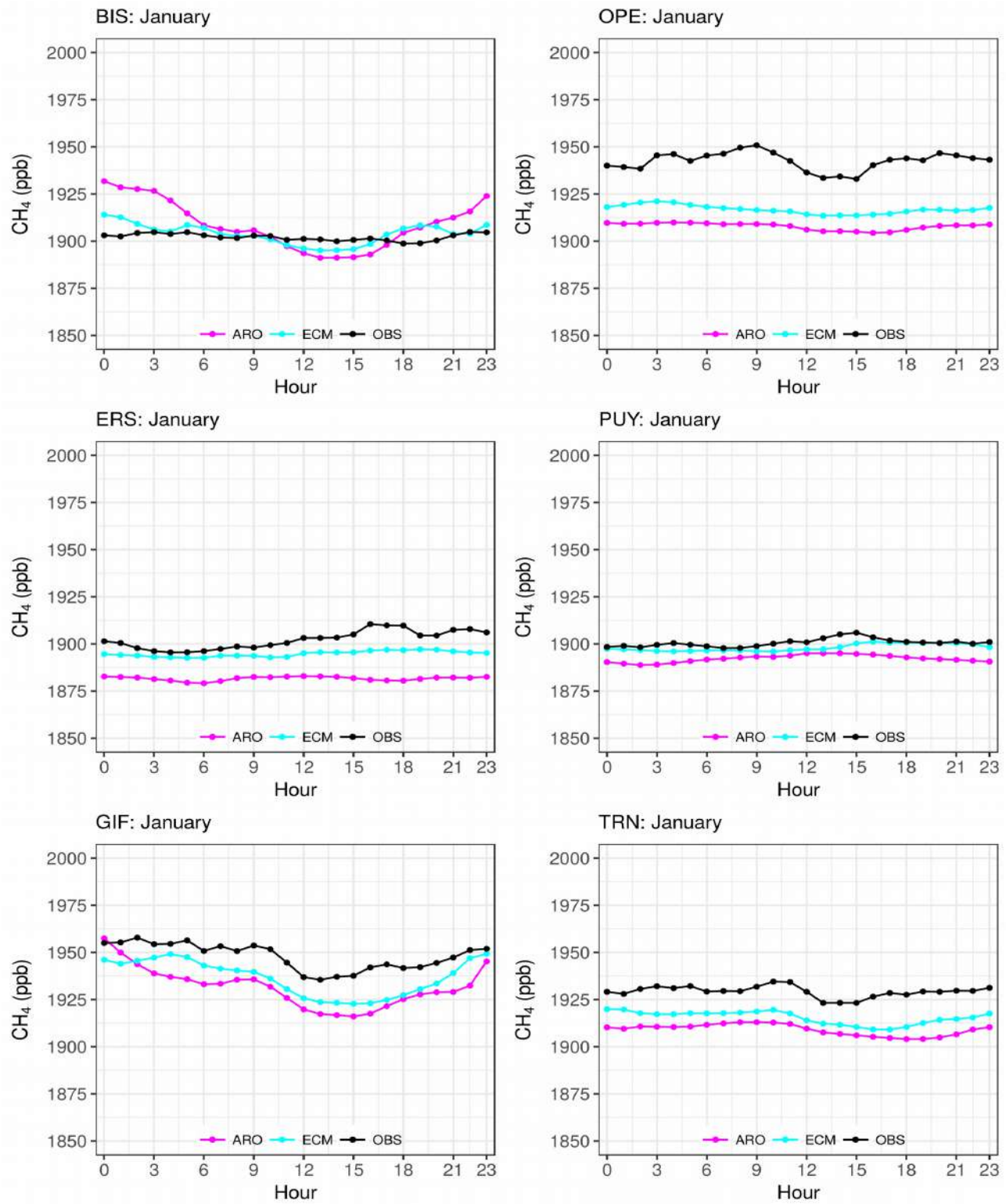

Figure III.12: CH_4 average diurnal cycle at BIS, OPE, PUY, TRN, ERS, and GIF, for the observed (black) and the simulated (red and blue for AROME and ECMWF respectivly) concentrations during January.

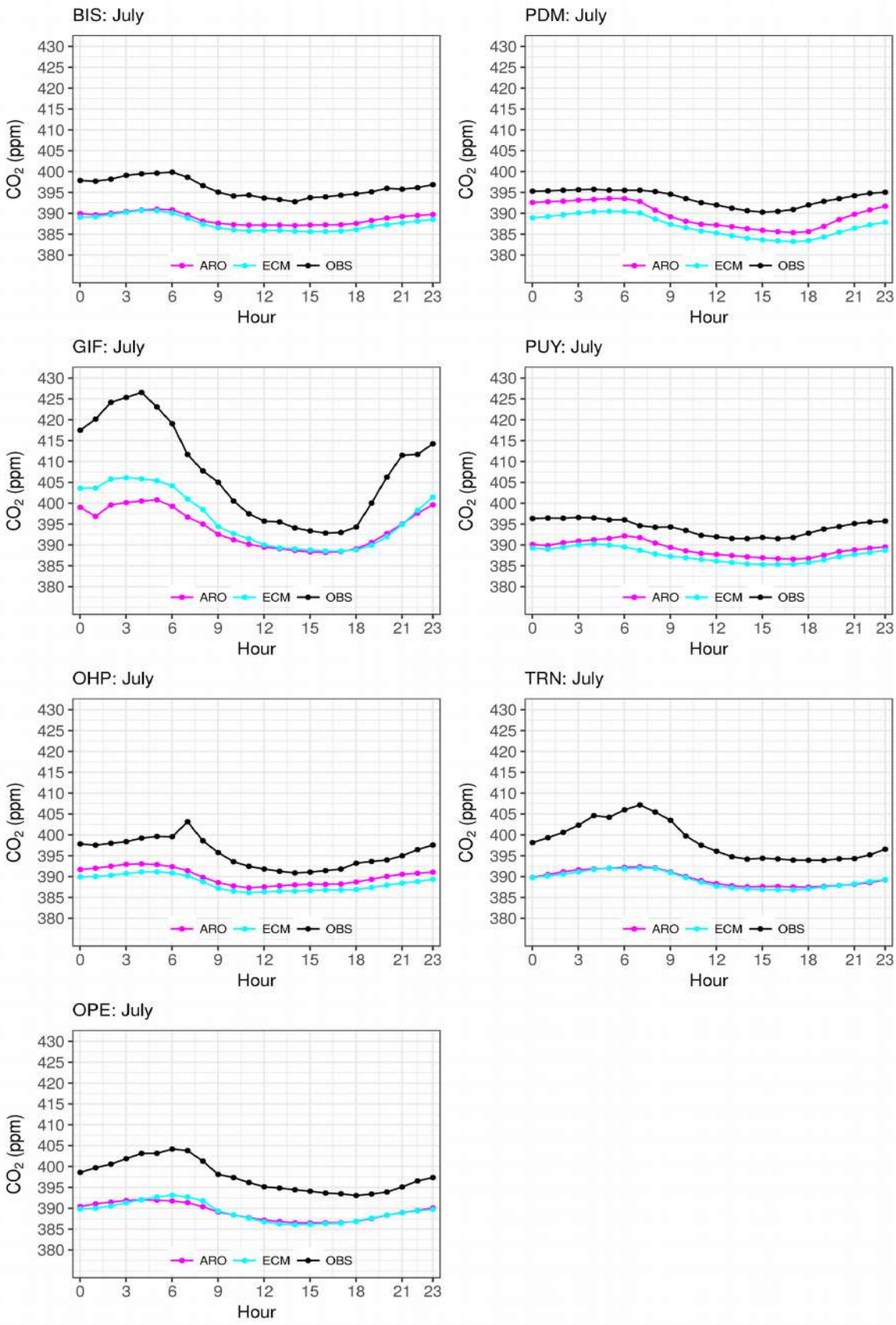

Figure III.13: CO_2 average diurnal cycle at BIS, GIF, OHP, OPE, PDM, PUY, and TRN, for the observed (black) and the simulated (red and blue for AROME and ECMWF respectivly) concentrations during July.

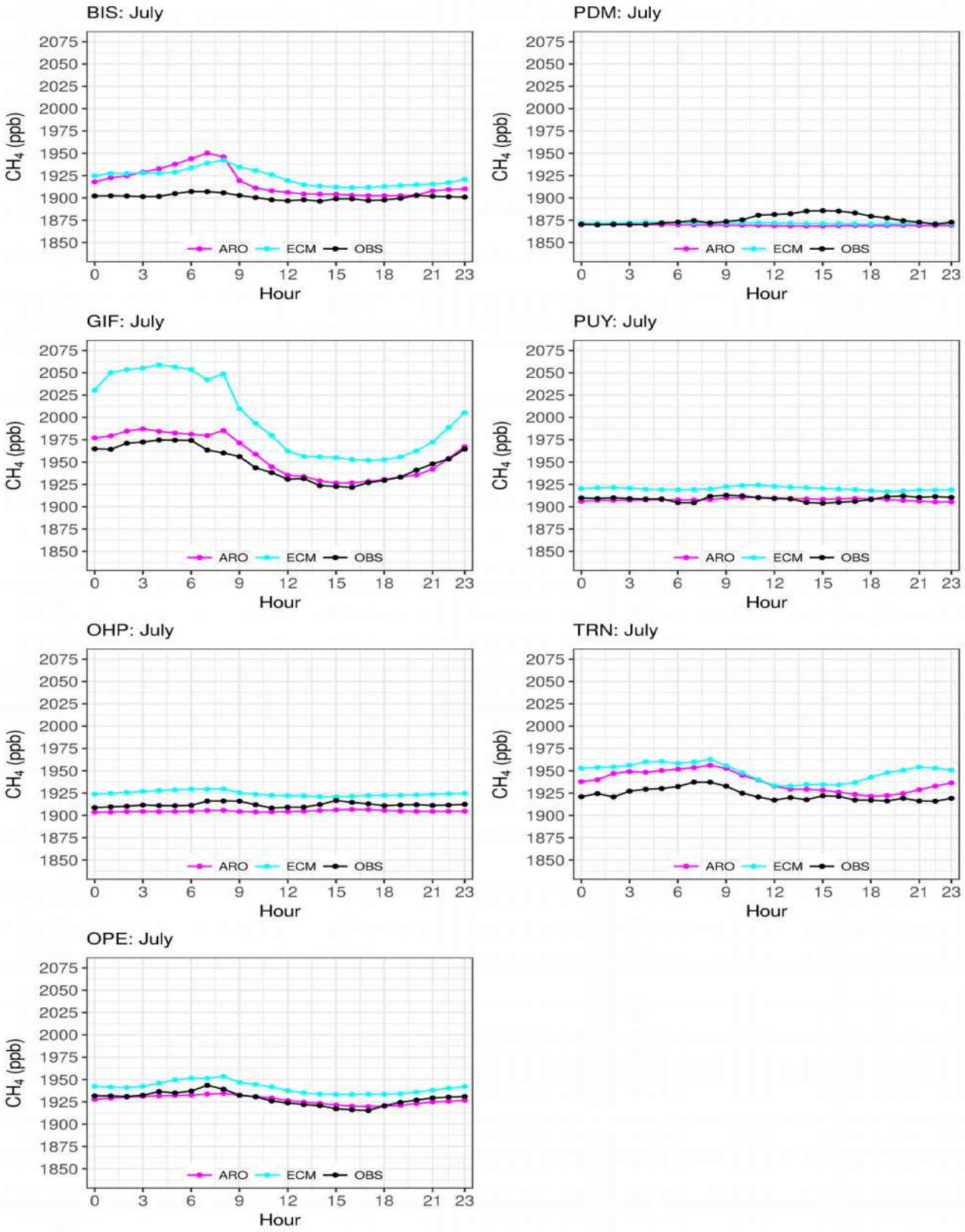

Figure III.14: CH_4 average diurnal cycle at BIS, GIF, OHP, OPE, PDM, PUY, and TRN, for the observed (black) and the simulated (red and blue for AROME and ECMWF respectivly) concentrations during July.

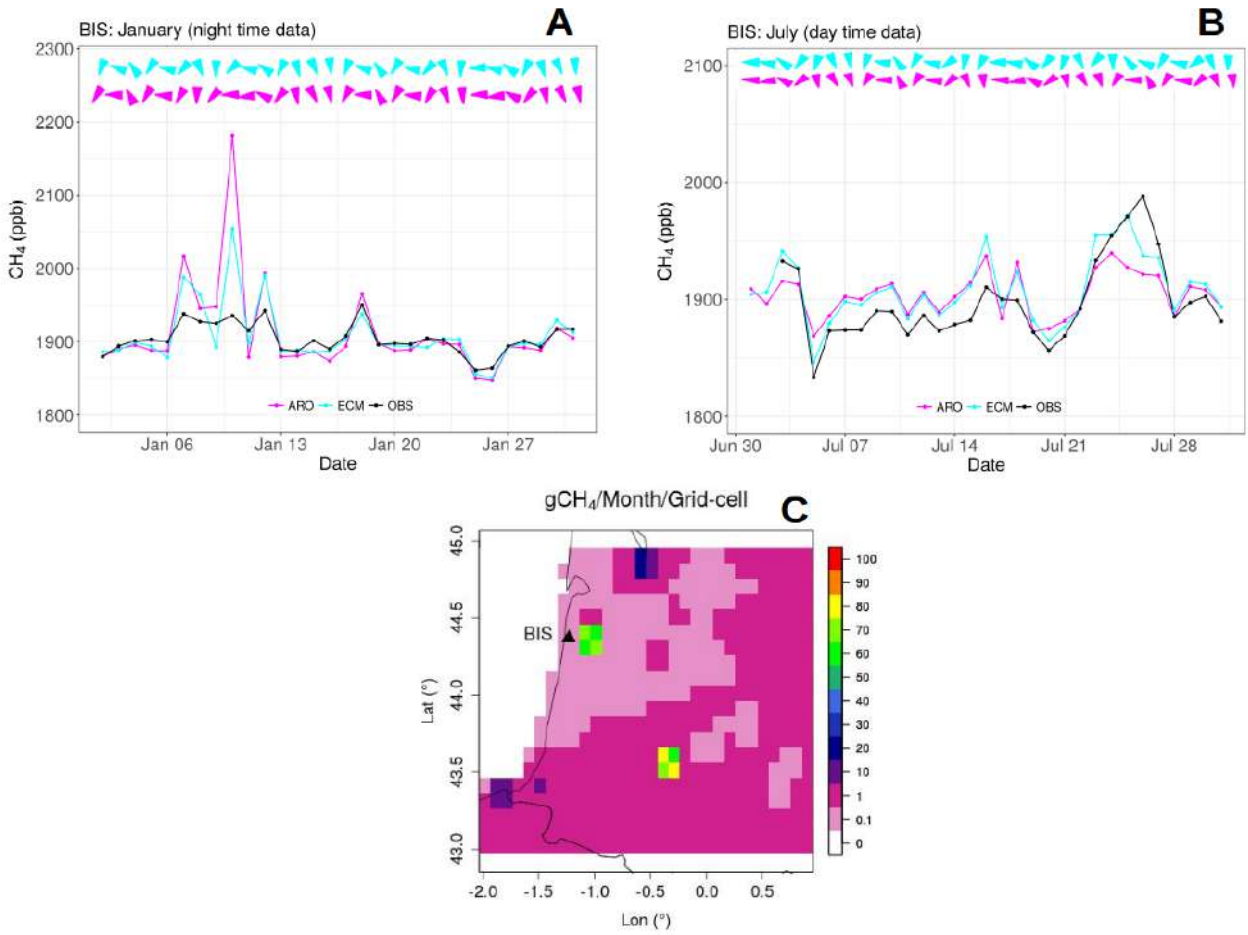

Figure III.15: CH_4 daily average at BIS using the nighttime data (00:00 to 06:00) for January (A), using the afternoon data (12:00 to 18:00) for July (B). The arrows on the top of panels A and B stand for the wind direction simulated by the AROME (magenta) and ECMWF (cyan).Figure (C) represent the spatial distribution of the CH_4 surface fluxes retreived from EDGARv4.2 FT2010 inventory.

III.3.5.1.2 Seasonal cycle

Figures III.16 and III.17 represent the variations of the daily averaged afternoon (from 12:00 to 18:00) observed and simulated concentrations for CO_2 and CH_4 for low altitude sites and nighttime data (from 00:00 to 06:00) at the mountain sites. Note that the observed data are available only from January to June for ERS, and start from May and June for PDM and OHP respectively. CO_2 is characterized by a well pronounced (10 to 20 ppm) seasonal cycle with a minimum occurring in July and a broad maximum between November and March. Conversely, the seasonal cycle of CH_4 is relatively weak (20 to 60 ppb) compared to the month to month variability. However similarly to CO_2, we observe at most sites a minimum concentration occurring late summer (between August and September) and a maximum between November and March.

Among the 8 sites (figures III.16 and III.17), the seasonal cycle of the ECMWF and AROME simulations are similar, with a correlation coefficient (between the two models) larger than 0.9 for both CO_2 and CH_4. There is no significant change in the phase of the simulated cycles when using one model or the other. The monthly differences between the two simulations range by ±3 ppm for CO_2, and from 5 to 15 ppb for CH_4. The CH_4 concentrations simulated using ECMWF meteorology are systematically higher compared to the AROME simulation. As detailed previously with the description of the mean diurnal cycles, the situation is different for CO_2. Due to the higher sensitivity to the surface flux with ECMWF compared to AROME, the simulated concentrations using ECMWF meteorology are generally lower in summer and higher in winter. Both models overestimate the amplitude of the seasonal cycles compared to the observations (Figure III.16), and the overestimation is 15% larger with ECMWF compared to AROME. However, it should be noted that the wintertime concentrations simulated with ECMWF are generally closer to the observations, and the reverse in spring and summer. For CH_4 both models underestimate the seasonal cycle (Figure III.17) and the month to month variability observed at the sites, and it remains difficult to say that one model performs better than the other.

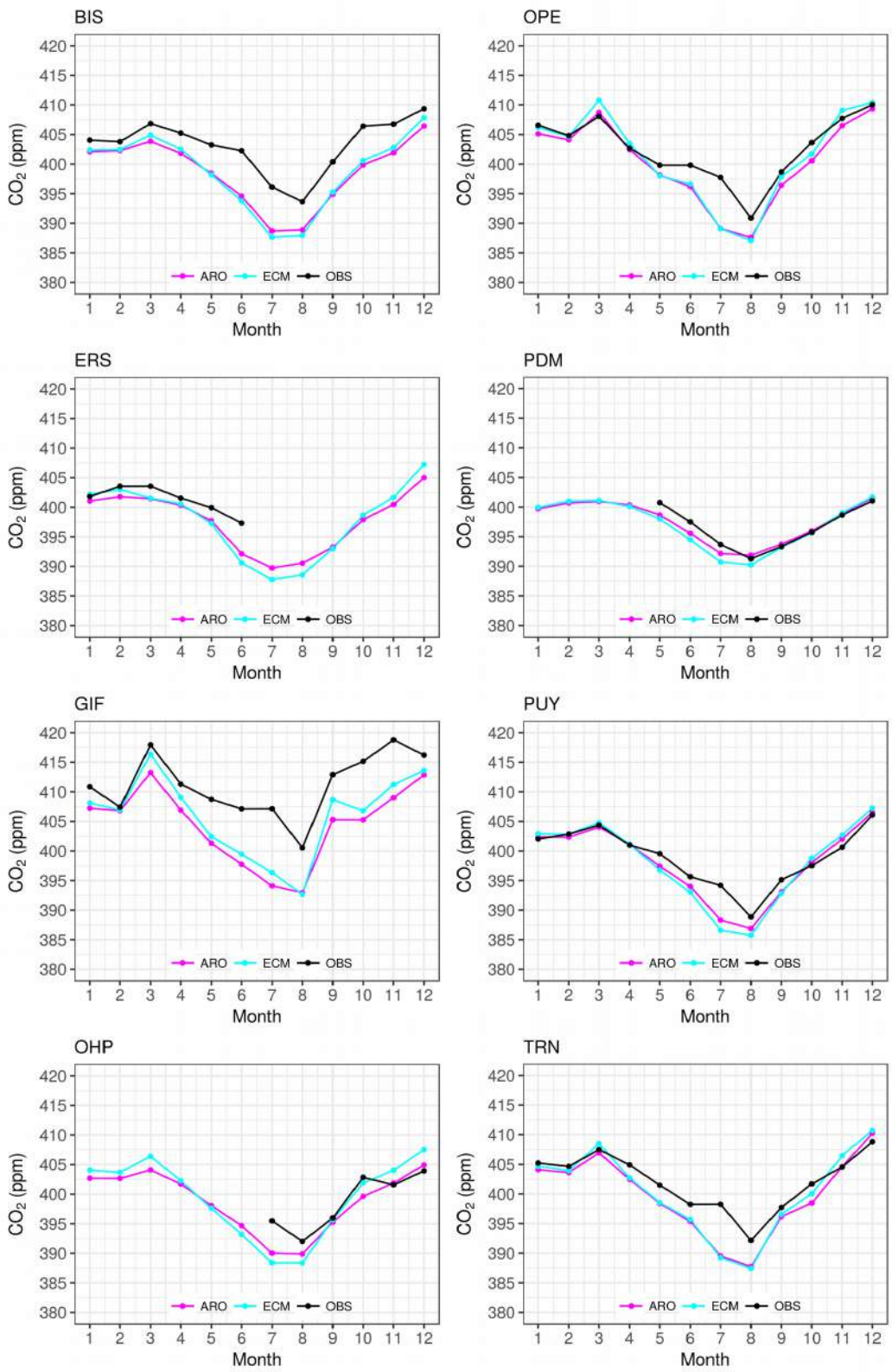

Figure III.16: CO_2 seasonal cycle at BIS, ERS, GIF, OHP, OPE, PDM, PUY, and TRN, for the observed (black) and the simulated (red and blue for AROME and ECMWF) concentrations. The monthly mean is calculated using the afternoon data (from 12:00 to 18:00) for low altitude sites and nighttime data (from 00:00 to 06:00) at the mountain sites.

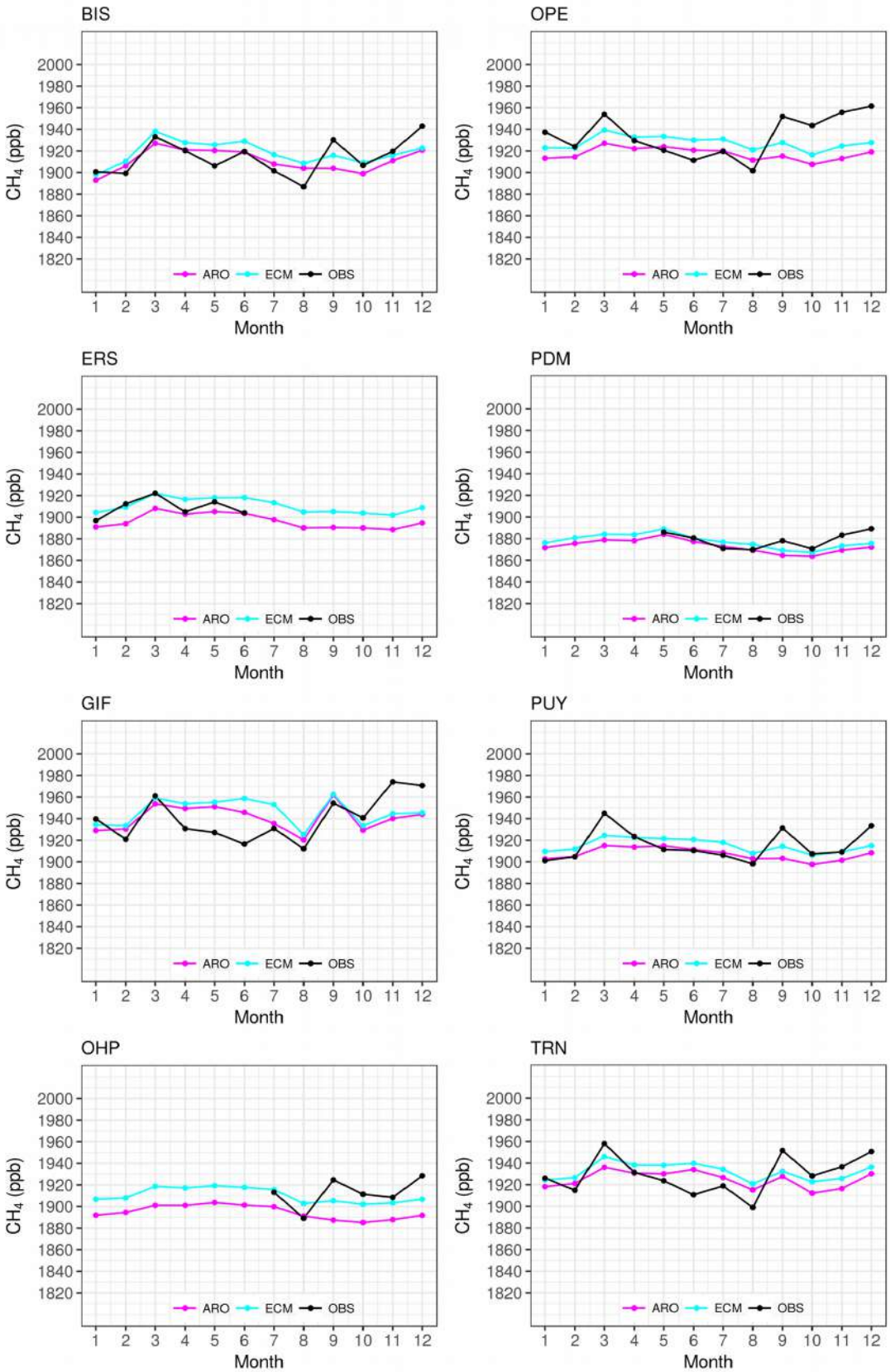

Figure III.17: CH_4 seasonal cycle at BIS, ERS, GIF, OHP, OPE, PDM, PUY, and TRN, for the observed (black) and the simulated (red and blue for AROME and ECMWF) concentrations. The monthly mean is calculated using the afternoon data (from 12:00 to 18:00) for low altitude sites and nighttime data (from 00:00 to 06:00) at the mountain sites.

III.3.6 Spatial distribution of the AROME/ECMWF differences

Beyond the comparison of the AROME and ECMWF simulations at a limited number of monitoring sites, figures III.18 and III.19 represent the differences over the domain of the study for CO_2 and CH_4 respectively. Each map represents the atmospheric concentration differences at the first level (from 0 to ~5magl) of the model for CO_2 (figure III.18), and CH_4 (figure III.19), using the afternoon selected data (data from 12:00 to 18:00) for January and July. All the monthly comparisons can be found in the appendix (figures SIII.12, SIII.13, SIII.14, and SIII.15).

In coherence with our analysis for the sensitivity of the CO_2 concentration at the monitoring sites, the absolute difference between the two atmosphere fields does not exceed 1 ppm at large part of the domain. For example, during January the major part of France is characterized by low differences that range between -0.5 and 0.5 ppm. These differences increase slightly to reach on average 0.8 ppm of difference over France as a maximum in September (Figure SIII.13). Important transport related discrepancies are identified in mountain regions (e.g., Alpes mountains), where the impact of the difference between AROME and ECMWF may reach more than 3 ppm especially during summer (e.g., June, July, and August). This issue is probably related to the large differences of topography between the two models (different horizontal resolution) which impact significantly the simulated meteorological flows (Pillai et al,. 2011). In fact, the use of AROME with a resolution more than 30 time higher than ECMWF, provide a better representation of mountainous regions, which lead to larger sensitivity to the surface fluxes for CO_2 with higher values in January and lower values in July.

For CH_4 the differences between the two meteorological models (AROME and ECMWF) do not exceed 10 ppb over France. The impact of the meteorological data on the monthly mean of CH_4 atmospheric concentrations is lower than 8 ppb during all the year (Figures SIII.14 and SIII.15), with few exceptions. Indeed, higher differences in CH_4 concentrations can be seen in the Alps and north of Italy, where the AROME minus ECMWF simulation reach more than 15 ppb of difference. Also, there are few hotspots in the spatial distribution of the differences which correspond to cities (e.g. Paris, London, Madrid) or high emission area (e.g. between Angers and Tours). As explained previously for BIS, close to a hotspot of emission any difference in the meteorological wind fields leads to high concentration differences.

Compared to flat regions, the mountain area impacts the regional circulation patterns leading to local flow circulation which influences the atmospheric concentrations by up to 3 ppm for CO_2 and 20 ppb for CH_4. In fact, the local circulation can be related to mountain valley flow caused by the surface temperature (heating

and cooling), and to the gravity waves, also called mountain waves, that occur when stable flow crosses the mountains.

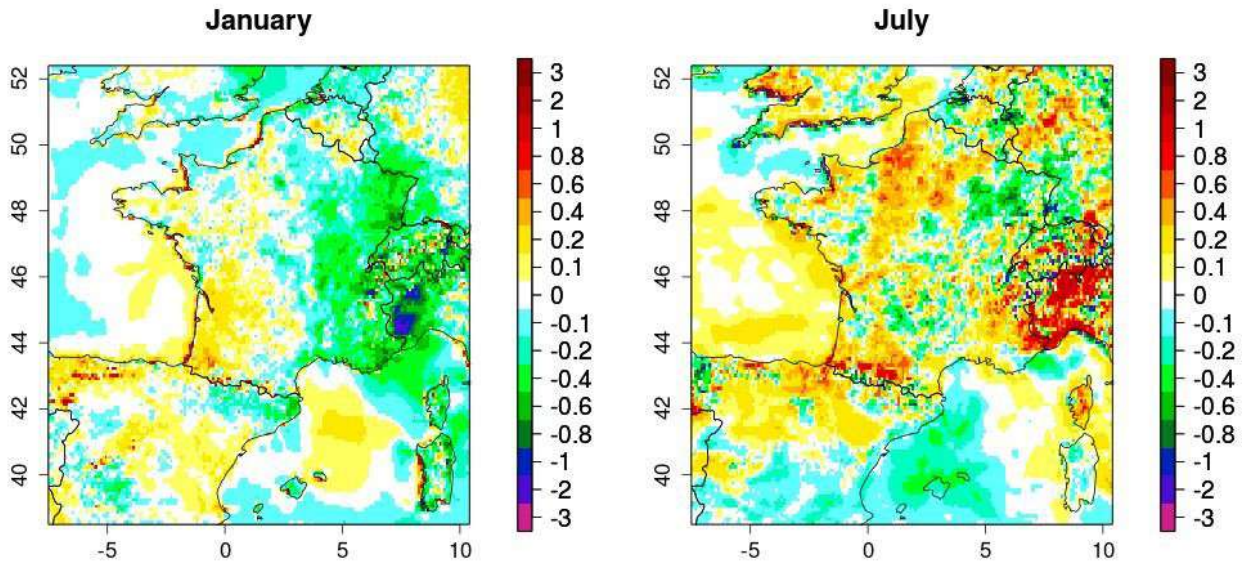

Figure III.18: Spatial distribution of the CO_2 monthly differences (ppm) between the CHIMERE simulations runing with two meteorological models (AROME minus ECMWF), using the data from 12:00 to 18:00 at the first level of the model.

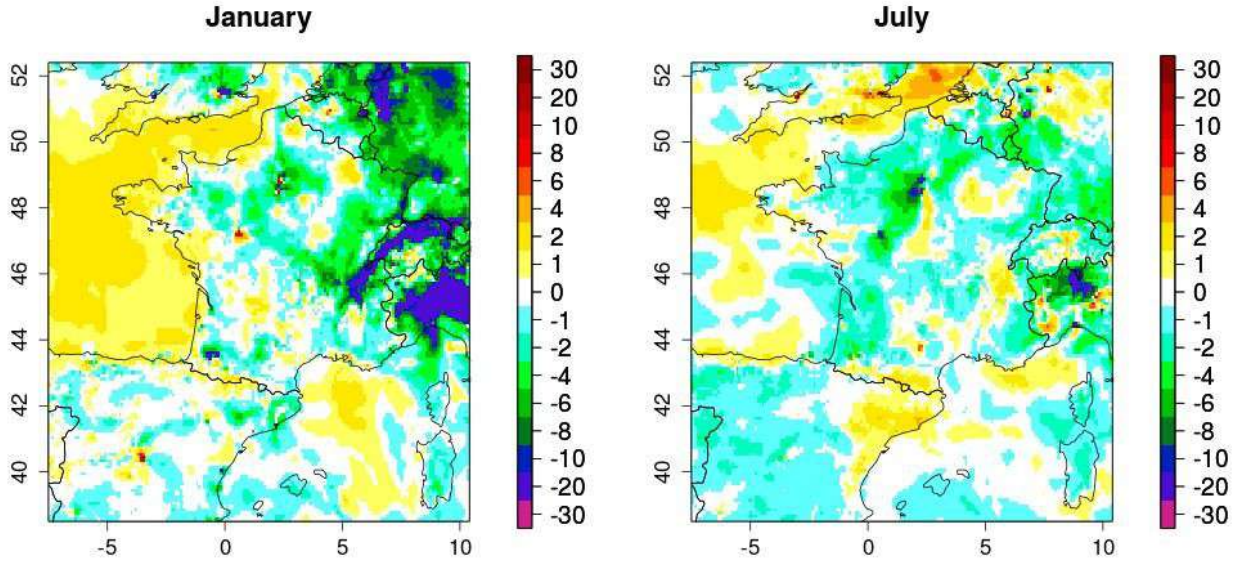

Figure III.19: Spatial distribution of the CH_4 monthly differences (ppb) between the CHIMERE simulations runing with two meteorological models (AROME minus ECMWF), using the data from 12:00 to 18:00 at the first level of the model.

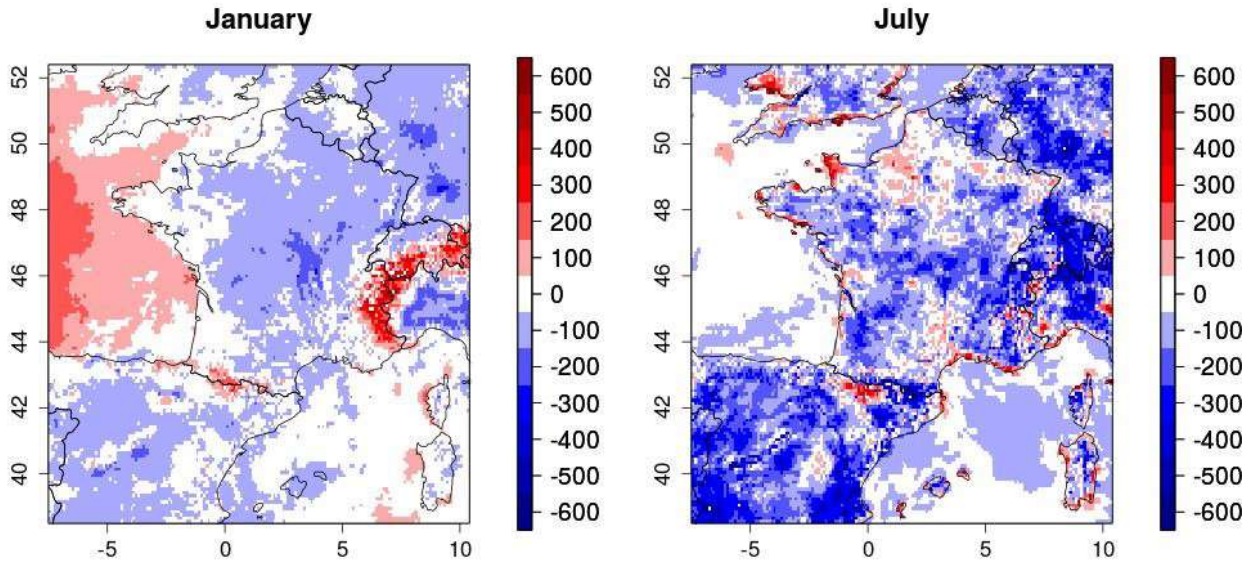

Figure III.20: Spatial differences of the simulated boundary layer height (PBL in m) between the two meteorological models (AROME minus ECMWF), using the data from 12:00 to 18:00.

III.3.7 Sensitivity of the concentrations to the surface fluxes

In this section, we present the sensitivity of the simulated CO_2 and CH_4 concentrations using to the different emission maps presented in section III.2.3. For CO_2, we ran four simulations using the two NEE models (CTESSEL and VPRM), and the two anthropogenic emission maps (IER and EDG). For CH_4, since the biogenic fluxes from the natural emissions (e.g. wetlands and termites) were neglected, we ran two simulations using only the two anthropogenic emission maps. All simulations are performed over the domain of our study, using the CHIMERE model driven by ECMWF meteorology. Similar to the section III.3.5, the discussion is supported by the French sites, the remaining European stations are presented in the appendix, and the results are presented at the diurnal and the seasonal scales.

III.3.7.1 Diurnal cycle

The comparison between the simulated and observed diurnal cycles is presented for January (figure III.21 and III.22 for CO_2 and CH_4 respectively) and July (figure III.23 and III.24 for CO_2 and CH_4 respectively). For CO_2, the comparison is performed between the set of fluxes CTESSEL+EDGAR (noted by CTS_EDG) and VPRM+EDGAR (noted by VPM_EDG).

As shown in section III.3.1, the difference between the two CO_2 total anthropogenic emissions (IER, EDGAR) does not exceed 2% at the annual scale. This difference increases after the spatio-temporal distribution of the total emissions especially near the emission hotspots. Thus, we expect that the impact on the atmospheric concentrations will be larger near big cities and highly industrialized areas. Figures SIII.16, SIII.17, SIII.18, and SIII.19 (appendix), showing that the difference of CO_2 concentrations between IER and EDGAR vary between 0.1 and 0.5 ppm at most sites, and may reach 0.8 ppm in the suburban site GIF (Figure SIII.18). This confirms that the background sites are less sensitive to the difference between the anthropogenic emission maps compared to the stations located near the emission hotspots.

The difference between CTS_EDG and VPM_EDG, varies between 2 ppm (e.g. BIS) and 6 ppm (e.g. GIF) during January, and between 1 ppm (e.g. BIS) and 10 ppm (e.g. GIF) during July. These differences are related to the different NEE models as shown in section III.3.4. By using CTESSEL rather than VPRM the CO_2 concentrations are systematically lower, and clearly underestimated compared to the observations (Figure III.21). In fact, the negative bias of the CTESSEL model for the NEE (section III.3.4) leads to a

significant underestimation of CO_2 atmospheric concentrations during winter. During July the difference between CTS_EDG and VPM_EDG decreases slightly and ranges between 1 and 5 ppm, except at GIF where the difference reaches more than 10 ppm. This difference can be explained by the discrepancy in NEE fluxes near the Paris area, since VPRM uses urban land cover information (implicitly in the EVI satellite fields) to produce small NEE fluxes over urban areas (Mahadevan et al., 2008) whereas CTESSEL has active vegetation everywhere in urban areas.

Figures III.21 and III.23 also show a phase difference of CO_2 between the two simulations. The VPM_EDG simulation reproduces quite well the timing of the observed diurnal cycle, but a lag of 2 to 3 hours can be seen in CTS_EDG simulation especially at BIS, GIF, and TRN. The CTESSEL fluxes used as an input of the transport models are available at 3 hours time resolution, whereas a 1 hour time resolution was used for VPRM. This phase difference is also highlighted in the biogenic flux evaluation section in figure III.9. In fact, every 3 hours (00:00, 03:00, 06:00, 09:00, 12:00, 15:00, 18:00, 21:00), CHIMERE interpolates the NEE missing hours using a linear temporal interpolation tool. This difference in the temporal resolution and NEE interpolation during the diurnal cycle may explain thus partly the phase difference between the two simulations.

Contrary to CO_2, the CH_4 inter-flux differences (Figures III.22 and III.24) are on average smaller, and on the same order of magnitude compared to the inter-transport ones (Figures III.12 and III.14). At GIF the difference between IER and EDGAR reaches a daily maximum during the night. In the daytime, these differences decrease to 7 ppb on average during January and 20 ppb during July. This is related to the significant differences between the two emission maps near the Paris urban area (see section III.3.2). For the low altitude sites (BIS, ERS, OPE, and TRN) the differences range between 5 and 10 ppb during the January and may reach 20 ppb for TRN during July. These sites are characterized by larger concentrations during the nighttime than during daytime. Since the temporal factors were applied only on secondary CH_4 emission sectors that represent less than 10 % from the total emissions (section III.3.1), we assume that the simulated CH_4 diurnal cycle is highly controlled by the atmospheric mixing and the spatial distribution of the emissions sources. For CH_4 lowest differences between IER and EDGAR (less than 5 ppb) occur at the mountain sites (e.g. PUY, PDM, JFJ, SCH, and PRS), whereas the maximum differences occur at GIF. This confirms that the high altitude sites are less sensitive to the change in the surface fluxes. At the remote and high-altitude stations, the time series analysis showed a weak diurnal cycle with an amplitude less than 5 ppb during both January and July (figures III.22 and III.24). Some exceptions can be seen for PUY during winter (figure

III.22), and PDM during summer (figure III.24), where high atmospheric concentrations can be lifted up by the upslope winds (Patra et al., 2008), leading to an increase of the CH_4 atmospheric concentrations during the day.

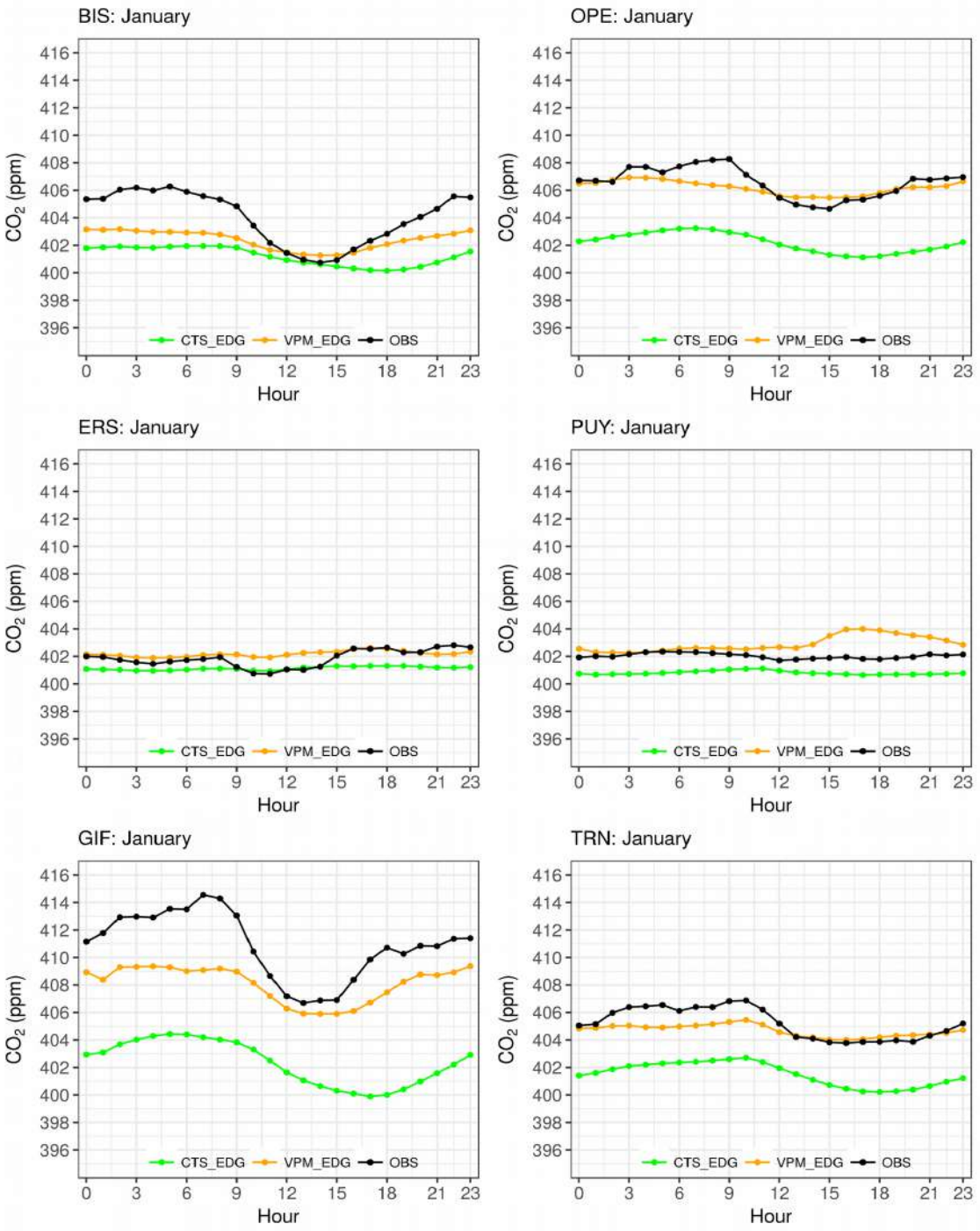

Figure III.21: CO_2 average diurnal cycle at BIS, OPE, PUY, TRN, ERS, and GIF, for the observed (black) and the simulated (green and orange for CTESSEL and VPRM respectively) concentrations during January.

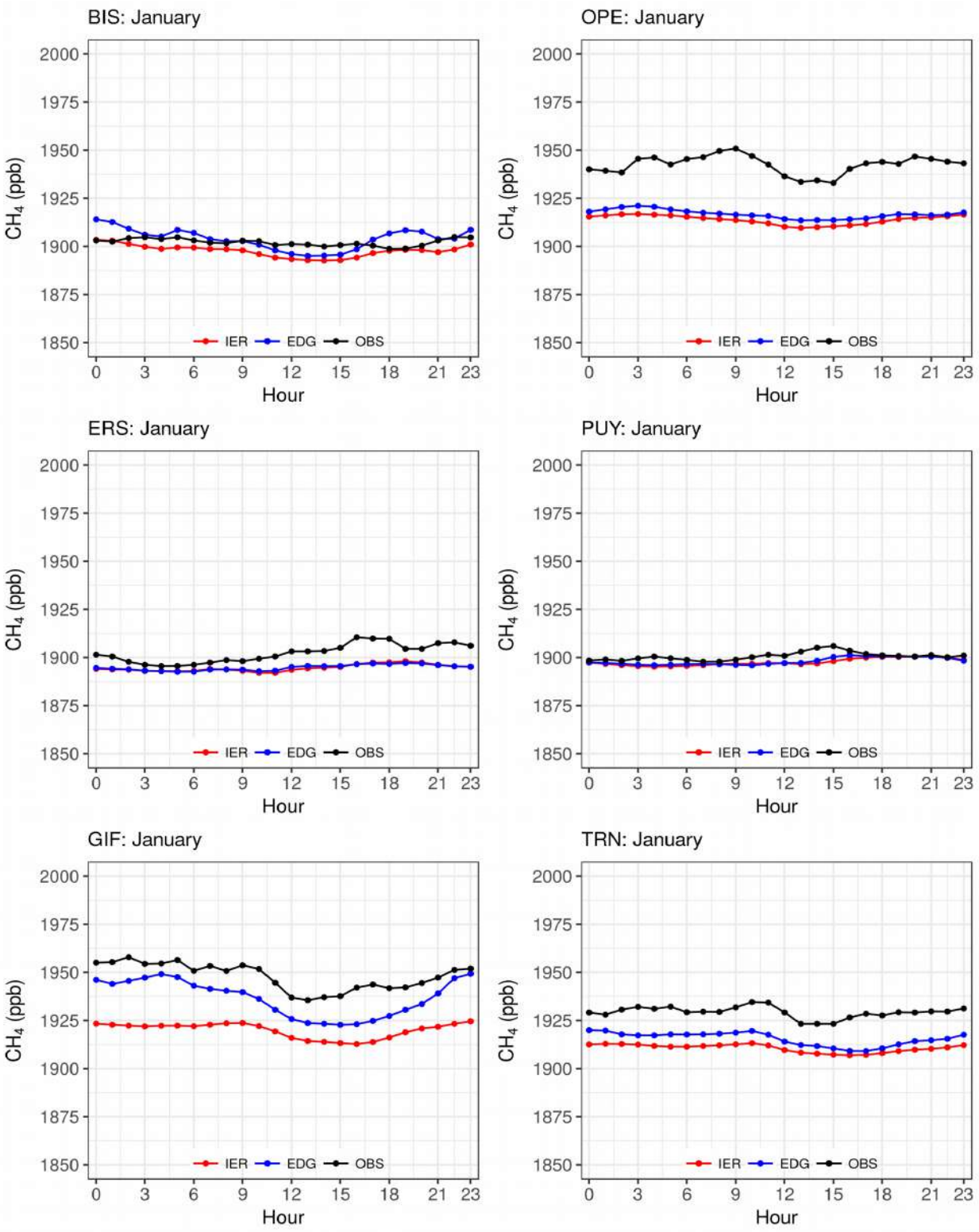

Figure III.22: CH_4 average diurnal cycle at BIS, OPE, PUY, TRN, ERS, and GIF, for the observed (black) and the simulated (red and blue for IER and EDGAR respectively) concentrations during January.

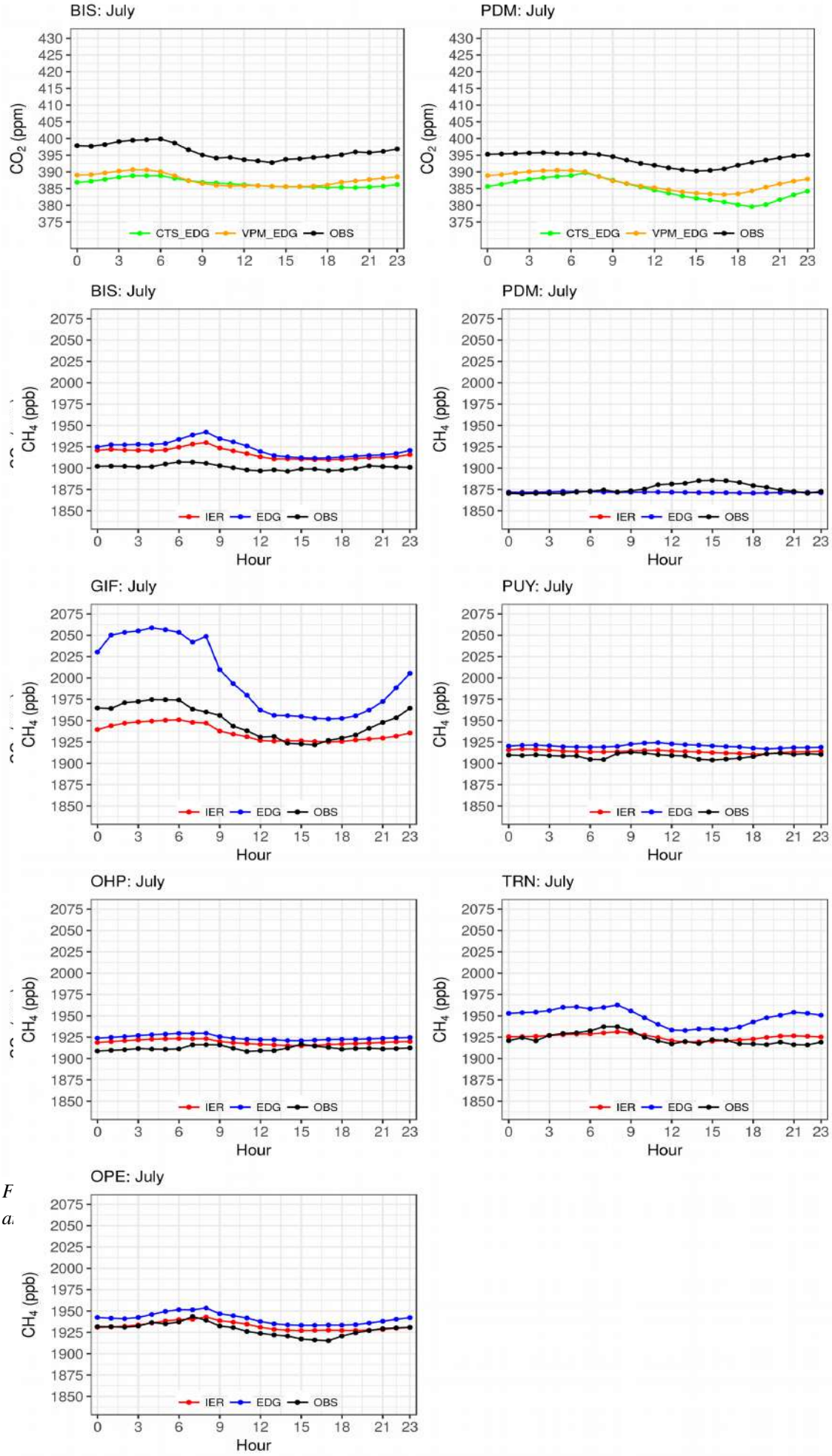

Figure III.24: CH_4 average diurnal cycle at BIS, GIF, OHP, OPE, PDM, PUY, and TRN, for the observed (black) and the simulated (red and blue for IER and EDGAR respectively) concentrations during July.

III.3.7.2 Seasonal cycle

Figures III.25 and III.26 display the monthly means of the atmospheric concentrations for CO_2 and CH_4 respectively. Since the sensitivity of the CO_2 averaged diurnal cycle to the two anthropogenic inventories does not exceed 1 ppm at most sites (figures SIII.16, SIII.17, SIII.18, and SIII.19), the seasonal cycles are compared for the total of the biogenic and the anthropogenic emissions. For CH_4, the seasonal cycle is computed for both EDGAR and IER (figure III.26). In this section devoted to the seasonal cycles, we will focus on the periods of the day where the processes should be more representative of a large scale, and therefore better represented by the models. For Both CO_2 and CH_4, we have selected daytime values (between 12:00 and 18:00) for low altitude sites and nighttime data (between 00:00 and 06:00) for the mountain stations. As demonstrated by Broquet et al., 2011, and as shown in the previous paragraphs, atmospheric models have more difficulty to represent the nighttime/daytime values at surface/mountain sites due to the discrepancies in the vertical mixing and the different representation of the topography.

The CO_2 atmospheric concentrations show a clear seasonal cycle ranging from 10 ppm to 20 ppm (Figure III.25). The largest amplitudes are noticed in the low altitude sites (e.g. TRN, OPE, GIF). In winter the simulated CO_2 concentrations are higher at continental surface sites (such as OPE, TRN, and GIF) compared to the mountain sites (e.g. PUY and PDM). This is because of the accumulation of CO_2 from emissions (biogenic and anthropogenic) near the surface, due to the relatively low vertical dispersion illustrated by lower values of PBL (figures SIII.1, SIII.2, SIII.3, andSIII.4). The mountain sites sample quite often the free tropospheric air during winter. In summer, the CO_2 concentration is lower at the low altitude sites due to the action of the photosynthesis activity (see the biogenic flux evaluation section III.3.4). The comparison between the simulated and the observed simulations show higher coefficients of correlation (R2) with observations for VPM_EDG simulation compared the CTS_EDG. They vary between 0.8 and 0.9 for VPM_EDG, but for CTS_EDG this correlation decreases to 0.7 (e.g. GIF). This is mainly related to the bias and phase difference noticed especially for the CTESSEL model (section III.3.4.2). Panareda et al (2014) demonstrated that the CTESSEL bias leads to small correlations between the simulated and the observed CO_2 concentration in Europe. The VPM_EDG simulation differs from the observations by 1 to 5 ppm during winter, and by up to 15 ppm as a maximum for GIF in summer. The CTS_EDG simulation shows higher differences with observed CO_2 all along the year, with biases ranging between 5 and 20 ppm. The monthly analysis shows significant biases starting from spring. This period is very critical since the biogenic models have to correctly reproduce the change of NEE fluxes from a predominant respiration of winter to the

predominant photosynthesis uptake in spring. The sign and the timing of this shift may vary from one model to the other. It is interesting to note that the VPRM runs correctly the spike observed at most sites in March, and the minimum concentration in August, while the CTESSEL simulation peaks in July and shows flat signal in March. For CTESSEL the transition from spring to summer is weaker compared to VPRM, due to the underestimation of the respiration and the persistence of photosynthesis in the NEE during winter over a large part of France (see section III.3.4.1). Panareda et (2014) showed that CTESSEL simulations underestimate the CO_2 concentration by a value ranging between -5 and -10 ppm, with a significant impact during the summer time. The corrected version of CTESSEL developed by Panareda et al (2016), but not available for this study, reduces this bias by a factor of 2 in Europe.

For CH_4 the seasonal cycles are less marked than for CO_2, and the simulations with different emission maps (EDGAR and IER) both underestimate the seasonal and the month to month variabilities, like the spike concentrations observed at several stations in March and September. Higher variations are noticed for GIF station for both observed and simulated CH_4 concentrations, due to the influence of the Paris region. The amplitude of the seasonal cycle varies between 10 and 50 ppb at low altitude sites, and less than 10 ppb at the mountain sites. The coefficient of correlation (R2) calculated between the observed and the simulated seasonal cycle for both EDG and IER, range between 0.8 and 0.9, except for GIF where the correlation decreases to 0.7. For the mountain sites and some remote station (e.g. ERS and OHP), the differences between IER and EDG do not exceed 5 ppb. For the stations that are located near an emission source, the difference range between 5 and 10 ppb (e.g. OPE and TRN), and can be more than 20 ppb for GIF. These differences can be explained by the errors related to the emission factors, and the different spatial distribution of the emissions sources near the highly industrialized area. Overall IER simulation leads to lower concentrations which are generally closer to the observations in summer, but further away in winter.

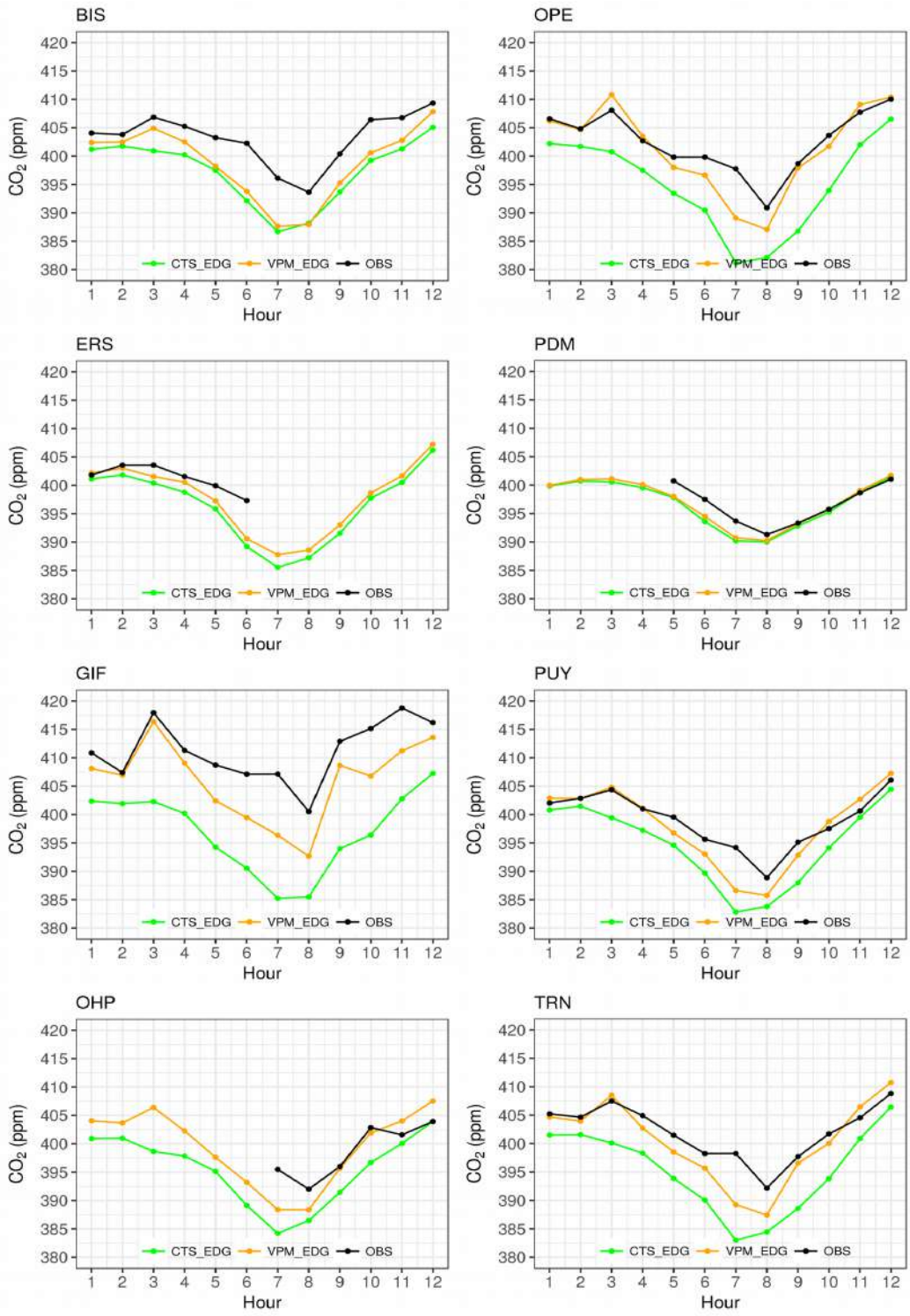

Figure III.25: CO_2 average seasonal cycle at BIS, ERS, GIF, OHP, OPE, PDM, PUY, and TRN, for the observed (black)and the simulated (green and orange for CTESSEL and VPRM respectivly) concentrations. The monthly mean is calculated using the afternoon data (from 12:00 to 18:00) for low altitude sites and nighttime data (from 00:00 to 06:00) at the mountain sites.

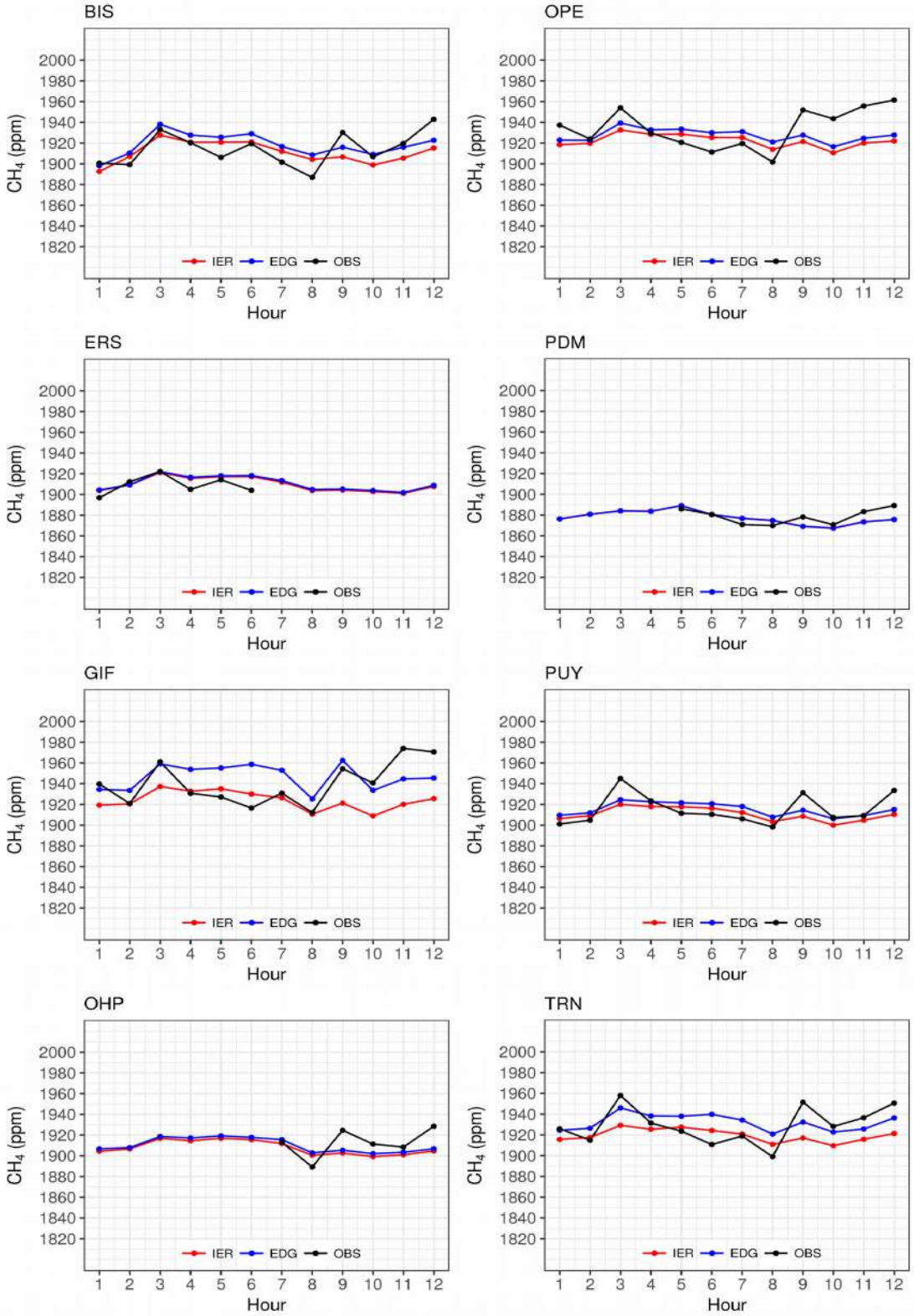

Figure III.26: CH_4 average seasonal cycle at BIS, ERS, GIF, OHP, OPE, PDM, PUY, and TRN, for the observed (black) and the simulated (red and blue for IER and EDGAR respectivly) concentrations. The monthly mean is calculated using the afternoon data (from 12:00 to 18:00) for low altitude sites and nighttime data (from 00:00 to 06:00) at the mountain sites.

III.3.8 Spatial distribution of the surface flux differences

The sensitivity of the surface level CO_2 concentrations to the differences between the biogenic models (CTESSEL minus VPRM) is presented as a map in panel ΔBio (figure III.27), whereas the panel ΔAnthro represents the sensitivity to the two anthropogenic inventories (IER minus EDGAR) for CO_2 (figure III.27) and CH_4 (figure III.28). The difference maps are generated using the afternoon data (data between 12:00 and 18:00) at the first level of the model (~ 5 m) for January and July (the remaining months are presented in the appendix Figures SIII.26, SIII.27, SIII.28, SIII.29, and SIII.30).

For CO_2 the spatial distribution of the Δbio and Δanthro are characterized by higher differences over France between the biogenic models compared to the anthropogenic inventories. During January, the CTESSEL model underestimates the CO_2 concentrations compared to VPRM. The few sites discussed in the previous paragraph are quite representative, since the differences are relatively homogeneous over France with values ranging from -2 to -6 ppm for the difference CTESSEL minus VPRM. As explained earlier, CTESSEL simulates a significant photosynthesis activity in January over a large part of France with some exceptions in Landes forest, Massif Central, and Pyrénées regions. These three regions are the ones characterized by the lowest contrast between CTESSEL and VPRM in wintertime, with a difference of less than 2 ppm (figure III.27-ΔBio). In July, positive differences (~2 ppm) between the two biogenic flux models occur in the south and west side of France, meaning that the CO_2 concentrations using CTESSEL are higher than VPRM. These positive differences can be explained by the larger photosynthesis activity modeled by VPRM leading to a more pronounced CO_2 uptake compared to CTESSEL (figure III.8, section III.3.4.1). For example, flux differences ranging between 100 and 200 gCO_2/m^2/month in the Landes forest (figure III.8-July), impact the CO_2 concentrations by a value within a range from 1 to 3 ppm (figure III.27-July panel ΔBio). North, central and east parts of France are characterized by negative values, meaning higher CO_2 concentrations using VPRM, as it was shown at most monitoring sites (Figure III.25). The highest differences between VPRM and CTESSEL occurs during spring and autumn leading to differences in CO_2 concentration of more than 7 ppm in March and November. Some small-scale patterns can be seen near big cities, such as Paris and London (figure III.27- ΔBio and figure SIII.27-ΔBio for May), showing very high differences that may reach 8 ppm. This sensitivity is related to the difference for computing the biogenic fluxes in the urban area.

The sensitivity of surface level CO_2 and CH_4 concentrations to the anthropogenic inventories are presented respectively in figure III.27-ΔAnthro and figure III.28-ΔAnthro. Over large parts of France, the impact of the difference between the two anthropogenic fluxes (IER minus EDGAR) does not exceed 1 ppm for CO_2 (figure III.27-ΔAnthro), and 5 ppb for CH_4 (figure III.28-ΔAnthro). This impact increases significantly near big cities, such as Paris, where the differences may reach 10 ppm for CO_2 and 60 ppb for CH_4. This increase can be explained by important uncertainties related to the anthropogenic emission fluxes in over the highly industrialized areas. Similar differences can be seen over cities in large parts of Germany, Belgium, and the Netherlands, especially for CO_2. The seasonal variation of sensitivity of the anthropogenic maps (Figures SIII.26, SIII.27, SIII.28, SIII.29, and SIII.30) shows larger differences during winter compared to summer (especially for CO_2). Near the important emission sources, the CO_2 differences may exceed 10 ppm, but during summer these differences decrease and vary between 2 and 8 ppm (Figures SIII.27, and SIII.28).

The spatial distribution of the IER minus EDGAR simulation shows two dipoles for the CH_4 concentrations in France (figure III.28-ΔAnthro). The first dipole is located in the region of Paris, and the second one is located south-west of Paris, between Angers and Tours (easily noticed during November Figure SIII.30). These two concentration dipoles are related to the different localization of an emission source in the anthropogenic emission maps (Figure III.5). Near these two regions, the atmospheric concentration is very sensitive to the wind direction. During August (figure SIII.30), a wide positive plume (IER minus EDGAR) is emitted from these two dipoles and impact the CH_4 concentrations in West France, by a value ranging between 5 and 15 ppb (20 ppb near the dipole). However, during September a negative plume impacts the CH_4 atmospheric concentrations by the same amplitude (value ranging between 5 and 20 ppb). This variation in the sign of the anthropogenic differences might be related to a slight change in wind direction, since the two emission sources of the dipole are located one grid cell apart from each other. Similar patterns can be seen during November and December (figure SIII.30). In fact, the two inventories use different proxies (for EDGAR proxy listed in table III.2, for IER SNAP sectors section III.2.3.1) to distribute the total emissions from the national scale to the level of the grid (0.1° for our study). However, using different proxy data may lead to the misallocation of the emission sources (Hogue et al., 2016). Moreover, Hutchins et al (2016) showed that the use of different proxies results in different allocations of the emission, which increase as the size of the grid-cell decrease. Hogue et al (2016) estimated a distance of 120 km to be the maximum difference in location between the real localization (extracted from Google Earth satellite imagery) of the emissions sources and the reported location in the inventories.

The distribution of the spatial differences in concentrations due to different fluxes confirms the larger sensitivity of the CO_2 concentrations to the biogenic fluxes compared to the anthropogenic fluxes. The sensitivity of the atmospheric concentration to the anthropogenic emission is significant only near the highly emitting sources for both CO_2 and CH_4. Gurney et al (2009) showed that for the same national total, the spatial localization of the anthropogenic fluxes may impact the CO_2 atmospheric concentrations by a value ranging between 3 and 4 ppm. Other studies evaluating the modeled atmospheric CO_2 were in general agreement with our finding, showing a difference up to 5 ppm due to the difference in the localization of the emission sources, most often near urban areas (Corbin et al.,2010, Schuh et al., 2010).

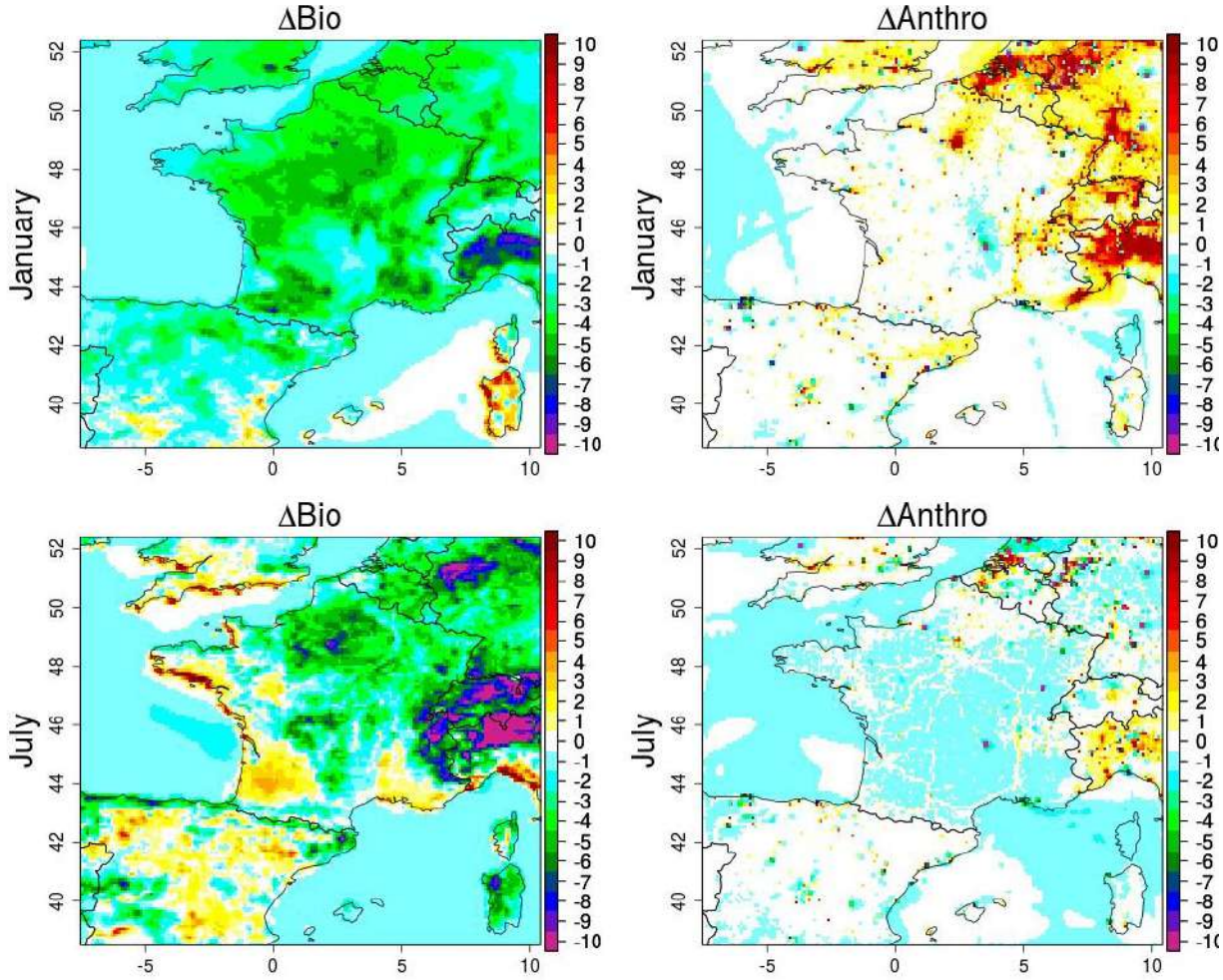

Figure III.27: Spatial distribution of the surface level CO_2 monthly differences (ppm) between the two biogenic models (CTESSEL minus VPRM) panel ΔBio, and between the two anthropogenic inventories (IER minus EDGAR) panel ΔAnthro, using the data from 12:00 to 18:00 at the first level of the model.

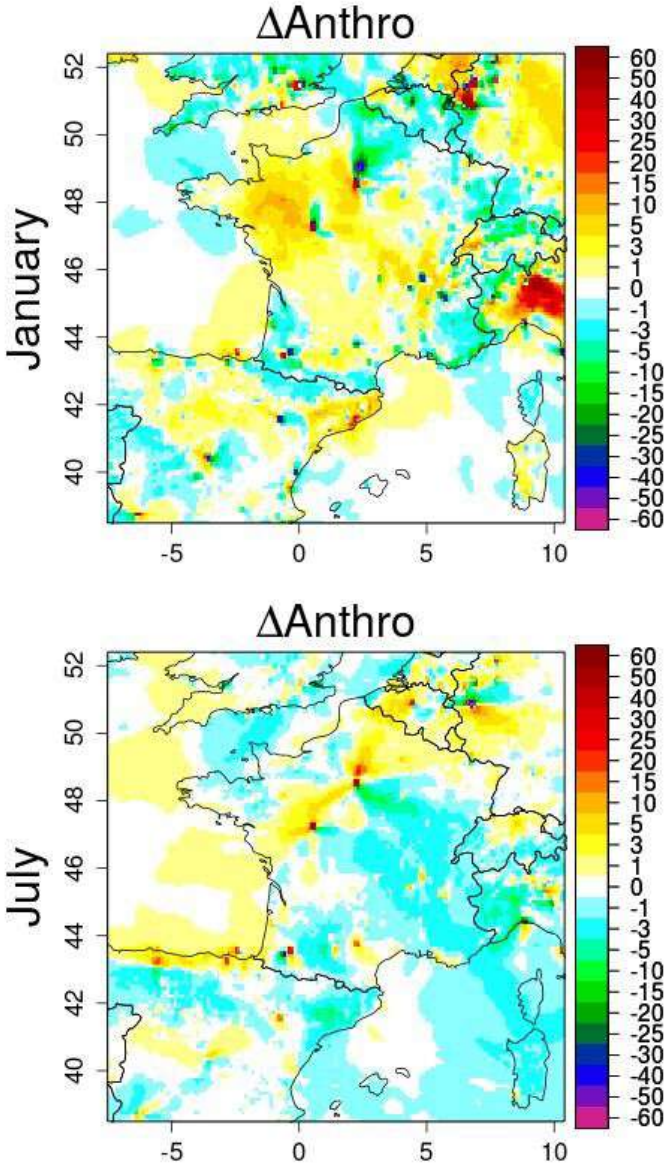

Figure III.28: Spatial distribution of the surface level CH_4 monthly differences (ppb) between the two anthropogenic inventories (IER minus EDGAR) panel ΔAnthro, using the data from 12:00 to 18:00 at the first level of the model.

III.4 Conclusions

This study focuses on evaluating the sensitivity of the simulated CO_2 and CH_4 concentrations, using two meteorological fields, two vegetation-atmosphere CO_2 models, and two anthropogenic emission maps. We performed 8 regional simulations using the chemistry transport model CHIMERE centered over France with a horizontal resolution of 0.1x0.1°. We apply temporal profiles on the yearly emission maps in order to estimate hourly varying anthropogenic emissions used as an input for the transport simulations. The analysis focuses on the evaluation of the capability of the model to simulate the CO_2 and the CH_4 variabilities at seasonal, synoptic, and diurnal scales, the quantification of the impact of the different input data on the simulated concentrations. The main objective of this study is to improve our understanding of the aspect (flux variabilities and transport processes) influencing the simulation of the CO_2 and CH_4 atmospheric concentrations, which we summarize in the following.

First, the comparison of the anthropogenic emission between the two inventories showed an offset that does not exceed 10% of the annual totals. This offset remains below the anthropogenic emission uncertainties estimated for CO_2 by Peylin et al., (2011) and for CH_4 by Peng et al., (2016). The differences between the annual national totals were assumed to be related to the definition of the sectors boundaries, such as the biofuels and the bunker fuels, which may increase the national budget by up to 10%. The spatial distribution of the difference between the emission maps remains in general below 20kgCO_2/yr for CO_2 and 60 gCH_4/yr for CH_4. The significant contrast between the emission maps occurs near big cities and emission hotspots, such as the Paris area. The difference between the inventories increased significantly after the application of the temporal profiles and reached more than 30% in winter. Despite the good agreement of the anthropogenic national totals (uncertainties less than 10%), the distribution of the emission budget in space and time leads to significant uncertainties.

Second, the evaluation of the two biogenic fluxes shows the agreement of the two models for simulating a CO_2 uptake between late spring and early summer. The two models do not diverge much at this season even if the VPRM model estimates the maximum uptake one month after CTESSEL. The difference is more important in winter, where VPRM estimates positive CO_2 fluxes compared to CTESSEL who remains negative all year round. The comparison between the two models at a regional scale showed that negative bias of CTESSEL was related to the overestimation of the CO_2 uptake in the north part of France. The evaluation of the modeled CO_2 fluxes against the eddy covariance estimates showed an underestimation of the

simulated fluxes by a factor that may reach 3, especially during July. The differences between the simulated and the observed sites at the cultivated sites are related to the site's management (e.g. sowing, irrigation, and harvesting) which are not explicitly resolved by the used models. For the forest sites, the difficulties in simulating the CO_2 fluxes was associated to the misrepresentation of the phenology which is calculated in the models using satellite greenness observations (not at the point scale of the measurement sites).

Third, the sensitivity of the simulated concentrations regarding the meteorological fields showed significant differences at the mountain sites and near the high emission sources. For the mountain regions, the difference between the ECMWF and AROME are related to the difficulty in representing the meteorological parameters that control the transport of the CO_2 and CH_4 concentrations (e.g. the horizontal and the vertical mixing). Near the high emission sources, we showed that a small change in the wind fields may lead to a significant difference in the simulated concentration. The comparison between the simulated and the observed concentrations confirmed that the transport models are less biased during mid-afternoon time window for the low altitude sites, whereas for the mountain sites the use of the nighttime data seems the most appropriate.

Lastly, the use of these different surface fluxes allowed us to quantify the sensitivity of the simulated concentration regarding the anthropogenic and the biogenic fluxes.

For CO_2, the evaluation of the modeled data showed an important underestimation of the simulated concentration compared to the observations. This underestimation increases significantly for the CTESSEL simulations, especially during winter. Compared to VPRM, the negative CO_2 fluxes estimated by CTESSEL during January impacts the atmospheric concentrations by more than 5 ppm (e.g. GIF station). For the anthropogenic emission, the differences between IER and EDGAR simulation impact the modeled concentration by less than 1 ppm on average at the level of the atmospheric sites. The sensitivity of the simulated CO_2 concentration regarding the anthropogenic emissions becomes more significant near high emission sources, where the difference may reach 10 ppm.

For CH_4, We showed that the significant differences between IER and EDGAR simulations occur for the low altitude sites with a value ranging between 5 and 20 ppb. Similar to CO_2, the differences between the two anthropogenic emissions impact significantly the simulated CH_4 concentrations near important emission areas, with a high impact in winter. The spatial distribution of the difference between IER and EDGAR simulations showed the impact of the emission hotspots leading to important small-scale patterns called by emission dipoles. These dipoles are responsible for the plumes that may impact the atmospheric

concentration up to 40 ppb. Atmospheric inversion is expected to decrease the impact of these plumes and to reduce the differences between the simulated and observed concentration. This will be further investigated in the next chapter.

Chapter IV: The potential of a European network for the optimization the CO_2 and the CH_4 surface fluxes in France

IV.1 Introduction

The quantification of the carbon dioxide (CO_2) and methane (CH_4) surface fluxes represent a critical task to better understand the present-day carbon and methane budget. To achieve this purpose, two techniques known by bottom-up and top-down approach are commonly used. The bottom-up approach provides estimates of the greenhouse gases based on geo-referenced fields of socio-economic data and emission factors, or process-based biogeochemical models. However, due to the inaccurate emission factors and activity statistics, the bottom-up approach can lead to significant uncertainties. In this study, we will improve the estimation of the GHG fluxes using the top-down approach, called hereafter by inverse modeling, which reduces the uncertainties of the temporal and the spatial variability of the CO_2 and CH_4 fluxes. This approach estimate optimized fluxes using information from prior surface fluxes (generally from bottom-up approaches), transport model, and observations. This set of information represents the principal ingredients to perform the Bayesian inversion aiming to quantify the CO_2 and CH_4 sources and sinks in France (Tarantola, 2005).

The Bayesian inversion framework can assimilate data provided by in-situ surface stations (Bergamaschi et al., 2018, Kountouris et al., 2018, Pison et al., 2018), and/or remote sensing data provided by satellite-based spectrometer (Broquet et al., 2018, Bergamaschi et al., 2009). Here, we use surface measurement provided by the European network of Integrated Carbon Observation System (ICOS), completed with several stations from different national networks. Based on these observations, the inversion system can optimize the surface fluxes using the transport model which links the prior fluxes to the observations.

The performance of the inversion framework depends on the ability of the atmospheric transport models to accurately reproduce the influence of the sources and sink at the level of the sampling sites. Whether we use coarse or high-resolution transport models, the quality of simulating the atmospheric concentrations can be declined due to the influence of different uncertainties. First, the transport errors (Geels et al., 2007, Ahmadov et al., 2007, Prather et al., 2008) which represent the difficulty of the model to reproduce the

transport processes (e.g. horizontal and vertical mixing). Second, the representation errors (Tolk et al., 2008) which are related to the problem in the localization of the sampling sites in the model. Third, the aggregation errors (Bocquet et al., 2011, Kaminski et al 2001) that represents the misfits of the model-obs concentrations due to the imperfections in representing the flux patterns. These errors are very critical and can degrade substantially the performance of the inversion framework.

The implementation of the Bayesian inversion framework requires the definition of the statistics of measurement errors, transport errors, representation errors, in addition to the uncertainties of the prior fluxes prescribed in the system. Most of the earlier inversion studies estimate empirically these errors. In this study, the error statistics will be assigned objectively using statistical methods (e.g. Wahba et al., 1994 Desroziers et Ivanov, 2001) which were used to estimate the different errors in a geostatistical implementation of the atmospheric GHG inversion problems (Pison et al., 2018, Berchet et al. 2015, Berchet et al., 2013, Michalak et al., 2005). Thus, the used inversion framework relies on an automatic diagnosis of the error statistics. The method still uses some expert knowledge information for the determination of the patterns of the flux aggregation and the sampling procedure in agreement with the performance of the transport model and the available computation resources.

This chapter aims at implementing and applying a dedicated atmospheric inversion modeling framework to estimate the CO_2 and the CH_4 surface fluxes in a domain centered over France. This study uses the atmospheric transport model CHIMERE (described in Chapter III), embedded in the inversion framework PYMAI developed by Berchet et al (2013, and 2015). This system uses a statistical algorithm to estimate objectively the most critical sources of errors in the inversion. The error quantification is performed used a Monte-Carlo approach incorporated into Maximum of Likelihood estimators (Berchet et al., 2015). We will compare the inversions errors estimated objective by the maximum of the likelihood algorithm to the empirical error estimation in order to study the relevance and the robustness of the inversion system. The system uses atmospheric observations provided by ICOS and other national networks in order to constrain the CO_2 and CH_4 surface fluxes. Section IV.2 provides a detailed description of the inversion system, the statistical method used to quantify the inversion errors, prior information, and the surface measurements of 16 stations. Section IV.3 represents the inversion results presented separately for CO_2 and CH_4 fluxes. In the following section, we list the results for the CH_4 inversion. The same structure will be followed for the CO_2 inversion with a separation between the anthropogenic and the biogenic fluxes. In section IV.3.1.1 we present the used atmospheric CH_4 measurements and the impact of the observation in the inversion system. Section

IV.3.1.2 compares the errors estimated by the automatic algorithm to an analytical estimation of the errors based on Chapter III results. In section IV.3.1.3 we study the fit to the observed atmospheric concentrations. Section IV.3.1.4 focuses on a description of the region constrained by the inversion and the sensitivity of the atmospheric sites to the surface fluxes. In section IV.3.1.5 we study the separability of the inferred fluxes based on the posterior uncertainties. Section IV.3.1.6 concerns the spatiotemporal scales resolved by the inversion. Section IV.3.1.7 represents a comparison between the optimized fluxes and the bottom-up flux estimates used as prior information by the inversion system.

IV.2 Methods

IV.2.1 Inverse problem formalism

IV.2.1.1 Inversion formalism

The estimation of greenhouse gas sources and sinks using the inverse modeling formalism is based on the assumption that the control vector X, can be related to measurements of the atmospheric concentrations Y_0, using a transport model H (Bouttier and Courtier, 2002).

$$Y_0 = H(X) + \varepsilon_Y \quad \text{(IV.1)}$$

The control vector may include the contribution of all data used as an input by the transport model such as the surface fluxes (called hereafter by prior fluxes), initial conditions, and boundary conditions. ε_Y represents the differences between the concentrations simulated by the transport model H and the measurements. The aim of inverse modeling is to estimate an optimized control vector that minimizes ε_Y. Even if we consider that the control vector used as an input is perfect, the difference between the observations and the simulations is not zero, due to the imperfections of the transport model and the measurement errors (called altogether observation errors). The refinement of the control vector is usually achieved through the optimization of the surface fluxes and the reduction of their uncertainties (called hereafter by prior errors) for a targeted spatial and temporal scale. The optimization is generally performed using inverse modeling frameworks, which consist of finding the best estimate of the surface fluxes using information from the observations, the transport model, and the prior fluxes.

The exact value of the observation and the prior errors is unknown since we ignore the real values of the concentrations and the control vector. These errors can be estimated based on some statistical calculations which indicate their probable amplitude and spatiotemporal distributions. In fact, the complexity of the inverse problem relays on the estimation of the different errors, since they influence strongly the inversion results. In this study, we will focus on the optimization of the surface flux components of the control vector.

IV.2.1.2 Inverse problem constraints

In the case of greenhouse gas flux estimations, we may face ill-posed mathematical inverse problems, when the number of constraints (observations) is very small compared to the number of the unknowns (fluxes to be optimized). At the global scale, the available measurements have always been considered as relatively few compared to the surface fluxes. In Europe, this issue is still relevant, but it has been reduced by the development of regional greenhouse gas atmospheric networks, such as ICOS (Integrated Carbon Observation System https://www.icos-ri.eu/), and also by the emergence of new national networks, such as ClimaDat Spanish project (available at http://www.climadat.es/). In this study, we use hourly observations at 16 stations from national and European networks, in order to constrain the inverse problem. Theoretically, the more observations we have, the closer we get towards estimating the real fluxes. However, in practice, the flux estimation depends also on the quality of the control vector and the ability of the transport model to reproduce correctly the simulated concentrations.

IV.2.1.3 Regularization of the inverse problem

Theoretically, having a small number of constraints implies an important number of possible flux distributions that minimize the difference between the modeled and the observed concentrations. It is thus essential to regularize the inverse problem using information that is independent from the measurements, in order to reduce the range of the possible flux distributions and to provide realistic solutions. In this study, we chose the Bayesian regularization that uses prior information of the fluxes (noted in this study by x_b) and their corresponding errors (Tarantola, 2005). This regularization is convenient for our study since we can use prior flux estimate based on biogeochemical models (e.g. VPRM and CTESSEL see section III.2.3.2), and gridded emissions inventories (e.g. IER and EDGAR see section III.2.3.1).

The optimized fluxes will depend on the quality of the prior fluxes, the observed data, the transport model, as well as the characterization of the corresponding errors (flux errors, and observation errors). In this study, we

assume that both the flux and the observation errors follow unbiased Gaussian distributions. These errors are crucial for our study since they indicate the range in which the inverse problem solution may exist. In this study, the observation and the prior flux errors will be estimated by the statistical inversion system itself using an extension of the traditional scheme developed by Berchet et al (2013) (see section IV.2.3).

IV.2.2 The solution of the inverse problem:

Resolving the inverse problem means finding the density probability function $\rho(x)$ of the "true" fluxes (equation IV.2) given the prior statistical information on the fluxes x_b and the set of in situ measurements of atmospheric concentrations Y_0. The optimized fluxes estimated by the inversion method (called the posterior fluxes) represent the value of fluxes that maximize the density probability $\rho(x)$. The errors on the posterior fluxes follow an unbiased Gaussian distribution since the observation and the prior fluxes errors are assumed to be unbiased and Gaussian. Following Tarantola, (2005):

$$\rho(x) = Cst \times \exp\left(\frac{-1}{2}\left[(Y_0 - H(x))^T R^{-1}(Y_0 - H(x)) + (x_b - x)^T B^{-1}(x_b - x)\right]\right) \quad \text{(IV.2)}$$

R and B represent the variance-covariance matrices of the observation and the prior flux errors respectively. Cst is a constant, and it does not interfere in the calculation of the maximum and covariance of $\rho(x)$ (equation IV.2). The transport model that connects the control vector to the observation space, here the unknown fluxes to the measured atmospheric concentrations, is usually represented by a chemistry-transport model (CTM) that mix and transport the control vector components. In this study, the chemistry module, along with the transport in our domain (~2000 Km from west to east), is deactivated for the CO_2 (inert gas), and for CH_4 whose the mean lifetime in the atmosphere is about 12 years (Prather et al., 2007).

According to equation IV.2, the optimal solution, called x_a hereafter, can be found by minimizing the following cost function.

$$J(x) = -\ln\left(\frac{\rho(x)}{Cst}\right) \quad ; \quad J(x) = \frac{1}{2}\left[(Y_0 - H(x))^T R^{-1}(Y_0 - H(x)) + (x_b - x)^T B^{-1}(x_b - x)\right] \quad \text{(IV.3)}$$

In this study, we make an additional assumption that the atmospheric transport is linear. This hypothesis is valid for all tracers which are passive at our temporal scales (such as CO_2 and CH_4). Therefore, the observation operator can be expressed by the matrix H ($H(x) = Hx$), which distribute the spatial and the

temporal flux patterns in respect with the control vector components (see Section IV.2.4.4). The optimal fluxes x_a corresponds to the value of x where the gradient of $J(x)$ equals zero (Tarantola, 2005):

$$x_a = x_b + K(Y_0 - Hx_b) \quad \text{(IV.4)}$$

Where K is called the Kalman gain matrice

$$K = BH^T(R + HBH^T)^{-1} \quad \text{(IV.5)}$$

The variance-covariance matrix of the optimal fluxes x_a using the Gaussian assumption can be expressed by the following equation (Tarantola, 2005):

$$P^a = B - KHB \quad \text{(IV.6)}$$

We can limit the dimension of the observation and control vectors, so that, with respect to the available calculation resources, the inversion, i.e., equations IV.4 and IV.6, can be performed analytically.

IV.2.3 The inversion setup:

IV.2.3.1 Estimation of the observations and prior variance-covariance matrices

An accurate estimation of the of the error variance-covariance matrices (R, and B), for the observations and the prior fluxes respectively, represent an important task for the estimation of the posterior fluxes (equation IV.4) and their related uncertainties (equation IV.6). Previous flux estimation studies were carried out using an estimation of the observation and prior errors based on expertise and knowledge of the model performances (e.g. Kountouris et al., 2018). Differently, other methods estimate the R and B matrices objectively along with the posterior statistics of the fluxes, within the statistical inverse modeling procedure, based on the model-data misfits (e.g. Pison et al., 2018, Berchet et al., 2015, Michalak et al., 2005). In these statistical methods, both R and B have been considered as diagonal matrices. The diagonal terms of R ($\sigma^2_{R,i}$) stand for the variance of the observation errors, and the diagonal elements of B ($\sigma^2_{B,i}$) represent the error variance of the prior fluxes (equations IV.7).

In this study, we will use the maximum of likelihood method, implemented by Berchet et al (2013), to estimate the parameters required for the diagonal variance-covariance matrices (R and B). Applying the

method for non-diagonal variance-covariance matrices implies drastically higher computational costs and intensive memory usage. In order to provide the variance-covariance matrices with small computational costs, we need to reduce the size of parameters to estimate. In fact, the likelihood maximization of the diagonal matrices presents then the best compromise between the estimation of realistic observation and prior errors (Berchet et al., 2013), as well as lighter memory usage. The variance-covariance matrices can be presented as follows:

$$R=\begin{matrix}\sigma^2_{R,1} & 0 & \dots & 0\\ 0 & \sigma^2_{R,2} & \dots & 0\\ \dots & \dots & \dots & \dots\\ 0 & \dots & 0 & \sigma^2_{R,i}\end{matrix} \quad ; \quad B=\begin{matrix}\sigma^2_{B,1} & 0 & \dots & 0\\ 0 & \sigma^2_{B,2} & \dots & 0\\ \dots & \dots & \dots & \dots\\ 0 & \dots & 0 & \sigma^2_{B,i}\end{matrix} \qquad \text{(IV.7)}$$

In order to estimate the diagonal elements of the variance-covariance matrices, we calculate the probability density function of R and B, given the observation Y_0, the prior estimates x_b, and the transport model H. Using the formalism of Bayes, the probability density function of R and B can be defined as:

$$p(R,B|Y_0,X_b,H)=\frac{p(Y_0|X_b,H,R,B).\,p(R,B|X_b,H)}{p(Y_0|X_b,H)} \qquad \text{(IV.8)}$$

We assume that we do not have any prior knowledge about R and B matrices parameters. More precisely, we turn this assumption into the assumption that, over a finite positive interval, the probability of R and B is uniform $p(R,B|X_b,H)\propto 1$. Then, over this finite positive interval, equation IV.8 becomes:

$$p(R,B|Y_0,X_b,H)\propto p(Y_0|X_b,H,R,B) \qquad \text{(IV.9)}$$

The best estimate of the R and B variance matrices parameters are the set of values that maximize the likelihood of the observations. These observations are related to the prior fluxes by the observation operator H $Y_0=Hx_b+\varepsilon_y$.

Then the expected value of Y_0 is

$$E[Y_0]=E[Hx_b+\varepsilon_y]=Hx_b \qquad \text{(IV.10)}$$

and its covariance is

$$E[(Y_0 - E[Y_0])(Y_0 - E[Y_0])^T] = E[(Hx_b + \varepsilon_Y - E[Hx_b + \varepsilon_Y])(Hx_b + \varepsilon_Y - E[Hx_b + \varepsilon_Y])^T]$$

$$E[(Y_0 - E[Y_0])(Y_0 - E[Y_0])^T] = HBH^T + R \quad \text{(IV.11)}$$

From equation IV.10 and IV.11, we can use the expected value and the covariance of the observation to define the Gaussian probability density function of $p(Y_0|X_b, H, R, B)$, which is (from equation IV.9) proportional to $p(R, B|Y_0, X_b, H)$

$$p(R, B|Y_0, X_b, H) \propto \frac{1}{|HBH^T + R|^{(\frac{1}{2})}\sqrt{2\pi}} \exp\left(\frac{-1}{2}.(Y_0 - HX_b)^T.(HBH^T + R)^{-1}(Y_0 - HX_b)\right) \quad \text{(IV.12)}$$

Where | | stands for the matrix determinant. The estimation of the maximum likelihood covariance R and B parameters can be performed by the maximization of the equation IV.12, or the minimization of its negative logarithm (equation IV.13), using the iterative Gauss-Newton method (Gill et al., 1986).

$$L_{(R,B)} = \frac{1}{2}\ln|HBH^T + R| + \frac{1}{2}.(Y_0 - HX_b)^T.(HBH^T + R)^{-1}(Y_0 - HX_b) \quad \text{(IV.14)}$$

Thus the maximum likelihood algorithm optimizes ($R + HBH^T$) according to $(Y_0\text{-}H.X_b)(Y_0\text{-}H.X_b)^T$. Assuming diagonal R matrix, the only way to compensate the non-diagonal values of R is by setting higher values in B matrix through the HBH^T component (Berchet et al 2013). For example, if the operator H is close to the reality, the maximum of likelihood algorithm would compensate the information of $(Y_0\text{-}H.X_b)(Y_0\text{-}H.X_b)^T$ in B matrix, and assign relatively lower values for R.

The algorithm may converge to a local maximum (the convergence to a global maximum is not insured (Berchet et al 2013)). This maximum is called the likelihood maximum, and it takes into consideration the information of the difference between the prior fluxes and the measured concentrations ($Y_0\text{-}Hx_b$).

IV.2.3.1.1 Monte-Carlo sampling

The estimation of the observation and the prior variance-covariance matrices R and B allows the estimate of the optimized fluxes and their corresponding uncertainties using the analytical inversion equations (equation IV.4 and IV.6). In order to take into consideration the uncertainties in the observation and the prior error estimates provided by the maximum of likelihood (ML) algorithm, we will use the marginalization method of the error statistics developed by Berchet et al (2015). This approach consists in sampling the probability

density of the of the variance-covariance matrices using a Monte-Carlo algorithm. The complexity of this method is associated with the need to define accurate probability density function of variance-covariance matrices. Here, we approximate the distribution of the variance-covariance matrices by the distribution of the diagonal observation and prior error matrices (R and B matrices) provided by ML algorithm.

In this study, we perform a Monte-Carlo the sampling using 10000 members, and we calculate the inversion result for each member as presented in Figure IV.1. This approach is based on several inversions. However, one atmospheric inversion may take from few days to few weeks of computing time. It is thus important to define an appropriate dimension of the inverse problem in order the perform the 10000 inversions in affordable time.

To summarize, the maximum of the likelihood algorithm is first resolved using the Gauss-Newton method. This step provides a single couple (R, B). Afterward, a Monte-Carlo ensemble on R and B matrices is performed to get a sample (10000 members) of the whole distribution of the posterior fluxes $p(x|Y_0,x_b)$ (Figure IV.1). The retained posterior fluxes x_a is retrieved from the median of the Monte-Carlo ensemble x_a=median(x_{ai}), and the posterior uncertainty is defined as the standard deviation of the posterior control vectors (x_{ai}) from the tolerance interval covering 68,27% of the Monte-Carlo ensemble (Berchet et al., 2015).

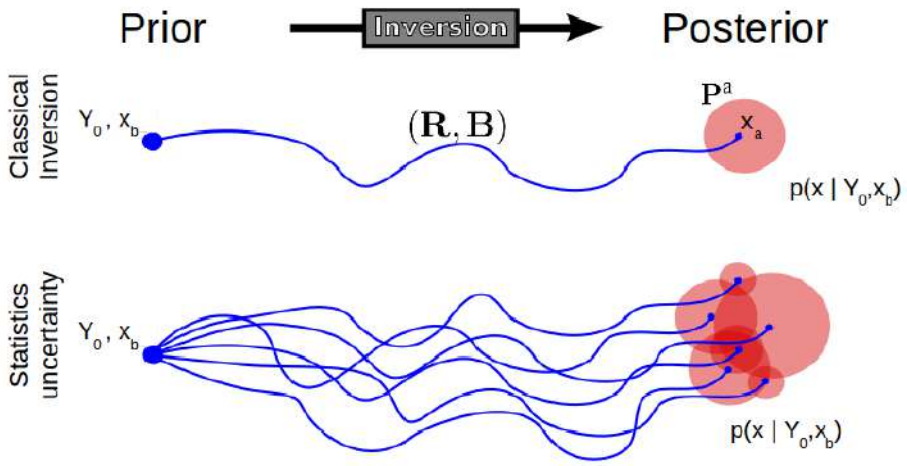

Figure IV.1 Statistic uncertainty in the Bayesian inversion. The inversion computes the posterior control vector xa using the observation Y0 and the prior xb. In the classical inversion (top), xa is estimated together with its uncertainty Pa from the observation and the prior covariance matrices (R and B). In order to take into consideration the uncertainties in the error statistics, an ensemble of the couples (R and B) is used to estimate an ensemble of xa and Pa, which stand for p(x|Y0,xb). The Figure is taken from Berchet. A thesis 2014

IV.2.3.1.2 Filter on the under-constrained emission fluxes

The likelihood maximum algorithm offers the possibility to eliminate the under-constrained control parameters. The control vector parameters which are not constrained enough will be rejected by the algorithm, in order to avoid numerical artifacts (Berchet et al., 2013). This filter is processed using the diagonal elements of the influence of matrix KH (Cardinali et al., 2004), calculated at each iteration of the maximum likelihood algorithm. Note that KH matrix depends on the estimated observation and prior errors (equation IV.5). The diagonal elements of the KH matrix represent the sensitivity of each component of the control vector to the inversion. These elements vary within the range 0 to 1. In order to filter the under-constrained fluxes, we eliminate the control vector components whose KH value is lower than 0.5 (Berchet et al. 2013). Thus only the components of the control vector that are enough constrained will be operated by the inversion.

IV.2.3.1.3 Filter on the emission hotspots

The misrepresentation of the surface fluxes can lead to significant spatial and temporal model-obs mismatches. For example, surface emissions can influence a sampling site in the reality, but not in the model

if these emission sources are assigned with inaccurate fluxes and/or incorrect spatial distribution. This may lead to substantial differences between the observed and the simulated concentrations. The maximum likelihood algorithm (ML) assigns such mismatch to observation errors and/or prior errors. Thus the high values of ML errors (section IV.2.3.1) represent an indication of these mismatches. The data that correspond to the high errors must be filtered out, since they may correspond to sharp synoptic events which are very difficult to simulate by the transport models. The identification of these sharp events is performed by analyzing the diagonal elements of R and B matrices (section IV.2.3.1). The ML algorithm proposes to filter out measurements and surface fluxes characterized by an ML error higher than a given threshold. In this study, we use the threshold that corresponds to 95 % percentile of the observation and the prior errors (Berchet et al., 2013). With this configuration, the ML algorithm filters out the observations poorly represented by the transport model, and rejects the surface fluxes responsible for sharp synoptic events at the sampling sites.

IV.2.4 The definition of the inverse problem

In this study, we will perform an analytical inversion over France for CO_2 and CH_4 fluxes using the inversion framework PYMAI developed by Berchet et al., (2013, and 2015). The inversion is carried out for two months: one month in winter (January) and one month in summer (July), in order to estimate the optimized fluxes for two contrasted periods. The list of the variable defining the inverse problem is presented in the following parts.

IV.2.4.1 Control vector

Ideally, we would like to provide a refined control vector at the highest, possible, temporal and spatial resolutions (e.g. flux optimization for each grid cell and each hour). However, the solution of such a high-dimension control vector inverse problem will be limited by the capacity of calculation resources, by the lack of capacity to characterize the spatial and temporal structures in the prior uncertainties at such a resolution (especially since the system used here ignores the correlations between uncertainties in different control variables). For this reason, it was necessary to make a compromise by reducing the inverse problem dimension. The reduction of the control vector dimension is usually performed by the aggregation of the flux budget spatially over a geographical region and temporally during a specific period of time. In the analytical approach used here, the control vector does not include directly the flux budget. The control vector components represent the scaling factors that are applied to the fluxes. Each scaling factor corresponds to the

flux budget aggregated for a given region, for a distinct time period, and for an individual control parameter (surface fluxes, boundary conditions, and initial conditions).

For both CO_2 and CH_4 surface fluxes, we aggregated the surface fluxes on 26 regions over France (regions from 1 to 26), 15 regions for the neighbouring countries (regions from 83 to 97), in addition to one region for the Atlantic ocean (region 98) and one region (region 99) for the Mediterranean sea (Figure IV.2). For the temporal aggregation of the CO_2 and CH_4 fluxes, we split the months (January and July) into 31 days, further subdivided into 6 hourly time windows (from 00:00 to 06:00, from 06:00 to 12:00, from 12:00 to 18:00, and from 18:00 to 00:00). For the CO_2 and CH_4 boundary conditions, we define 5 edges of the domain North, South, East, West (dashed lines Figure IV.2) and one edge on the top (not presented in Figure IV.2). For the temporal resolution, we selected the same number of days (31 days), with 12 hourly time windows. The first time window represents the night time data (from 18:00 to 06:00), and the second time window stands for the daytime data (from 06:00 to 18:00). For the initial conditions, we define one component that covers all the domain during the first day of each month.

While this approach decreases the dimension of the control vector, it may lead to some errors that impact the quality of the optimized fluxes (Bocquet et al.,2011, and Kaminski et al 2001). These errors are known as the aggregation errors and represent the misfits between the modeled and the observed CO_2 and CH_4 concentrations due to errors in the flux patterns of the control region and temporal window. In order to reduce the impact of the regional flux distribution on the atmospheric concentrations at the sampling site level, the 43 control regions were defined based on the analysis of the emission maps (Figure SIV.1) and the spatial distribution of vegetation types (Figure SIV.2 ECOCLIMAP database, Champeaux et al., 2005). For a given flux, the control region is defined in a way that each type of flux (biogenic or anthropogenic) remain relatively homogeneous within the selected region. In the following, we summarize the component of the CO_2 and CH_4 control vector.

The control vector X for each month (January and July) for CH_4 is composed of 5643 components:

- One component for the initial conditions.
- 310 components for the boundary conditions (5 edges x 31 day x 2 time windows per day).
- 5332 components for the emission fluxes (43 regions x 31 days x 4 time windows per day).

The control vector x for each month (January and July) for CO_2 is composed of 10975 components:

- One component for the initial conditions.
- 310 components for boundary conditions (5 edges x 31 x 2 time windows).

- 5332 components for the anthropogenic emission fluxes (43 regions x 31 x 4 time windows).
- 5332 components for the biogenic emission fluxes (43 regions x 31 x 4 time windows).

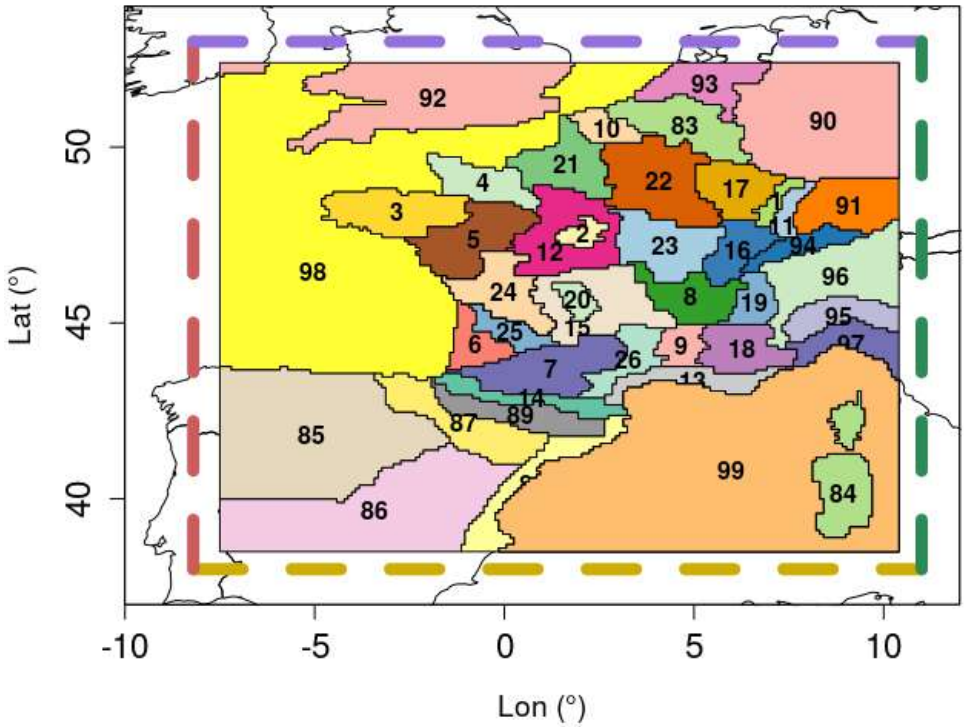

Figure IV.2: Illustration of the 43 emission regions (colored area) and boundary conditions edges (4 lateral colored dashed lines + 1 top edge) used for the control vector calculation.

IV.2.4.2 Observation vector

In order to constrain the inverse problem, we use a vector of observations (Y_0) which can include for example direct surface measurement or remote sensing using satellites. In this study, we used only continuous surface measurements from 14 stations in January, and 15 in July. The list of the stations was presented in chapter III (Figure III.3, and Table III.3).

In order to perform the inversion problem, the variance-covariance matrices of the observation errors (R) must be small enough (due to the calculation limitations). Moreover, the used observations should be consistent with the spatial and the temporal resolutions of the atmospheric transport model. Therefore, we

have done a data selection in order to reject observations which cannot be properly represented by the transport model. This step was described in the previous chapter (Section III.3.5), and we provide here only a short reminder of the data selection process. We use the hourly averages of continuous measurements performed at the atmospheric sites presented in table III.3. We select the mid-afternoon data (14:00 to 18:00 local time) for low elevation sites and nighttime data (00:00 to 06:00 local time) for the mountain stations. For stations that are characterized by more than one sampling level (e.g., OPE, TRN, RGL, and CBW), only the highest level is selected, since the transport models are not able to optimally reproduce the vertical mixing close to the surface. Note that during January measurements from PDM and OHP stations are not available, whereas ERS measurements were interrupted in July (Figure IV.3). This leads to an unequal spatial distribution of the observation sites, with no observation site available to constrain the emission fluxes in the south-east of France in January.

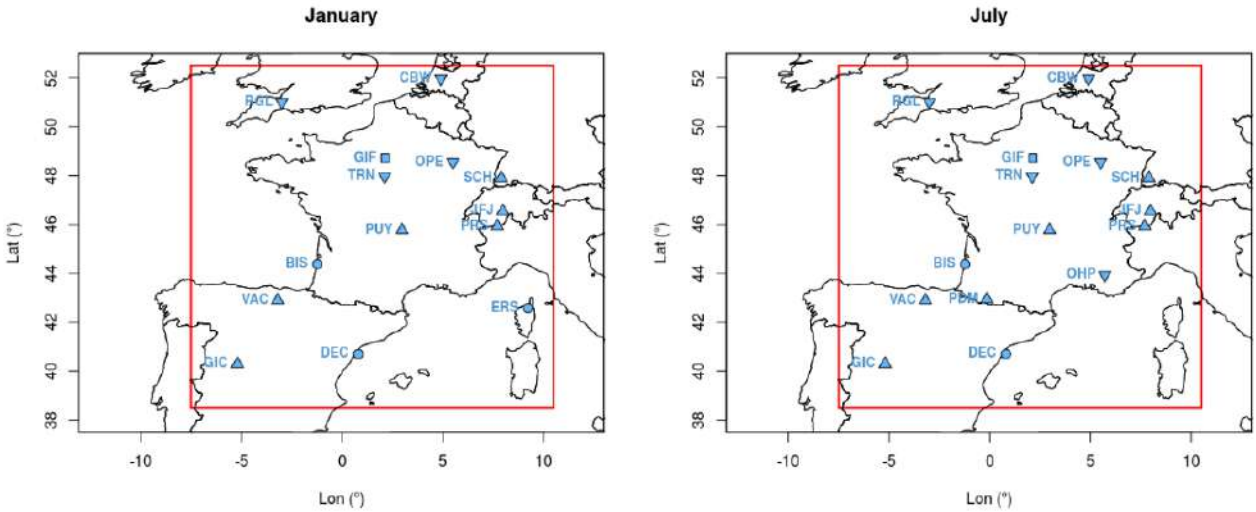

Figure IV.3: Stations providing measurements of CO_2 and CH_4 during January (left) and July (right) 2014. Note PDM and OHP sites (south of France) were not available for Janary, and ERS measurements (located in Corsica) were interrupted during July. the atmospheric sites are grouped into four categories according to their characteristics (e.g. topography and environment): coastal (circle), mountain stations (triangle), Peri-urban (square for GIF only), and tall towers (inverse dtriangle). The red box shows the limit of the model domain.

IV.2.4.3 Surface fluxes

The surface flux information used in our inverse modeling framework is calculated using the bottom-up approaches. These estimates represent the prior information of the flux budgets for different regions and time windows of the control vector (section IV.2.4.1). The used estimates are thus processed to provide the spatiotemporal distribution of the surface fluxes within the control region and time windows, as part of the observation operator (section IV.2.4.2). For the CO_2 and CH_4 anthropogenic emissions, we used the emission fluxes prescribed by EDGAR (Emission Database for Global Atmospheric Research, available at **http://edgar.jrc.ec.europa.eu/-overview. php?v=42**) version 4.2FT2010. For the natural fluxes, only the Net Ecosystem Exchange (NEE), provided by the VPRM model (Vegetation Photosynthesis and Respiration Model, Mahadevan et al., 2008), is used to represent the CO_2 biogenic fluxes. The natural CH_4 emissions, such as natural wetlands, were neglected in this study due to the lack of accurate estimations and the low extension of these emission sources in our domain (Champeaux et al., 2005). The list of the prescribed surface fluxes was presented in detail in section III.2.3. In table IV.1 we summarize the main characteristics of the used fluxes.

Flux category	Flux	Spatial resolution	Temporal resolution	Reference
CO_2 anthropogenic	EDGARv4.2FT2010	0.1° x 0.1°	Hourly*	Maenhout et al., 2017
CO_2 biogenic	VPRM 2014	0.125°x 0.08°	Hourly	Mahadevan et al., 2008
CH_4 anthropogenic	EDGARv4.2FT2010	0.1° x 0.1°	Hourly*	Maenhout et al., 2017

Table_IV. 1: Characteristics of the surface fluxes used as prior in the inverse framework. (*) means that the corresponding fluxes were produced using hourly temporal profils applied on the yearly totals (Section III.2.3)

IV.2.4.4 Observation operator

The surface flux budget is projected into the space of concentrations using the linear observation operator H (equation IV.1). Each element of H indicate the modeled concentrations at a sampling site for a certain time and a given surface flux. The linear observation operator can be decomposed into three sub-operators H_{dist}, H_{trans}, and H_{sample} where $H=H_{dist}.H_{trans}.H_{sample}$.

H_{dist} is built on hourly anthropogenic and biogenic fluxes (section IV.2.4.3) at the horizontal resolution of the transport model. It implies the CO_2 and CH_4 surface fluxes to distribute the spatial and the temporal flux patterns within the control regions and the time periods. This operator uses the scaling factor of the control vector to rescale the surface fluxes on the grid of the transport model in each region and for each 6 hourly time period.

H_{trans} stand for the atmospheric transport. It is used to process the impact on the concentration of each surface flux that corresponds to a control vector component. It includes also the signature of the initial conditions and the boundary conditions. In this study, we transport the CO_2 and the CH_4 concentrations using the atmospheric transport model CHIMERE (http://www.lmd.polytechnique.fr/chimere/ Menut et al .,2013). The transport model was described in details in section III.2.1. CHIMERE is forced by the ECMWF meteorological analysis (European Centre for Medium-range Weather Forecast). For initial and boundary conditions of CO_2 and CH_4, CHIMERE is forced by the global model MACC at 0.15°x 0.15° degree and three hours time step (Marécal et al. 2015). Both initial and boundary condition are linearly interpolated to the CHIMERE domain grid (0.1°x 0.1°) and 1-hour time resolution. The transport modeling domain is centered over France with an extended area that covers a part of the neighboring countries (e.g. Spain, Germany, Belgium) in order to reduce the risk of the aggregation errors due to the coarse spatial distribution of the boundary conditions (Figure IV.2). In fact, these errors are thus mixed and attenuated over a large area (hundreds of kilometer) before reaching the observation sites.

H_{sample} operates the simulated CO_2 and CH_4 field to retrieve a simulated concentration vector that corresponds to the used observation vector (section IV.2.4.2). The simulated 4-D atmospheric concentrations are operated by selecting the modeled concentration of the grid-cells whose center is at the nearest horizontal and vertical position of measurement points and extracted for the time that corresponds to observed hourly data.

Building the observation operator

In order to perform the analytical inversion (equation IV.4 and IV.6), the observation operator is built using the different sub-operator described above. Each column of H is constituted by a response function (Enting et al., 2002), which represent the response of the CO_2 or CH_4 concentration to a control vector component. One response function is calculated by applying the observation operator to the control vector with 1 for the control parameter and zero for the remaining parameters. For example, for the initial conditions, we perform a simulation in which only the prior initial concentrations are used with zero surface fluxes and boundary

conditions. For the component which corresponds to the emission region 1 during the first time window, we apply H to the control vector in which only the fluxes of region 1 of this day and of this time window are used, with zero initial conditions, zero boundary conditions, and zero fluxes for the other regions and time windows. We repeat this process individually for each component of the control vector. Thus, H matrix is formed using the response functions of all control vector components (5643 components for CH_4 and 10975 components for CO_2, see section IV.2.4.1).

IV.3 Results

The results of the atmospheric inversions are presented separately for CH_4 and CO_2. The inversion system (presented in section IV.2.3) provides an estimation of the optimized fluxes and their associated uncertainties, as well as few other indicators which help to analyze the sensitivity of the inversion results to the input dataset. For both CH_4 (section IV.3.1) and CO_2 (section IV.3.2), we will present first the data selection applied to the atmospheric concentration time series, with an analysis of the weight of the observations in the flux inversion. Second, we will investigate the observation and prior flux errors estimated by the maximum of likelihood algorithm (section IV.2.3.1). Third, we will present the constraint applied to the fluxes, and the ability to separate the signal from different regions and type of fluxes. Then, we will discuss the regional fluxes deduced from the inversion.

IV.3.1 Inversion of the CH_4 fluxes

IV.3.1.1 Weight of the CH_4 atmospheric observations in the inversion.

As explained before we have used the CH_4 concentrations measured at 16 stations (Figure IV.3) in January and July 2014. Even if all stations are measuring continuously the concentrations, the time series suffer from data gaps due to maintenance, calibrations or instrumental failures, which reduce the amount of data available for the inversion (grey color in Figures IV.4 and IV.5, and Table SIV.1). For example, at VAC the measurements were available only for 4 days (between January 1 and 4), which correspond to 86 data (Figure IV.5, and Table SIV.1). Note that during January, PDM and OHP data are missing, as well as ERS data in July.

IV.3.1.1.1 Data selection

From all the available measurements we apply a data selection in order to reject those measurements which cannot be optimally reproduced by the atmospheric transport model, like the daytime orographic flows and

the nighttime stratifications close to the surface. In general, the selected data (see section IV.2.4.2) represent 20% to 25% of the total available data (illustrated by black in Figure IV.4, SIV.3, SIV.4, SIV.5, SIV.6, and Table SIV.1). This selection filters out the daily periods where the atmospheric model is not always able to reproduce correctly the transport processes (vertical and horizontal mixing), as shown in section III.3.5 for the low altitude sites during the nighttime and the mountain stations during the daytime.

IV.3.1.1.2 The maximum likelihood (ML) data filtering

In addition to this systematic screening of the input dataset, the maximum likelihood (ML) algorithm implemented by Berchet et al (2013), proposes to filter out additional measurements whose representativeness appears to be incompatible with the simulated data. This is the case for the observations that occur during short-term synoptic events which are very difficult to simulate by the transport models (see section IV.2.3.1). In Figure IV.4, we illustrate by red color the data filtered by the ML algorithm for OPE and PUY stations (other sites are shown in Figures SIV.3, SIV.4, SIV.5, and SIV.6). The percentage of data rejected by the ML algorithm varies between 1% and 3% (Table SIV.1). The lowest percentages of rejected data occur at the mountain stations (Table SIV.1), suggesting that these stations are less sensitive to non-modeled surface fluxes causing short-term variations of CH_4.

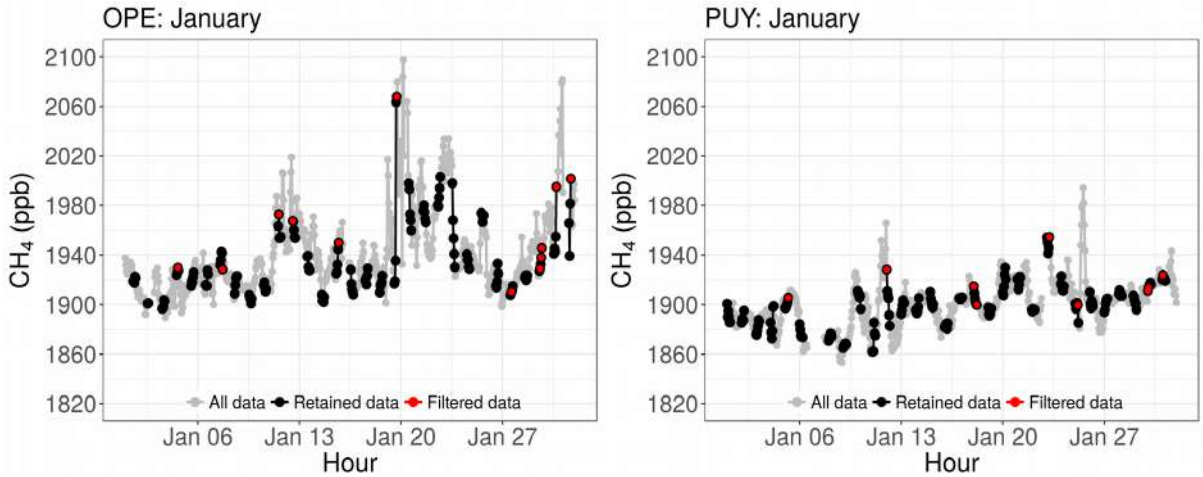

Figure IV.4: CH_4 hourly data at OPE (left) and PUY (right) in January 2014. The grey color represents the available observations for each site during January. The back data point stands for the retained data during the mid-afternoon(data between 14:00 and 18:00) for low altitude sites (OPE), and the nighttime (data between 00:00 and 06:00) for mountain stations (PUY). The red data show the observations rejected by the ML algorithm (see section IV.2.3.1)

IV.3.1.1.1 Weight of the observations

One important diagnostic of the inversion is the weight of each observation in the process of fluxes optimization, which can be determined by the diagonal terms of the sensitivity matrix HK (see details in Cardinali et al., 2004). For a given atmospheric data, a low observation error increases the contribution of this data to the inversion (see the gain matrix K, equation IV.5). On the other hand, the contribution of one individual observation will be reduced if the information provided by this data is redundant with other observations close in time (same synoptic event), or in space (atmospheric sites that are spatially close). Consequently, a station surrounded by relatively high local emissions will have a high sensitivity (high HK values) leading to high weights of the observations. In Figure IV.5, we represent the weights of the retained CH_4 observations during 6 hour time window (maximum value = 6) for January and July. At BIS, for example, we notice larger weights of atmospheric observations between January 7 and 14 (more than the equivalent of three data) compared to the period between January 20 and 27 where less than two data per 6 hourly window were used by the inversion. On average, the inversion exploits an equivalent of two to three hourly data per 6 hour's time window (Figure IV.5).

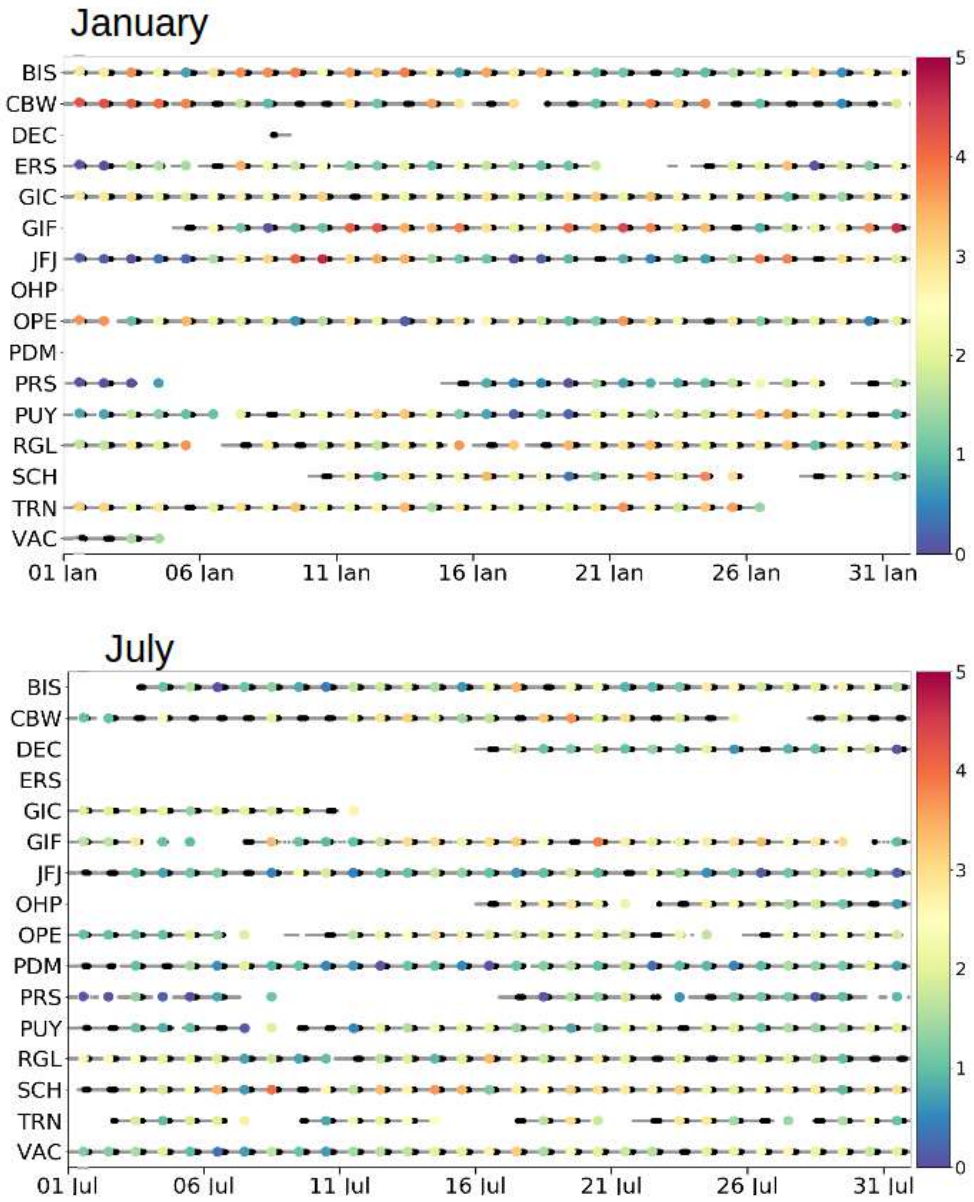

Figure IV.5: Representation of the availability of the CH_4 observed data and their contribution to the inversion for each site. The grey line represents the available data. Black dots stand for the retained measurements (data between 14:00 and 18:00 for low altitude sites, and data between 00:00 and 06:00 for mountain sites). The color points represent the amount of information used each day by the inversion system (value 1 indicate that the inversion uses the equivalent of one hourly data). These information are calculated from the diagonal terms of the sensitivity matrix HK

IV.3.1.2 Comparison of observation and prior flux errors with independent empirical estimates

Before analyzing the optimized fluxes, we have evaluated the observation and the prior flux errors provided by the maximum of likelihood (ML) algorithm (Berchet et al., 2013), from the diagonal matrices B and R (section IV.2.3.1). The aim of this evaluation is to investigate the distributions of the observation and prior errors and to study whether they are consistent with independent empirical estimates using the differences between two emission inventories and transport models.

The observation errors include the uncertainties related to the measurements and the transport model (transport errors). The latter can be associated to the uncertainties in the horizontal transport (advection), vertical transport (mixing height), and the unresolved flux patterns by the models. Since the measurement errors can be neglected compared to transport errors (Andrews et al., 2014; Ramonet et al., 2011), we have compared the observation errors provided by the ML algorithm (diagonal elements of R matrix) to the absolute differences between the two transport models (ECMWF minus AROME, section III.3.5). For the prior errors, we have compared the output from ML algorithm (diagonal element of B matrix) to the absolute differences between the anthropogenic emission maps (EDGAR minus IER, section III.3.6).

IV.3.1.2.1 Observation errors

Figure IV.6 represents the distribution of the observation errors estimated by the ML algorithm (orange) against the absolute differences of concentrations simulated with ECMWF and AROME (green) for January (top) and July (bottom). The data filtered out by the ML algorithm (e.g. short-term event) were also eliminated from ECMWF and AROME simulations. In January and July, the comparison shows that the interquartile range of the ML observation errors is smaller than the differences between the two transport models. At most sites, the two methods differ by a factor of 1.2 to 1.5, except at sites like GIF (July) where the ML error interquartile interval is two times smaller than the transport model differences. The high difference between ECMWF and AROME at this sub-urban station is related to the high gradient of surface emissions in the Paris area (Section III.3.6). In such a case, a small difference in wind fields between the two transport models may lead to significant differences at the station (see section III.3.5). The comparison between the two months shows that both the ML and the transport difference methods increase the observation errors in July by a factor of ~1.5 compared to January. As shown in section III.3.5, the increase of the model differences in July is related to the differences between the wind fields and boundary layer

height, especially for the mountain sites. Note that the ML algorithm estimates the errors using the ECMWF transport data, whereas the model difference method provides empirical errors using two transport models. In principle, the ML observation errors should be higher than the ones provided by the transport models differences, since the ML algorithm estimates the total observation errors that include transport errors, representativeness errors, and the aggregation errors. The fact that we find lower errors with the ML method indicates that for the used spatio-temporal resolution, the dominant errors are the ones related to the transport processes.

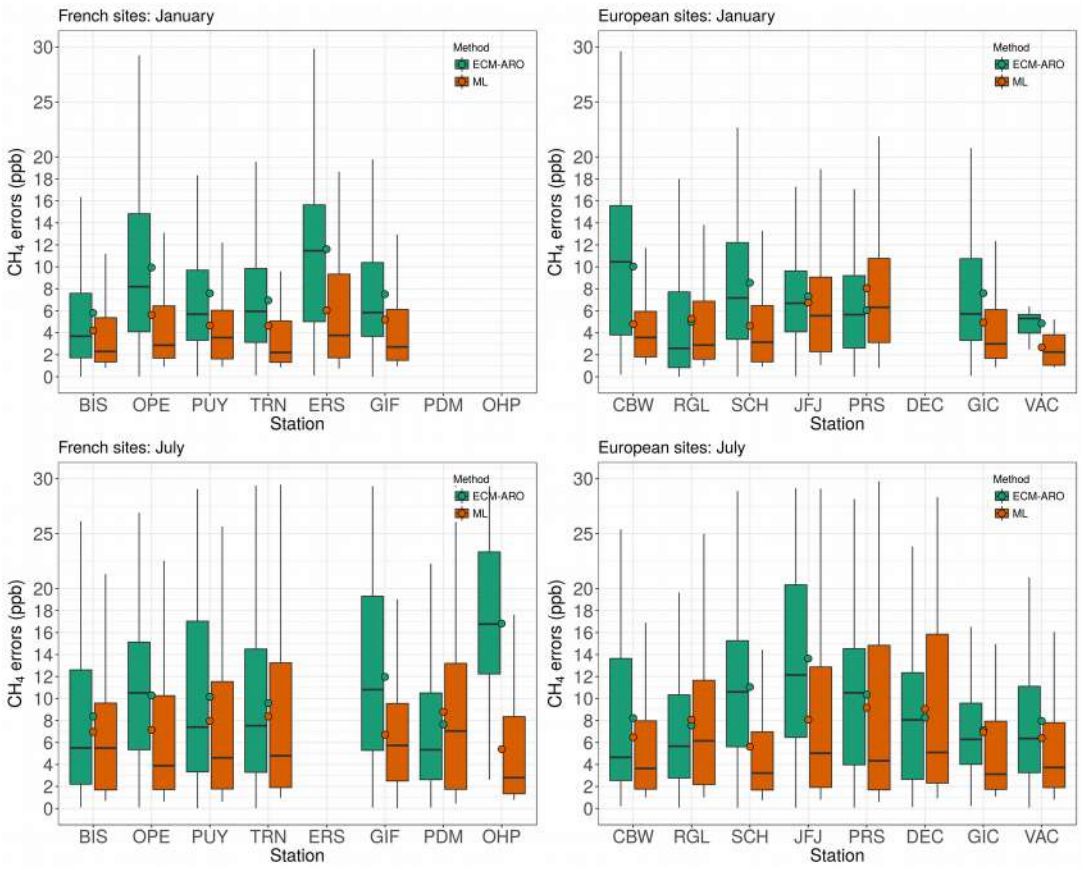

Figure IV.6: Comparison of the CH_4 observation errors calculated by the maximum of likelihood algorithm (ML) and the absolute difference between the two transport models (ECMWF minus AROME). The errors are presented using boxes (errors between the 25th and the 75th quantiles), the horizontal black line for the median, and the mean as shown by the colored dots.

IV.3.1.2.1 Prior flux errors

In Figure IV.7 we compare the spatial distribution of the prior flux errors provided by the maximum likelihood (ML) algorithm against the spatial distribution of the absolute difference between EDGAR and IER. The errors provided by the two methods are normalized according to the monthly budget and expressed

in percentages of the monthly fluxes for January (Figure IV.7-top) and July (Figure IV.7-bottom). We observe that the ML algorithm assigns higher prior errors compared to the absolute differences between the two anthropogenic maps for both January and July. In France the difference between EDGAR and IER range between 10 and 50 % of the monthly budget, whereas the ML algorithm provides prior flux errors that range between 60 % and 200 % of the monthly budget (more than 200 % in some specific region such as regions 3, 22, and 23). The comparison of the ML prior error between the two months shows slightly higher errors in January compared to July which is also the case when comparing the two anthropogenic emission maps (section III.3.3).

Considering that the ML algorithm estimates the prior errors based on the differences between the model and the observations (see section IV.2.3.1 for observation covariance which equals $HBH^t + R$), it is very likely that the low values of the observation errors are somehow compensated by higher uncertainties assigned to the prior fluxes (R and B matrices are interdependent, section IV.2.3.1).

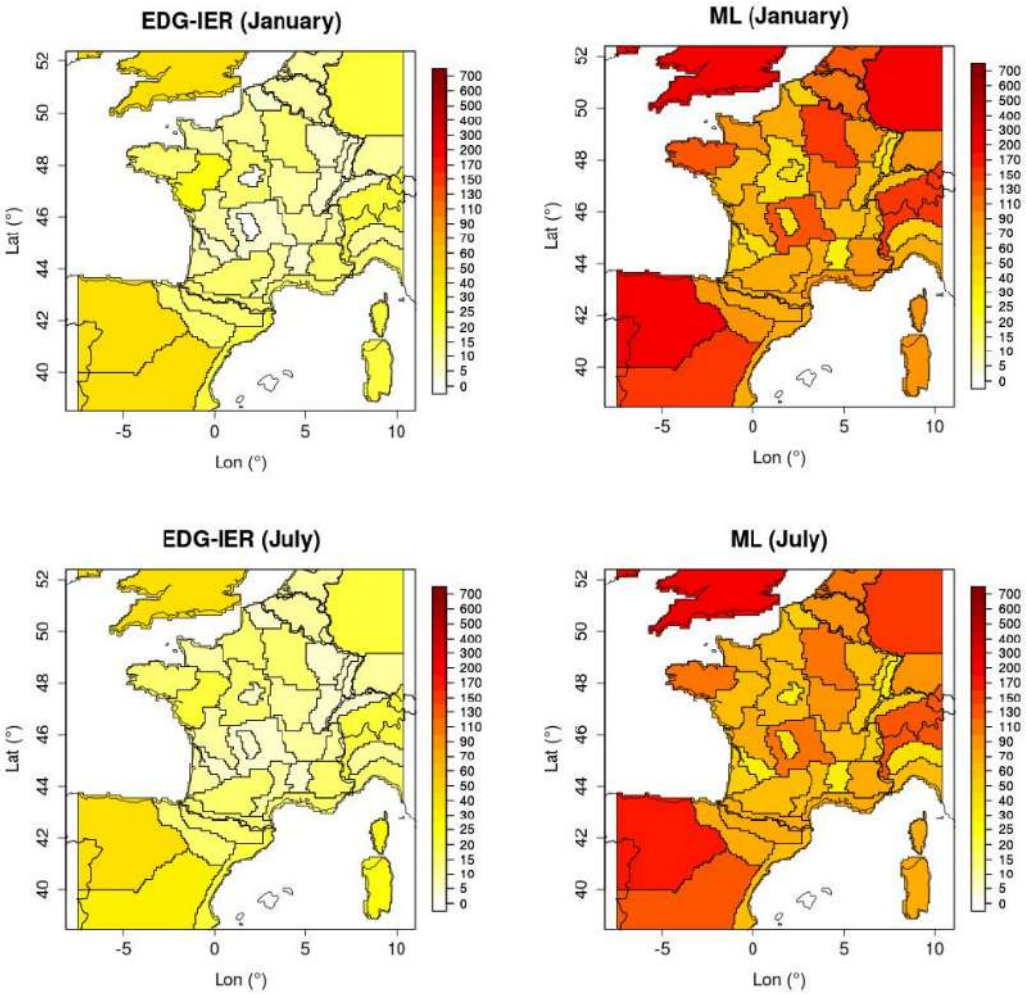

Figure IV.7: Comparison of the prior flux errors calculated by the maximum of likelihood algorithm (ML) and the absolute difference between the two anthropogenic maps (EDGAR minus IER). The errors are presented in percentage according to the monthly fluxes for January (top) and July (bottom).

IV.3.1.3 Fit of posterior concentrations to observations

Figures IV.8 and IV.9 present the comparison of the CH_4 measurements with the simulated concentrations before and after the inversion, for January and July 2014 at eight stations in France. Results for the stations outside France are presented in the Appendix (Figures SIV.7 and SIV.8). The differences with prior concentrations which range from 10 to 30 ppb (up to 60 ppb at GIF), are reduced to 4 to 15 ppb after the inversion. Overall, the inversion reduces the mismatch with observations by a factor of 2 to 3. Larger corrections are observed for some synoptic events at BIS in January (Figure IV.8) and GIF in July (Figure IV.9).

The comparison shows that before the inversion the R2 ranges between 0.6 and 0.8 for January and between 0.5 and 0.9 for July (R2 presented at the top of each panel of Figures IV.8 and IV.9). After the inversion, the range is reduced by a factor of ~2 for both months. The highest R2 occurs at BIS, OHP, TRN, and PUY with values exceeding 0.95. The increase of the coefficient of correlation indicates that the inversion improves the representation of the phase of the day to day variability. However, some exceptions occur during periods where the prior concentrations exhibit sharp synoptic changes. This is, for example, the case at GIF with a sharp CH_4 increase observed in July due to the influence of Paris emissions (25 km away) which cannot be reproduced by the model even after the optimization.

As shown by the shaded areas in Figures IV.8 and IV.9, the inversion reduces the uncertainty of the prior concentrations by 10 to 30 %. We observe a relatively lower uncertainty reduction for PUY and PDM, probably due to the lower sensitivity of mountain sites to the optimized surface fluxes. Larger error reductions are obtained at the low altitude sites (GIF, OPE, and TRN) which are located closer to emission sources (e.g. 30% reduction at OPE).

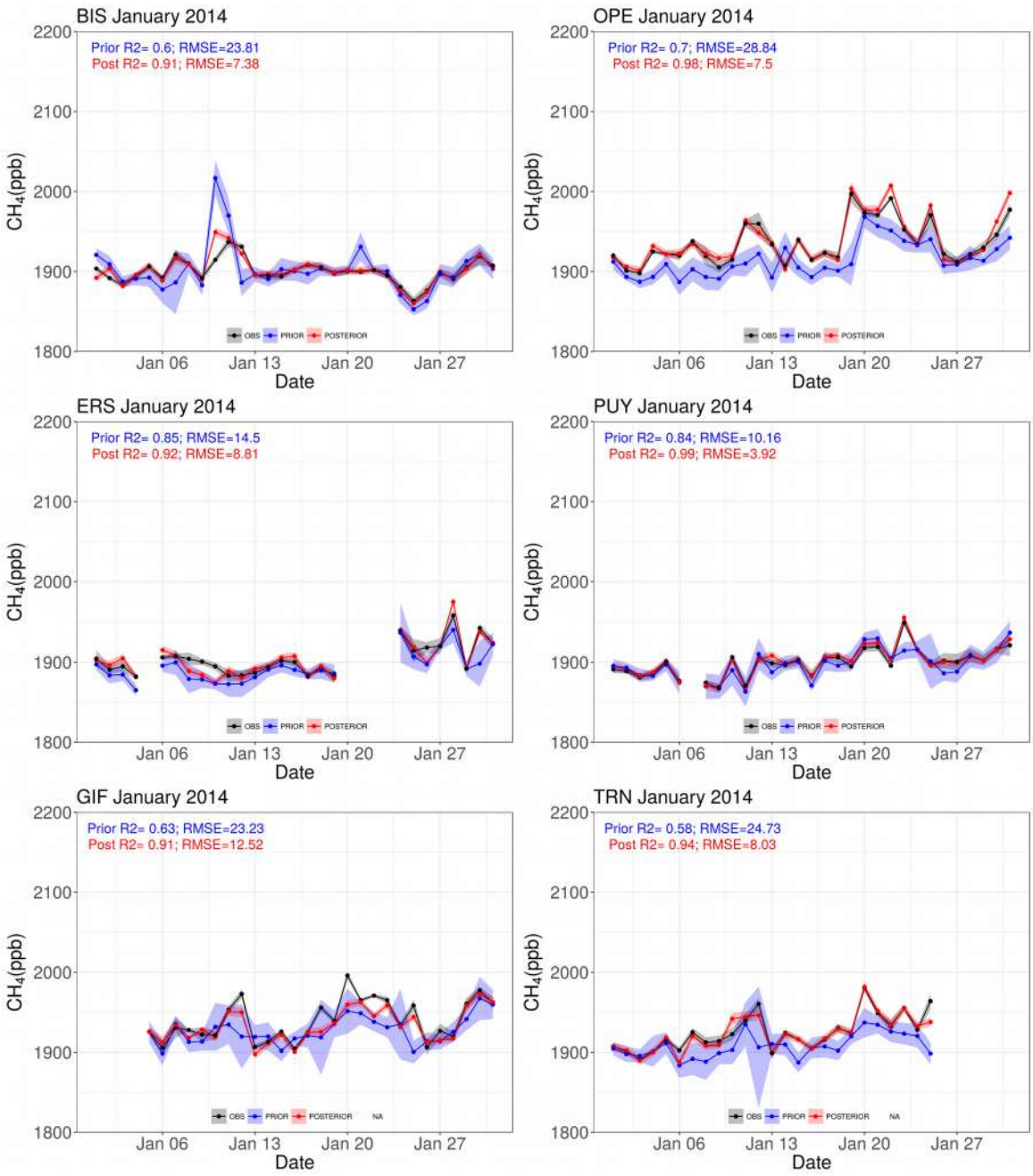

Figure IV.8: Observed (black) and simulated prior (blue) and posterior (red) CH_4 daily averages for the French atmospheric sites (BIS, GIF, OPE, PUY, TRN, and ERS) during January. The shaded areas represent the uncertainties of the observed (grey) and simulated prior (shaded blue) and posterior (shaded red) CH_4 concentrations. For each sites we calculate the root mean square error (RMSE) and the coefficient of correlation (R2) for the prior and the posterior concentration.

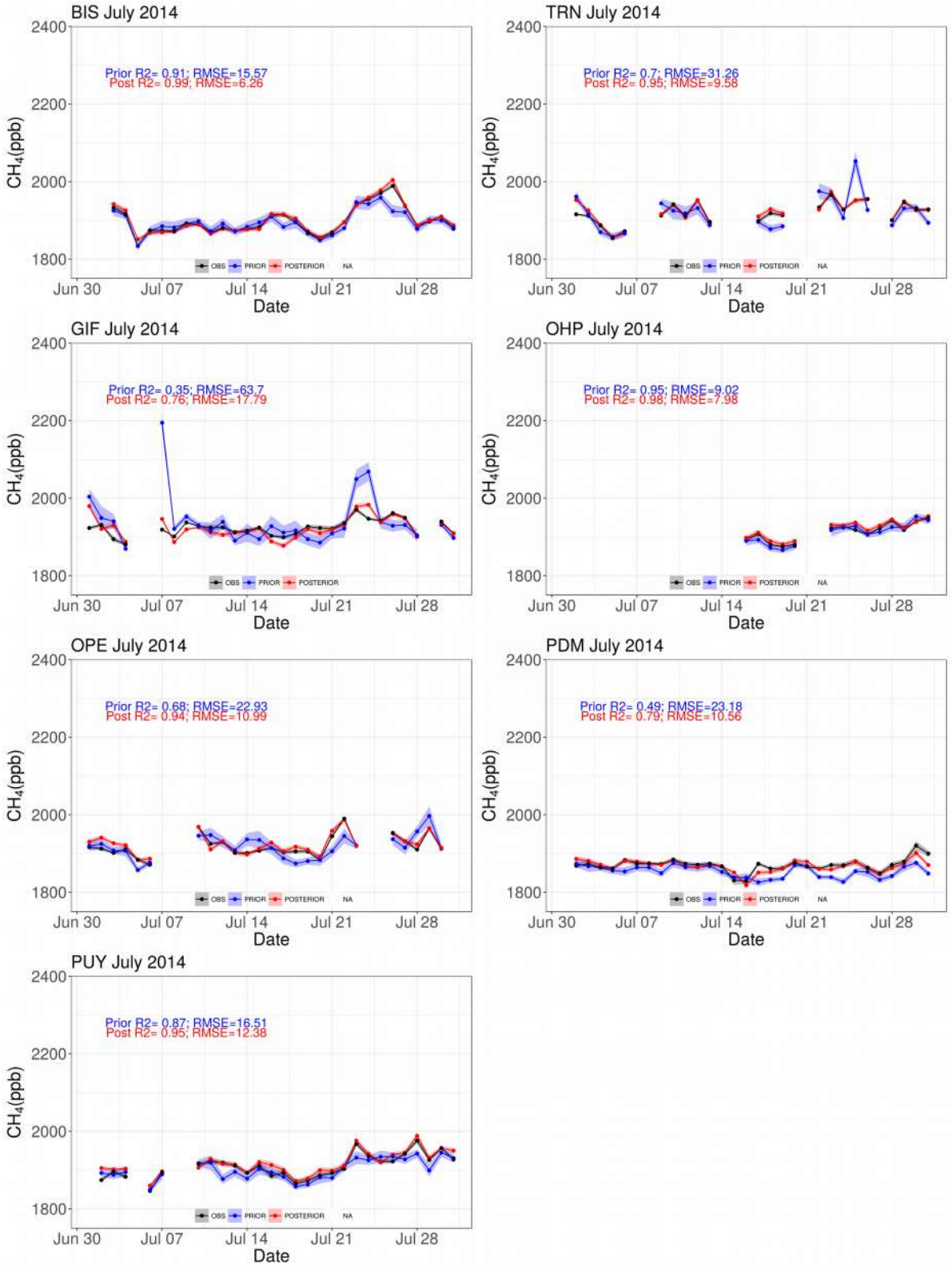

Figure IV.9: Observed (black) and simulated prior (blue) and posterior (red) CH_4 daily averages for the French atmospheric sites (BIS, GIF, OPE, PUY, TRN, OHP, and PDM) during July. The shaded areas represent the uncertainties of the observed (grey) and simulated prior (shaded blue) and posterior (shaded red) CH_4 concentrations. For each sites we calculate the root mean square error (RMSE) and the coefficient of correlation (R2) for the prior and the posterior concentration.

IV.3.1.4 Emission regions constrained by the inversion

The diagonal elements of the KH matrix provide the information about which components of the control vector are constrained by the observation sites (Cardinali et al. 2004). Note that one component of the control vector represents a region for a given day and during a specific time window (see section IV.2.4.1). In this section, the spatial distribution of the constraint on the fluxes is calculated by convolving KH with the prior distribution fluxes (Figure IV.10 and IV.11). Regions, where the fluxes are small/null, will be characterized by small/null constraints. The constraint information at a given region depends on the intensity of the emissions fluxes, transport fields, and the location of observation sites receiving tracer from this region (Pison et al., 2018).

In the Figures (IV.10 and IV.11), we have also represented the weight of measurement sites (colored triangles) in the inversion using the sensitivity matrix HK (see section IV.3.1.1). The measurement weights indicate the contribution of each station to constrain all fluxes without separation between regions. In January and July, data from GIF, OPE, and TRN stations provide the maximum constraint on CH_4 fluxes. In contrast, the contribution of PUY is weaker, this mountain site being less sensitive to surface fluxes. As can be seen in Figures IV.10 and IV.11, using a domain that contains stations from the neighboring countries allows constraining fluxes and the boundary conditions of the external area of France. For instance, CBW and SCH (located in the Netherlands and Western Germany) provide significant constraints to the emission fluxes in the North and East regions of France, respectively (Figures IV.10 and IV.11).

The CH_4 fluxes are better constrained in the west of France compared to the east (Figures IV.10 and IV.11). The regions that are best constrained during January and July are regions 3, 4, 5 (Brittany regions), and 21 (Île-de-France region). This can be explained by the intensity of the CH_4 emissions fluxes (~30% of the national total), and by the location of the atmospheric stations downwind those regions. The white areas indicate regions that are not constrained by the inversion system or where the fluxes are null (e.g. ocean). In January when data from OHP in Provence are missing, the south-east of France is not constrained. In July, the OHP station fills the gap in most part of south-east France, but due to the gap of ERS measurement the Corsica region (region 84) is not constrained (Figure IV.11).

As expected, the problem of under-constrained regions is directly related to the design of the monitoring network. In some cases the atmospheric measurements at a given station can be strongly influenced by

emission hotspots in the nearby region, leading to very high variability of the concentrations. In such cases, we have seen that the ML algorithm may filter out the spikes due to the difficulty of the transport model to reproduce them correctly. In such situations, we are penalized by the weaknesses of the transport model. Moreover, in other cases, we are also penalized by the weakness of the observation network when there is no station downwind a given region. This is the case for regions 18, 19, 9, and 26 whose emissions are not influencing the available stations in January (Figure IV.10). Pison et al (2018) showed that the best-constrained fluxes are located at an intermediate distance upwind of stations (few hundreds of km). In Figures IV.10 and IV.11, the Brittany region (region 3), located 300 km west of GIF and TRN stations, is significantly constrained thanks to its high CH_4 emissions and the effect of westerly winds carrying the signal to GIF and TRN station. This result supports the conclusions of Pison et al (2018), showing that high flux constraints can still be found over regions far from an observation site if advection brings air parcels from this region to the station.

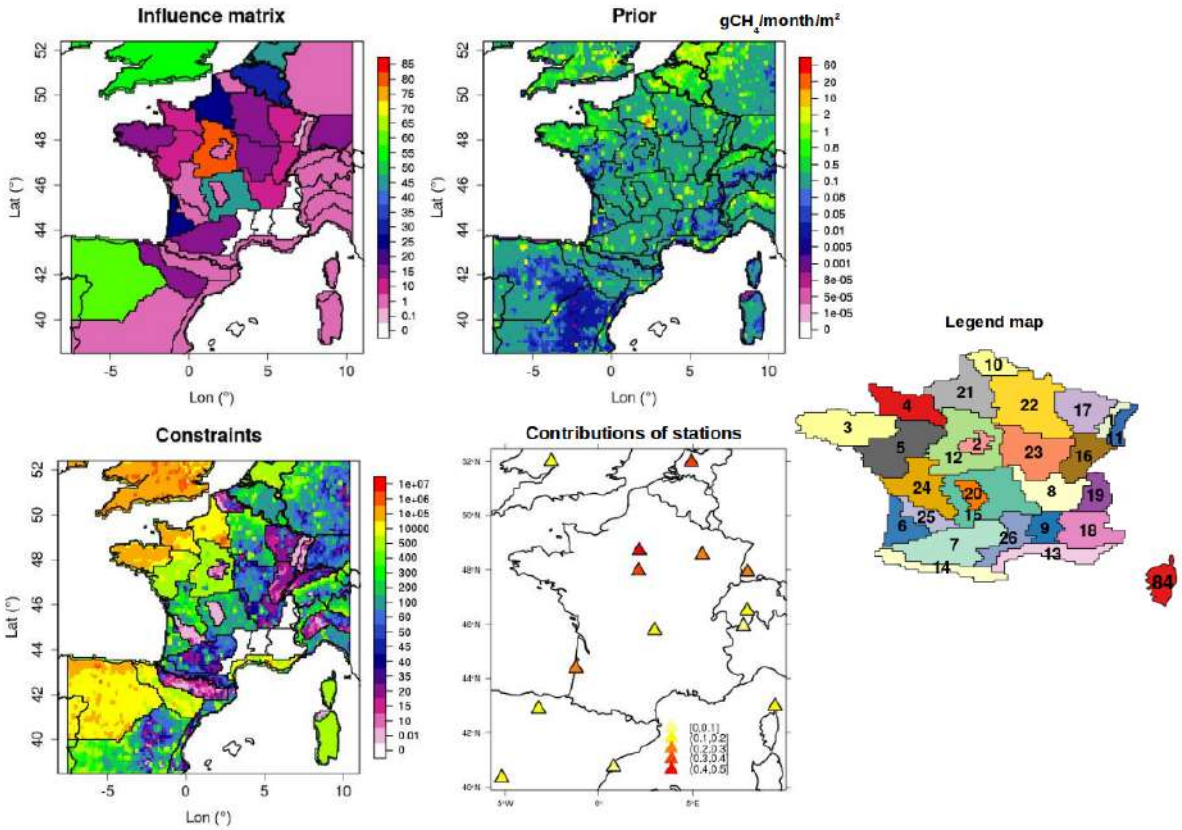

Figure IV.10: Spatial distribution of the influence matrices, prior fluxes, the constraint on regions, and the contribution of the stations for the inversion during January. The constraint map is generated by convolving the influence matrix KH (presented in the figure by % over the month) with the prior fluxes. The contribution of the station in the inversion for January is presented using the diagonal terms of the sensitivity matrix HK. The scales of the constraints maps and the contribution of the station were chosen arbitrary, in respect with the range of the two maps. The map in the right (legend map) is presented as a support for number of regions.

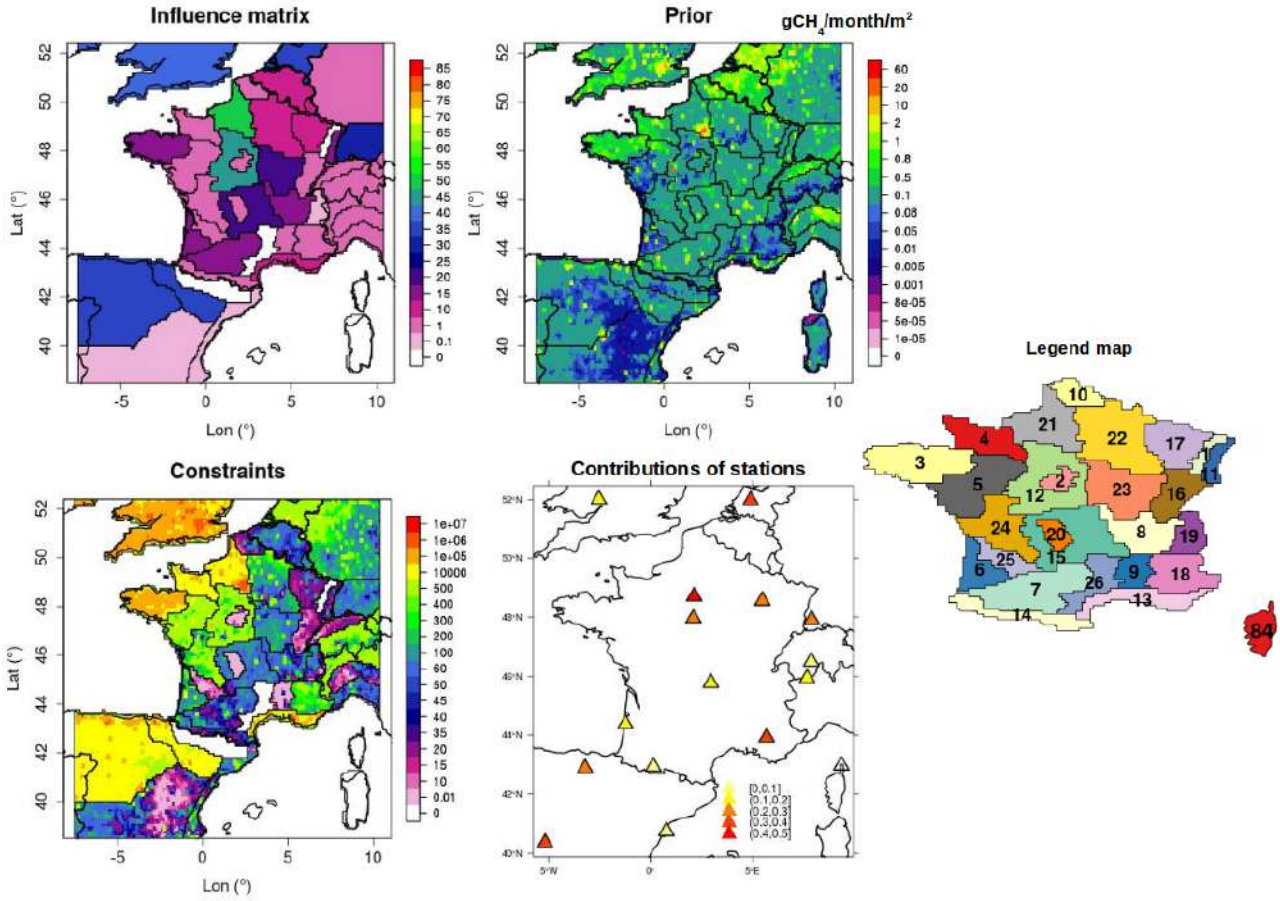

Figure IV.11: Spatial distribution of the influence matrices, prior fluxes, the constraint on regions, and the contribution of the stations for the inversion during July. The constraint map is generated by convolving the influence matrix KH (presented in the figure by % over the month) with the prior fluxes. The contribution of the station in the inversion for July is presented using the diagonal terms of the sensitivity matrix HK. The scales of the constraints maps and the contribution of the station were chosen arbitrary, in respect with the range of the two maps. The map in the right (legend map) is presented as a support for number of regions.

IV.3.1.5 Spatial correlation of the flux errors

The potential of the inversion to separate emissions from different regions is limited by the density of the network, leading to spatial and temporal correlations between optimized fluxes. Poor flux separation can be associated with the limited number of observations coupled to wind speed and direction changes that control the influence of each region at the monitoring stations. Non-separable fluxes between regions can be diagnosed by high negative or positive correlations of posterior errors and low uncertainty reduction. In order to investigate this problem, we present in figure IV.12 the posterior error correlation between the regions for January and July. This analysis is completed by the monthly uncertainty reduction presented in Figure IV.13.

Low posterior error correlations (|R2| < 0.2) between regions in the North-west (NW) of France (3, 4, and 5) and the rest of regions (Figure IV.12), indicates that the NW sector is correctly separated from the NE, SE

and SW sectors (Figure IV.12). This is mostly related to the presence of GIF and TRN stations, which are sensitive to emissions from regions 3, 4, and 5 (48 $GgCH_4$/month). We notice a relatively high error anti-correlation (~ -0.6) between regions 12 and 21, indicating that these two regions were not efficiently separated by the inversion. In the opposite, the high uncertainty reduction of region 3 (35%) confirms that this region is separated from the remaining NW regions (Figure IV.13). In the North-east (NE) sector, the low posterior error correlations (|R2| < 0.5) and the high uncertainty reduction (40% for regions 22 and 23) illustrate the efficient flux separation by the inversion. The good flux separation in the NE sector can be related to the localization of GIF, OPE, and SCH sites, nearly in the same latitude from west to east, allowing the separation of the optimized fluxes.

This analysis shows that the inversion was able to separate the emission fluxes between most regions since the absolute value of posterior error correlation does not exceed 0.3. The few limitations of the flux separation occur for some adjacent regions, such as regions 25 and 6 in January, where the posterior error correlation is 0.7, and the uncertainty reduction is less than 25%. Thus except these few limitations, the posterior error correlations indicate a relatively good separation of the sub-national flux budgets.

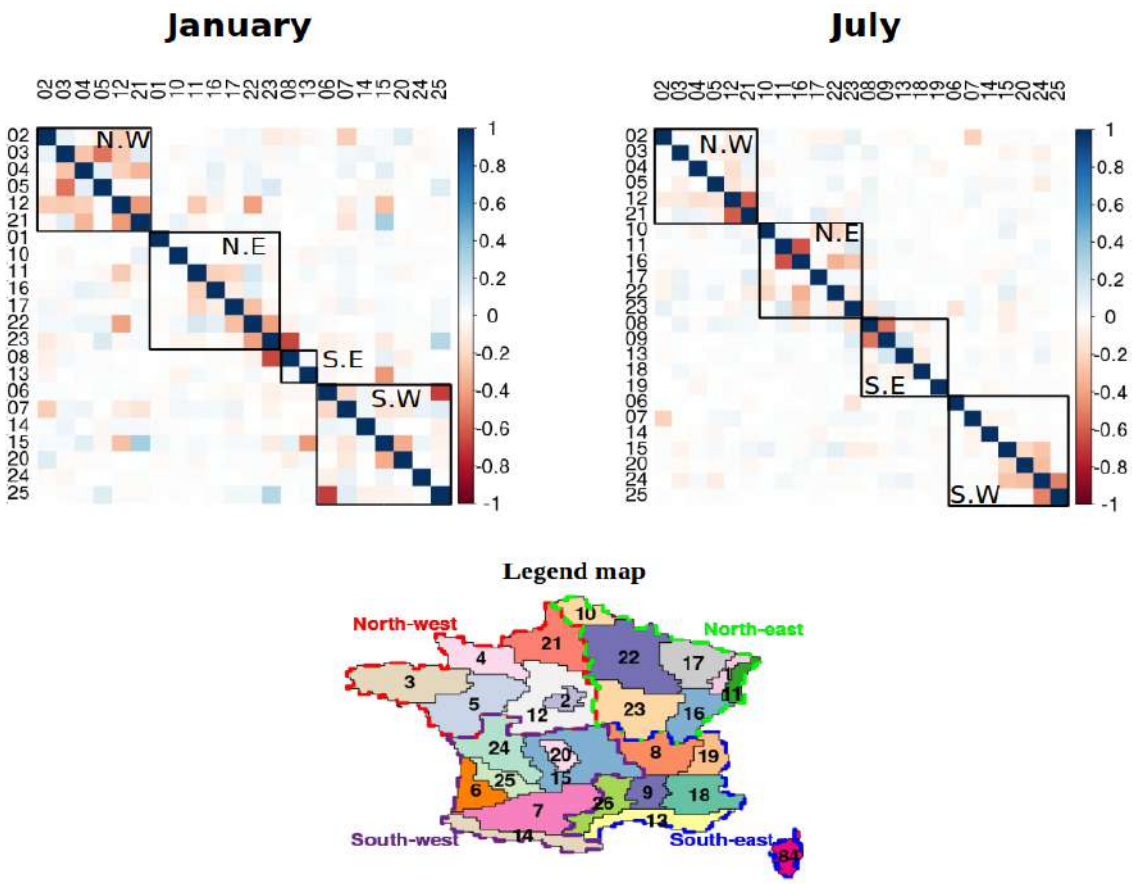

Figure IV.12: Representation of the posterior error correlation between the 22 constrained regions during January (left panel), and the 24 constrained region during July (right panel). Because of the problem of under-constrained regions (section IV.3.1.4), regions 9, 18, 19, and 26 in January, and regions 1 and 26 in July are not presented. The map in the bottom is displayed as a support for the region numbers. The regions are grouped into four sectors: North-west (NW), North-east (NE), South-east (SE), and South-west (SW) sectors, as shown in the legend map and the posterior error correlation matrices. One sector represents the aggregation of several regions close to each others.

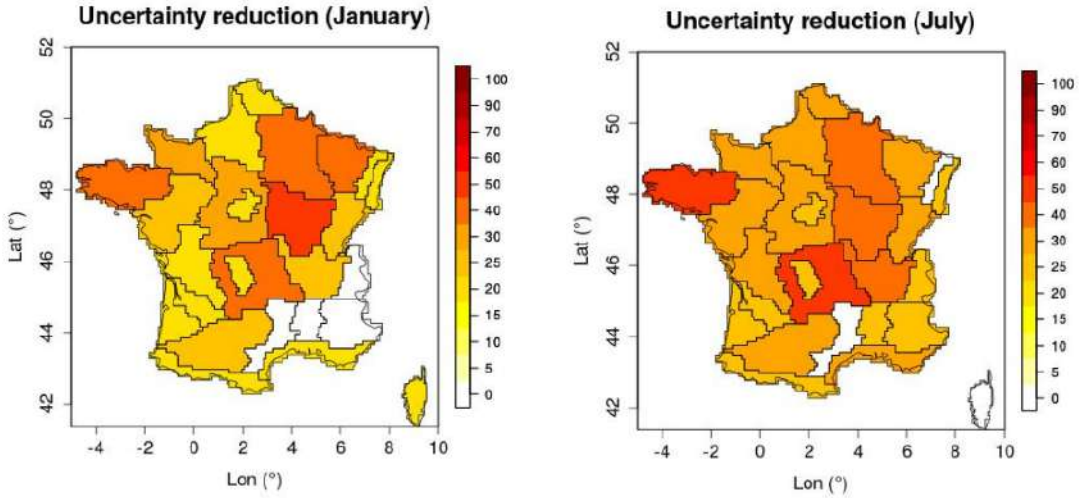

Figure IV.13: Spatial distribution of the monthly uncertainty reduction for the constrained regions for January (left) and July (right). The uncertainty reduction is presented percentage (%) according to the prior flux errors.

IV.3.1.6 The spatio-temporal scales resolved by the inversion

The determination of the spatio-temporal scales resolved by the inversion is performed using the posterior covariance matrix Pa. When posterior error correlations between control vector components are higher than a given threshold, these components will be merged in the same group. The given groups are thus formed by emission fluxes for different regions, and may also include information from initial and boundary conditions. In this section, the correlation threshold will be selected in order to make use of the possible information provided by the inversion excluding the interpretation of information that is correlated with the initial conditions and the boundary conditions.

As explained by Berchet et al (2014), the selection of the appropriate correlation threshold must avoid two issues. First, a high threshold may lead to the separation of all component which involves the risk of over-interpreting small scale results. Second, the small threshold leads to large groups that cover a wide area of the domain. A correlation threshold (R2) of 0.5 was chosen in previous studies that used the same ML algorithm at a continental scales in Siberia (Berchet et al 2013, and Berchet et al 2014), and at a national scale in France (Pison et al., 2018). This threshold was chosen empirically based on the analysis of Pa matrix. Before choosing the correlation threshold that we will use for our inversion, we tested several R2 values (from 0.1 to 0.9) in order to investigate the sensitivity of the inversion results to this threshold (Figures IV.14 and IV.15).

For each correlation threshold (from 0.1 to 0.9) in the X axis, Figure IV.14 presents in panels A (January) and D (July) the total number of groups that are independent from the initial conditions (IC) and boundary conditions (BC). Panels 14-B (January) and 14-E (July) present the number of groups composed by at least two regions without IC/BC. Panels C and F show for each correlation threshold the mean time difference of the groups (groups may include regions with different time intervals). The mean time difference of each threshold is defined as follows: first, we calculate the difference between the maximum time (day and hour) minus the minimum time of each group, then we compute the average of these differences in order to get an averaged time for each R2. In Figure IV.14 C-F, we notice that the mean time difference does not exceed 1.5 days, whatever the threshold is, meaning that the constituted groups contain mainly regions with adjacent time periods. Thus, the 6 hourly resolution seems near to the appropriate temporal resolution where the inversion is informative. This result indicates that the temporal resolution was not defined at a too coarse resolution, nor too fine since only regions that are close in time periods are correlated.

For January, a high correlation threshold (R2 = 0.7 Figure IV.14-B) leads to a large number of separable regions and an important number of separable groups without IC/BC (more than 400 groups out of a total of ~ 500). This choice constrains 21% of the monthly emission budget (Figure IV.15-B), but it may lead to the over-interpretation of small scales inversion results as shown in Figure IV.15-A (mean area coverage of ~ 25 000 km^2). A lower correlation threshold (R2 < 0.3) leads to a small number of separable groups (less than 80 groups without IC/BC) that cover a large part of the domain (more than 70 000 km^2), and constrains up to 10% of the total emission budget of France (Figures IV.15-B). For both January and July, we selected a threshold of 0.5, which gives a balance between the number of separable groups, the mean area covered by these groups, and a large fraction of the constrained national emissions. For example in Figure IV.14-B, the R2 of 0.5 corresponds to 100 groups of regions that are independent from initial conditions and boundary conditions. These groups cover an area of ~ 44 000 km^2, and sum up to 18% of the monthly emissions for January. The chosen correlation threshold was used to reconstruct the national optimized fluxes at the monthly scale presented in the following section.

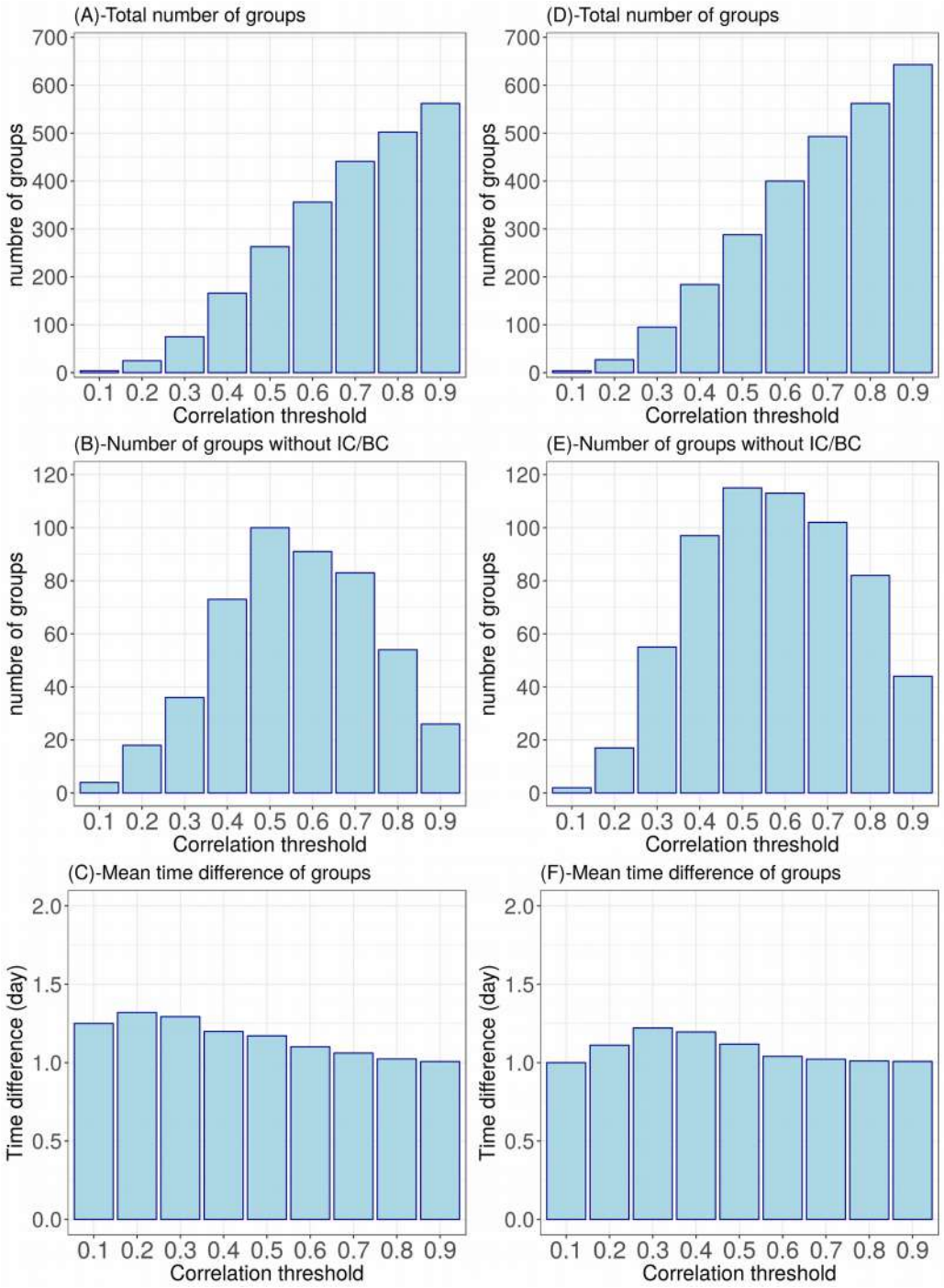

Figure IV.14: Panels A (January) and D (July) stand for the monthly total number of groups (y-axis) of the control vector components independent from initial conditions (IC) and boundary conditions (BC) for different correlation threshold (the groups may also be formed by only one components). B (January) and E (July) represent the monthly number of groups formed by at least 2 component of the control vector independent from IC/BC for several correlation thresholds. The larger the correlation threshold is, the larger total number of groups is (panels A and D), and the lower number of groups formed by at two components is (panels B and E), since small number of regions are correlated together (see section IV.3.1.4). The mean time difference between the component of the groups (in days) is presented for January (C) and July (F).

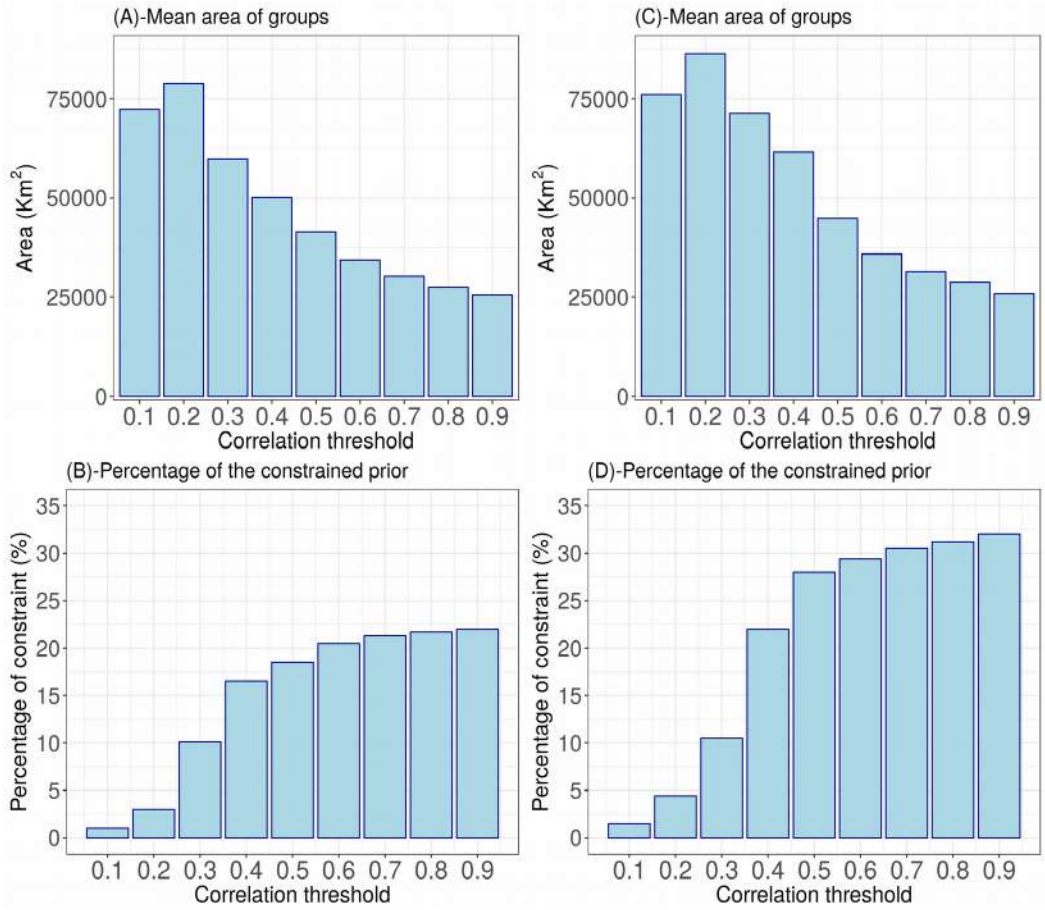

Figure IV.15: Panels A (January) and C (July) represent the monthly mean area (y-axis) covered by the groups for each correlation threshold (x-axis). The percentage of the national emissions constrained by the groups (independent from intitial conditions and boundary conditions) is presented for January (B) and July (D).

IV.3.1.7 Optimized fluxes

The optimized fluxes have been generated for separable groups using the threshold R2 = 0.5 (section IV.3.1.6). These groups are constituted by regions for different time periods of the month. However, due to the problem of under-constrained regions (see section IV.3.1.4), the groups may be formed with regions that do not cover the full domain (France), neither the full month. To provide monthly fluxes for all France, we use posterior emission for regions and periods constrained by the inversion (see section IV.3.1.4), and prior emission otherwise. Similar to monthly fluxes, the uncertainties of the optimized fluxes are calculated using the same combination of the prior and the posterior uncertainties, assuming that they are independent of each other.

The prior CH_4 emission in France is equal to 291±42 $GgCH_4$ for January and 277±51 $GgCH_4$ in July (Table IV.2). The inversion increases by 8% the emission from the prior in January (316±34 $GgCH_4$), and increase more significantly (39%) the July emission over France to reach 385±33 $GgCH_4$ (Table IV.2). A similar tendency was found by Pison et al., (2018) for the national CH_4 inversion during the year 2012 using a less dense measurement network. At the level of France, the inversion provides an uncertainty reduction of 20% for January and 35% for July. The increase of the uncertainty reduction for July compared to January may be associated to the higher number of observation sites (13 sites in January, and 15 sites in July), the higher prior uncertainty, and the higher percentage of constrained fluxes (Figure IV.15).

Block	January			July		
	Prior fluxes ($GgCH_4$)	Optimized fluxes ($GgCH_4$)	Uncertainty reduction (%)	Prior fluxes ($GgCH_4$)	Optimized fluxes ($GgCH_4$)	Uncertainty reduction (%)
North-west	125 ± 41	115 ± 33	18 %	118 ± 46	148 ± 30	34 %
North-east	64 ± 13	81 ± 9	30 %	61 ± 11	91 ± 7	37 %
South-east	42 ± 10	41 ± 8.5	15 %	40 ± 10	57 ± 7	33 %
South-west	60 ± 16	79 ± 12	25 %	58 ± 17	89 ± 11	36 %
Total France	291 ± 42	316 ± 34	20 %	277 ± 51	385 ± 33	35 %

Table IV.2: Inversion results of total prior and optimized fluxes over France, and over the four sectors: the North-west (NW), the North-east (NE), the South-east (SE), and the South-west (SW). The limits of these sectors can be found in the legend map Figure IV.16.

At the sub-national scale, some significant changes in monthly fluxes from the prior can be seen in Figure IV.16 (January) and Figure IV.17 (July). The inversion correct in the same direction most of the emission regions in January and July. In the Paris area (region 21) the inversion reduces the prior flux from 47±32 $GgCH_4$ to 44±27 $GgCH_4$ in January, and from 42±28 $GgCH_4$ to 29±19 $GgCH_4$ in July. In contrast, a significant increase in CH_4 emission can be seen for Brittany (region 3), and central France (region 15). This increase is associated with a significant uncertainty reduction > 30% (Figure IV.13). The performance of the inversion system for the regions 3 and 15 can be related to the high intensity of the emissions, which allow them to be seen by remote sites (PUY in region 15). As presented in section VI.3.1.3, the enhancement of the optimized fluxes in region 15 reduces the differences between the observed and the simulated concentrations at PUY by a factor of ~2 (Figures IV.8 and IV.9). Similar performance can be seen in region 12, where the uncertainty reduction exceeds 30% especially in July (region 12 is located close to TRN and GIF station). The significant uncertainty reduction occurs mainly for regions characterized by important emissions. For the

regions that are not constrained by the inversion at all, the uncertainty reduction is null by definition since the prior fluxes equal the optimized fluxes (e.g. regions 18, 19, 26, and 9 Figure IV.11).

To sum up, the inversion leads to higher emissions compared to the prior at the national scale. The regional analysis of the monthly fluxes shows that the North-west sector is the main CH_4 emission source in France with a total of 115±33 $GgCH_4$ in January and 148±30 $GgCH_4$ in July. Pison et al (2018) have shown that a large contribution of the CH_4 emissions in the NW sector comes from agriculture. The lowest CH_4 emissions in France is in the south-east sector with less than 60 $GgCH_4$ for both months. This study shows the impact of OHP station in January and ERS in July, which contribute to better constrain the south-east regions and consequently to increase the uncertainty reduction. Even if the actual spatial distribution of the observation sites in France provides significant uncertainty reduction at most of the regions, having more sites will likely contribute to increase the percentage of the constrained regions. The impact of the observation sites can be confirmed by the future atmospheric station ROC (Roc'h Trédudon) located in Brittany (west of region 3), which may contribute to control more efficiently North-west sector.

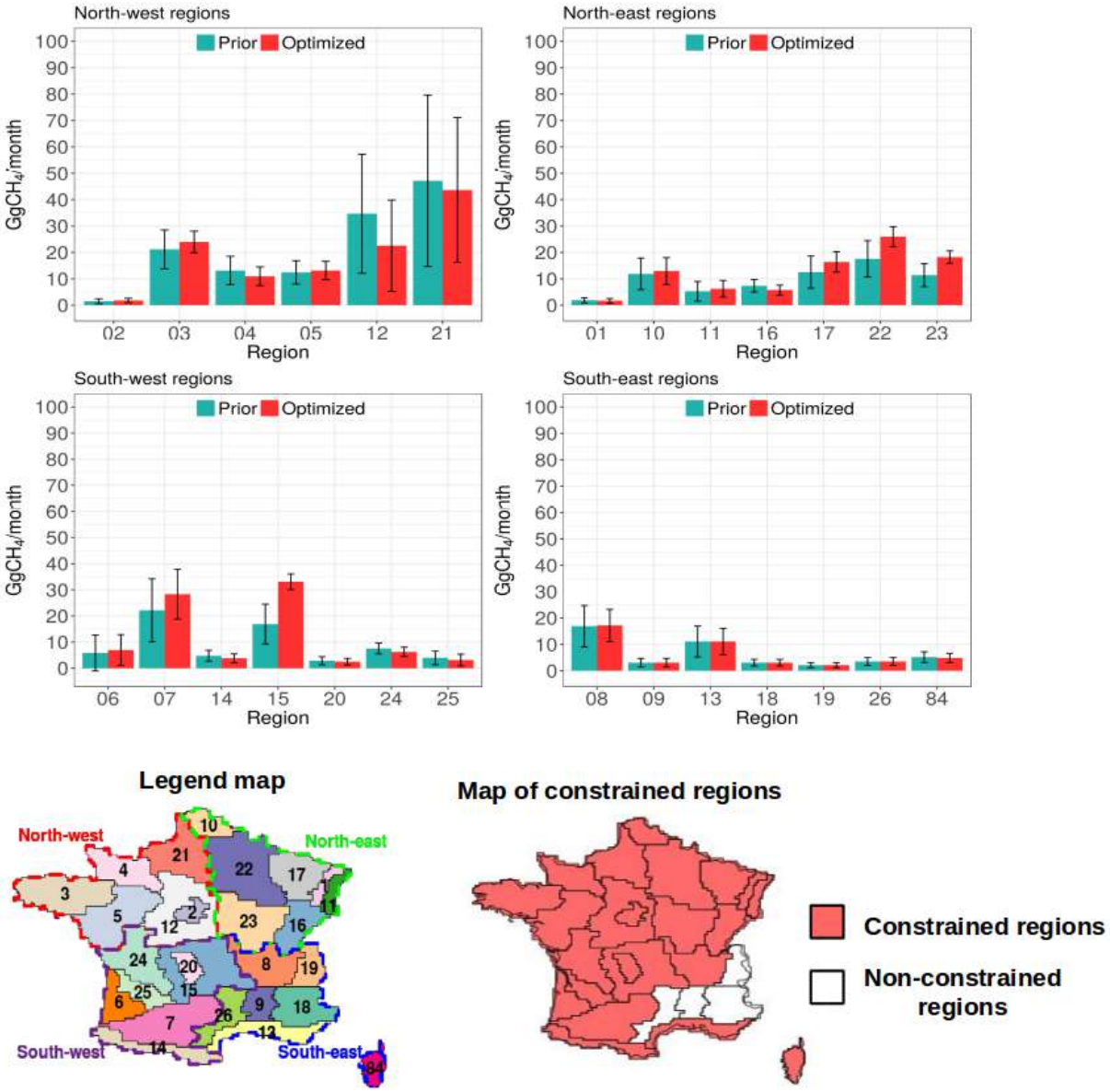

Figure IV.16: Total prior (blue) and optimized (red) CH_4 emissions over the 27 French regions during January. The uncertainty related to the prior and optimized emissions are represented by the error bar. The maps in the bottom can be used as a legend for the number of regions (left) and the constrained regions (right).

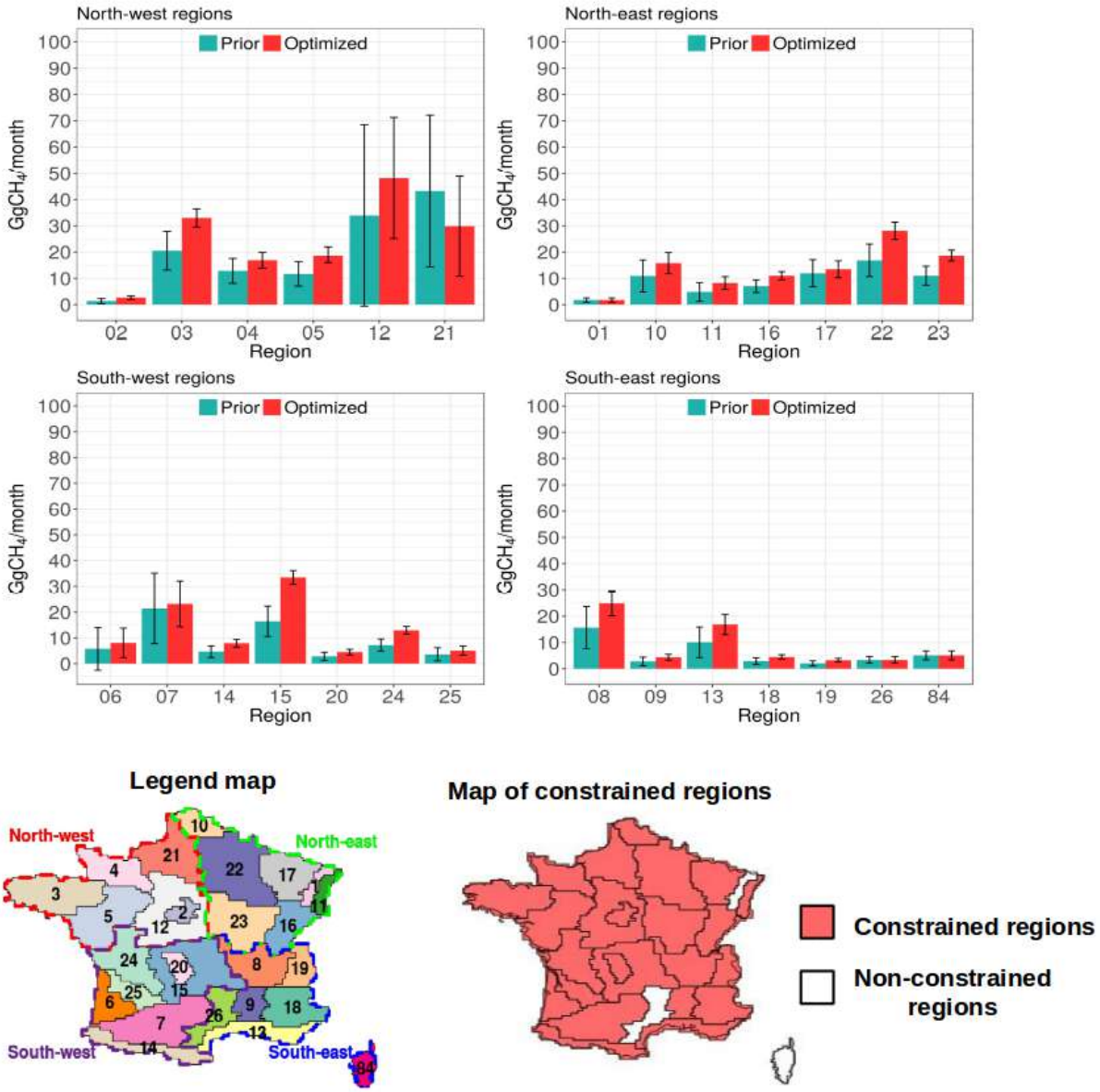

Figure IV.17: Total prior (blue) and optimized (red) CH_4 emissions over the 27 French regions during January. The uncertainty related to the prior and optimized emissions are represented by the error bar. The maps in the bottom can be used as a legend for the number of regions (left) and the constrained regions (right).

IV.3.2 Inversion of the CO_2 fluxes.

IV.3.2.1 Weight of the CO_2 atmospheric observations in the inversion.

Just like for the CH_4, we used the CO_2 measurements from 16 monitoring stations to estimate CO_2 fluxes with the inverse method in January and July 2014 (Figure IV.3). DEC station, where the CH_4 measurements were available for one day only provides continuous CO_2 measurements with 382 data from January 16 until the end of the month (Figure IV.19, Table SIV.2). For PDM and OHP, data were not available in January, and data from ERS are missing in July.

IV.3.2.1.1 Data selection

Similar to CH_4, we have selected the hourly averages of the CO_2 measurements during the mid-afternoon for low altitude sites, and the nighttime data for mountain stations (see section IV.2.4.2). This selection is illustrated by black data in Figure IV.18 for OPE and PUY, the remaining sites being presented in the appendix (Figures SIV.10, SIV.11, SIV.12, and SIV.13). Overall, the data selected for the inversion range from 17% to 25% for January, and from 18% to 27% for July (Table SIV.2). The variations of the percentage of measurement selected for the inversion are mainly controlled by the data gaps, as showed in Figures IV.18 and IV.19.

IV.3.2.1.2 The maximum likelihood (ML) data filtering

After this first data selection, the ML algorithm was applied to filter out the measurements that occur during short-term synoptic events which are difficult to reproduce by the transport model (see section IV.2.3.1). These data are illustrated by red color for OPE and PUY sites in Figure IV.18 (remaining sites are presented in the appendix Figures SIV.10, SIV.11, SIV.12, and SIV.13). The percentage of the data filtered by the ML algorithm vary between 1% and 3% for both January and July (Table SIV.2). Similar to CH_4, the lowest numbers of the filtered data occur at the mountain sites (Table SIV.2), confirming the low sensitivity of those sites to the surface fluxes.

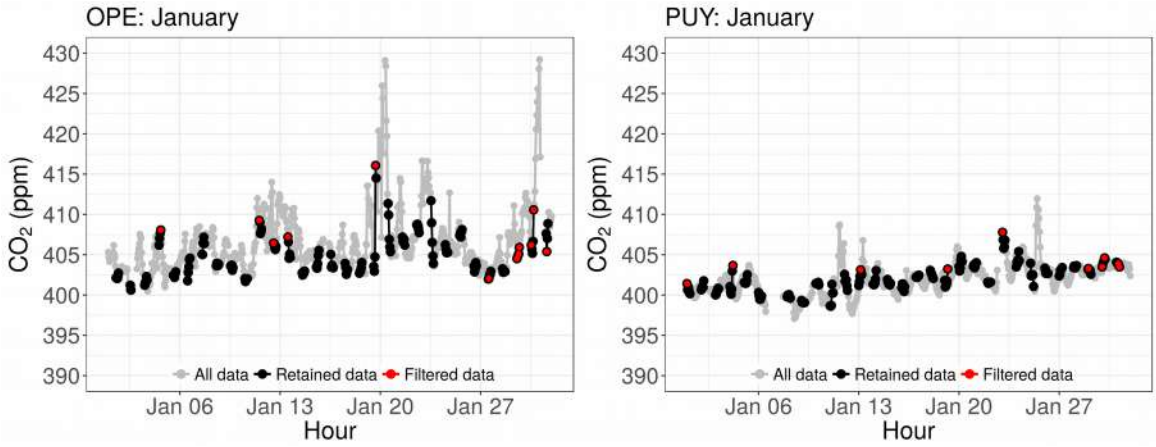

Figure IV.18: CO_2 hourly data at OPE (left) and PUY (right) during January. The grey color represents the available observations for each site during January. The back data point stands for the retained data during the mid-afternoon (data between 14:00 and 18:00) for low altitude sites (OPE), and the nighttime (data between 00:00 and 06:00) for mountain stations (PUY). The red data show the observations rejected by the ML algorithm (see section IV.2.3.1).

IV.3.2.1.2 Weight of the observations

Figure IV.19 shows the weights of the observations calculated as the sum of the diagonal elements of the sensitivity matrix HK (see section IV.3.1.1.1). This analysis shows a higher impact of the CO_2 observations (Figure IV.19) compared to CH_4 (Figure IV.5). The difference between CH_4 and CO_2 can be related to the combined contributions of positive fluxes (anthropogenic emissions and respiration) and negative fluxes (photosynthesis uptake). The amplitude of the two contributions varies according to hours of the day and seasons (section III.3.4.2). For example during the afternoon, fluxes are dominated by photosynthesis in July (section III.3.4.2). The contribution of the biogenic fluxes, being spatially uniform, influences more the observations compared to the anthropogenic emissions which are more locally distributed and generally far from the background measurement sites. This configuration may lead to under-constrain the anthropogenic fluxes. Thus the contribution of the biogenic and the anthropogenic emissions for total CO_2 fluxes may explain the increase of the weight of the observation compared to CH_4. In general, the inversion operates an equivalent between three and four averages per 6 hourly time window and may reach five averages in July.

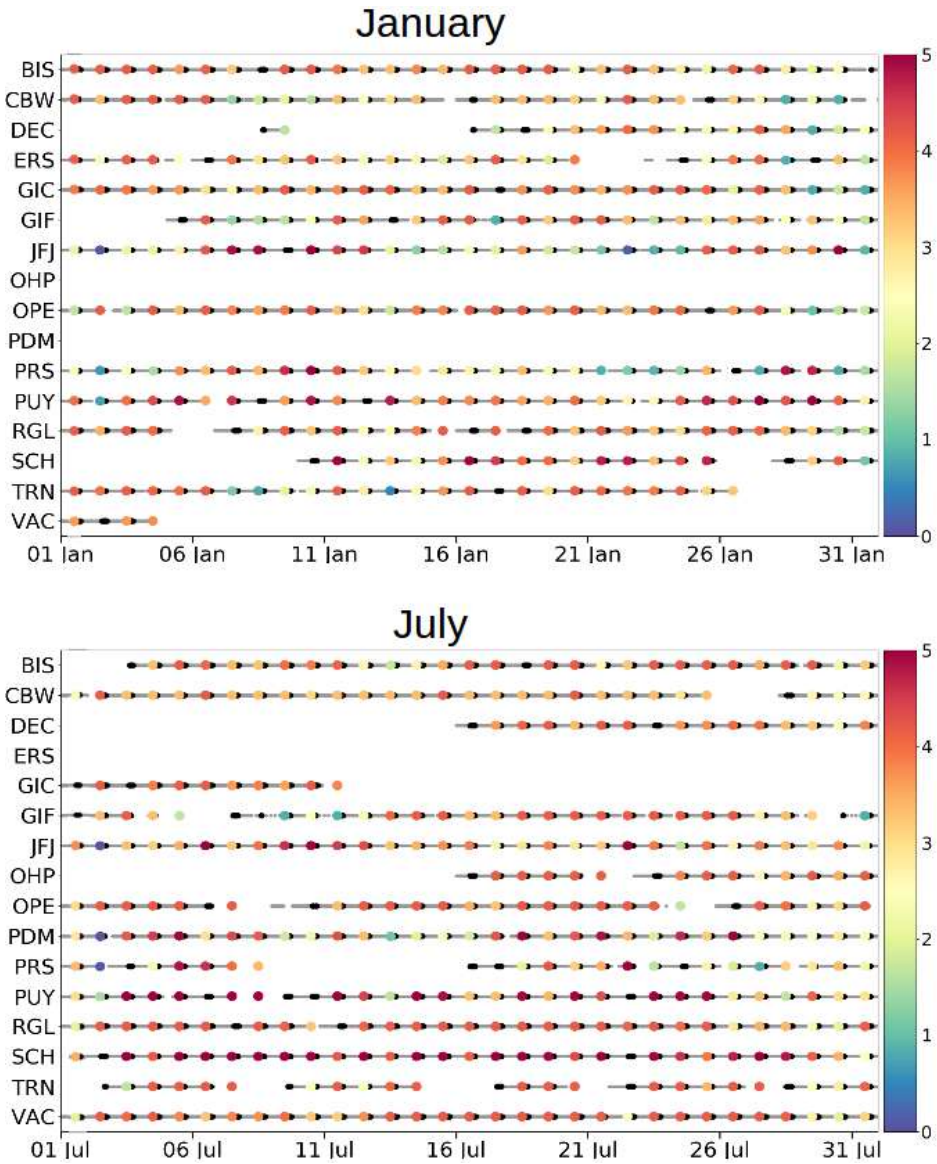

Figure IV.19: Representation of the availability of the CO_2 observed data and their contribution to the inversion for each site. The grey line represents the available data. Black dots stand for the retained measurements (data between 14:00 and 18:00 for low altitude sites, and data between 00:00 and 06:00 for mountain sites). The color points represent the amount of information used each day by the inversion system (value 1 indicate that the inversion uses the equivalent of one hourly data). These information are calculated from the diagonal terms of the sensitivity matrix HK

IV.3.2.2 Investigation of the observation and the prior flux errors

In this section, we compare the observation and prior flux errors estimated by the ML algorithm for CO_2 (section IV.2.3.1) with empirical estimates. Similar to CH_4 (section IV.3.1.2), The ML observation error (Figure IV.20) being the diagonal elements of the R matrix, is compared to an empirical estimate of the transport error given by the absolute difference of simulated CO_2 from two transport fields used in

CHIMERE (ECMWF minus AROME, section III.3.5). For the ML prior flux errors, they are separated between biogenic and the anthropogenic flux errors. For biogenic fluxes, we compared the ML error being the diagonal terms of B to the absolute difference of fluxes from two vegetation models (VPRM minus CTESSEL, section III.3.4.2). The ML prior flux errors for anthropogenic emissions are compared to the absolute difference between two emission maps (EDGAR minus IER, section III.3.4.1).

IV.3.2.2.1 Observation errors

Figure IV.20 shows smaller ML observation errors compared to the difference between the two transport fields, especially during July. Like for CH_4, the mean ML observation errors is smaller by a factor of 1.2 to 1.5 than the empirical estimation, and two times smaller at some specific mountain sites (e.g. SCH in January). This confirms the results found for CH_4 indicating that the transport errors seem to be more important than the representativeness and the aggregation errors at the used spatial resolution. The comparison between the two months shows an increase of the mean and the interquartile range (colored whiskers) of observation errors in July by a factor between 1.5 and 2 compared to January. Like for CH_4, this confirms the ability of the ML algorithm to reproduce accurately the higher observation errors in July compared to January.

One interesting point is that the ML algorithm generally allocates higher observation errors at mountain sites compared to low altitude stations, with higher errors in July (up to 3 ppm) than in January (Figure IV.20). This is probably related to the difficulty to reproduce accurately the orography, which influences the representation of the mesoscale driven flows at the mountain stations (section III.3.6).

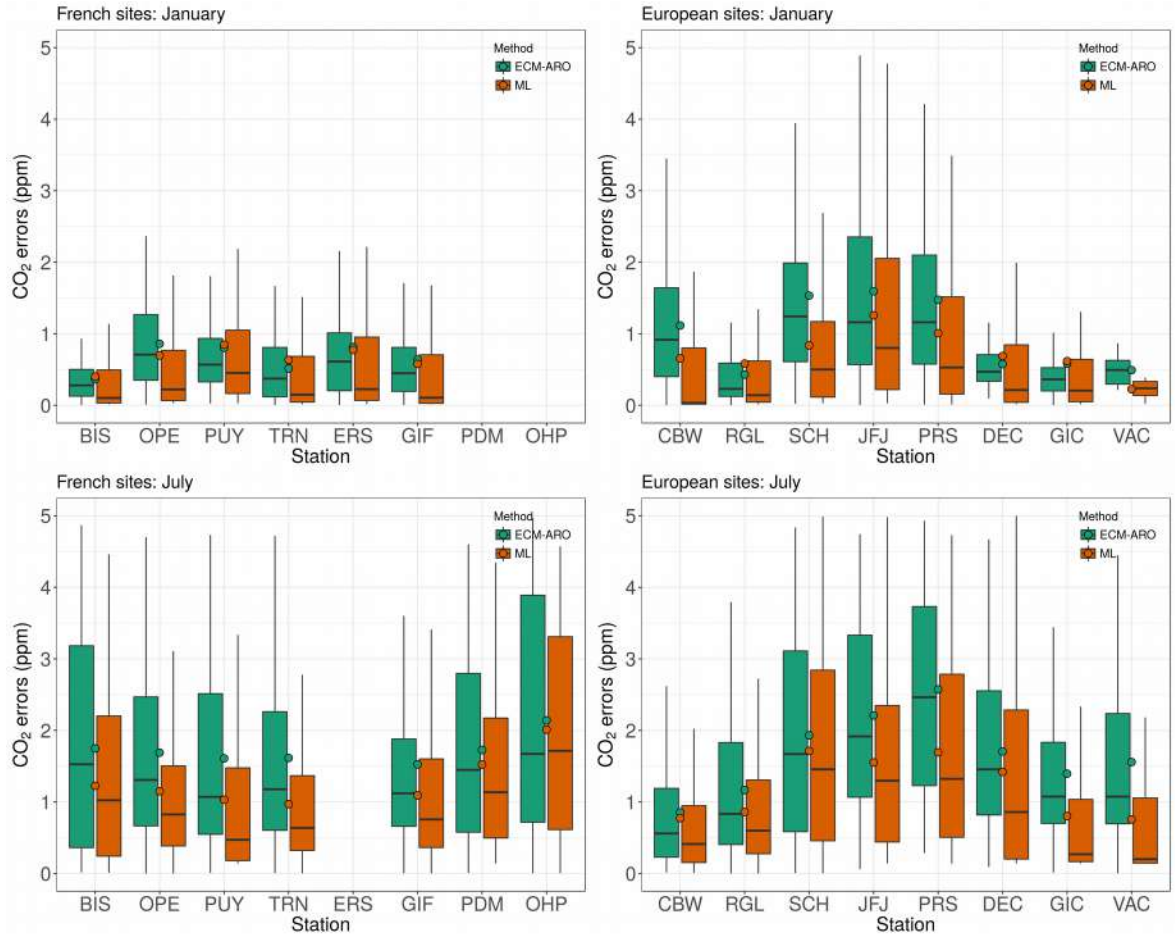

Figure IV.20: Comparison of the CO_2 observation errors calculated by the maximum of likelihood algorithm (ML, section IV.2.3.1) and the absolute difference of simulated concentration between the two transport models (ECMWF minus AROME). The errors are presented using whiskers for errors between the 25th and the 75th quantiles, the horizontal black line for the median, and the colored dots for the mean observation error.

IV.3.2.2.1 Prior flux errors

The spatial distribution of the ML prior flux errors is compared to the absolute difference between anthropogenic emissions maps in Figure IV.21, and between vegetation flux models in Figure IV.22. Similar to CH_4 (section IV.3.1.2), the flux errors are expressed in percentage of the flux budgets at the monthly scale per region. For both anthropogenic and biogenic prior flux errors, the ML algorithm estimates higher values than the difference between the emissions maps. Over France, the ML algorithm estimate prior flux errors exceeding 150%, whereas the empirical error estimation varies between 15% and 60% for anthropogenic fluxes (Figure IV.21), and between 10% and 120% for biogenic fluxes (Figure IV.22). The comparison of the ML prior errors between the two months shows relatively higher errors in January compared to July, especially for the anthropogenic emissions. The highest ML prior errors are found for the biogenic fluxes in

the south of France and Corsica region during July. Similar to CH_4, these high ML prior errors probably compensate the low observation errors estimated by the ML algorithm because the two matrices R and B are mutually dependent (section IV.2.3.1).

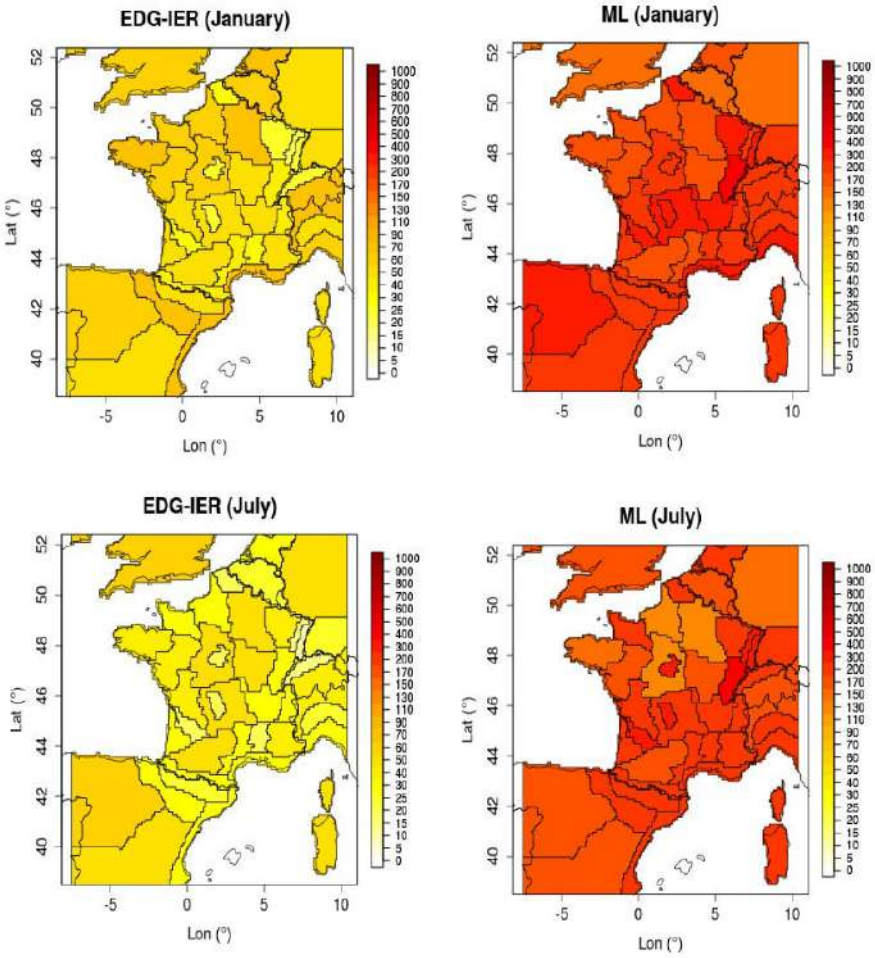

Figure IV.21: Comparison of the prior flux errors calculated by the maximum of likelihood algorithm (ML) and the absolute difference between the two anthropogenic maps (EDGAR minus IER). The errors are presented in percentage of flux budgets at the monthly scale per region forJanuary (top) and July (bottom).

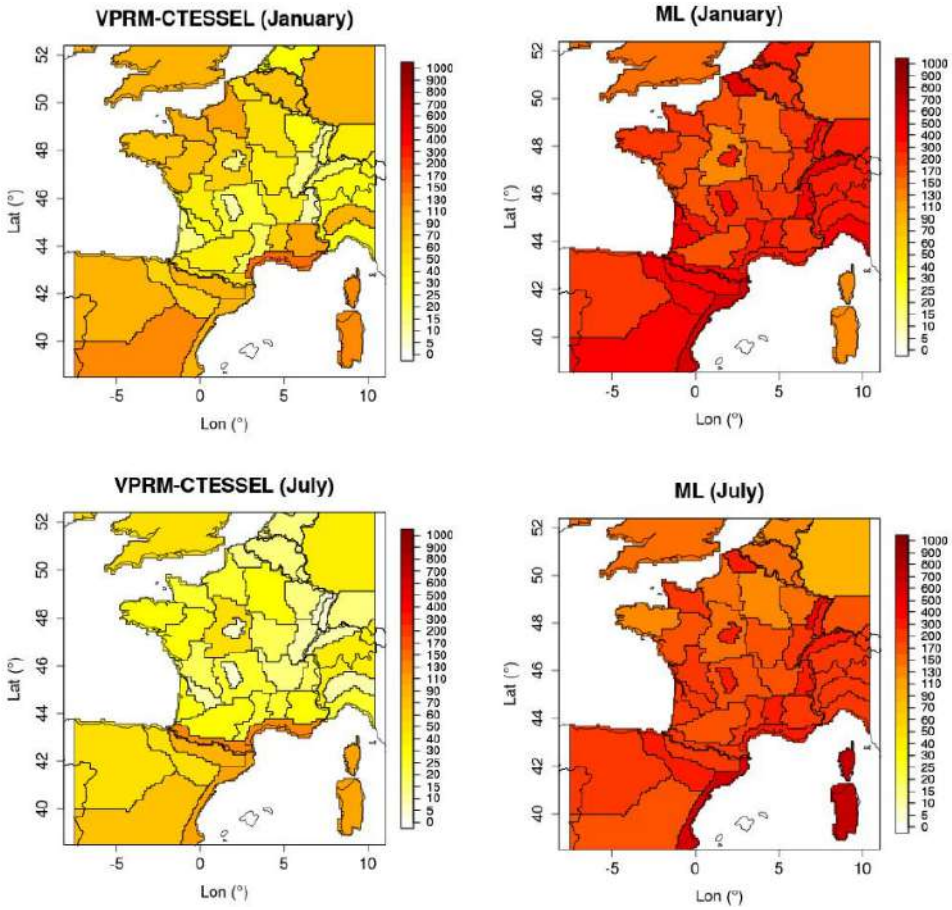

Figure IV.22: Comparison of the prior flux errors calculated by the maximum of likelihood algorithm (ML) and the absolute difference between the two anthropogenic maps (VPRM minus CTESSEL). The errors are presented in percentage of flux budgets at the monthly scale per region forJanuary (top) and July (bottom).

IV.3.2.3 Fit of posterior concentrations to observations

The fit of posterior CO_2 concentrations to observations is presented for atmospheric stations in France in Figure IV.23 (January) and Figure IV.24 (July). Figures for stations outside France can be found in the appendix (Figure SIV.14 and SIV.15). The inversion reduces significantly the distance between observed and modeled concentrations. After the inversion, the differences between the prior (blue) and the observation (black) are reduced by a factor of ~2 in January (Figure IV.23), and ~3.5 in July (Figure IV.24). For example at BIS, PUY, and GIF, the prior concentration was underestimated by 10 to 15 ppm between July 21 and 27. After the inversion, this bias is reduced by a factor of ~3 (Figure IV.24).

In both months, the inversion reduces uncertainties by a factor of 1.2 - 2. The largest uncertainty reduction occurs at low altitude sites, especially in January. For example, at BIS and OPE the reduction of the posterior concentration uncertainties reaches 30% (Figure IV.23). For mountain sites (e.g. PDM in Figure IV.24) the

error reduction is less than 20% due to the smaller sensitivity of mountain stations to surface fluxes. The posterior concentrations are generally within the range of the ML observation errors (±1σ). We observe higher concentration uncertainties in July compared to January, probably due to the more pronounced and spatially diffused biogenic fluxes in summer (section III.3.4.2).

Before the inversion, the R2 range from 0.6 to 0.8 for January and between 0.2 and 0.7 in July. After the inversion, the R2 exceed 0.9 for January and range from 0.6 to 0.9 in July. The highest R2 corrections occur at OPE in July, where the inversion increases the R2 from 0.2 to 0.88. The general enhancement of the R2 after the inversion is related to the improvement of the representation of the synoptic events phasing. Few exceptions occur at GIF during July where the atmospheric concentrations exhibit some sharp synoptic changes. Similar to CH_4, the difficulty to optimize the atmospheric concentrations at GIF is associated with the influence of the emission fluxes from the Paris region.

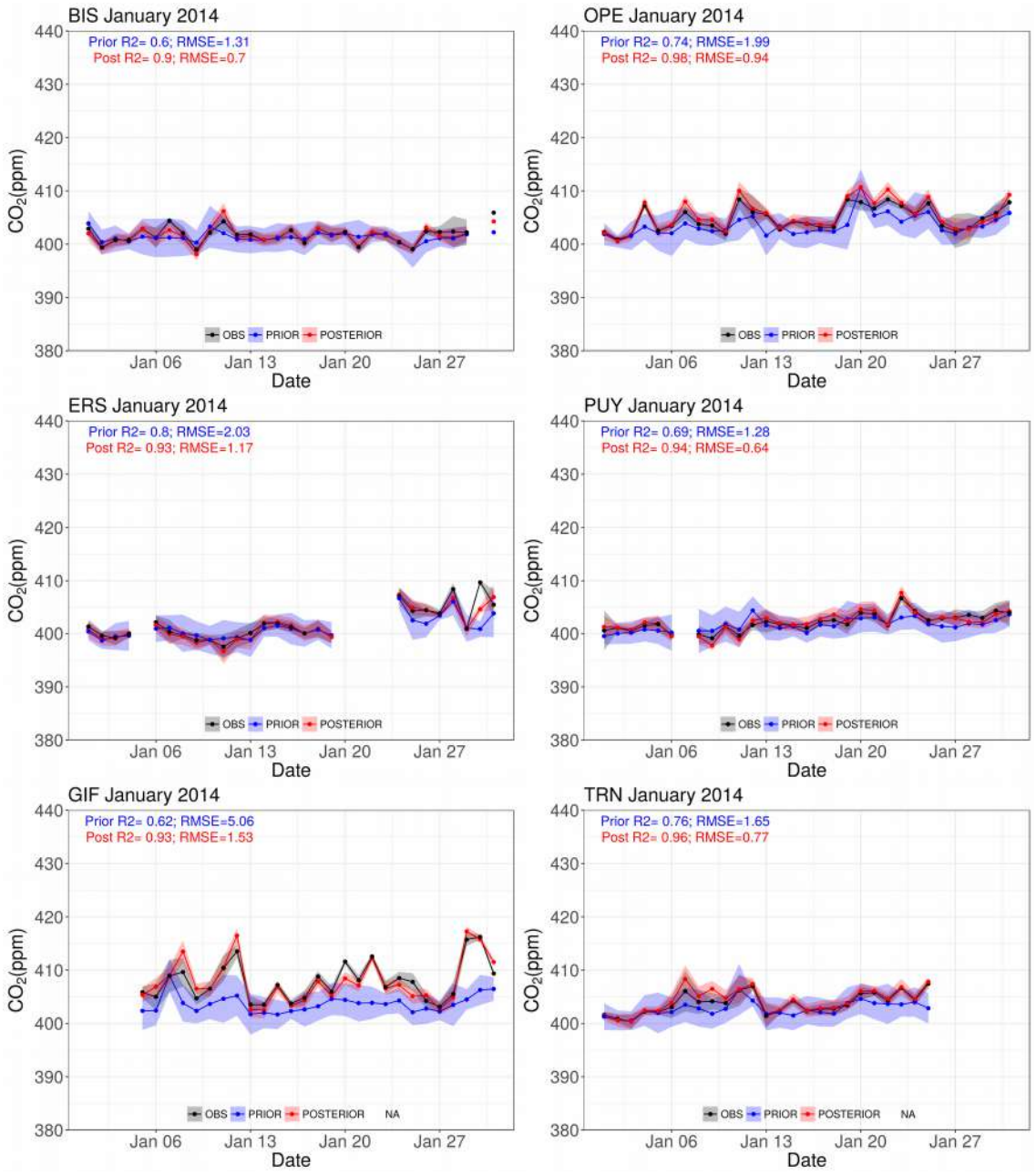

Figure IV.23: Observed (black) and simulated prior (blue) and posterior (red) CO_2 daily averages for theFrench atmospheric sites (BIS, GIF, OPE, PUY, TRN, and ERS) during January. The shaded areasrepresent the uncertainties of the observed (grey) and simulated prior (shaded blue) and posterior (shadedred) CO_2 concentrations. For each sites we calculate the root mean square error (RMSE) and thecoefficient of correlation (R2) for the prior and the posterior concentration.

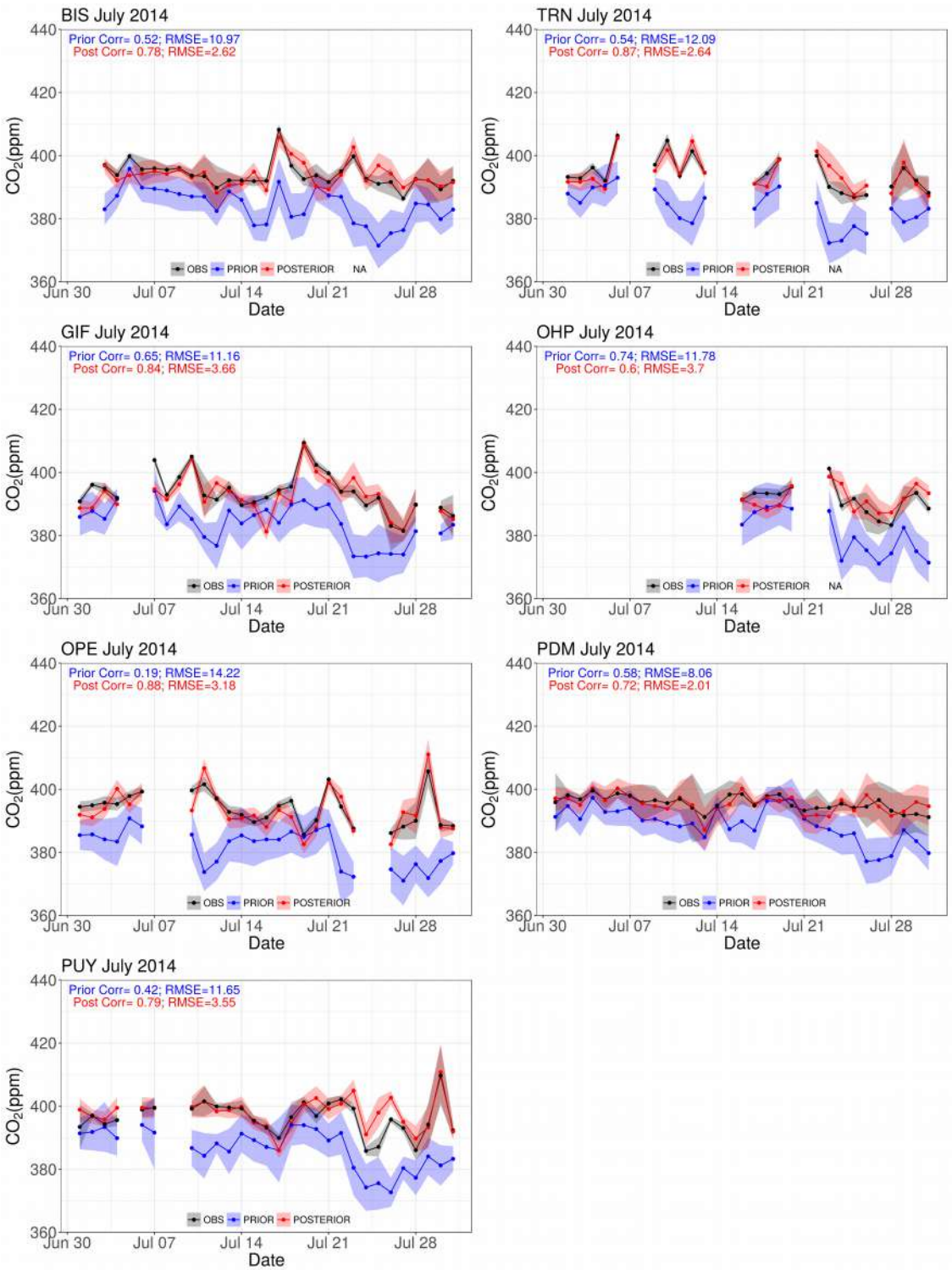

Figure IV.24: Observed (black) and simulated prior (blue) and posterior (red) CO_2 daily averages for theFrench atmospheric sites (BIS, GIF, OPE, PUY, TRN, OHP, and PDM) during July. The shaded areasrepresent the uncertainties of the observed (grey) and simulated prior (shaded blue) and posterior (shadedred) CO_2 concentrations. For each sites we calculate the root mean square error (RMSE) and thecoefficient of correlation (R2) for the prior and the posterior concentration.

IV.3.2.4 Flux regions constrained by the inversion

The regional constraints brought by the atmospheric measurements are analyzed for CO_2 separately for anthropogenic emissions (Figures IV.25 and IV.26), and biogenic fluxes (Figures IV.27 and IV.28). Similar to CH_4, each constraint distribution is calculated by the application of the influence matrix KH to the prior fluxes (see section IV.3.1.4). The strength of the constraints depends on the intensity of the fluxes and how well these fluxes are seen by the inversion given the location of stations and the transport fields.

In January, both anthropogenic and biogenic fluxes are better constrained in the west of France compared to the east (Figures IV.25 and IV.26). Similar to CH_4, the regions (18, 19, and 9) in the south-east of France are not constrained at this period due to the missing data of OHP station. In July (Figure IV.26) several anthropogenic emission regions in the west and the south of France were not constrained by the inversion system. On the other hand, the same regions are significantly constrained for the biogenic fluxes (Figure IV.28). Because of the localization of the atmospheric sites (GIF, TRN, and PUY) far from regions 3, 4, 5, 24, 25, 7, and 14, the inversion system could not extract the signal of the anthropogenic emissions from the total CO_2 signal. In July, the best-constrained anthropogenic emission regions are located close to atmospheric sites (regions 6, 15, 12, and 21). For biogenic fluxes, all regions are rather well constrained by the inversion, except region 84 (Corsica) due to the lack of ERS data in July (Figure IV.28).
Figures IV.25 to IV.28 also represent the monthly weight of the stations in the inversion system calculated by adding the diagonal elements of the sensitivity matrix HK (see section IV.3.1.1). In both months, the low altitude stations BIS, GIF, TRN, and OPE have larger weights, meaning that they contribute significantly to constrain CO_2 fluxes. In the opposite, low weights are found for mountain sites (PUY, JFJ, PRS, and PDM) being more decoupled to surface fluxes. The same result was found for CH_4 (section IV.3.1.4), confirming that mountain sites are less effective to constrain surface fluxes.

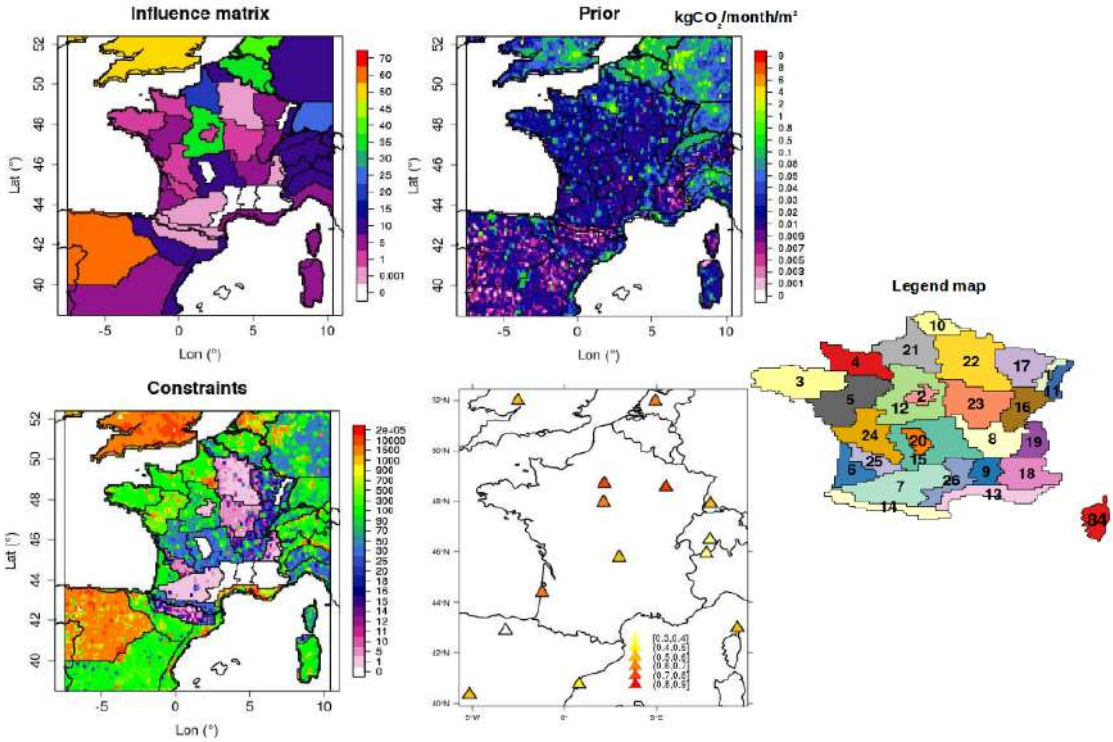

Figure IV.25: Spatial distribution of the influence matrices, prior fluxes, the constraint on regions, and the contribution ofthe stations for the inversion in January. The constraint map is generated by convolving the influence matrix KH(presented in the figure by % over the month) with the prior anthropogenic emissions. The contribution of the station in the inversion forJanuary is presented using the diagonal terms of the sensitivity matrix HK. The scales of the constraints maps and thecontribution of the station were chosen arbitrary, in respect with the range of the two maps. The map in the right(legend map) is presented as a support for number of regions.

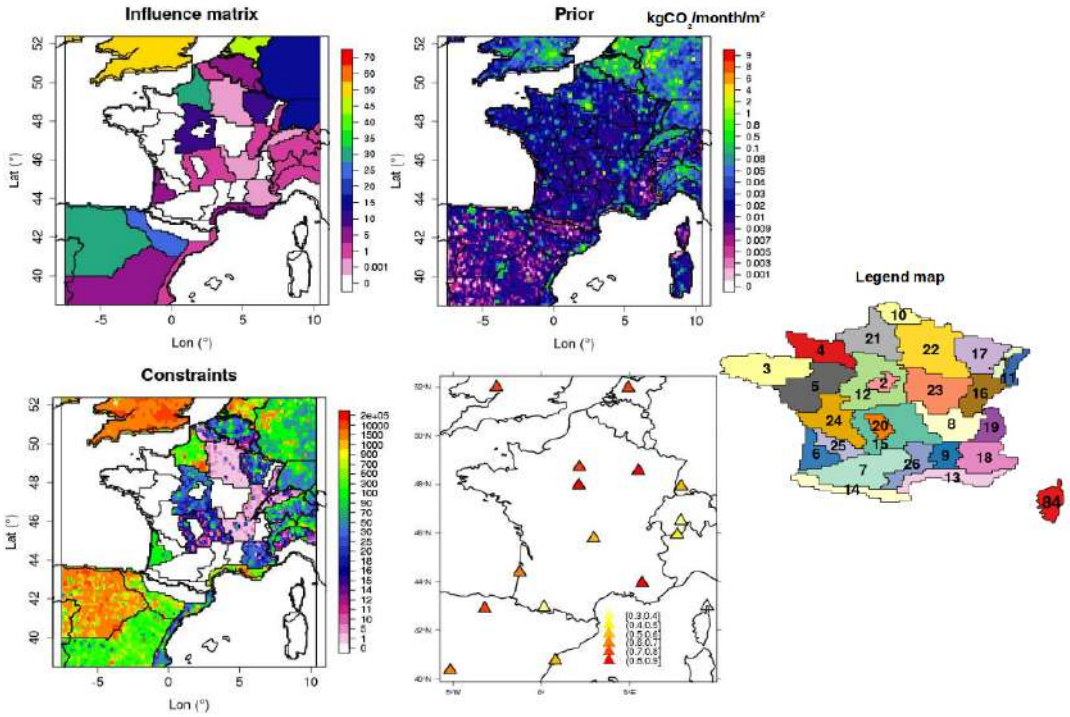

Figure IV.26: Same as figure 25 in July (anthropogenic fluxes).

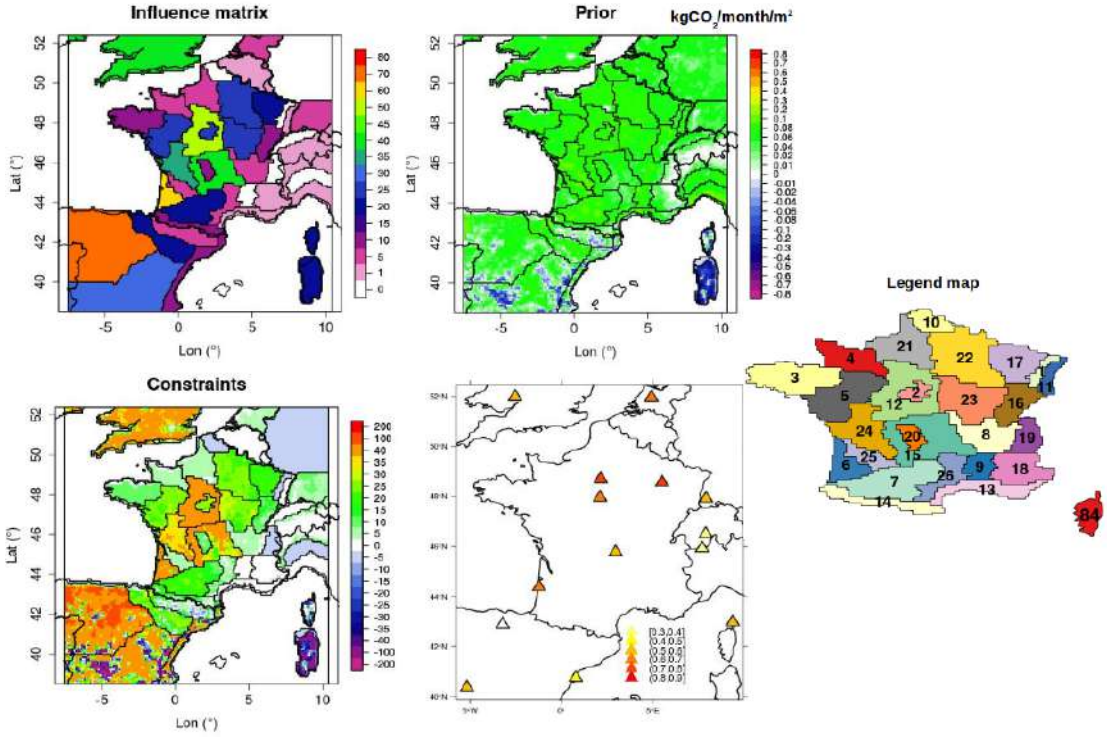

Figure IV.27: Same as figure 25 for biogenic fluxes.

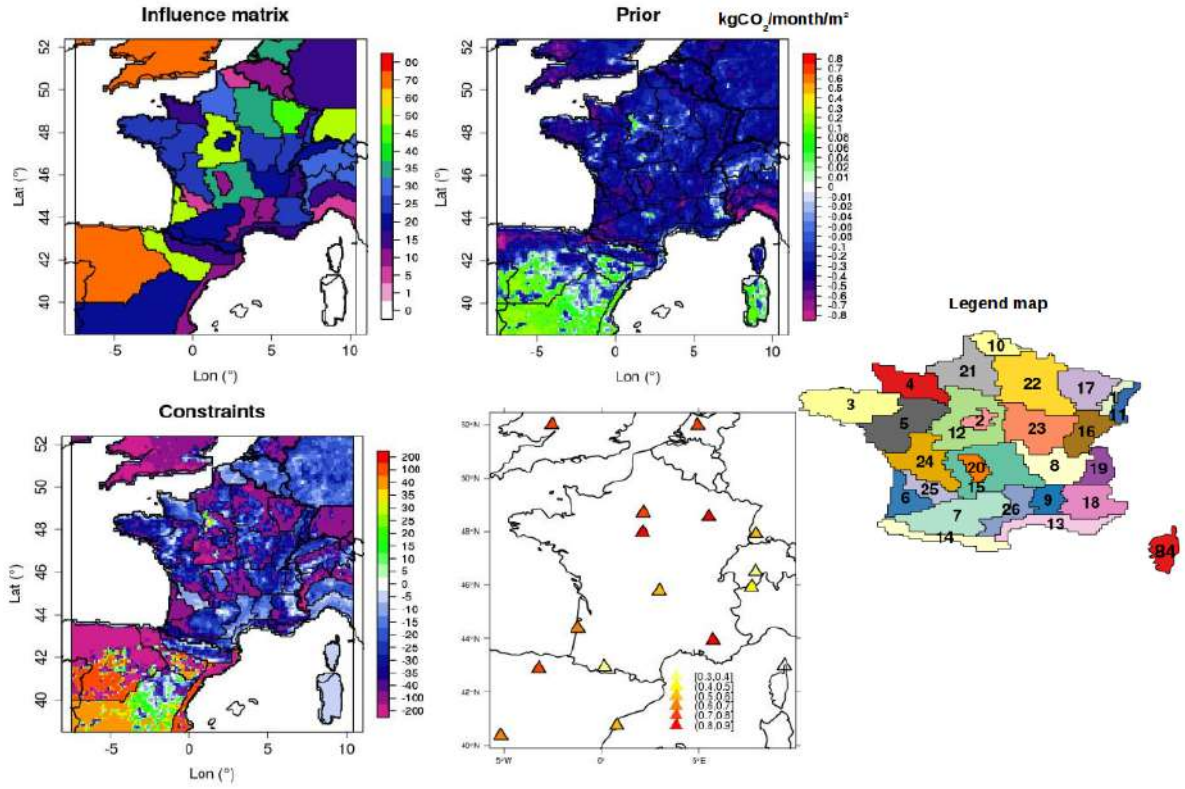

Figure IV.28: Same as figure 27 in July (biogenic fluxes).

IV.3.2.5 Spatial correlation of the anthropogenic and biogenic flux errors

The CO_2 observations from the atmospheric stations over France are regularly influenced by the anthropogenic emissions, but the variabilities in the concentrations are dominated by the influence of seasonal and diurnal variations of the biogenic fluxes. Thus separating the signals of the anthropogenic emissions from the biogenic fluxes in the inversion system is challenging. To evaluate the ability of the inversion to discriminate between the two contributions, we have calculated the posterior error correlation using the Pa matrix. As for CH_4, the separability between regions and/or fluxes (anthropogenic and biogenic fluxes) is illustrated by the posterior error correlations (Figure IV.29) and the uncertainty reduction (Figure IV.30) for January and July.

Figures IV.29-A and IV.29-E, show the posterior error correlation between the anthropogenic emissions in France (21 constrained regions in January and 12 constrained regions in July, see section IV.3.2.4). For the two months, low posterior error correlation (|R2| < 0.2) of anthropogenic emission can be seen between the different sectors (NW, NE, SE, and SW sectors). These low correlations are associated with moderate uncertainty reductions (Figure IV.30), indicating that emissions in those four sectors are separated by the inversion. In Figure IV.29-A and IV.29-E, we can notice that most of the regions that are located far from each other are also efficiently separated, with a posterior error correlation varying between -0.3 and 0.3. The separation between the regions for anthropogenic emission can be explained by the spatial distribution of the observation sites (BIS, PUY, GIF, TRN, and OPE) which control the emissions from the nearby regions. Moderate posterior error correlations occur between some adjacent regions, such as regions 4 and 5 in the NW sector (Figures IV.29-A). For these regions, the posterior error anti-correlation is ~-0.6, indicating the limited separation of the anthropogenic emissions.

For biogenic fluxes, the posterior error correlations are shown for all regions in July (Figure IV.29-H), and for the 22 constrained regions in January (Figure IV.29-D). The analysis of the posterior error correlation shows moderate correlations (|R2| ~0.5) between the North-west (NW) and the South-west (SW) sectors in January (Figure IV.29-D). Similar correlations occur also between the SW and SE sector in July (Figure IV.29-H). The later correlations are associated with an uncertainty reduction ranging between 20% and 30%, meaning a limited biogenic flux separation between the SE and the SW sectors in July. At the regional scale, relatively high posterior error correlations occur for the adjacent regions. For example between regions 6, 7, and 14, the

posterior error correlation exceeds 0.7 (Figure IV.29-H), and the uncertainty reduction remain less than 40%. Due to the westerly winds in July (Figure SIV.9), biogenic fluxes from the SW sectors will impact concentrations at a sampling site located more in the East (e.g. OHP), rather than the closer station of BIS. Similar to CH_4, this result confirms the problem of the flux separation for the regions located far away from the atmospheric sites.

The posterior error correlations between the anthropogenic and the biogenic fluxes are presented in Figures IV.29-B (January) and IV.29-F (July). The diagonal elements of each panel give the correlation between anthropogenic and biogenic fluxes for the same regions. The non-diagonal elements are the correlation between the anthropogenic and the biogenic fluxes for distinct regions. Note that due to the different number of constrained regions between the biogenic and the anthropogenic fluxes, the two matrices (28-B and 28-F) are not square. In general, the inversion separates efficiently anthropogenic and the biogenic fluxes for distinct regions ($|R2| < 0.3$). For the same regions (diagonal elements), the absolute value of the posterior error correlation varies between 0.3 and 0.5. This indicates that the inversion separates efficiently the biogenic and the anthropogenic fluxes for most regions. Few exceptions occur for example for regions 22 and 23 in January, where the |R2| reach 0.8. For these regions, the inversion does not correctly separate between anthropogenic and biogenic fluxes, since the corresponding uncertainty reduction remains below 25%.

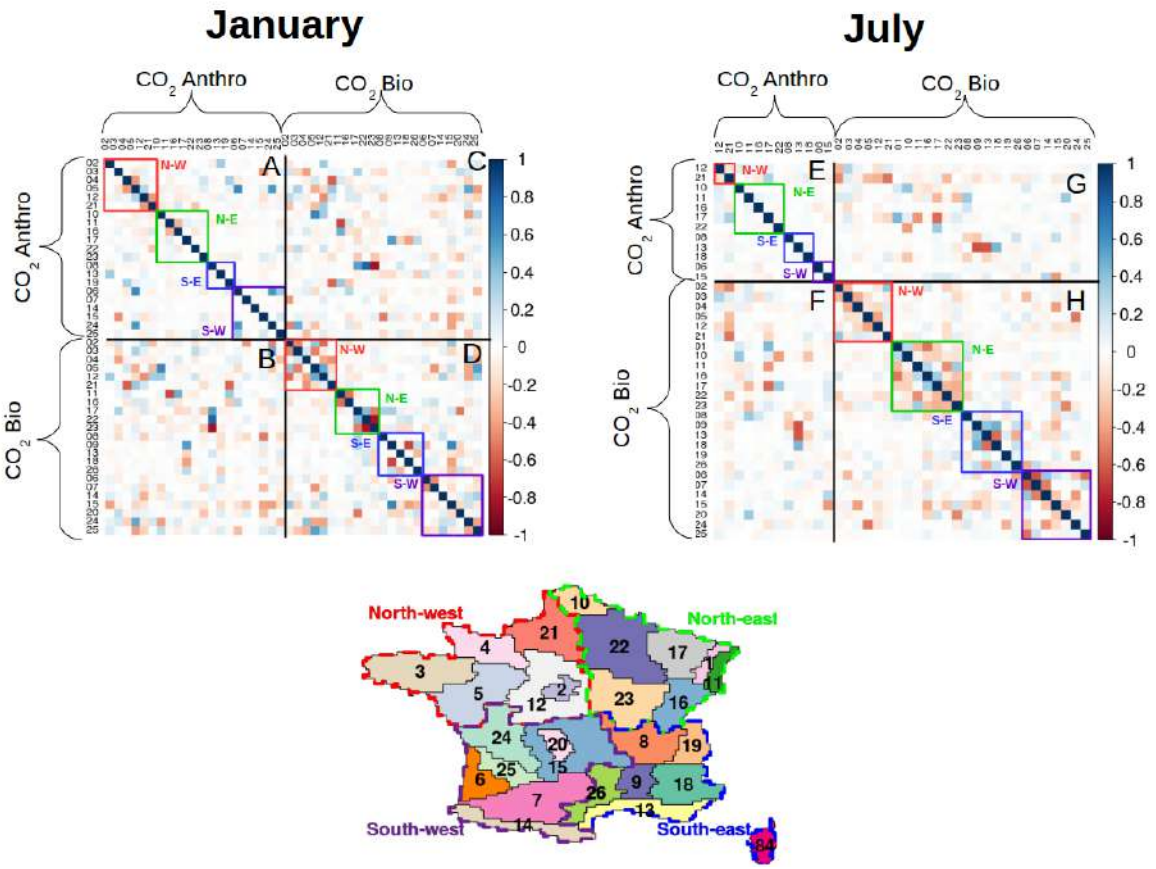

Figure IV.29: Panel A (January) and E (July) represent the posterior error correlation between the constrained anthropogenic emission regions in France (section IV.3.2.4). Panel D (January) and H (July) represent the posterior error correlation between the constrained biogenic flux regions in France (section IV.3.2.4). Panel B (January) and F (July) stand for posterior error correlation between the anthropogenic and the biogenic fluxes for the constrained regions in France. Note that panels C and G show the same information as B and F (the posterior error matrice is symetric). The map in the bottom is desplayed as a support for the region numbers. The regions are grouped into four sectors: North-west (NW), North-east (NE), South-east (SE), and South-west (SW) sectors, as shown in the legend map and the posterior error correlation matrices. One sector represents the aggregation of several regions close to each others.

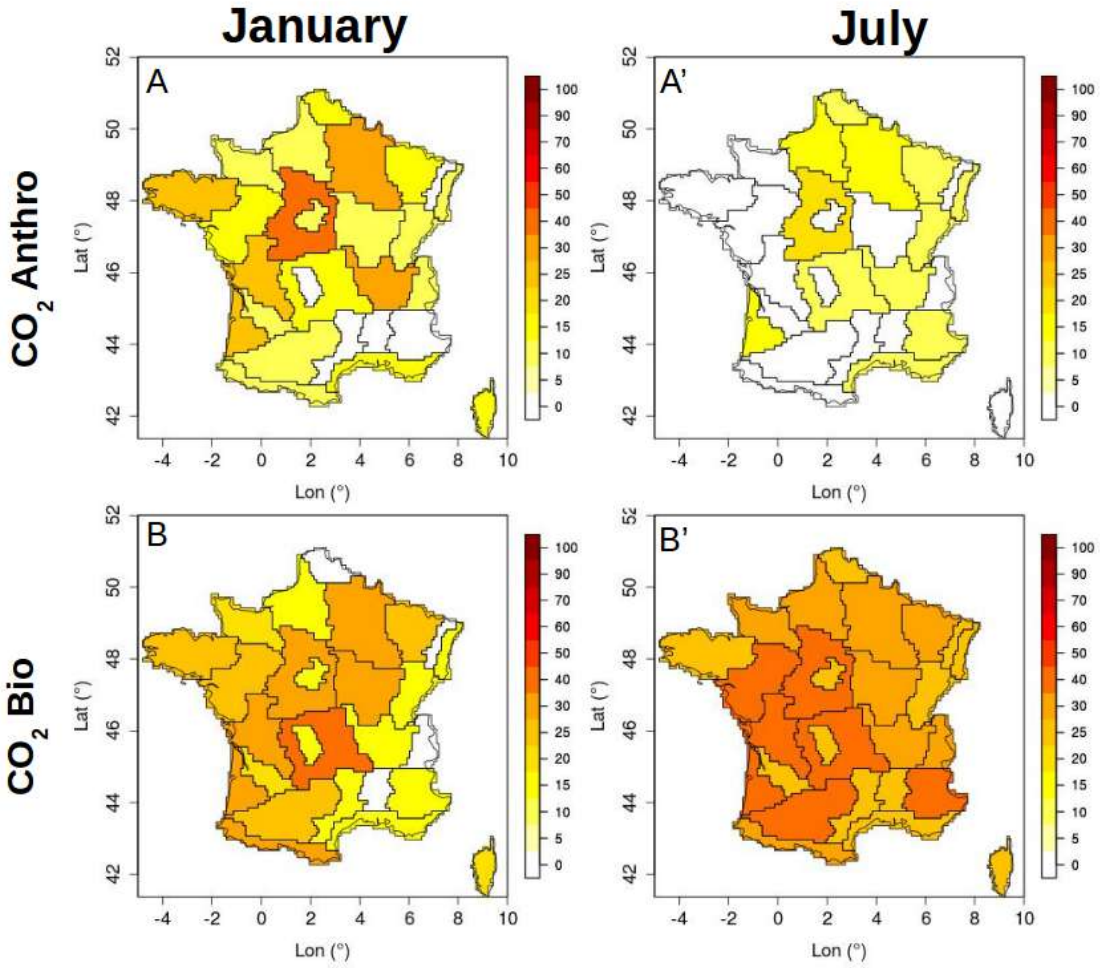

Figure IV.30: Spatial distribution of the monthly uncertainty reduction for the constrained anthropogenic emission (CO_2 anthro) and biogenic fluxes (CO_2 Bio) for January and July. The uncertainty reduction is presented in percentage (%) according to the prior flux errors.

IV.3.2.6 The spatio-temporal scales resolved by the inversion

As for CH_4 I have tested different correlation thresholds (0.1 to 0.99) of the posterior covariance matrix Pa in order to evaluate the spatial and the temporal scales resolved by the inversion (see section IV.3.1.6). Each component of the control vector represents the anthropogenic or the biogenic flux emitted by a region for a given day and during a specific time window (see section IV.2.4.1).

Figure IV.31 shows the number of groups, independent from initial conditions (IC) and boundary conditions (BC), calculated for different correlation thresholds for January (Figure IV.31-A) and July (Figure IV.31-C). The number of groups assembled by at least two control vector components and without IC/BC is shown in Figure IV.31-B for January and Figure IV.31-D for July. For each correlation threshold, we calculate the

mean time difference (see section IV.3.1.6), the percentage of the constrained prior, and the mean area covered by the formed groups for anthropogenic emissions (Figure IV.32) or biogenic fluxes (Figure IV.33). Similar to CH_4, the selection of the correlation threshold depends on information provided by the spatial coverage of the groups, the percentage of the constrained fluxes, and the temporal correlation of the regions.

The largest number of groups (more than 180) constituted by at least two regions and without IC/BC occur for R2 set to 0.8 (Figure IV.31). Lower correlation thresholds (e.g. R2 < 0.5) lead to less than 40 groups (Figure IV.31-B and 31-C), that cover a large area (area > 100 000 km), and constrain less than 7% of the total anthropogenic emissions and less than 18% of the total biogenic budget (Figures IV.32 and IV.33). Moreover, we notice that for these low correlation thresholds (R2 < 0.5), the groups mean time difference may exceed 1 week (Figures IV.32-A and IV.33-A). This result indicates that the low thresholds provide groups with distant time periods for both the anthropogenic and the biogenic fluxes (only a small number of regions with adjacent time periods are grouped). For this reason, we avoid the selection of correlation thresholds lower than 0.5.

For the high thresholds, the inversion constrains higher percentages of the national budget. As can be seen in Figure IV.32, For R2 > 0.7 the inversion constrains more than 10% of the anthropogenic monthly emissions in January and more than 7% for July. For the biogenic fluxes, the same thresholds constrain more than 15% of the biogenic flux budget in January, and up to 40% for July (Figure IV.33). The difference in the percentage of the constrained national budget depends on the number of the constrained regions (see section IV.3.2.4).

For CO_2 (both anthropogenic and biogenic emissions), we selected a correlation threshold of 0.8, which takes into consideration: the highest number of groups composed by at least to regions without IC/BC; a low temporal correlation between regions (up to 1.7 days); a high percentage of the constrained anthropogenic and biogenic total fluxes; and a small mean area covered by the groups (between 20 000 km^2 and 50 000 km^2). This choice corresponds to 188 groups in January and 220 groups in July without IC/BC (Figure IV.31). Selecting R2 of 0.8 will allow us to interpret the inversion results that constrain 13% of the total anthropogenic emissions in January and 8% in July, and 20% of the national biogenic budget in January and 41% in July.

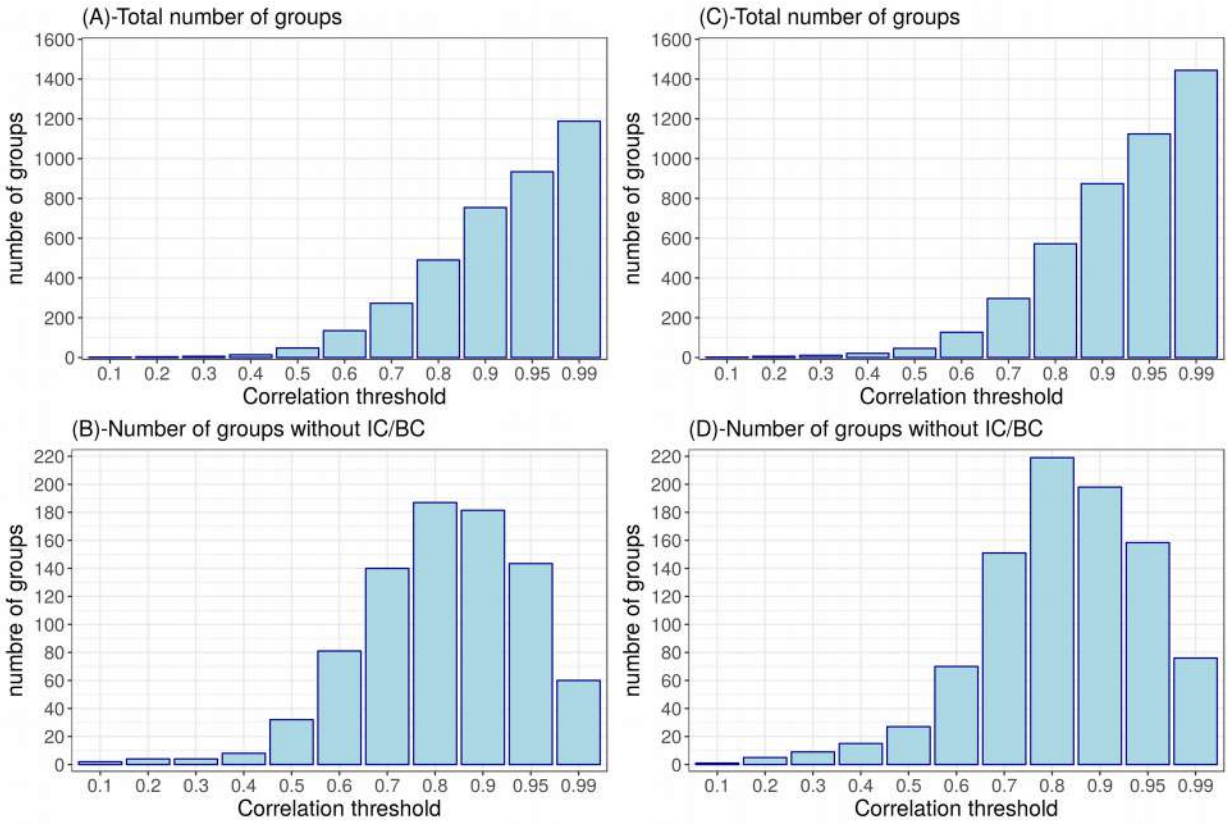

Figure IV.31: Panels A (January) and C (July) stand for the monthly total number of groups (y-axis) of the control vector components independent from initial conditions (IC) and boundary conditions (BC) for different correlation thresholds (the groups may also be formed by only one component). B (January) and D (July) represent the monthly number of groups formed by at least two components of the control vector independent from IC/BC for several correlation thresholds. The larger the correlation threshold is, the larger total number of groups is (panels A and C), and the lower number of groups formed by at two components is (panels B and D), since small number of regions are correlated together (see section IV.3.2.5).

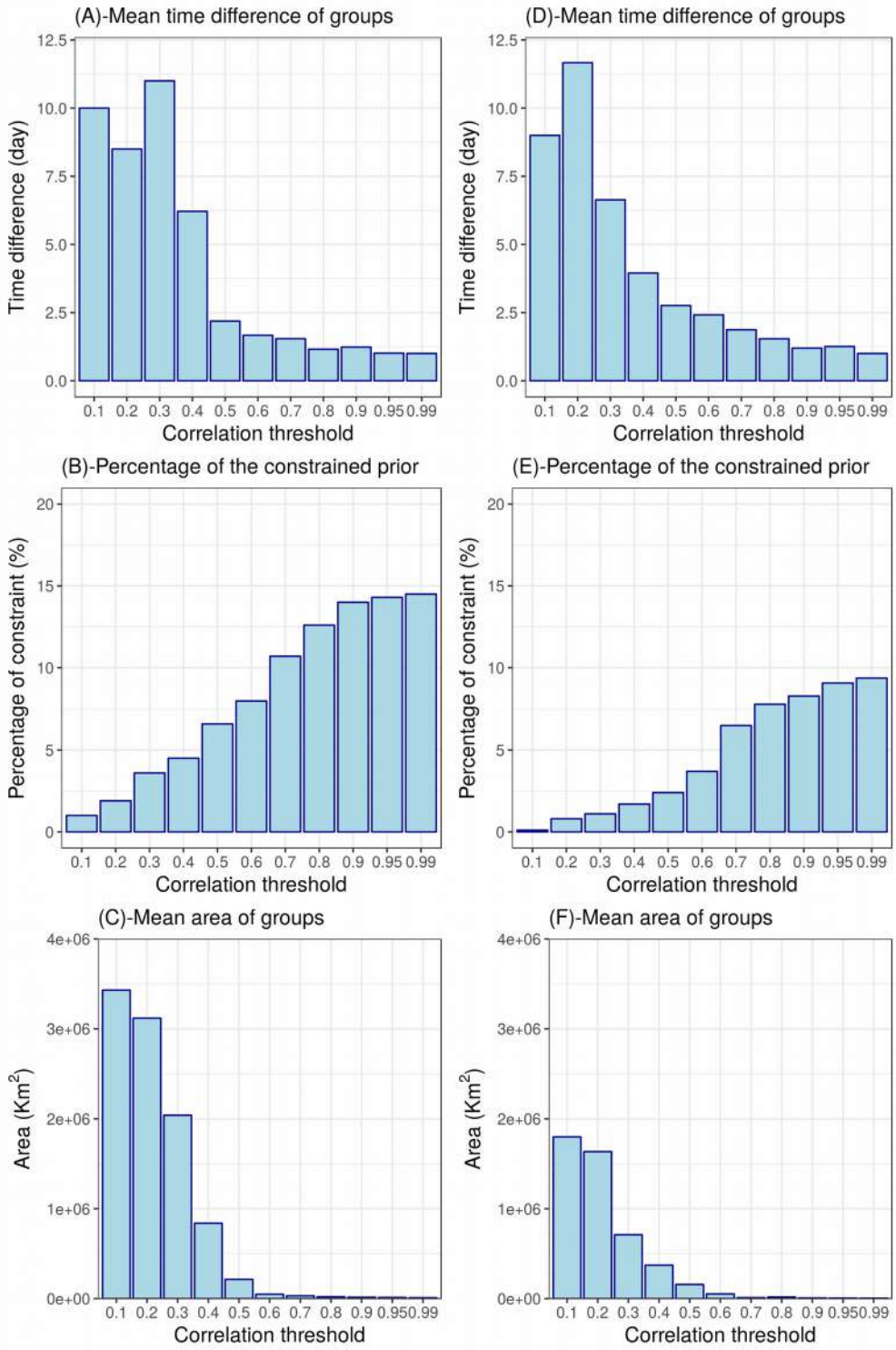

Figure IV.32: Panels A (January) and D (July) represent the monthly mean time difference (in days) calculated between the component of the groups for the anthropogenic emissions. Panels B (January) and E (July) stand for the percentage of the anthropogenic emissions constrained by the groups formed independently from initial conditions (IC) and boundary condition (BC). Panels C (January) and F (July) display the monthly mean area covered by the groups without IC/BC for the anthropogenic emissions.

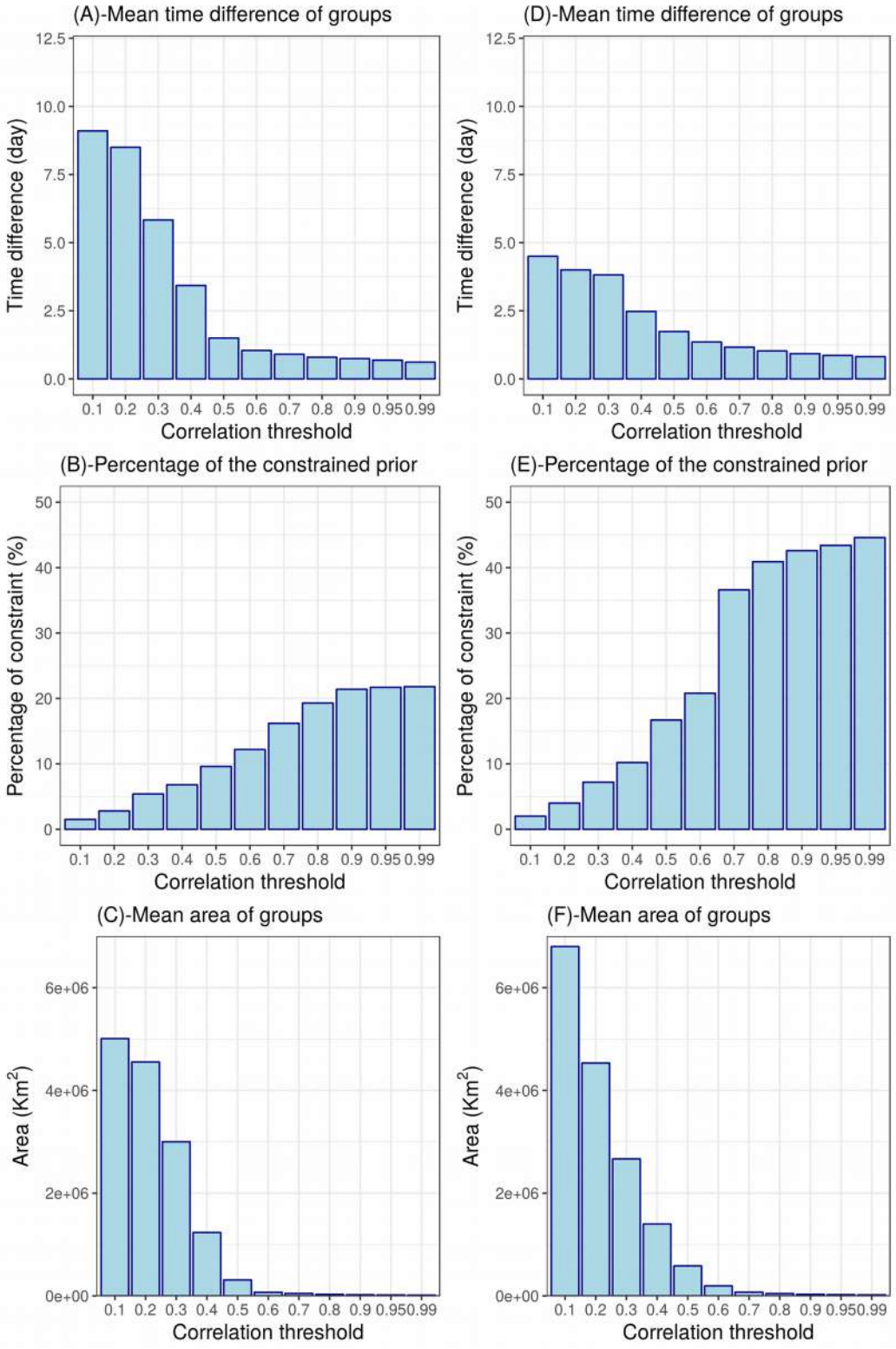

Figure IV.33: Same as figure 32 for the biogenic fluxes.

IV.3.2.7 Optimized fluxes

In this section, we present the optimized anthropogenic and biogenic fluxes using groups constituted by the correlation threshold 0.8 (see section IV.3.2.6). Figures IV.34, IV.35, and table IV.3 represent the inversion results of the anthropogenic emissions for January and July respectively. The inversion results of the optimized biogenic fluxes are displayed in Figures IV.36, IV.37, and table IV.4.

IV.3.2.7.1 Optimized anthropogenic emissions

Over France, prior anthropogenic fluxes from EDGAR inventory equals 29±20 $MtCO_2$ for January and 25±14 $MtCO_2$ for July (Table IV.3). The atmospheric inversion increases by 19% the anthropogenic emissions in January (34±17 $MtCO_2$), and do not change significantly the July emission (Table IV.3). At the national scale, the inversion reduces the anthropogenic emission uncertainties by 18% in January and only 11% for July. The lower uncertainty reduction for July is associated with the lower percentage of the constrained anthropogenic emissions (see section IV.3.2.6). The increase of the optimized emissions in January is mostly related to the substantial increase estimated in the north-east sector (+52%). For the remaining sectors (NW, SE, SW) small increase of the anthropogenic fluxes occurs after the inversion. In July, small changes in the anthropogenic emissions occur for all sectors.

Block	January			July		
	Prior fluxes ($MtCO_2$)	Optimized fluxes ($MtCO_2$)	Uncertainty reduction (%)	Prior fluxes ($MtCO_2$)	Optimized fluxes ($MtCO_2$)	Uncertainty reduction (%)
North-west	9.3 ± 11	9.5 ± 9	16 %	7.7 ± 7	6.6 ± 6.1	13 %
North-east	9.2 ± 15	14 ± 13	13 %	7.5 ± 10.6	6.9 ± 9.3	12 %
South-east	4.5 ± 8.7	4.6 ± 7.2	17 %	4.3 ± 6.3	4.1 ± 5.7	9 %
South-west	5.8 ± 12	6.1 ± 9.2	23 %	5.5 ± 7.5	5.6 ± 6.7	10 %
Total France	28.8 ± 20	34.2 ± 17	18 %	25 ± 13.9	23.3 ± 12.4	11 %

Table IV.3: Inversion results of total prior and optimized CO_2 anthropogenic fluxes over France, and over the four sectors: the North-west (NW), the North-east (NE), the South-east (SE), and the South-west (SW). The limits of these sectors can be found in the legend map Figure IV.34.

For the region 21 (Paris area), the highest CO_2 anthropogenic emission region, the inversion tends towards lower fluxes (~ 4.7 $MtCO_2$) compared to the prior for both January and July (Figures IV.34 and IV.35). Similar results were found in earlier studies showing a decrease of the anthropogenic fluxes in the Paris area

after the inversion (e.g. Bréon et al., 2015, and Staufer et al., 2016). These studies estimated a monthly total of ~4 $MtCO_2$ for the Paris region, with less than 1 $MtCO_2$ of difference compared to our results. This difference can be explained by the limits of the area used for the CO_2 inversions. Both Bréon et al (2015) and Staufer et al (2016) studies defined a region that contains only the city of Paris and its suburban area, which is significantly smaller compared to our area (region 21 in Figure IV.34). They were also using more atmospheric measurements from stations located close to Paris.

Since the optimized fluxes are calculated based on the posterior fluxes for the constrained regions and periods, completed with the prior for the non-constrained fluxes, the difference between the optimized fluxes and the prior are more important for the constrained regions (e.g. region 3, 21, 10, and 13). For the non-constrained regions, the prior and the optimized fluxes are similar (e.g. regions 1, 20, 26, 8, and 18 in January).

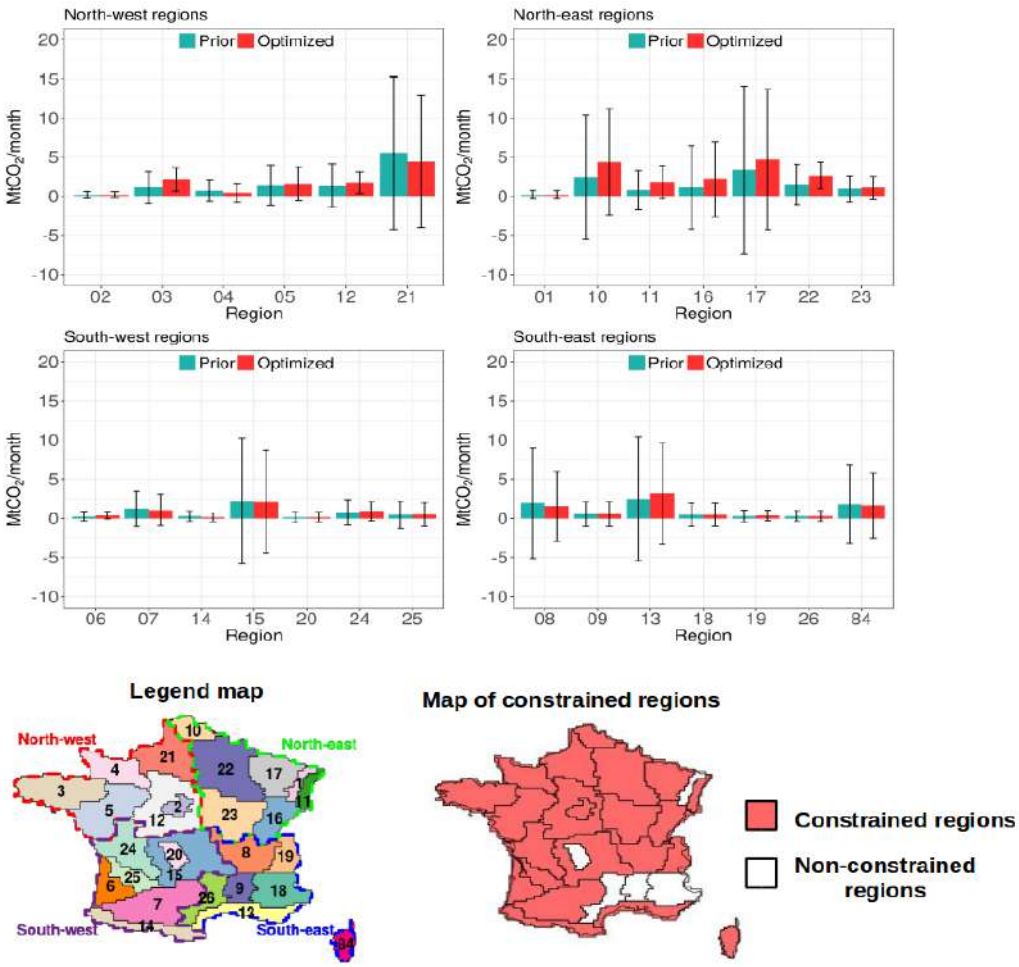

Figure IV.34: Total prior (blue) and optimized (red) anthropogenic CO_2 emissions over the 27 French regions during January. The uncertainty related to the prior and optimized emissions are represented by the error bar. The maps in the bottom show the number of regions (left) and the constrained regions (right).

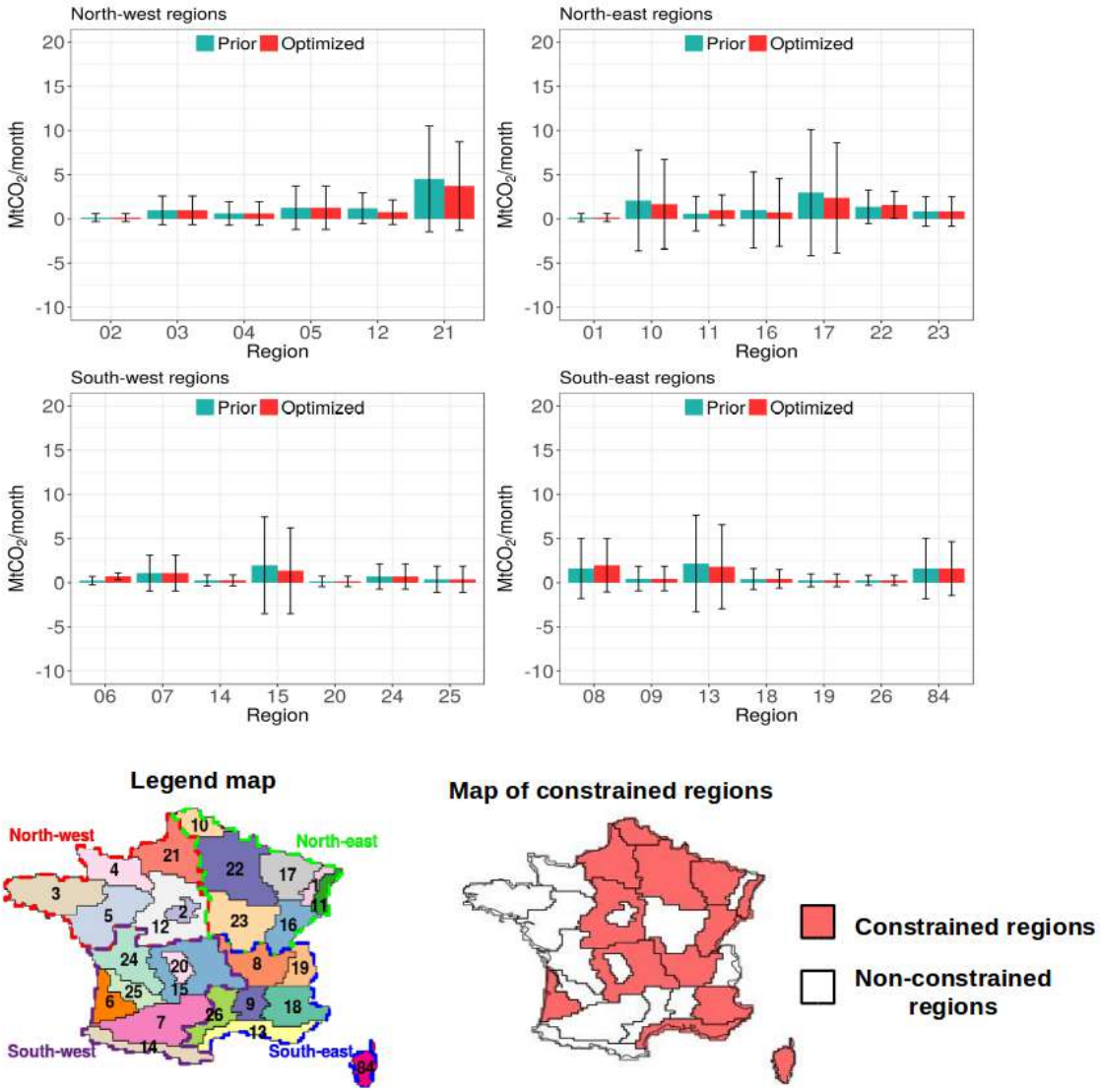

Figure IV.35: Same as figure 34 for July

IV.3.2.7.1Optimized biogenic fluxes

The inversion system constrains a higher number of regions for the biogenic fluxes compared to the anthropogenic emissions. In January the fluxes are constrained for the 18% of national budget, and in July the coverage increases to 41%. The increase in the percentage of the constrained region in July can be explained by two elements. First, the availability of more atmospheric sites, such as OHP, help to capture efficiently the biogenic fluxes in the south-east sector (Figure IV.28). Second, the higher amplitude of the biogenic fluxes in July compared to January generates higher signals to be detected at the sampling sites (see section III.3.4.2).

Block	January			July		
	Prior fluxes ($MtCO_2$)	Optimized fluxes ($MtCO_2$)	Uncertainty reduction (%)	Prior fluxes ($MtCO_2$)	Optimized fluxes ($MtCO_2$)	Uncertainty reduction (%)
North-west	12.7 ± 13.8	13.6 ± 10.3	25 %	-35 ± 23.5	-22 ± 15	36 %
North-east	11.2 ± 14.5	10.5 ± 11.4	21 %	-31 ± 20.5	-32 ± 14	31 %
South-east	2.4 ± 12.7	4.6 ± 12	5 %	-45 ± 34	-40 ± 20	41 %
South-west	12.6 ± 16	-4.8 ± 13.6	15 %	-23 ± 22	-15 ± 15	32 %
Total France	39 ± 27.6	24 ± 23	18 %	-134 ± 50	-109 ± 32	36 %

Table IV.4: Inversion results of total prior and optimized CO_2 biogenic fluxes over France, and over the four sectors: the North-west (NW), the North-east (NE), the South-east (SE), and the South-west (SW). The limits of these sectors can be found in the legend map Figure IV.36

Over France, the prior biogenic budget estimated from VPRM model equals 39±28 $MtCO_2$ for January and -134±50 $MtCO_2$ for July (Table IV.4). The optimized biogenic budget is 24±23 $MtCO_2$ in January, and -109±32 $MtCO_2$ in July. At the national scale, the inversion tends to decrease the biogenic fluxes for the two months (CO_2 winter respiration and summer uptake). In January, the decrease of the optimized biogenic fluxes compared to the prior is associated with a significant CO_2 uptake in the South-west sector (Table IV.4), where the inversion estimates a CO_2 sink of -4.8 $MtCO_2$ instead of a source of 12 $MtCO_2$. We have compared those results to the eddy flux measurements performed at Le Bray (Sarrat et al., 2007) located in region 6, and Lamarquere (Béziat et al., 2009) located in region 7, despite the fact that the spatial representativeness of the eddy flux measurement (on the order of one hectare) is much lower than the regional fluxes estimated by the atmospheric inversion. Considering the area of regions 6 and 7, the optimized biogenic fluxes are equal to 20±65 $KgCO_2$/m2/month for region 7, and -47±54 $KgCO_2$/m2/month for region 6. For the same period, the eddy flux measurements sum up to 77 $KgCO_2$/m2/month for Lamasquere (cultivated site), and -33 $KgCO_2$/m2/month for Le Bray (pine forest site), which are within the range of the optimized biogenic flux uncertainties (±1σ). This comparison confirms the CO_2 uptake in region 6 in January as deduced from the inversion.

In July, most regions are characterized by lower CO_2 sinks after the inversion (Figure IV.36). The decrease of the fluxes occurs in the four sectors, with a significant reduction in the NW block (13 $MtCO_2$ of difference between the prior and the optimized fluxes). This decrease is associated with an uncertainty reduction up to 36% (Table IV.4). The performance of the inversion system for the NW sector is related to the availability of GIF and TRN sites, which constrain the biogenic signal of these regions due to the westerly winds. The

decrease of the CO_2 sink and the increase of the anthropogenic emission in the NW block after the inversion, reduce the negative bias of the atmospheric concentrations at both GIF and TRN sites (Figures IV.23 and IV.24).

To sum up, the CO_2 inversion leads to an increase of the anthropogenic emission and a decrease of the biogenic fluxes over France. At the regional scale, the north of France (NW and NE sectors) is characterized by the highest anthropogenic emissions, whereas in the south of France, the CO_2 uptake is more pronounced for both months. All regions showed a significant uncertainty reduction of 20-50% for the biogenic fluxes, except the SE sector in January. For anthropogenic emissions, most regions also showed an uncertainty reduction, but limited to 10-30%. The posterior uncertainties remain larger than the net regional fluxes (by 80% on average). Low posterior error correlations (|R2| < 0.3 in Figure IV.29) between anthropogenic and biogenic flux regions and moderate posterior uncertainties (~20 - 50%) indicate that the two optimized fluxes should be relatively well separated. Overall, the posterior error correlations for distinct regions remains below 0.5, especially for the anthropogenic fluxes. However, some cases of high posterior error correlations (~0.6 - 0.8) occurred between anthropogenic and biogenic fluxes at regions located upwind of sampling sites (e.g. regions 22, 23).

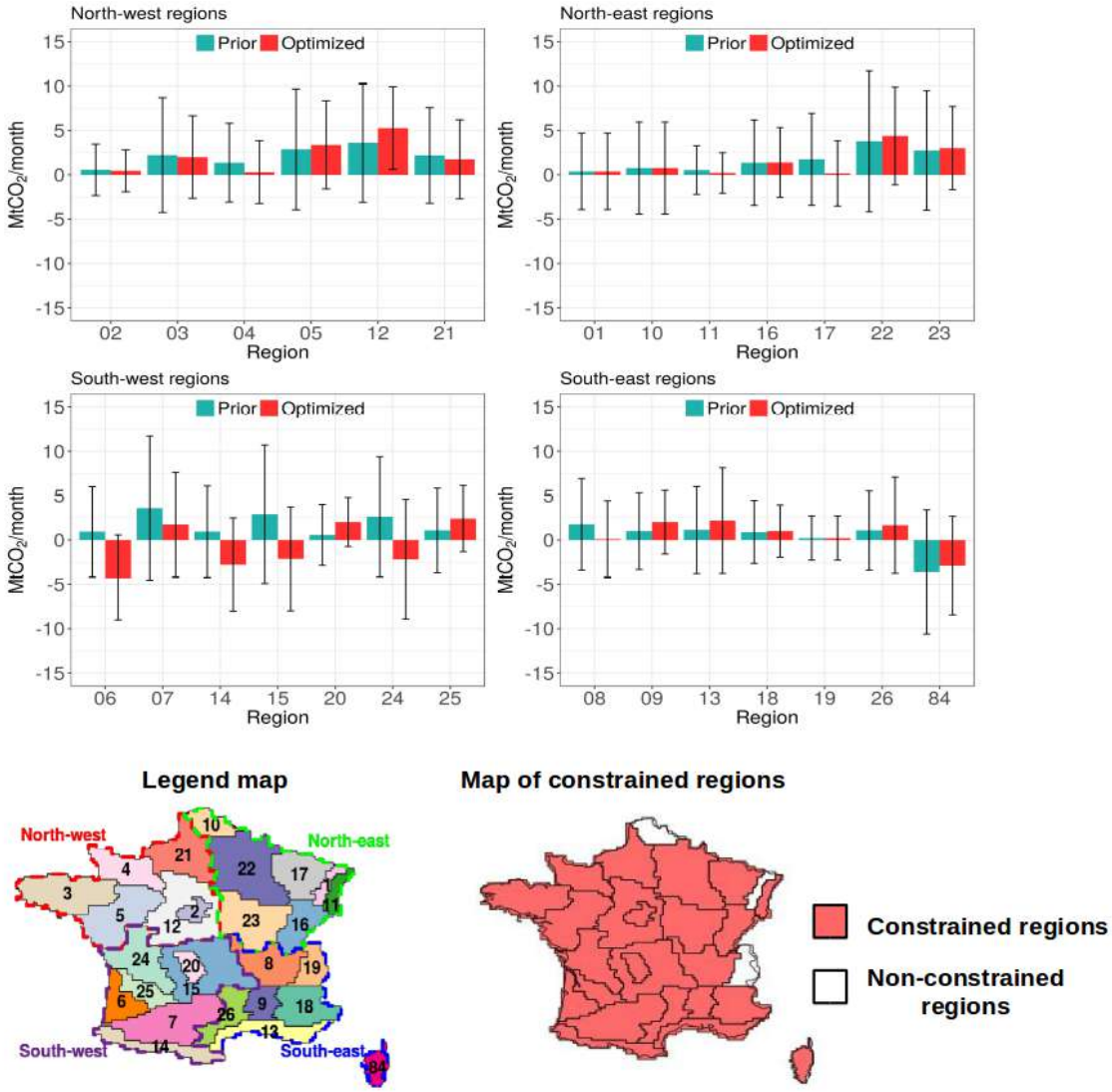

Figure IV.36: Total prior (blue) and optimized (red) biogenic CO_2 emissions over the 27 French regions during January. The uncertainty related to the prior and optimized emissions are represented by the error bar. The maps in the bottom show the number of regions (left) and the constrained regions (right).

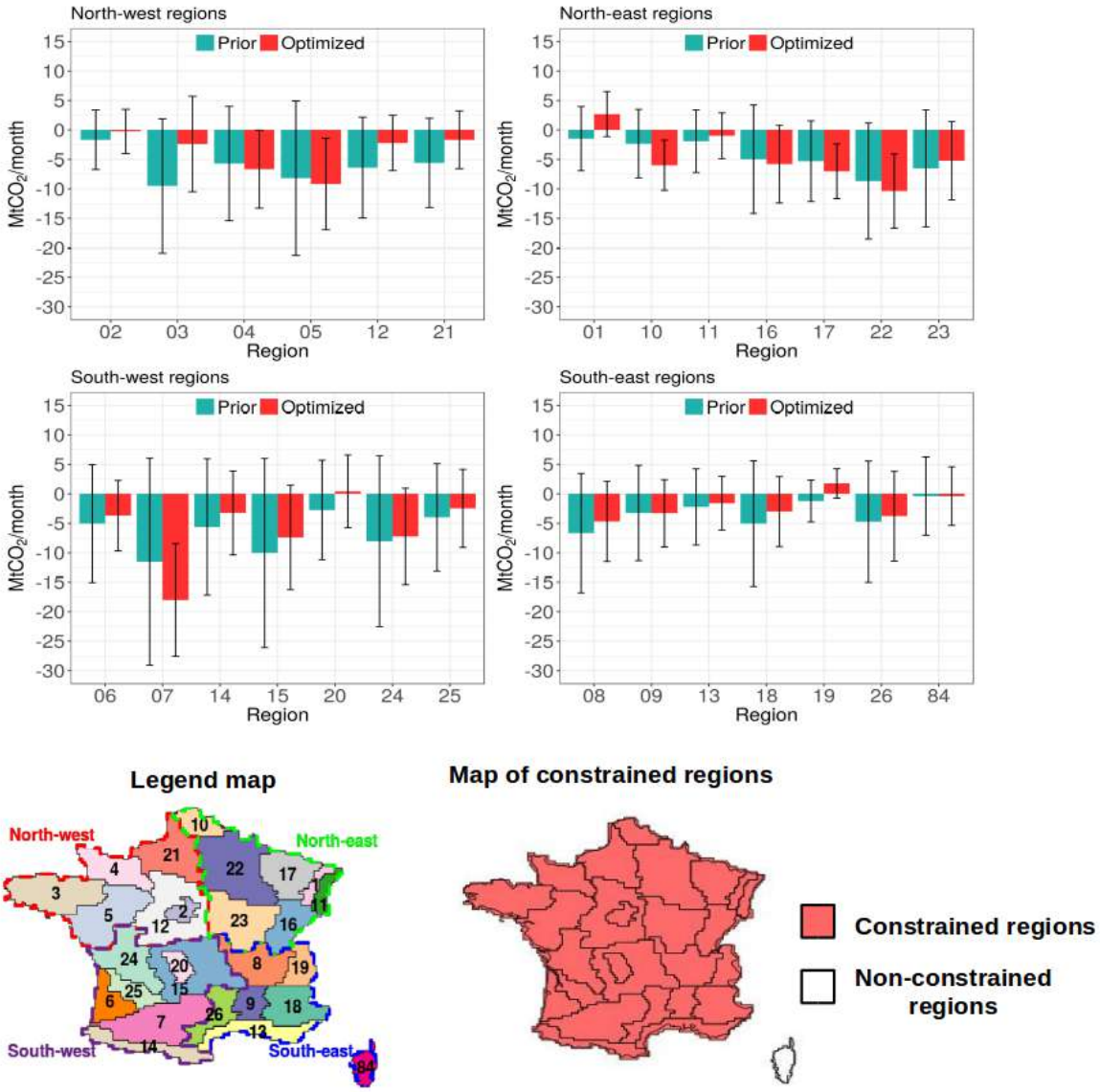

Figure IV.37: Total prior (blue) and optimized (red) biogenic CO_2 emissions over the 27 French regions during July. The uncertainty related to the prior and optimized emissions are represented by the error bar. The maps in the bottom show the number of regions (left) and the constrained regions (right).

IV.4 Conclusions

In this study, we estimated the CO_2 and the CH_4 surface emissions in France for January and July 2014 using the atmospheric transport model CHIMERE embedded in the inversion framework PYMAI (Berchet et al., 2013 and 2015), with a horizontal resolution of 0.1° x 0.1°. The inversion was performed using data collected during the year 2014 from 16 surface station (8 stations in France 8 stations in the neighbouring countries) measuring atmospheric CO_2 and CH_4 concentrations in the Western European region. We implemented the Bayesian inversion method developed by Berchet et al (2013) in order to estimate objectively the uncertainties in the inversion framework. The used system allowed us to investigate the weight of the used observation in the inversion, the spatial distribution of sensitivity of the surface fluxes, and to estimated the optimized fluxes at a national and sub-national scales.

To constrain the surface fluxes, the inversion system assimilates hourly mid-afternoon data for low altitude sites and nighttime data for the high altitude stations. This selection was based on the evaluation of the performance of CHIMERE for simulating the atmospheric concentration. After this first screening, the inversion system filters out data whose representativeness appears to be incompatible with the simulated data. This is, for example, the case of observations that occur during sharp synoptic events, which are very difficult to simulate by the transport models. This selection impacts more the low altitude sites, especially those located near high emission sources such as GIF and CBW sites. Overall, the inversion system rejects a percentage that varies between 1 % and 3 % compared to the total number of the hourly data used by the system. The investigation of the impact of the retained data on the inversion showed that the system uses the equivalent of 3 information per day for CH_4 and 5 information per day for CO_2. The higher weight of CO_2 observation was explained by the higher sensitivity of the inversion system regarding the biogenic fluxes, especially during the summer.

The used inversion system allows the investigation of the strength of the constraint, which mainly depends on the intensity of the emission fluxes, the transport, and the distance to the observation sites. This analysis showed that the surface fluxes in the West of France are significantly constrained. This was related to the impact of GIF and TRN sites, located a few hundreds of kilometers east of the emission sources, which capture efficiently the emission signal driven by the westerly winds. In agreement with earlier studies (e.g. Pison et al., 2018, and Berchet et al., 2015), this analysis confirms the ability of the inversion to principally constrain the emissions close to the atmospheric sites in a radius up to 500 km. Meanwhile, the regions that are located far from the observation sites were not constrained at all. That was the case for the south-east

regions of France, where the inversion did not optimize the corresponding fluxes due to lack of the observed data during January. The comparison between the two months showed the increasing percentage of the constrained CH_4 and the biogenic CO_2 fluxes in July, in agreement with the higher number of the measurement sites, compared to January. For the anthropogenic emission of CO_2, a lower percentage of the constrained fluxes was shown in July despite the increasing number of the operational atmospheric stations. This was explained by the incapability of the inversion system to correctly extract the signal of the anthropogenic emission from the total CO_2 fluxes, captured by the observation sites, due to the influence of the strong biogenic sink in July.

The investigation of the posterior error covariance allowed us to study the ability of the inversion system to efficiently separate de emission fluxes. Despite the low uncertainty reduction that ranges between 10 % and 40 %, we assumed that the inversion managed to correctly separate the emission fluxes between most regions. This was illustrated by the low posterior error correlations that did not exceed 0.5 for both CO_2 and CH_4 for most regions. The significant flux separation ($|R2| < 0.3$) was found between the distant regions thanks to the spatial distribution of the atmospheric sites in a south-west north-east axis. Few limitations for the flux separation was found between some adjacent regions characterized by a posterior error correlation that may reach 0.7 (e.g. regions 22 and 23).

Before analyzing the results of the optimized fluxes, first, we defined the spatiotemporal scales resolved by the inversion. This analysis was based on the posterior error covariance matrices. For CH_4, the correlation threshold of 0.5 allowed us to interpret the inversion results that constrain 18 % and 28 % of the national emissions for January and July respectively. The threshold of 0.5 provides the highest number of control vector component groups composed of at least two regions that cover an averaged area of 44 000 km². The component of each group was characterized by a mean time difference less than 1.5 days. This means that the interpretation of the inversion results will be based on regions characterized by an adjacent time period. We performed the same analysis for CO_2, but with a correlation threshold of 0.8. This threshold provides results that constrain between 8 % and 13 % of the national anthropogenic emission, and between 20 % and 41 % for the national biogenic budget. Based on these selections we summarize in the following the results of the optimized fluxes for CH_4 emissions, the anthropogenic and the biogenic CO_2 fluxes.

For CH_4, the inversion tends to increase the surface fluxes for both months, with higher emissions in July compared to January. This result confirms the conclusions of Pison et al (2018) and Bergamaschi et al (2018) who estimate higher CH_4 fluxes after the inversion in France compared to their prior emissions. Analysing

the inversion results at a sub-national scale, allowed us to determine the contribution of each region. Consistent with the prior emissions, the inversion estimated the highest CH_4 sources in the North-west of France with a total of 115±33 $GgCH_4$ in January and 148±30 $GgCH_4$ in July. The lowest CH_4 emissions in France were found in the South-east of France with less than 60 $GgCH_4$ for both months.

For the anthropogenic CO_2 emissions, the inversion provided higher emissions in January and slightly lower emission in July compared to the prior. The optimized emissions were associated with an uncertainty reduction of 18% in January and 11% for July. The decrease of the uncertainty reduction for July was related to the decrease in the percentage of the constrained CO_2 emissions. For the biogenic fluxes, the inversion decreases the national budget for both months. In January the respiration was decreased by 38 %, whereas in July the CO_2 sink was reduced by 18 % compared to the prior fluxes. The significant decrease of the biogenic emissions in January was associated with predominant CO_2 sink estimated after the inversion in the south-west region. In July the decline of the CO_2 sink impacted most regions, with a significant decrease of 30 % in the West of France. The Western regions were highly constrained by the inversion, but with some limitations regarding the separation between the anthropogenic and the biogenic fluxes. This result confirmed the need to use more observation data in order to improve the separability between the fluxes, and to increase the fraction of the constrained anthropogenic emissions..

Chapter V: Conclusions and perspectives :

V.1 Conclusion

The aim of this thesis is to enhance the knowledge of the CO_2 and CH_4 surface flux budget in France using a high-resolution inversion framework and atmospheric measurements provided by several surface stations. This thesis focuses particularly on exploring the capacity to quantify the national CO_2 and CH_4 surface fluxes using surface stations from a regional network such as ICOS, and to identify the main limitations and sources of uncertainties. The accuracy of the emissions derived from inverse modelling, and the spatial scales at which the emissions can be estimated, depending on the density of atmospheric measurement network and the quality of the atmospheric transport model. This study was motivated by the recent development of those two critical points. First, we have used a high-resolution modelling system which simulates the atmospheric concentrations at a regional scale and in a high frequency. Second, the national atmospheric measurement network has been significantly developed in France and neighbouring countries, and consequently, we could use precise atmospheric measurements from 16 stations.

The first step of the thesis was dedicated to the evaluation of three statistical methods (COV, SD, and REBS) to detect spikes associated with local contamination sources at four contrasted atmospheric measurement sites: a tall-tower station in France (OPE), a high-mountain station in France (PDM), a regional marine background site in Crete (FKL), and a marine clean-air site in the Southern Hemisphere (AMS) (Chapter II). This analysis aimed to filter out short-duration spikes (from few seconds to few minutes) in the continuous time series in order to keep only the measurements that are influenced by the regional and the large-scale fluxes and transport. Second, we evaluated the sensitivity of the simulated CO_2 and CH_4 concentrations to different forcing for the year 2014, using the regional chemistry-transport model CHIMERE (Chapter III), with the aim to provide the best input data that can be used with CHIMERE for inverse modelling. Third, we estimated the CO_2 and the CH_4 surface fluxes in France using the analytical inversion framework PYMAI and atmospheric measurements from 16 observation sites from national and European networks (Chapter IV). The main conclusions for the different sections are summarized as follows.

V.1.1 Spike detection algorithms

Applying the two automatic methods (SD and REBS) on the CO_2, CH_4, and CO continuous time-series has provided variable percentages of contaminated data that range between 0.1% and 15%. These percentages vary depending on the station localization and to the variabilities of the trace gases, except for the COV method where the percentage of data to be filtered has to be defined as an apriori parameter. Because of this limitation, the COV method was considered less flexible to perform regular data cleaning of the GHG time-series.

The SD and REBS methods have shown a surprisingly high percentage of contaminated data at Pic du Midi (PDM), a site located at the top of a 2877 m high mountain where we do not expect frequent contamination by local sources. The source of the local contamination has been identified thanks to a field campaign organized in 2015, which has revealed the influence of a small sewage treatment facility at the station, producing CH_4. Sampling the CH_4 concentrations 200m far away from the contaminated measurements points has provided a smoother atmospheric signal with a percentage of spikes data that did not exceed 0.8% instead of 7% closer to the source. The implementation of the spike detection algorithm in the ICOS data processing enables the filtering of the local contamination, but can also provide a warning for a station that would detect an abnormally high rate of spikes.

The performance of the automatic methods was analyzed by comparing the spikes detected by SD and REBS methods to the spikes identified manually by the station managers. This comparison has shown that the SD method was providing the best good overlapping with manual detection, and was consequently recommended for regular data processing of the ICOS continuous measurement.

Despite the multiple influences of the local emission sources on the 1-min data, the aggregation of the contaminated measurements at the hourly timescale has revealed a mean impact which generally remains lower than 0.2 ppm for CO_2 and 1 ppb for CH_4, except for few sites. Even if those biases are significant regarding the high precision which is sought for the background stations, they are weak compared to other sources of uncertainties when comparing the observations to the simulated concentrations.

V.1.2 Evaluation of the simulated CO_2 and CH_4 concentrations

In the second phase of this thesis, we evaluated the sensitivity of the transport model CHIMERE to the atmospheric transport and the surface emissions. For this, we used two meteorological fields (AROME and

ECMWF), two anthropogenic emission maps (IER and EDGAR), and two biogenic models for CO_2 (CTESSEL and VPRM). Eight simulations were performed using combinations of different input data in order to simulate the CO_2 and the CH_4 concentrations at a regional scale centered over France for the year 2014. we have compared the set of simulations to each other and to the observations provided by 16 atmospheric sites in order to study the capability of the transport model to reproduce the observed diurnal, synoptic, and seasonal variabilities.

We first investigated the discrepancies between the two anthropogenic maps and the biogenic fluxes. In France, the comparison between the two anthropogenic emission maps has shown a difference that remains below 10% of the annual total. This comparison confirmed our assumption for the anthropogenic emission uncertainties that were studied in earlier studies (e.g. Ciais et al., 2010, Peng et al., 2016, and Peylin et al., 2011). However, the differences between the two emission maps can be as high as 40% in some areas, especially near the emission hotspots and in winter. The evaluation of the biogenic models showed a relatively good agreement between VPRM and CTESSEL monthly budgets in summer and a higher contrast in winter. The important differences in wintertime were related to negative bias of CTESSEL which simulate, contrary to VPRM, a CO_2 sink through all the year. This bias was due to the overestimation of the photosynthesis activities in the north part of France by CTESSEL, which has been corrected but the latest version was not available for this work. The spatial distribution of the differences between VPRM and CTESSEL has revealed significant differences at the sub-national scale. This information about the differences between surface fluxes represents an important information about the uncertainty, which can be used to estimate the surface fluxes errors required as an input by the inversion systems. In this study, we used the differences between the two anthropogenic and biogenic emission maps to evaluate the surface flux errors estimated by the PYMAI inversion framework presented in Chapter IV.

The sensitivity of the simulated concentrations to the transport data was investigated based on the atmospheric concentrations simulated using the two meteorological fields provided by ECMWF and AROME, with the same surface GHG fluxes. This analysis has shown the significant sensitivity of the CO_2 and CH_4 concentrations to the transport fields at the mountain sites. At the low altitude stations, the difference between AROME and ECMWF impacted the atmospheric concentration by 1 ppm for CO_2 and 10 ppb for CH_4. These differences can increase significantly in the vicinity of emission hotspots. The comparison between the simulated and the observed concentrations confirmed the capability of CHIMERE to reproduce more accurately the atmospheric concentrations during the afternoon for the low altitude stations

and during the night at the mountain sites. This information was used to select the optimal atmospheric dataset in the inversion framework (Chapter IV).

The sensitivity of the simulated concentrations to the surface fluxes was carried out by running two simulations for the anthropogenic emissions (IER and EDGAR) and two simulations for the biogenic fluxes (CTESSEL and VPRM). The analysis of the simulated concentrations with two anthropogenic fluxes has confirmed the high uncertainty near big cities and the emission hotspots. For the biogenic fluxes, the negative bias of CTESSEL has led to a significant underestimation of the CO_2 concentrations compared to VPRM. The impact of the differences between the two biogenic models increases in summer, due to the higher amplitude of the surface fluxes, and reach more than 6 ppm for CO_2. The comparison between the simulated and the observed concentrations has shown that the simulation that uses ECMWF, VPRM and EDGAR simulate more accurately the CO_2 and the CH_4 concentrations in France. These data were thus used in Chapter IV to provide the prior estimates and the transport field used by the inversion system.

V.1.3 Estimation of the CO_2 and CH_4 fluxes in France

The CH_4 and the CO_2 emissions in France were estimated for two months, one month in winter (January) and one month in summer (July), using the analytical inversion systems PYMAI (Berchet et al., 2013 and 2015). The inversion was performed using the atmospheric transport model CHIMERE forced by the meteorological data provided by ECMWF. For the prior estimates, we used EDGAR for the anthropogenic emissions and VPRM for the CO_2 biogenic fluxes. The inversion system was constrained by continuous measurements provided from 16 atmospheric surface sites distributed in Western Europe. Running the analytical inversion system has provided an estimation of the optimized fluxes together with their uncertainties, as well as some indicators which can be used to analyze the sensitivity of the inversion results to the input dataset.

The investigation of the strength of the constrained fluxes has shown that the western regions of France were more highly constrained by the inversion system. The localization of GIF and TRN sites has contributed to constrain these regions thanks to the action of the westerly winds bringing information about the regional fluxes to the stations located few hundreds of kilometers away downwind. For regions where the surface fluxes did not influence enough the atmospheric concentrations at the sampling sites, the inversion system was not able to optimize the flux and reduce the associated uncertainties. This was the case for the anthropogenic emissions located far away from the sampling sites and for which the inversion could not extract the anthropogenic signal from the total CO_2 signal. This analysis has confirmed that the inversion

system constrains principally the biogenic fluxes at the sub-national scale. The optimization of the CO_2 anthropogenic fluxes at the sub-national remains clearly insufficient since only 8% of the monthly budget was constrained in July. On the other hand, the inversion system constrains efficiently the CH_4 anthropogenic emissions at the sub-national scale.

After the inversion, the total CH_4 emissions for France equals 316±34GgCH_4 in January and 385±33 GgCH_4 in July, which corresponds to an increase of the prior fluxes by 8% and 38% respectively. The analysis of the regional fluxes has shown that the highest CH_4 emissions occur in the Northwest of France with more than 35% of the national total. The increase of emission resulting from the inversion has reduced significantly the misfits between the observed and the optimized concentrations at the atmospheric sites (e.g. GIF, TRN, and PUY). The analysis of the CH_4 inversion results confirmed the capability of the atmospheric network to optimize the CH_4 emission at the level of France. Few limitations occur in some regions in the South of France which was not covered when the measurements at some stations were interrupted.

For the anthropogenic emission of CO_2, the inversions increased the prior fluxes by 18% in January to reach 34.2±34MtCO_2 , and decreased slightly the emissions in July from 25±13MtCO_2 to 23±12MtCO_2 . The minor optimization of the CO_2 anthropogenic emissions in July was related to the low percentage of the constrained fluxes which did not exceed 8%. This indicates that the current atmospheric network is still insufficient or not optimized, to constrain the CO_2 anthropogenic emissions in France. Indeed, the location of most stations was selected to be more representative of the natural fluxes. New atmospheric stations have been recently deployed around Paris that could enable better performances for the anthropogenic fluxes in this region. For the CO_2 biogenic fluxes, the inversion reduces the positive budget of January to 24±23Mt CO_2 and the CO_2 sink of July to -109±32 MtCO_2 . These estimates were associated with a percentage of the constrained fluxes that reaches 40% in July. Contrary to the anthropogenic emission, the used atmospheric network was able to significantly reduce uncertainties of the biogenic fluxes at the level of France.

The inversion results revealed that despite the satisfying flux optimization at the national scale in France, large uncertainties remain in the CO_2 and the CH_4 estimates at the regional scale. Thus, it is important to keep improving the regional GHG modelling practices in order to better optimize the fluxes at the sub-national scale. The recent progress of the atmospheric observation sites and the enhancement of the transport model performances provide the key ingredient to optimize the GHG fluxes at the regional scale, but their limits open to more improvements in the future. The new challenges that the regional inverse modelling should tackle are summarized in the following components.

V.2 Perspectives

V.2.1 Identification of the local contamination sources

As was shown in Chapter II, the local sources in the vicinity of stations can have significant impacts on atmospheric concentrations occasioning sharp and intense positive spikes. The statistical method that we have evaluated provide a tool to filter out the data influenced by local emissions from those representatives of larger fluxes and transport. However, this approach does not provide any information regarding the process responsible for the spike. Ideally, we would like to understand the origin of the contaminations in order to avoid them whenever it is possible. This identification issue could be addressed by matching the spikes detected by the automatic method with other observations like the meteorological data, such as wind fields, which would provide additional information about the contamination origins.

Figure IV.1-A illustrates a projection of the spikes identified at OPE by the SD method on the wind rose. This analysis shows that most of the spikes are related to winds from the west and the south of the OPE station. The investigation of the possible local sources near OPE reveals three possible origins as shown in Figure IV.1-B. The first source stands for the village of Houdelaincourt (400 inhabitants) located 1.3 km west of OPE. The second represents the Abainville village (300 inhabitants) located 1.8 km south OPE. Whereas the third potential source of contamination represents the car's traffic near the station (roads D960, D966, and D10 represented by yellow lines). This analysis can be applied to all sites in order to investigate and/or prevent future contaminations of the measured concentrations. We could complete this analysis with mobile measurement campaign around the atmospheric sites, in order to validate or invalidate the results provided by the wind rose study.

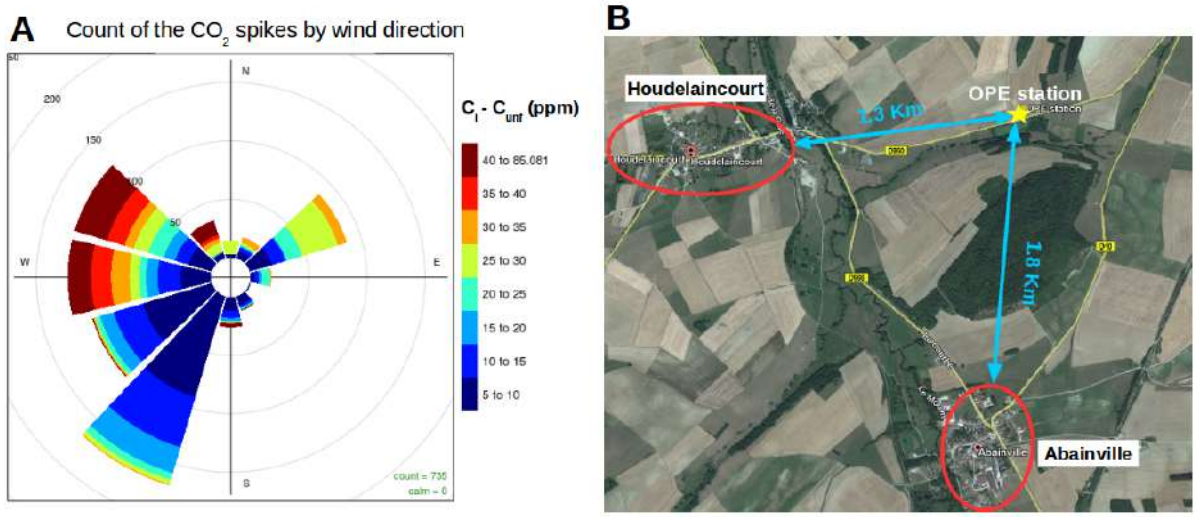

Figure V.1: A) Count of the CO_2 contaminated data by wind direction at OPE. The count is represented by grey circles (first circle=50 data, the second=100, and the third=150 data). The colors stand for the difference between contaminated data (Ci) and the last uncontaminated data (Cunf), using the SD method. B) represents a Google earth image of the OPE area.

V.2.2 Atmospheric modeling

The regional transport model CHIMERE has been evaluated by using different meteorological fields and different surface fluxes. The evaluation of the emission inventories has shown significant differences between the anthropogenic maps near the emission hotspots. More efforts are required to provide high-quality of the emission maps representing the emission hotspots more accurately. Moreover, the quantification of the impact of the temporal profile on the atmospheric concentrations is highly recommended. This quantification can be addressed by comparing the simulated concentrations using yearly emission maps to simulated concentrations presented in Chapter III. Additional improvements of the time-varying emission maps can be achieved by replacing the default profile by meteorological driven functions, for the emission sectors the most sensitive to the weather conditions (e.g. residential and the agriculture sectors).

The evaluation of the simulated concentrations at the hourly scale has revealed important model-observation misfits at the low altitude sites during the nighttime. The current limitations to simulate the atmospheric concentrations during the night are related to the dynamic of the boundary layer height that partly controls the GHG variabilities near the surface (Haszpra et al., 2014). It is then desirable to improve the

parametrization of the boundary layer height to further increase the model performance, especially in the nighttime. The analysis of the simulated concentrations using two different meteorological models showed also significant discrepancies in the simulated atmospheric concentrations in the mountainous regions. These differences are mainly related to horizontal and also the vertical resolution of the transport fields. Thus an improvement of the spatial resolution of the meteorological models is also required in order to improve the representation of the local processes in complex terrain. The improvement of both horizontal and vertical transport would allow the assimilation of a higher number of data by the inverse system (e.g. nighttime data for the low altitude sites).

V.2.3 Inverse modeling

The implementation of the PYMAI inversion framework (Berchet et al., 2013 and 2014) has provided very interesting results for the estimation of the CO_2 and CH_4 surface fluxes in France. The analysis of the inversion results showed the limits of the used inversion system to constrain high fractions of the monthly budget. This limitation could be overcome by providing additional atmospheric measurements. In the short term, in France, only the atmospheric sites ROC (Roc'h Trédudon) is planned to be installed in the north-west of France. We expect that this station may contribute to the increase of the constrained fraction of the national surface fluxes. On the other hand, there are few urban sites which are monitoring CO_2 for example in cities of Paris and Marseille, and there are few projects to develop this kind of urban networks based on low-cost sensors providing measurements with lower precision. Such data could provide new constraints on the CO_2 anthropogenic emissions. However, since they are located in a complex environment regarding the local emissions and atmospheric transport, integrating that dataset in the national inversion framework will be challenging in terms of data selection and high-resolution transport model.

Another challenging aspect would be the extension of the inversion system to assimilate satellite data that would contribute to constrain more efficiently the surface fluxes. For example, GOSAT and OCO-2 satellites provide observation of the total CO_2 column. Despite their sensitivity to the cloud cover, which reduces the cloud-free soundings columns they could provide additional observational constraints. The increase in the density of measurements will be accomplished in the near future by the launch of the additional satellites such as OCO-3 and MICROCARB, which will provide CO_2 measurement with an expected precision better than 1 ppm.

In addition to the increase in the amount of information provided to resolve the inverse problem, the system requires an evaluation of the impact of using objective estimates of the observation and the prior errors. This evaluation can be addressed by performing a flux inversion using the empirical estimates of the observation and the prior errors based on Chapter III results. In this study, we have assumed a diagonal error matrices by neglecting the error correlation between regions and time periods. However, some errors are known to be correlated such as the model error during the night (e.g. nighttime stratification near the surface), or the misrepresentation of the surface fluxes for a given vegetation type. It would be challenging to take into account the error correlations and to quantify their impact on the optimized fluxes. This improvement will require drastically higher computational costs, it is thus appropriate to validate it first in a simplified inversion framework.

Chapter VI: References

1. (PDF) Modeling atmospheric CO_2 concentration... Available at: https://www.researchgate.net/publication/26433299_Modeling_atmospheric_CO2_concentration_profiles_and_fluxes_above_sloping_terrain_at_a_boreal_site. (Accessed: 2nd August 2018)

2. Agustí-Panareda, A. et al. A biogenic CO_2 flux adjustment scheme for the mitigation of large-scale biases in global atmospheric CO_2 analyses and forecasts. Atmospheric Chemistry and Physics **16,** 10399–10418 (2016).

3. A coarse grid three-dimensional global inverse model of the atmospheric transport: 2. Inversion of the transport of CO_2 in the 1980s - Kaminski - 1999 - Journal of Geophysical Research: Atmospheres - Wiley Online Library.

4. Hutchins, M. G., Colby, J. D., Marland, G. & Marland, E. A comparison of five high-resolution spatially-explicit, fossil-fuel, carbon dioxide emission inventories for the United States. Mitig Adapt Strateg Glob Change **22,** 947–972 (2017).

5. Tiedtke, M. A Comprehensive Mass Flux Scheme for Cumulus Parameterization in Large-Scale Models. Mon. Wea. Rev. **117,** 1779–1800 (1989).

6. Wee, A., Grayden, D. B., Zhu, Y., Petkovic-Duran, K. & Smith, D. A continuous wavelet transform algorithm for peak detection. ELECTROPHORESIS **29,** 4215–4225 (2008).

7. A dynamic global vegetation model for studies of the coupled atmosphere-biosphere system - Krinner - 2005 - Global Biogeochemical Cycles - Wiley Online Library. Available at: https://agupubs.onlinelibrary.wiley.com/doi/full/10.1029/2003GB002199. (Accessed: 29th July 2018)

8. Broquet, G. et al. A European summertime CO_2 biogenic flux inversion at mesoscale from continuous in situ mixing ratio measurements. Journal of Geophysical Research: Atmospheres **116,**

9. Yver, C. E. et al. A new estimation of the recent tropospheric molecular hydrogen budget using atmospheric observations and variational inversion. Atmospheric Chemistry and Physics **11,** 3375–3392 (2011).

10. Ramonet, M. et al. A recent build-up of atmospheric CO_2 over Europe. Part 1: observed signals and possible explanations. Tellus B **62,** 1–13 (2010).

11. Marécal, V. et al. A regional air quality forecasting system over Europe: the MACC-II daily ensemble production. Geosci. Model Dev. **8,** 2777–2813 (2015).

12. Schuh, A. E. et al. A regional high-resolution carbon flux inversion of North America for 2004. Biogeosciences **7,** 1625–1644 (2010).

13. Balsamo, G. et al. A Revised Hydrology for the ECMWF Model: Verification from Field Site to Terrestrial Water Storage and Impact in the Integrated Forecast System. J. Hydrometeor. **10,** 623–643 (2009).

14. A satellite-based biosphere parameterization for net ecosystem CO_2 exchange: Vegetation Photosynthesis and Respiration Model (VPRM) - Mahadevan - 2008 - Global Biogeochemical Cycles - Wiley Online Library. Available at: https://agupubs.onlinelibrary.wiley.com/doi/full/10.1029/2006GB002735. (Accessed: 28th July 2018)

15. Troen, I. B. & Mahrt, L. A simple model of the atmospheric boundary layer; sensitivity to surface evaporation. Boundary-Layer Meteorol **37,** 129–148 (1986).

16. Ferrarese, S. et al. A study of seasonal and yearly modulation of carbon dioxide sources and sinks, with a particular attention to the Boreal Atlantic Ocean. Atmospheric Environment **36,** 5517–5526 (2002).

17. Enting, I. G., Trudinger, C. M. & Francey, R. J. A synthesis inversion of the concentration and μ13C of atmospheric CO_2. Tellus B: Chemical and Physical Meteorology **47,** 35–52 (1995).

18. Belviso, S. et al. A top-down approach of surface carbonyl sulfide exchange by a Mediterranean oak forest ecosystem in southern France. Atmospheric Chemistry and Physics **16,** 14909–14923 (2016).

19. Hildebrandt, L. et al. Aged organic aerosol in the Eastern Mediterranean: the Finokalia Aerosol Measurement Experiment – 2008. Atmospheric Chemistry and Physics **10,** 4167–4186 (2010).

20. Bréon, F. M. et al. An attempt at estimating Paris area CO_2 emissions from atmospheric concentration measurements. Atmospheric Chemistry and Physics **15,** 1707–1724 (2015).

21. Kountouris, P. et al. An objective prior error quantification for regional atmospheric inverse applications. Biogeosciences **12,** 7403–7421 (2015).

22. van den Hurk, B., Ettema, J. & Viterbo, P. Analysis of Soil Moisture Changes in Europe during a Single Growing Season in a New ECMWF Soil Moisture Assimilation System. J. Hydrometeor. **9,** 116–131 (2008).

23. Kountouris, P. et al. Atmospheric CO_2 inversions on the mesoscale using data-driven prior uncertainties: quantification of the European terrestrial CO_2 fluxes. Atmospheric Chemistry and Physics **18,** 3047–3064 (2018).

24. Sarrat, C. et al. Atmospheric CO_2 modeling at the regional scale: an intercomparison of 5 meso-scale atmospheric models. Biogeosciences **4,** 1115–1126 (2007).

25. Atmospheric composition in the Eastern Mediterranean: Influence of biomass burning during summertime using the WRF-Chem model - ScienceDirect. Available at: https://www.sciencedirect.com/science/article/pii/S1352231016301789. (Accessed: 2nd August 2018)

26. Hazan, L., Tarniewicz, J., Ramonet, M., Laurent, O. & Abbaris, A. Automatic processing of atmospheric CO_2 and CH_4 mole fractions at the ICOS Atmosphere Thematic Centre. Atmos. Meas. Tech. **9,** 4719–4736 (2016).

27. Ruckstuhl, A. F., Jacobson, M. P., Field, R. W. & Dodd, J. A. Baseline subtraction using robust local regression estimation. Journal of Quantitative Spectroscopy and Radiative Transfer **68,** 179–193 (2001).

28. Bayesian design of control space for optimal assimilation of observations. Part I: Consistent multiscale formalism - Bocquet - 2011 - Quarterly Journal of the Royal Meteorological Society - Wiley Online Library. Available at: https://rmets.onlinelibrary.wiley.com/doi/abs/10.1002/qj.837. (Accessed: 2nd August 2018)

29. Heerdegen, R. Book reviews: Houghton, J.T., Jenkins, G.J. and Ephraums, J.J. 1990: Climate change - the IPCC scientific assessment. Cambridge: Cambridge University Press for the Intergovernmental Panel on Climate Change (World Meteorological Organisation/United Nations Environmental Programme). xi + 368 pp. £40.00 cloth, £15.00 paper. ISBN 0 521 40360 X
, Book reviews: Houghton, J.T., Jenkins, G.J. and Ephraums, J.J. 1990: Climate change - the IPCC scientific assessment. Cambridge: Cambridge University Press for the Intergovernmental Panel on Climate Change (World Meteorological Organisation/United Nations Environmental Programme). xi + 368 pp. £40.00 cloth, £15.00 paper. ISBN 0 521 40360 X. Progress in Physical Geography: Earth and Environment **15,** 321–323 (1991).

30. Can we evaluate a fine-grained emission model using high-resolution atmospheric transport modelling and regional fossil fuel CO_2 observations?: Tellus B: Chemical and Physical Meteorology: Vol 65, No 1. Available at: https://www.tandfonline.com/doi/full/10.3402/tellusb.v65i0.18681. (Accessed: 28th July 2018)

31. Béziat, P., Ceschia, E. & Dedieu, G. Carbon balance of a three crop succession over two cropland sites in South West France. Agricultural and forest meteorology (2009).

32. Marquis, M. & Tans, P. Carbon Crucible. Science **320,** 460–461 (2008).

33. O'Keefe, A. & Deacon, D. A. G. Cavity ring-down optical spectrometer for absorption measurements using pulsed laser sources. Review of Scientific Instruments **59,** 2544–2551 (1988).

34. Lelieveld, J., Crutzen, P. J. & Dentener, F. J. Changing concentration, lifetime and climate forcing of atmospheric methane. Tellus B **50,** 128–150 (1998).

35. Menut, L. et al. CHIMERE 2013: a model for regional atmospheric composition modelling. Geosci. Model Dev. **6,** 981–1028 (2013).

36. Flanner, M. G., Huang, X., Chen, X. & Krinner, G. Climate Response to Negative Greenhouse Gas Radiative Forcing in Polar Winter. Geophysical Research Letters **45,** 1997–2004 (2018).

37. Lac, C. et al. CO_2 dispersion modelling over Paris region within the CO_2-MEGAPARIS project. Atmospheric Chemistry and Physics **13,** 4941–4961 (2013).

38. Pérez, I. A., Sánchez, M. L. & García, M. Á. CO<Subscript>2</Subscript> dilution in the lower atmosphere from temperature and wind speed profiles. Theor Appl Climatol **107,** 247–253 (2012).

39. CO_2 baseline concept in 3-D atmospheric transport models: Tellus B: Chemical and Physical Meteorology: Vol 48, No 4. Available at: https://www.tandfonline.com/doi/abs/10.3402/tellusb.v48i4.15929. (Accessed: 2nd August 2018)

40. Chevallier, F. et al. CO_2 surface fluxes at grid point scale estimated from a global 21 year reanalysis of atmospheric measurements. Journal of Geophysical Research: Atmospheres **115,**

41. CO_2 surface fluxes at grid point scale estimated from a global 21 year reanalysis of atmospheric measurements - Chevallier - 2010 - Journal of Geophysical Research: Atmospheres - Wiley Online Library. Available at: https://agupubs.onlinelibrary.wiley.com/doi/10.1029/2010JD013887. (Accessed: 29th July 2018)

42. Andrews, A. E. et al. CO_2, CO, and CH_4 measurements from tall towers in the NOAA Earth System Research Laboratory's Global Greenhouse Gas Reference Network: instrumentation, uncertainty analysis, and recommendations for future high-accuracy greenhouse gas monitoring efforts. Atmos. Meas. Tech. **7,** 647–687 (2014).

43. Geels, C. et al. Comparing atmospheric transport models for future regional inversions over Europe – Part 1: mapping the atmospheric CO_2 signals. Atmospheric Chemistry and Physics **7,** 3461–3479 (2007).

44. Ahmadov, R. et al. Comparing high resolution WRF-VPRM simulations and two global CO_2 transport models with coastal tower measurements of CO_2. Biogeosciences **6,** 807–817 (2009).

45. Saikawa, E. et al. Comparison of emissions inventories of anthropogenic air pollutants and greenhouse gases in China. Atmospheric Chemistry and Physics **17,** 6393–6421 (2017).

46. Stella, P. et al. Comparison of methods for the determination of NO-O3-NO2 fluxes and chemical interactions over a bare soil. Atmospheric Measurement Techniques Discussions **4,** 5481–5527 (2011).

47. Fang, S. X., Tans, P. P., Steinbacher, M., Zhou, L. X. & Luan, T. Comparison of the regional CO_2 mole fraction filtering approaches at a WMO/GAW regional station in China. Atmos. Meas. Tech. **8,** 5301–5313 (2015).

48. Lauvaux, T. et al. Constraining the CO_2 budget of the corn belt: exploring uncertainties from the assumptions in a mesoscale inverse system. Atmospheric Chemistry and Physics **12,** 337–354 (2012).

49. Zhao, L., Lee, X. & Liu, S. Correcting surface solar radiation of two data assimilation systems against FLUXNET observations in North America. Journal of Geophysical Research: Atmospheres **118,** 9552–9564

50. Peylin, P. et al. Daily CO_2 flux estimates over Europe from continuous atmospheric measurements: 1, inverse methodology. Atmospheric Chemistry and Physics **5,** 3173–3186 (2005).

51. Bouttier, F., Courtier, P., Courtier, P. & Courtier, P. Data Assimilation Concepts and Methods. (2002).

52. Tulet, P. Description of the Mesoscale Nonhydrostatic Chemistry model and application to a transboundary pollution episode between northern France and southern England. Journal of Geophysical Research **108,** (2003).

53. Drewnick, F. et al. Design of a mobile aerosol research laboratory and data processing tools for effective stationary and mobile field measurements. Atmos. Meas. Tech. **5,** 1443–1457 (2012).

54. Desroziers, G. & Ivanov, S. Diagnosis and adaptive tuning of observation-error parameters in a variational assimilation. Quarterly Journal of the Royal Meteorological Society **127,** 1433–1452 (2001).

55. Trenberth, K. E., Fasullo, J. T. & Kiehl, J. Earth's Global Energy Budget. Bull. Amer. Meteor. Soc. **90,** 311–324 (2009).

56. Champeaux, J. L., Masson, V. & Chauvin, F. ECOCLIMAP: a global database of land surface parameters at 1 km resolution. Meteorological Applications **12,** 29–32 (2005).

57. Eddy Covariance: A Practical Guide to Measurement and Data Analysis. (Springer Netherlands, 2012).

58. Janssens-Maenhout, G. et al. EDGAR v4.3.2 Global Atlas of the three major Greenhouse Gas Emissions for the period 1970–2012. Earth System Science Data Discussions 1–55 (2017). doi:https://doi.org/10.5194/essd-2017-79

59. European CO_2 fluxes from atmospheric inversions using regional and global transport models | SpringerLink. Available at: https://link.springer.com/article/10.1007/s10584-010-9908-4. (Accessed: 2nd August 2018)

60. Feng, L. et al. Evaluating a 3-D transport model of atmospheric CO_2 using ground-based, aircraft, and space-borne data. Atmospheric Chemistry and Physics **11,** 2789–2803 (2011).

61. Béziat, P. et al. Evaluation of a simple approach for crop evapotranspiration partitioning and analysis of the water budget distribution for several crop species. Agricultural and Forest Meteorology **177,** 46–56 (2013).

62. Delpierre, N. et al. Exceptional carbon uptake in European forests during the warm spring of 2007: a data–model analysis. Global Change Biology **15,** 1455–1474 (2008).

63. Jung, M., Henkel, K., Herold, M. & Churkina, G. Exploiting synergies of global land cover products for carbon cycle modeling. Remote Sensing of Environment **101,** 534–553 (2006).

64. Fifth Assessment Report - Climate Change 2013. Available at: http://www.ipcc.ch/report/ar5/wg1/. (Accessed: 1st August 2018)

65. Agustí-Panareda, A. et al. Forecasting global atmospheric CO_2. Atmospheric Chemistry and Physics **14,** 11959–11983 (2014).

66. Wickham, H. et al. ggplot2: Create Elegant Data Visualisations Using the Grammar of Graphics. (2018).

67. Peylin, P. et al. Global atmospheric carbon budget: results from an ensemble of atmospheric CO_2 inversions. Biogeosciences **10,** 6699–6720 (2013).

68. Global atmospheric methane | Philosophical Transactions of the Royal Society of London A: Mathematical, Physical and Engineering Sciences. Available at: http://rsta.royalsocietypublishing.org/content/369/1943/2058. (Accessed: 1st August 2018)

69. Quéré, C. L. et al. Global Carbon Budget 2015. Earth System Science Data **7,** 349–396 (2015).

70. Quéré, C. L. et al. Global Carbon Budget 2017. Earth System Science Data **10,** 405–448 (2018).

71. Saeki, T., Saito, R., Belikov, D. & Maksyutov, S. Global high-resolution simulations of CO_2 and CH_4 using a NIES transport model to produce a priori concentrations for use in satellite data retrievals. Geosci. Model Dev. **6,** 81–100 (2013).

72. Global increase in atmospheric methane concentrations between 1978 and 1980 - Blake - 1982 - Geophysical Research Letters - Wiley Online Library. Available at: https://agupubs.onlinelibrary.wiley.com/doi/abs/10.1029/GL009i004p00477. (Accessed: 1st August 2018)

73. Congalton, R. G., Gu, J., Yadav, K., Thenkabail, P. & Ozdogan, M. Global Land Cover Mapping: A Review and Uncertainty Analysis. Remote Sensing **6,** 12070–12093 (2014).

74. Stanley, K. M. et al. Greenhouse gas measurements from a UK network of tall towers: technical description and first results. Atmos. Meas. Tech. **11,** 1437–1458 (2018).

75. Patra, P. K. et al. Growth Rate, Seasonal, Synoptic, Diurnal Variations and Budget of Methane in the Lower Atmosphere. Journal of the Meteorological Society of Japan. Ser. II **87,** 635–663 (2009).

76. Gurney, K. R. et al. High Resolution Fossil Fuel Combustion CO_2 Emission Fluxes for the United States. Environ. Sci. Technol. **43,** 5535–5541 (2009).

77. Schmidt, M. et al. High-precision quasi-continuous atmospheric greenhouse gas measurements at Trainou tower (Orléans forest, France). Atmos. Meas. Tech. **7,** 2283–2296 (2014).

78. Hagler, G. S. W., Thoma, E. D. & Baldauf, R. W. High-Resolution Mobile Monitoring of Carbon Monoxide and Ultrafine Particle Concentrations in a Near-Road Environment. Journal of the Air & Waste Management Association **60,** 328–336 (2010).

79. Pillai, D. et al. High-resolution simulations of atmospheric CO_2 over complex terrain – representing the Ochsenkopf mountain tall tower. Atmospheric Chemistry and Physics **11,** 7445–7464 (2011).

80. Pison, I. et al. How a European network may help with estimating methane emissions on the French national scale. Atmospheric Chemistry and Physics **18,** 3779–3798 (2018).

81. Haszpra, L., Barcza, Z., Haszpra, T., Pátkai, Z. & Davis, K. J. How well do tall-tower measurements characterize the CO_2 mole fraction distribution in the planetary boundary layer? Atmos. Meas. Tech. **8,** 1657–1671 (2015).

82. Locher, R. & al, A. R. et. IDPmisc: Utilities of Institute of Data Analyses and Process Design (www.idp.zhaw.ch). (2012).

83. Locatelli, R. et al. Impact of transport model errors on the global and regional methane emissions estimated by inverse modelling. Atmospheric Chemistry and Physics **13,** 9917–9937 (2013).

84. Peylin, P. et al. Importance of fossil fuel emission uncertainties over Europe for CO_2 modeling: model intercomparison. Atmospheric Chemistry and Physics **11,** 6607–6622 (2011).

85. In situ measurements of atmospheric methane at GAGE/AGAGE sites during 1985–2000 and resulting source inferences - Cunnold - 2002 - Journal of Geophysical Research: Atmospheres - Wiley Online Library. Available at: https://agupubs.onlinelibrary.wiley.com/doi/full/10.1029/2001JD001226. (Accessed: 1st August 2018)

86. Influence of transport uncertainty on annual mean and seasonal inversions of atmospheric CO_2 data - Peylin - 2002 - Journal of Geophysical Research: Atmospheres - Wiley Online Library.

87. Influence-matrix diagnostic of a data assimilation system - Cardinali - 2004 - Quarterly Journal of the Royal Meteorological Society - Wiley Online Library. Available at: https://rmets.onlinelibrary.wiley.com/doi/abs/10.1256/qj.03.205. (Accessed: 2nd August 2018)

88. Inspection of high–concentration CO_2 events at the Plateau Rosa Alpine station - ScienceDirect. Available at: https://www.sciencedirect.com/science/article/pii/S1309104215302105. (Accessed: 28th July 2018)

89. Inspection of high–concentration CO_2 events at the Plateau Rosa Alpine station - ScienceDirect. Available at: https://www.sciencedirect.com/science/article/pii/S1309104215302105. (Accessed: 2nd August 2018)

90. Bubnová, R., Hello, G., Bénard, P. & Geleyn, J.-F. Integration of the Fully Elastic Equations Cast in the Hydrostatic Pressure Terrain-Following Coordinate in the Framework of the ARPEGE/Aladin NWP System. Mon. Wea. Rev. **123,** 515–535 (1995).

91. Interannual variability and trend of CH_4 lifetime as a measure for OH changes in the 1979–1993 time period - Dentener - 2003 - Journal of Geophysical Research: Atmospheres - Wiley Online Library. Available at: https://agupubs.onlinelibrary.wiley.com/doi/full/10.1029/2002JD002916. (Accessed: 2nd August 2018)

92. Peng, S. et al. Inventory of anthropogenic methane emissions in mainland China from 1980 to 2010. Atmospheric Chemistry and Physics **16,** 14545–14562 (2016).

93. Inverse modeling of global and regional CH_4 emissions using SCIAMACHY satellite retrievals - Bergamaschi - 2009 - Journal of Geophysical Research: Atmospheres - Wiley Online Library. Available at: https://agupubs.onlinelibrary.wiley.com/doi/10.1029/2009JD012287. (Accessed: 2nd August 2018)

94. Bergamaschi, P. et al. Inverse modelling of European CH_4 emissions during 2006–2012 using different inverse models and reassessed atmospheric observations. Atmospheric Chemistry and Physics **18,** 901–920 (2018).

95. Tarantola, A. Inverse Problem Theory and Methods for Model Parameter Estimation. (Society for Industrial and Applied Mathematics, 2005). doi:10.1137/1.9780898717921

96. Enting, I. G. Inverse Problems in Atmospheric Constituent Transport by I. G. Enting. Cambridge Core (2002). doi:10.1017/CBO9780511535741

97. Fu, X., Marusczak, N., Wang, X., Gheusi, F. & Sonke, J. E. Isotopic Composition of Gaseous Elemental Mercury in the Free Troposphere of the Pic du Midi Observatory, France. (2016). doi:10.1021/acs.est.6b00033

98. Maione, M. et al. Localization of source regions of selected hydrofluorocarbons combining data collected at two European mountain stations. Science of The Total Environment **391,** 232–240 (2008).

99. Maximum likelihood estimation of covariance parameters for Bayesian atmospheric trace gas surface flux inversions - Michalak - 2005 - Journal of Geophysical Research: Atmospheres - Wiley Online Library. Available at: https://agupubs.onlinelibrary.wiley.com/doi/abs/10.1029/2005JD005970. (Accessed: 2nd August 2018)

100. Prinn, R. G. Measurement Equation for Trace Chemicals in Fluids and Solution of its Inverse. in Inverse Methods in Global Biogeochemical Cycles 3–18 (American Geophysical Union (AGU), 2013). doi:10.1029/GM114p0003

101. Mesoscale covariance of transport and CO_2 fluxes: Evidence from observations and simulations using the WRF-VPRM coupled atmosphere-biosphere model - Ahmadov - 2007 - Journal of Geophysical Research: Atmospheres - Wiley Online Library.

102. Tsamalis, C., Ravetta, F., Gheusi, F., Delbarre, H. & Augusti, P. Mixing of free-tropospheric air with the lowland boundary layer during anabatic transport to a high altitude station. Atmospheric Research **143,** 425–437 (2014).

103. Brantley, H. L. et al. Mobile air monitoring data-processing strategies and effects on spatial air pollution trends. Atmos. Meas. Tech. **7,** 2169–2183 (2014).

104. Aalto, T. et al. Modeling atmospheric CO_2 concentration profiles and fluxes above sloping terrain at a boreal site. Atmospheric Chemistry and Physics **6,** 303–314 (2006).

105. Tolk, L. F. et al. Modelling regional scale surface fluxes, meteorology and CO_2 mixing ratios for the Cabauw tower in the Netherlands. Biogeosciences **6,** 2265–2280 (2009).

106. Tolk, L. F., Meesters, A. G. C. A., Dolman, A. J. & Peters, W. Modelling representation errors of atmospheric CO_2 mixing ratios at a regional scale. Atmospheric Chemistry and Physics **8,** 6587–6596 (2008).

107. Boussetta, S. et al. Natural carbon dioxide exchanges in the ECMWF Integrated Forecasting System: Implementation and offline validation. (2012).

108. Prather, M. J. & Hsu, J. NF3, the greenhouse gas missing from Kyoto. Geophysical Research Letters **35,** (2008).

109. Berchet, A. et al. Objectified quantification of uncertainties in Bayesian atmospheric inversions. Geosci. Model Dev. **8,** 1525–1546 (2015).

110. Levin, I. et al. Observations and modelling of the global distribution and long-term trend of atmospheric $14CO_2$. Tellus B **62,** 26–46 (2010).

111. Reimann, S. et al. Observations of long-lived anthropogenic halocarbons at the high-Alpine site of Jungfraujoch (Switzerland) for assessment of trends and European sources. Sci. Total Environ. **391,** 224–231 (2008).

112. On aggregation errors in atmospheric transport inversions - Kaminski - 2001 - Journal of Geophysical Research: Atmospheres - Wiley Online Library. Available at: https://agupubs.onlinelibrary.wiley.com/doi/abs/10.1029/2000JD900581. (Accessed: 2nd August 2018)

113. Kadygrov, N. et al. On the potential of the ICOS atmospheric CO_2 measurement network for estimating the biogenic CO_2 budget of Europe. Atmospheric Chemistry and Physics **15,** 12765–12787 (2015).

114. Courant, R., Isaacson, E. & Rees, M. On the solution of nonlinear hyperbolic differential equations by finite differences. Communications on Pure and Applied Mathematics **5,** 243–255

115. Ropkins, K. & Carslaw, D. C. openair - Data Analysis Tools for the Air Quality Community. The R Journal **4,** 20–29 (2012).

116. Gheusi, F. et al. Pic 2005, a field campaign to investigate low-tropospheric ozone variability in the Pyrenees. Atmospheric Research **101,** 640–665 (2011).

117. Gill, P. E., Murray, W. & Wright, M. Practical optimization. (1981).

118. Quantification of carbon dioxide, methane, nitrous oxide and chloroform emissions over Ireland from atmospheric observations at Mace Head: Tellus B: Chemical and Physical Meteorology: Vol 54, No 1. Available at: https://www.tandfonline.com/doi/abs/10.3402/tellusb.v54i1.16647. (Accessed: 2nd August 2018)

119. Mønster, J., Samuelsson, J., Kjeldsen, P. & Scheutz, C. Quantification of methane emissions from 15 Danish landfills using the mobile tracer dispersion method. Waste Management **35,** 177–186 (2015).

120. Prather, M. J., Zhu, X., Strahan, S. E., Steenrod, S. D. & Rodriguez, J. M. Quantifying errors in trace species transport modeling. PNAS **105,** 19617–19621 (2008).

121. Radiative forcing of carbon dioxide, methane, and nitrous oxide: A significant revision of the methane radiative forcing - Etminan - 2016 - Geophysical Research Letters - Wiley Online Library. Available at: https://agupubs.onlinelibrary.wiley.com/doi/full/10.1002/2016GL071930. (Accessed: 1st August 2018)

122. Myhre, G. et al. Radiative forcing of the direct aerosol effect from AeroCom Phase II simulations. Atmospheric Chemistry and Physics **13,** 1853–1877 (2013).

123. Williams, A. G. et al. Radon as a tracer of atmospheric influences on traffic-related air pollution in a small inland city. Tellus B: Chemical and Physical Meteorology **68,** 30967 (2016).

124. Reactive greenhouse gas scenarios: Systematic exploration of uncertainties and the role of atmospheric chemistry - Prather - 2012 - Geophysical Research Letters - Wiley Online Library. Available at: https://agupubs.onlinelibrary.wiley.com/doi/full/10.1029/2012GL051440. (Accessed: 1st August 2018)

125. Ciais, P., Peylin, P. & Bousquet, P. Regional Biospheric Carbon Fluxes as Inferred from Atmospheric CO_2 Measurements. Ecological Applications **10,** 1574–1589 (2000).

126. Broquet, G. et al. Regional inversion of CO_2 ecosystem fluxes from atmospheric measurements: reliability of the uncertainty estimates. Atmospheric Chemistry and Physics **13,** 9039–9056 (2013).

127. Fleming, Z. L., Monks, P. S. & Manning, A. J. Review: Untangling the influence of air-mass history in interpreting observed atmospheric composition. Atmospheric Research **104–105,** 1–39 (2012).

128. Review: Untangling the influence of air-mass history in interpreting observed atmospheric composition - ScienceDirect. Available at: https://www.sciencedirect.com/science/article/pii/S0169809511002948. (Accessed: 2nd August 2018)

129. Ruckstuhl, A. F. et al. Robust extraction of baseline signal of atmospheric trace species using local regression. Atmos. Meas. Tech. **5,** 2613–2624 (2012).

130. Reuter, M. et al. Satellite-inferred European carbon sink larger than expected. Atmospheric Chemistry and Physics **14,** 13739–13753 (2014).

131. Quéré, C. L. et al. Saturation of the Southern Ocean CO_2 Sink Due to Recent Climate Change. Science **316,** 1735–1738 (2007).

132. Allard, V., Ourcival, J. M., Rambal, S., Joffre, R. & Rocheteau, A. Seasonal and annual variation of carbon exchange in an evergreen Mediterranean forest in southern France. Global Change Biology **14,** 714–725

133. Sampson, D. A., Janssens, I. A. & Ceulemans, R. Simulated soil CO$_2$ efflux and net ecosystem exchange in a 70-year-old Belgian Scots pine stand using the process model SECRETS. Ann. For. Sci. **58,** 31–46 (2001).

134. Savitzky, A. & Golay, M. Smoothing and Differentiation of Data by Simplified Least Squares Procedures. Analytical chemistry **36,** 1627–1639 (1964).

135. Wahba, G., Wang, Y., Gu, C., Klein, R. & Klein, B. Smoothing spline ANOVA for exponential families, with application to the Wisconsin Epidemiological Study of Diabetic Retinopathy : the 1994 Neyman Memorial Lecture. Ann. Statist. **23,** 1865–1895 (1995).

136. Source areas for scalars and scalar fluxes | SpringerLink. Available at: https://link.springer.com/article/10.1007/BF00713146. (Accessed: 1st August 2018)

137. Pérez, I. A., Sánchez, M. L., García, M. Á. & Pardo, N. Spatial analysis of CO_2 concentration in an unpolluted environment in northern Spain. Journal of Environmental Management **113,** 417–425 (2012).

138. Szczypta, C. et al. Suitability of modelled and remotely sensed essential climate variables for monitoring Euro-Mediterranean droughts. Geosci. Model Dev. **7,** 931–946 (2014).

139. Kountouris, P. et al. Technical Note: Atmospheric CO_2 inversions on the mesoscale using data-driven prior uncertainties: methodology and system evaluation. Atmospheric Chemistry and Physics **18,** 3027–3045 (2018).

140. Hatfield, J. L. & Prueger, J. H. Temperature extremes: Effect on plant growth and development. Weather and Climate Extremes **10,** 4–10 (2015).

141. Temporal variations of surface regional background ozone over Crete Island in the southeast Mediterranean - Kouvarakis - 2000 - Journal of Geophysical Research: Atmospheres - Wiley Online Library.

142. Courtier, P., Freydier, C., Geleyn, J.-F., Rabier, F. & Rochas, M. The Arpege project at Meteo France. (1991).

143. The Concentration and Isotopic Abundances of Carbon Dioxide in the Atmosphere - Keeling - 1960 - Tellus - Wiley Online Library. Available at: https://onlinelibrary.wiley.com/doi/abs/10.1111/j.2153-3490.1960.tb01300.x. (Accessed: 1st August 2018)

144. Giostra, U. et al. The determination of a "regional" atmospheric background mixing ratio for anthropogenic greenhouse gases: A comparison of two independent methods. Atmospheric Environment **45,** 7396–7405 (2011).

145. Ciais, P. et al. The European carbon balance. Part 1: fossil fuel emissions. Global Change Biology **16,** 1395–1408 (2009).

146. Pikridas, M. et al. The Finokalia Aerosol Measurement Experiment – 2008 (FAME-08): an overview. Atmospheric Chemistry and Physics **10,** 6793–6806 (2010).

147. Staufer, J. et al. The first 1-year-long estimate of the Paris region fossil fuel CO_2 emissions based on atmospheric inversion. Atmospheric Chemistry and Physics **16,** 14703–14726 (2016).

148. Saunois, M. et al. The global methane budget 2000–2012. Earth System Science Data **8,** 697–751 (2016).

149. The growth rate and distribution of atmospheric methane - Dlugokencky - 1994 - Journal of Geophysical Research: Atmospheres - Wiley Online Library. Available at: https://agupubs.onlinelibrary.wiley.com/doi/abs/10.1029/94JD01245. (Accessed: 1st August 2018)

150. Broquet, G. et al. The potential of satellite spectro-imagery for monitoring CO_2 emissions from large cities. Atmos. Meas. Tech. **11,** 681–708 (2018).

151. Schmidt, M., Graul, R., Sartorius, H. & Levin, I. The Schauinsland CO_2 record: 30 years of continental observations and their implications for the variability of the European CO_2 budget. Journal of Geophysical Research: Atmospheres **108,**

152. Corbin, K. D., Denning, A. S. & Gurney, K. R. The space and time impacts on U.S. regional atmospheric CO_2 concentrations from a high resolution fossil fuel CO_2 emissions inventory. Tellus B **62,** 506–511

153. Kaplan, J. O. & Melton, J. R. The Wetland and Wetland CH_4 Inter-comparison of Models Project (WETCHIMP) data archive. (2018). doi:https://doi.org/10.1594/PANGAEA.887208

154. Lopez, M. et al. Three years of semicontinuous greenhouse gas measurements at the Puy de Dôme station (central France). Atmos. Meas. Tech. **8,** 3941–3958 (2015).

155. Gerbig, C. et al. Toward constraining regional-scale fluxes of CO_2 with atmospheric observations over a continent: 2. Analysis of COBRA data using a receptor-oriented framework. Journal of Geophysical Research: Atmospheres **108,**

156. Berchet, A. et al. Towards better error statistics for atmospheric inversions of methane surface fluxes. Atmospheric Chemistry and Physics **13,** 7115–7132 (2013).

157. Towards robust regional estimates of CO_2 sources and sinks using atmospheric transport models | Nature. Available at: https://www.nature.com/articles/415626a. (Accessed: 2nd August 2018)

158. Towards robust regional estimates of CO_2 sources and sinks using atmospheric transport models | Nature. Available at: https://www.nature.com/articles/415626a. (Accessed: 2nd August 2018)

159. van Leer, B. Towards the ultimate conservative difference scheme. V. A second-order sequel to Godunov's method. Journal of Computational Physics **32,** 101–136 (1979).

160. TransCom 3 CO_2 inversion intercomparison: 1. Annual mean control results and sensitivity to transport and prior flux information - GURNEY - 2003 - Tellus B - Wiley Online Library. Available at: https://onlinelibrary.wiley.com/doi/full/10.1034/j.1600-0889.2003.00049.x. (Accessed: 2nd August 2018)

161. Patra, P. K. et al. TransCom model simulations of hourly atmospheric CO_2: Analysis of synoptic-scale variations for the period 2002–2003. Global Biogeochemical Cycles **22,**

162. TransCom model simulations of hourly atmospheric CO_2: Experimental overview and diurnal cycle results for 2002 - Law - 2008 - Global Biogeochemical Cycles - Wiley Online Library. Available at: https://agupubs.onlinelibrary.wiley.com/doi/full/10.1029/2007GB003050. (Accessed: 29th July 2018)

163. TransCom model simulations of hourly atmospheric CO_2: Experimental overview and diurnal cycle results for 2002 - Law - 2008 - Global Biogeochemical Cycles - Wiley Online Library. Available at: https://agupubs.onlinelibrary.wiley.com/doi/full/10.1029/2007GB003050. (Accessed: 2nd August 2018)

164. Patra, P. K. et al. Transport mechanisms for synoptic, seasonal and interannual SF_6 variations and 'age' of air in troposphere. Atmospheric Chemistry and Physics **9,** 1209–1225 (2009).

165. Chevillard, A. et al. Transport of 222Rn using the regional model REMO: a detailed comparison with measurements over Europe. Tellus B: Chemical and Physical Meteorology **54,** 850–871 (2002).

166. Tropospheric methane in northern Finland: seasonal variations, transport patterns and correlations with other trace gases: Tellus B: Chemical and Physical Meteorology: Vol 59, No 2. Available at: https://www.tandfonline.com/doi/abs/10.1111/j.1600-0889.2006.00248.x. (Accessed: 29th July 2018)

167. Saikawa, E. et al. Uncertainties in emissions estimates of greenhouse gases and air pollutants in India and their impacts on regional air quality. Environ. Res. Lett. **12,** 065002 (2017).

168. Hogue, S., Marland, E., Andres, R. J., Marland, G. & Woodard, D. Uncertainty in gridded CO_2 emissions estimates. Earth's Future **4,** 225–239

169. Kopanakis, I. et al. Variability of ozone in the Eastern Mediterranean during a 7-year study. Air Qual Atmos Health **9,** 461–470 (2016).

170. Gerbig, C., Lin, J. C., Munger, J. W. & Wofsy, S. C. What can tracer observations in the continental boundary layer tell us about surface-atmosphere fluxes? Atmospheric Chemistry and Physics **6,** 539–554 (2006).

171. WMO Greenhouse Gas Bulletin (published annually). World Meteorological Organization (2015). Available at: https://public.wmo.int/en/resources/library/wmo-greenhouse-gas-bulletin. (Accessed: 1st August 2018)

172. Schaap, M., M. Roemer, F. Sauter, G. Boersen, R. Timmermans, P.J.H. Builtjes, LOTOS-EUROS: Documentation, TNO report B&O-A, 2005-297, Apeldoorn 2005.

VI.1 Appendix

VI.1.1 Chapter II

Sites	Species	Contaminated data percentages (%)									
		β = 1	β = 2	β = 3	β = 4	β = 5	β = 6	β = 7	β = 8	β = 9	β = 10
AMS	CH_4	15	5.2	2.3	1.2	0.7	0.4	0.3	0.2	0.2	0.1
	CO_2	18.3	10.6	6.9	4.8	3.5	2.7	2	1.5	1.2	1
FKL	CH_4	15.5	8.1	4.8	3.7	2	1.5	1	0.8	0.6	0.4
	CO_2	15.6	7.5	4.2	2.6	1.7	1.2	0.9	0.6	0.5	0.4
	CO	13.4	3.4	1.2	0.6	0.4	0.3	0.2	0.1	0.1	0.1
OPE	CH_4	4.3	2.5	1.8	1.3	1	0.8	0.7	0.5	0.5	0.4
	CO_2	4.1	2.3	1.6	1.2	0.9	0.8	0.7	0.5	0.5	0.4
	CO	3.6	1.6	1	0.7	0.6	0.5	0.4	0.3	0.3	0.3
PDM	CH_4	19.5	11.5	7.8	5.6	4.3	3.4	2.7	2.2	1.9	1.6
	CO_2	18	9.1	5.2	3.6	2.2	1.5	1.1	0.8	0.6	0.4
	CO	14.5	3.9	1.5	0.8	0.5	0.3	0.2	0.2	0.1	0.1

Table SII.1: Sensitivity of REBS spike detection method for β ranging between 1 and 10 for the four stations and all species during the year 2015.

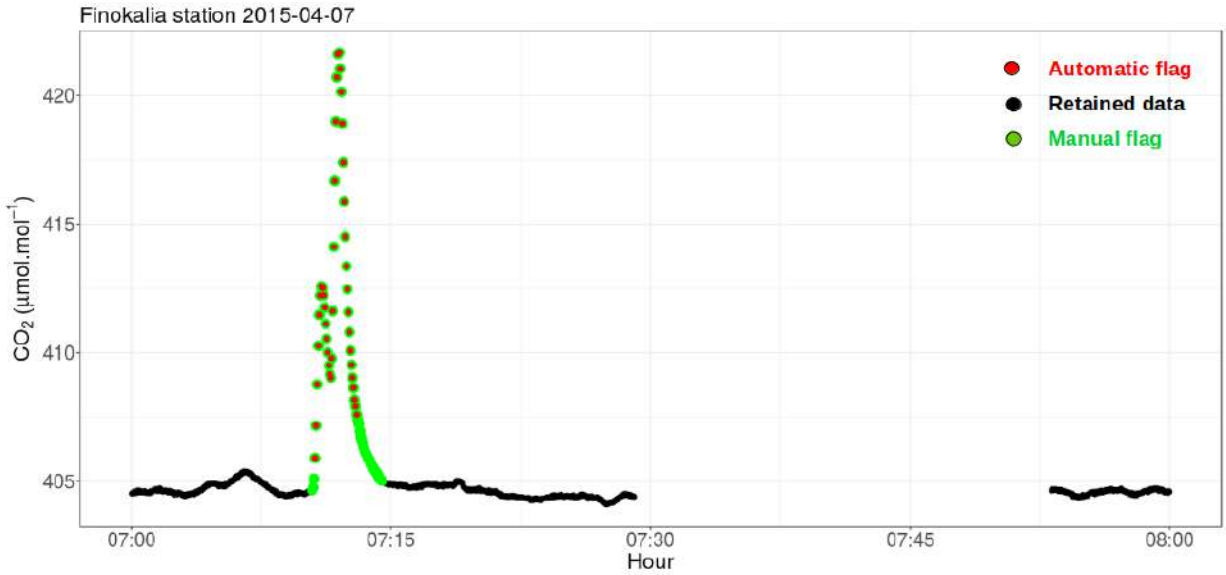

Figure SII.1: Comparison between manual and automatic flagging (SD method), at Finokalia station. Green and red colors represent data flagged by manual and automatic flagging respectively, black color shows the retained data.

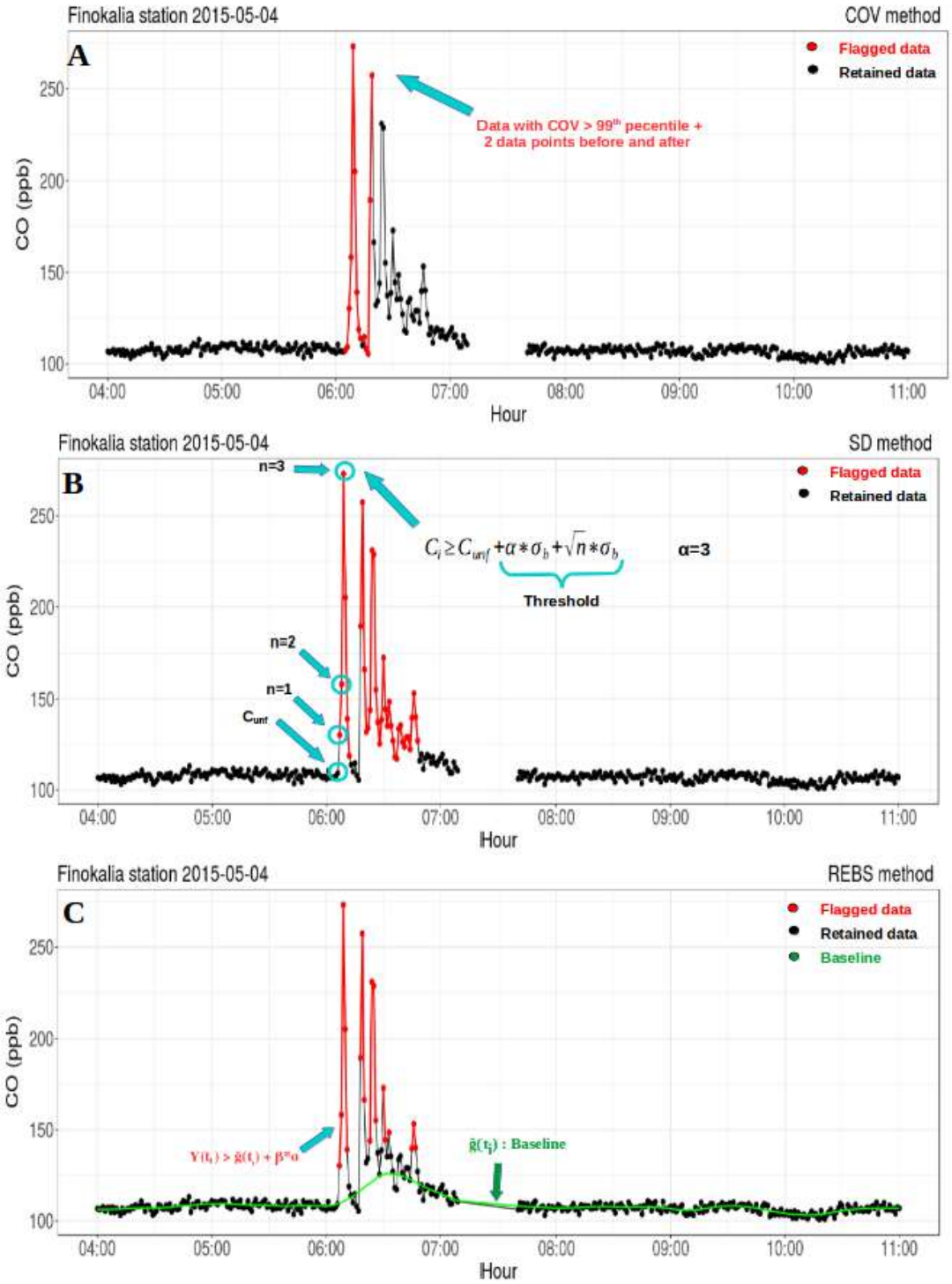

Figure SII.2: Example of a known contamination episode (between 6:00 a.m and 7:00 a.m) for CO measurements detected by COV method (A), SD method (B), and REBS method (C)

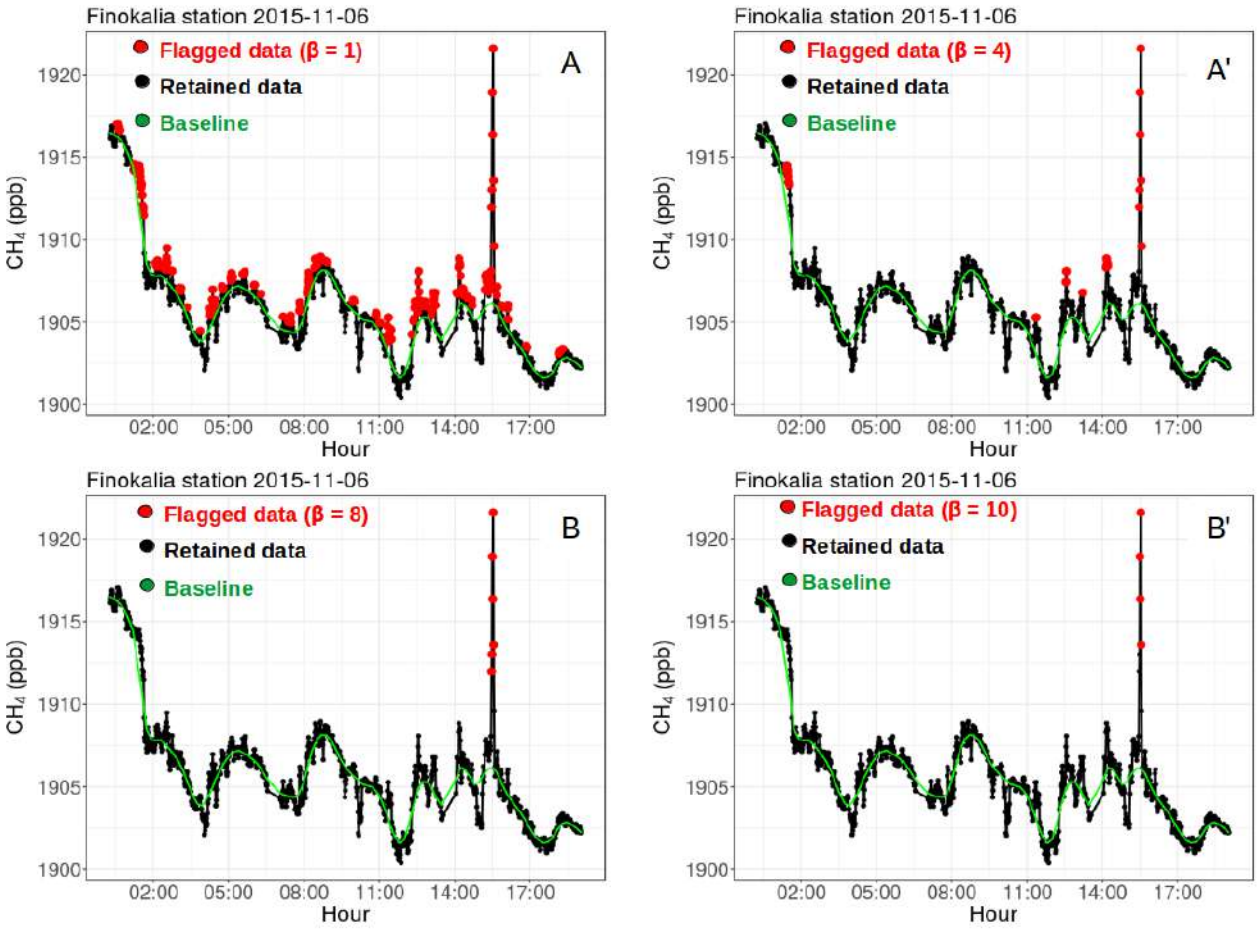

Figure SII.3: comparison between $\beta = 1, 4, 8,$ and 10 for REBS method. Red represents detected data applied on FKL measurement 6th of November 2014.

Figure SII.4: mage of PDM station showing the location of AN-1 site (T55 building), and AN-2 (TDF building). 200 m separate the two buildings

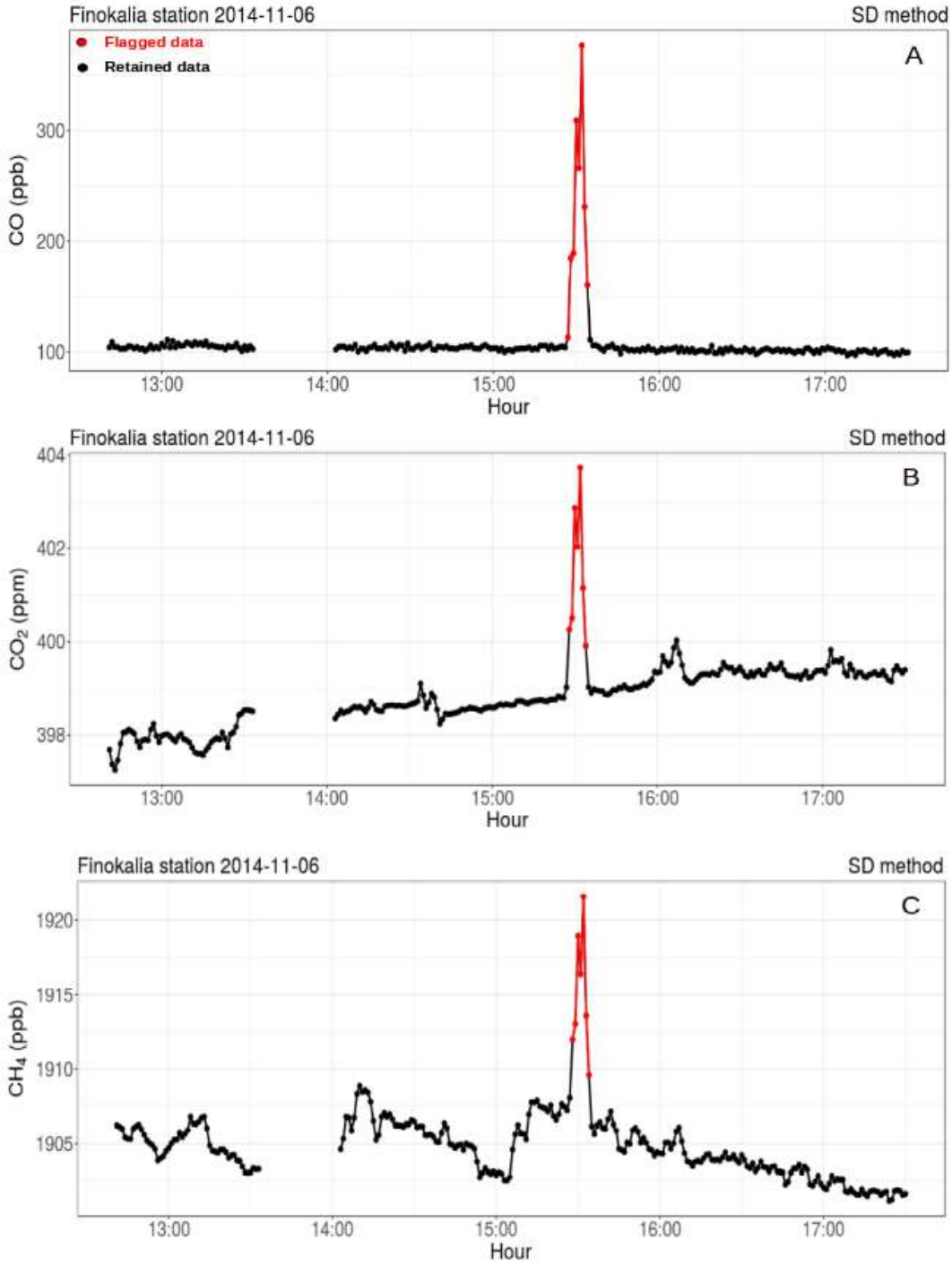

Figure SII.5: CO, CO_2 and CH_4 (A, B, and C) measurements during a waste burning episode (red points) at Finokalia from 1 p.m. to 5:30 p.m. on the 6th of November 2014

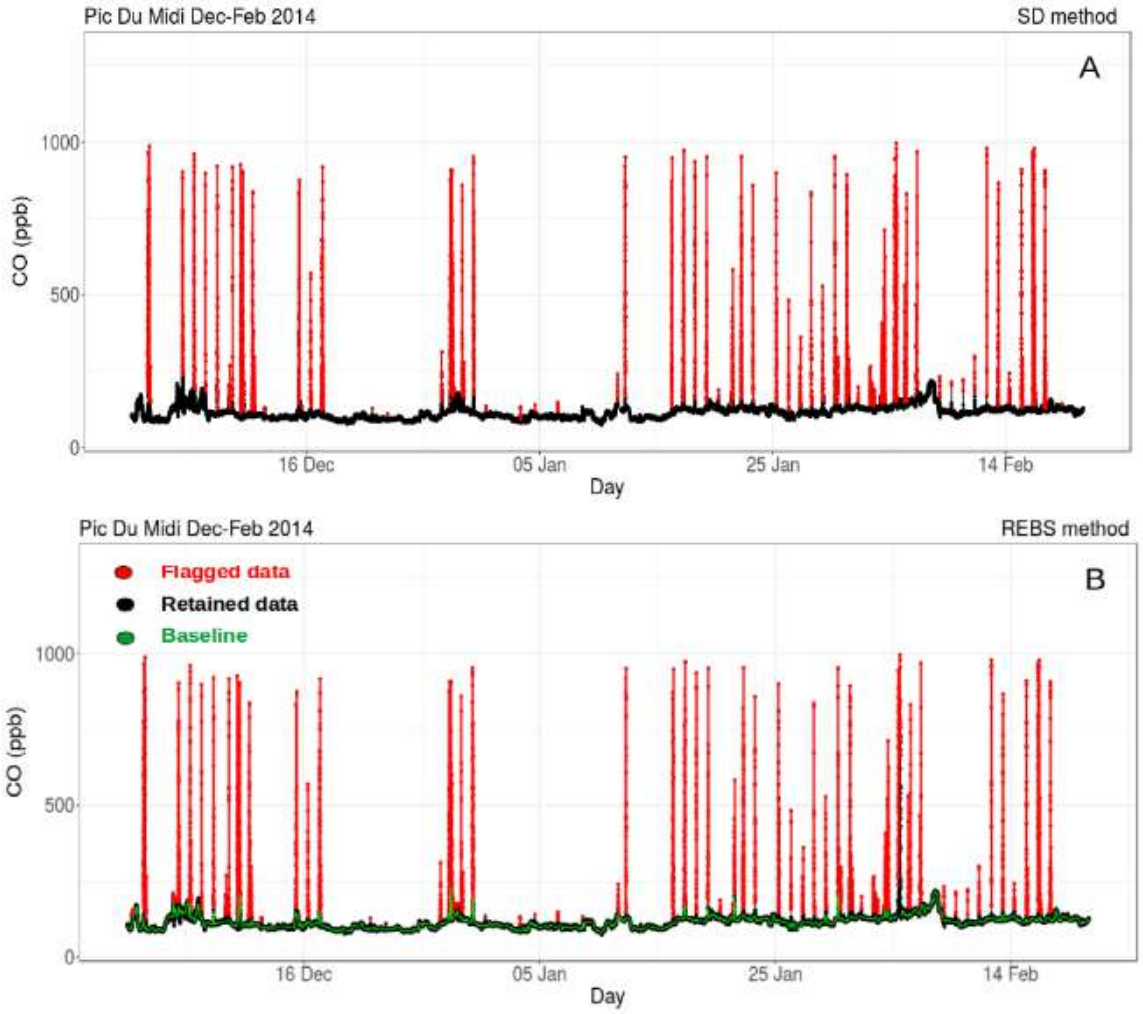

Figure SII.6: CO measurements from December to February 2014 at Pic Du Midi. Black (red) data points are the retained (flagged) measurements detected by SD method (A), and REBS method (B). The contaminated data linked to the snow removal are characterized by very high CO concentrations up to 1000 ppb.

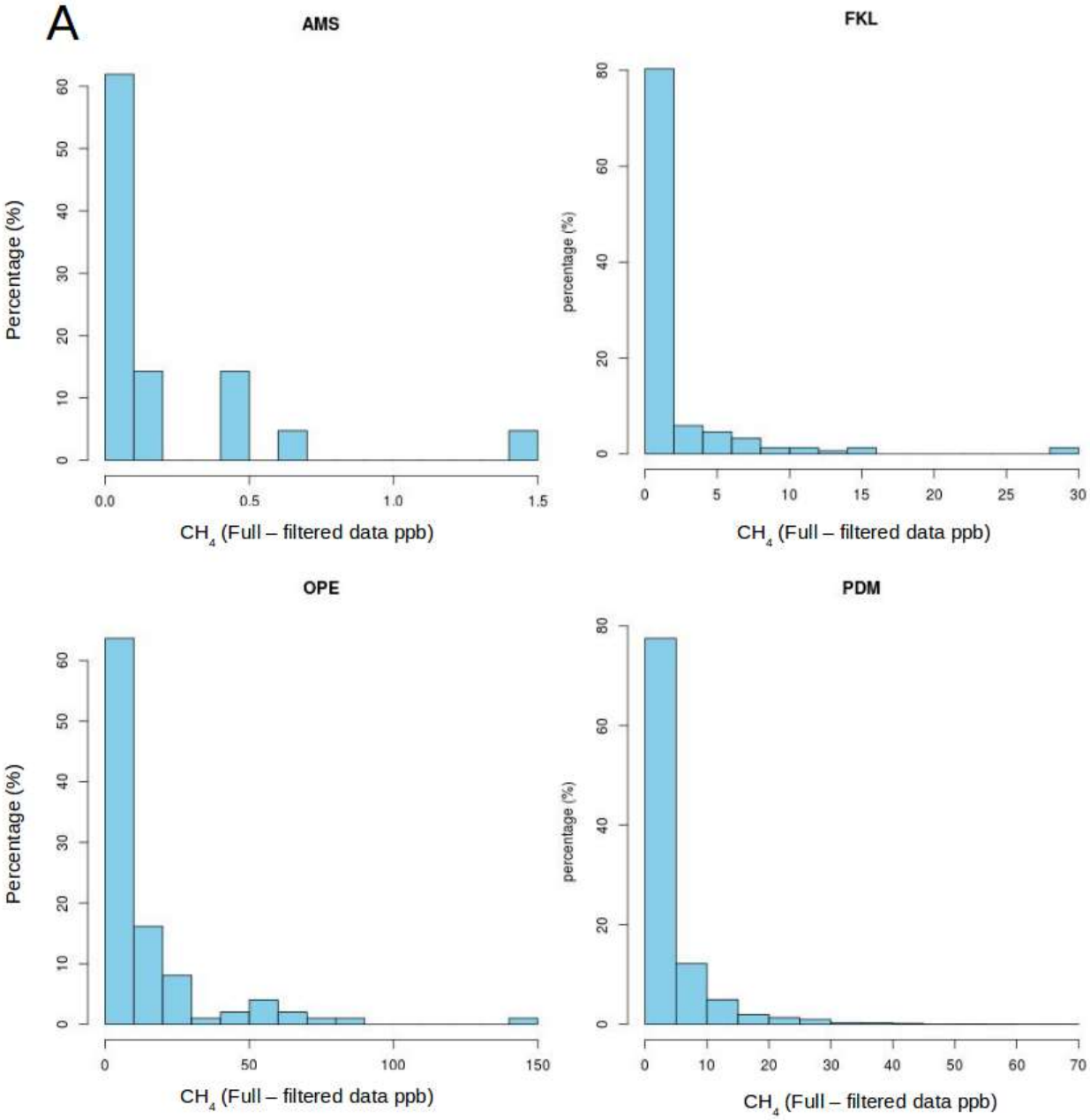
A
AMS
Percentage (%)
0
10
20
30
40
50
60
0.0
0.5
1.0
1.5
CH4 (Full – filtered data ppb)
FKL
percentage (%)
0
20
40
60
80
0
5
10
15
20
25
30
CH4 (Full – filtered data ppb)
OPE
Percentage (%)
0
10
20
30
40
50
60
0
50
100
150
CH4 (Full – filtered data ppb)
PDM
percentage (%)
0
20
40
60
80
0
10
20
30
40
50
60
70
CH4 (Full – filtered data ppb)

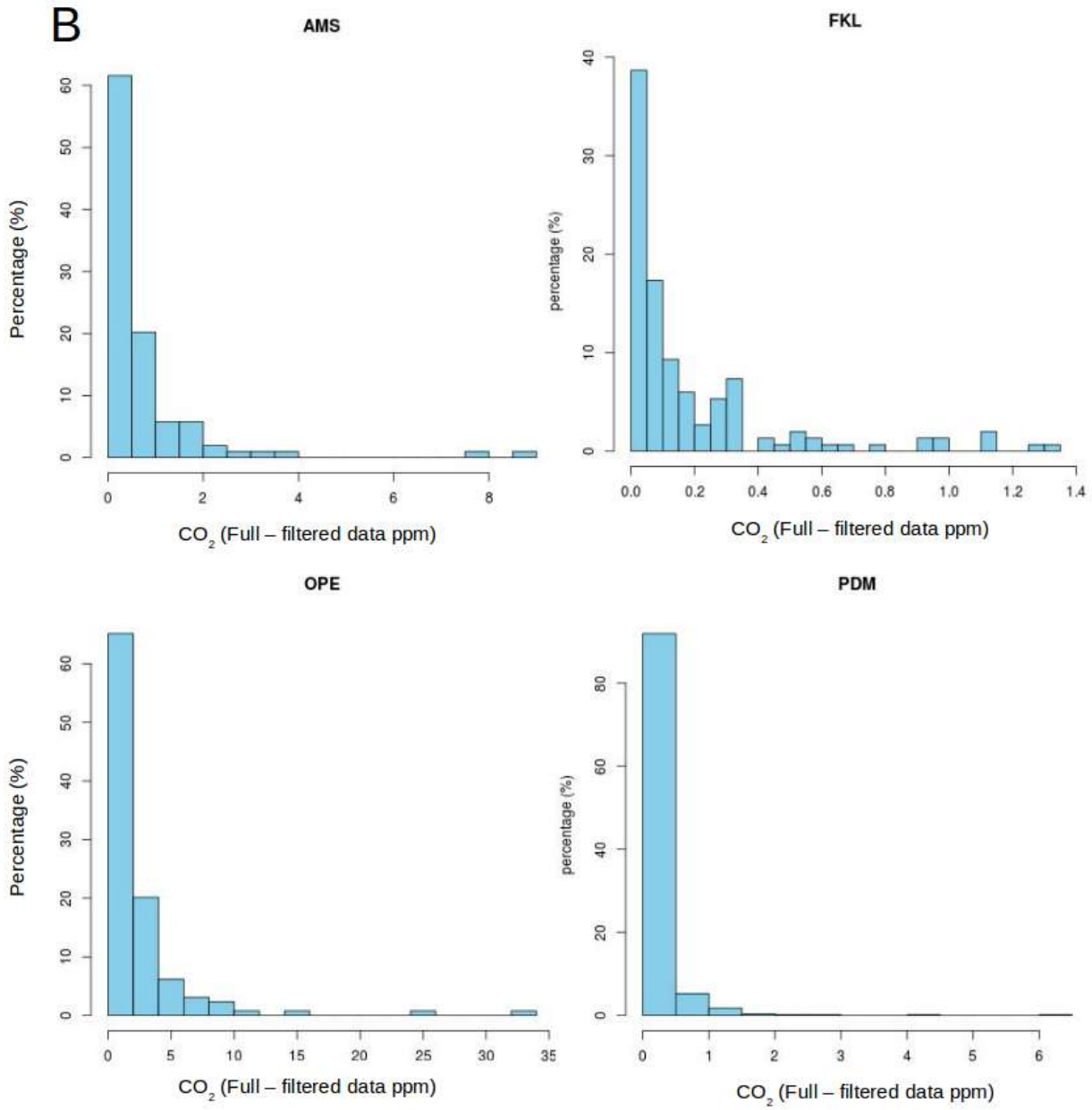

Figure SII.7: Histograms of differences between filtered and the non-filtered time-series averaged at a hourly scale at OPE for CH_4 (plot A), CO_2 (Plot B), and CO (plot C). The x axis represents the value of differences in (ppm) for CO_2 and (ppb) for CH_4 and CO. The y axis represents the percentage of the impacted hours

VI.1.2 Chapter III

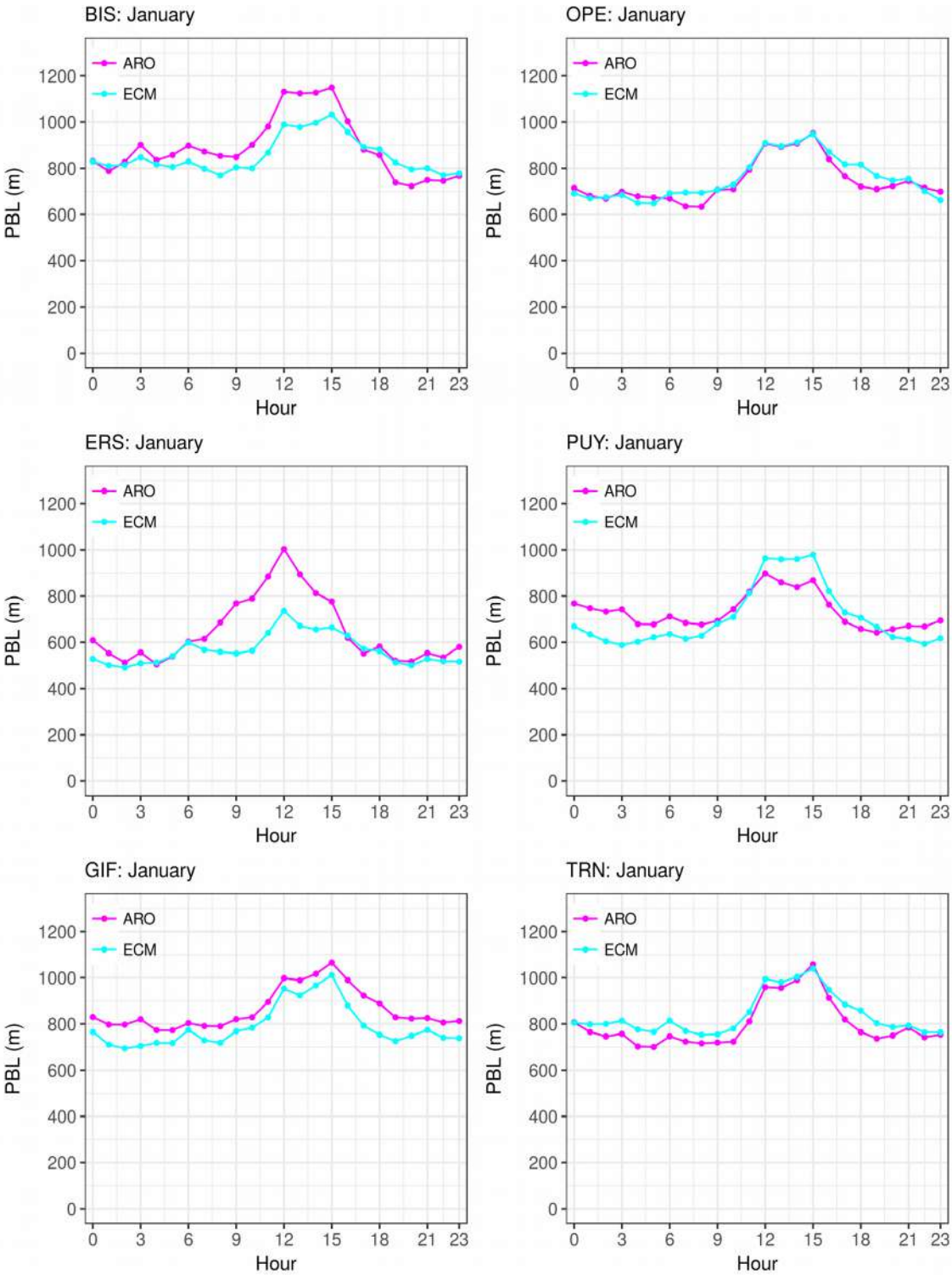

Figure SIII.1: Simulated boundary layer height (PBL) diurnal cycle at the French sites (6 stations) for Janury 2014.

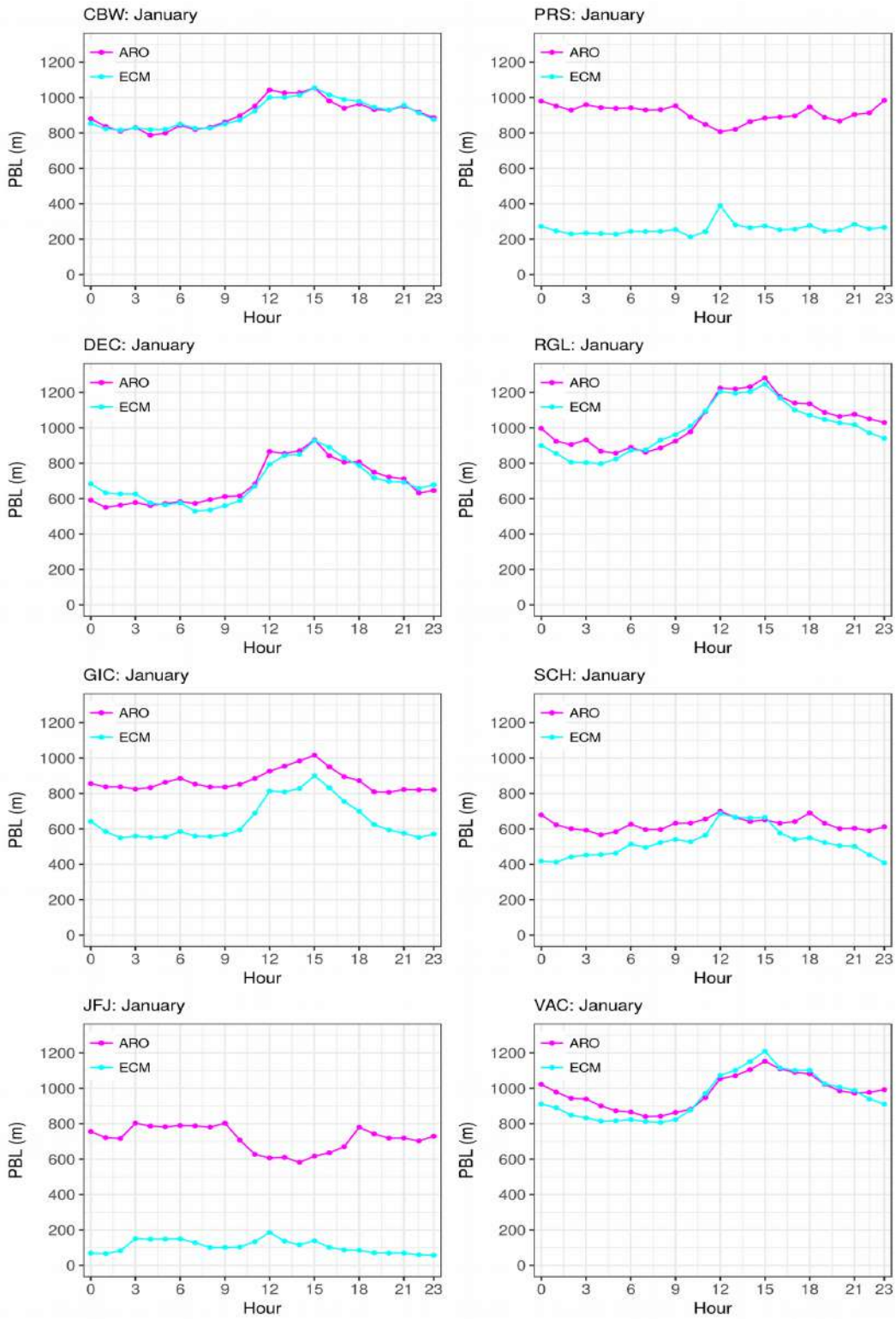

Figure SIII.2: Simulated boundary layer height (PBL) diurnal cycle at the sites outside of France (8 stations) for Janury 2014.

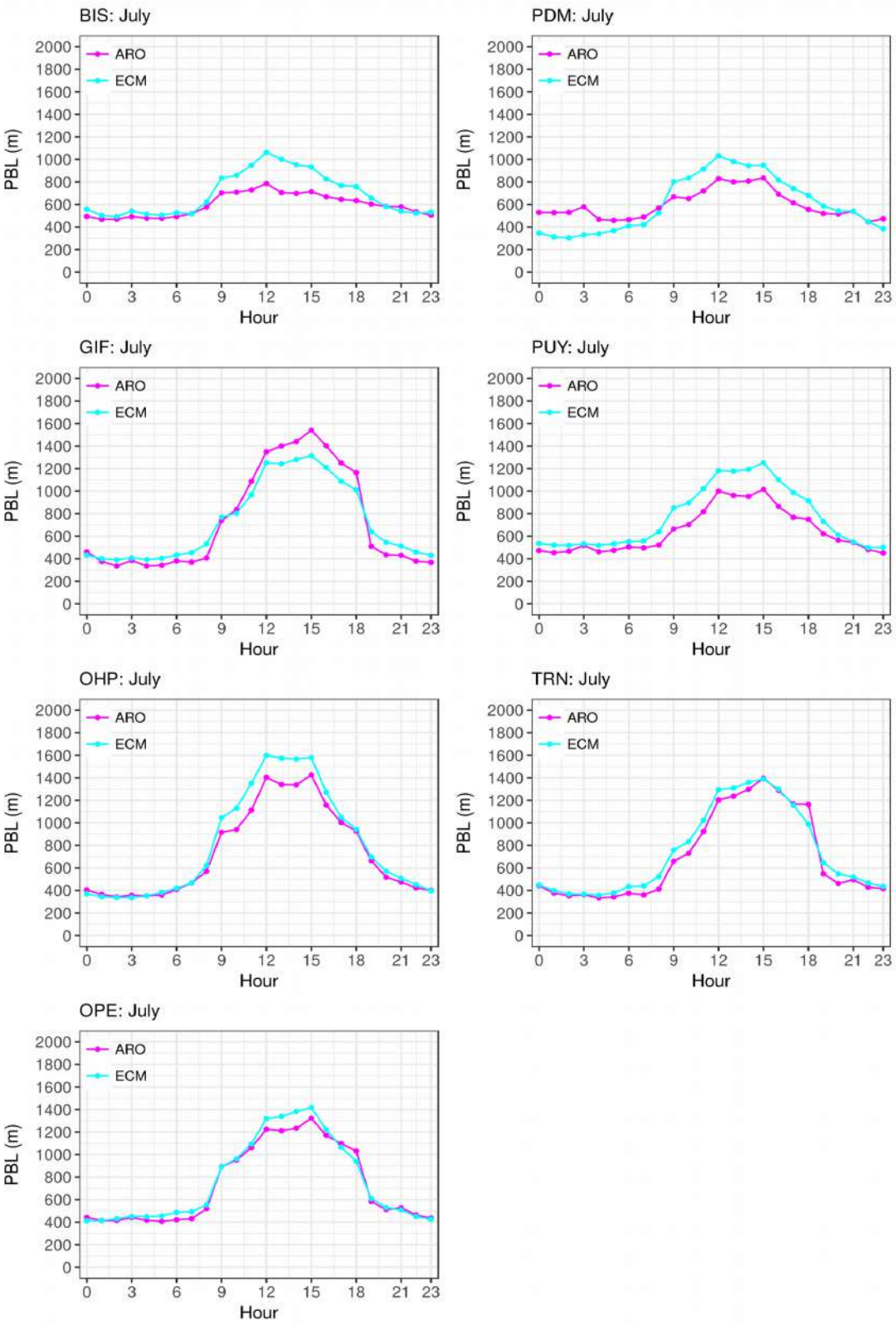

Figure SIII.3: Simulated boundary layer height (PBL) diurnal cycle at the French sites (6 stations) for July 2014.

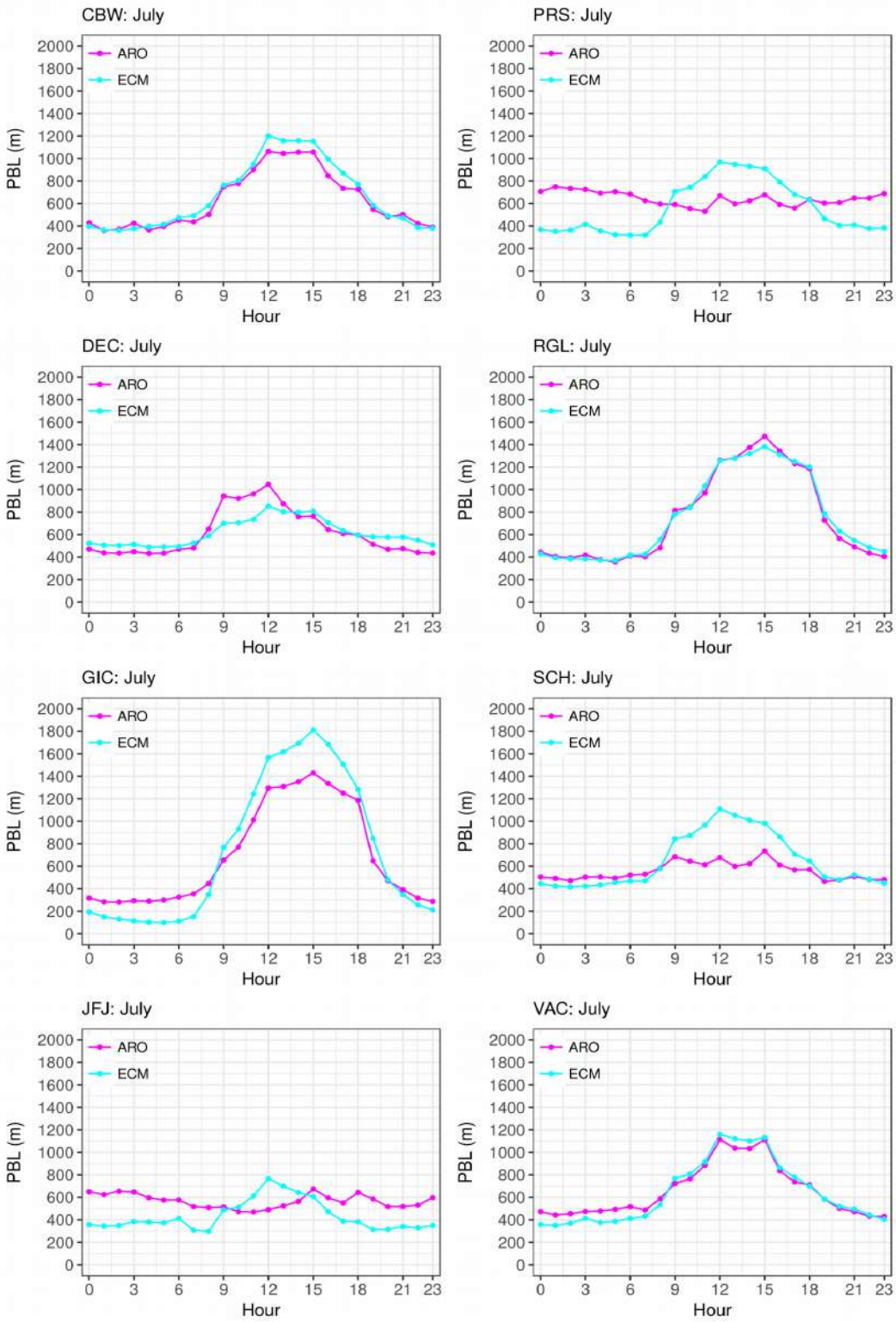

Figure SIII.4: Simulated boundary layer height (PBL) diurnal cycle at the sites outside of France (8 stations) for July 2014.

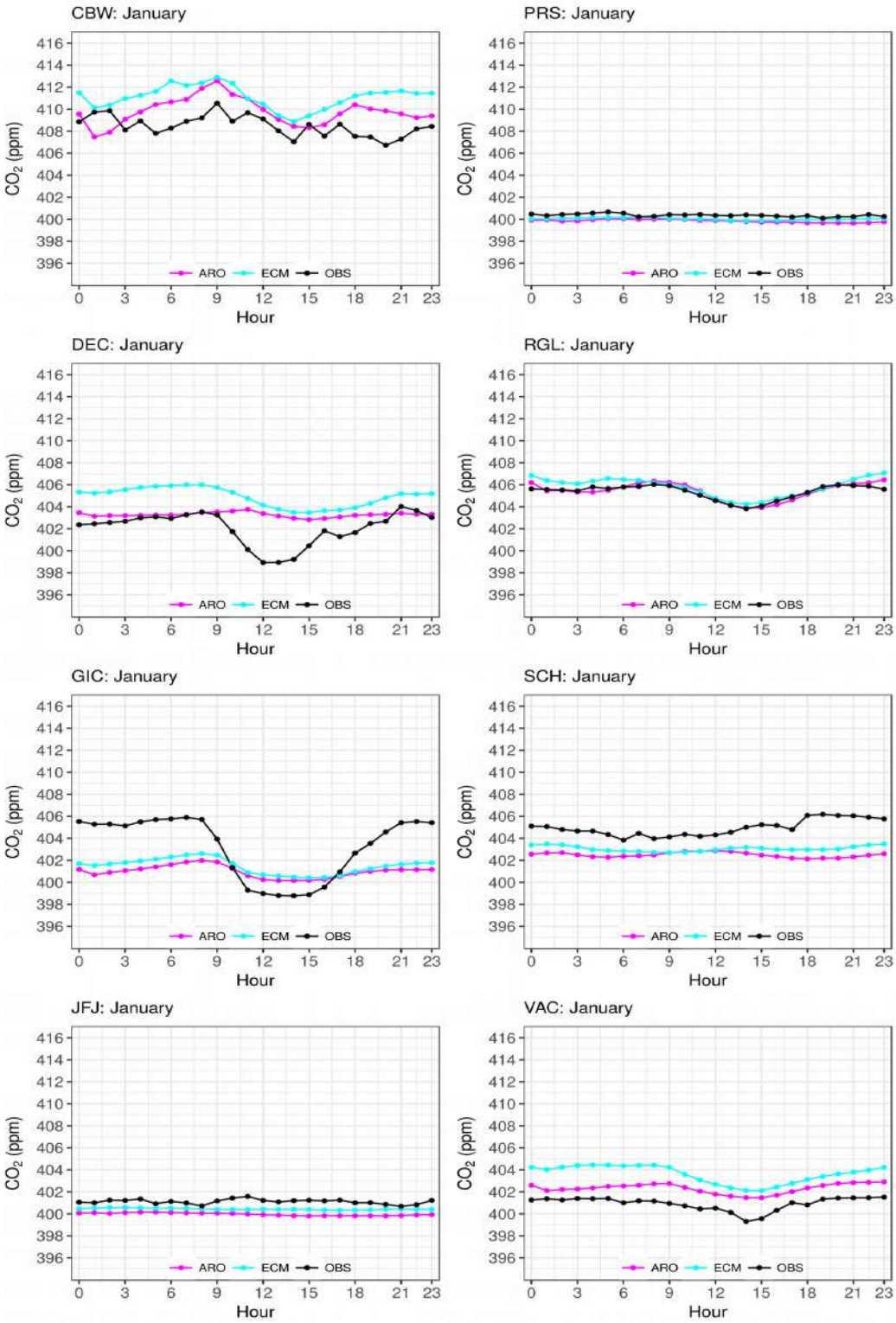

Figure SIII.5: CO_2 average diurnal cycle at CBW, DEC, GIC, JFJ, PRS, RGL, SCH, and VAC for the observed (black) and the simulated (red and blue for AROME and ECMWF respectivly) during January.

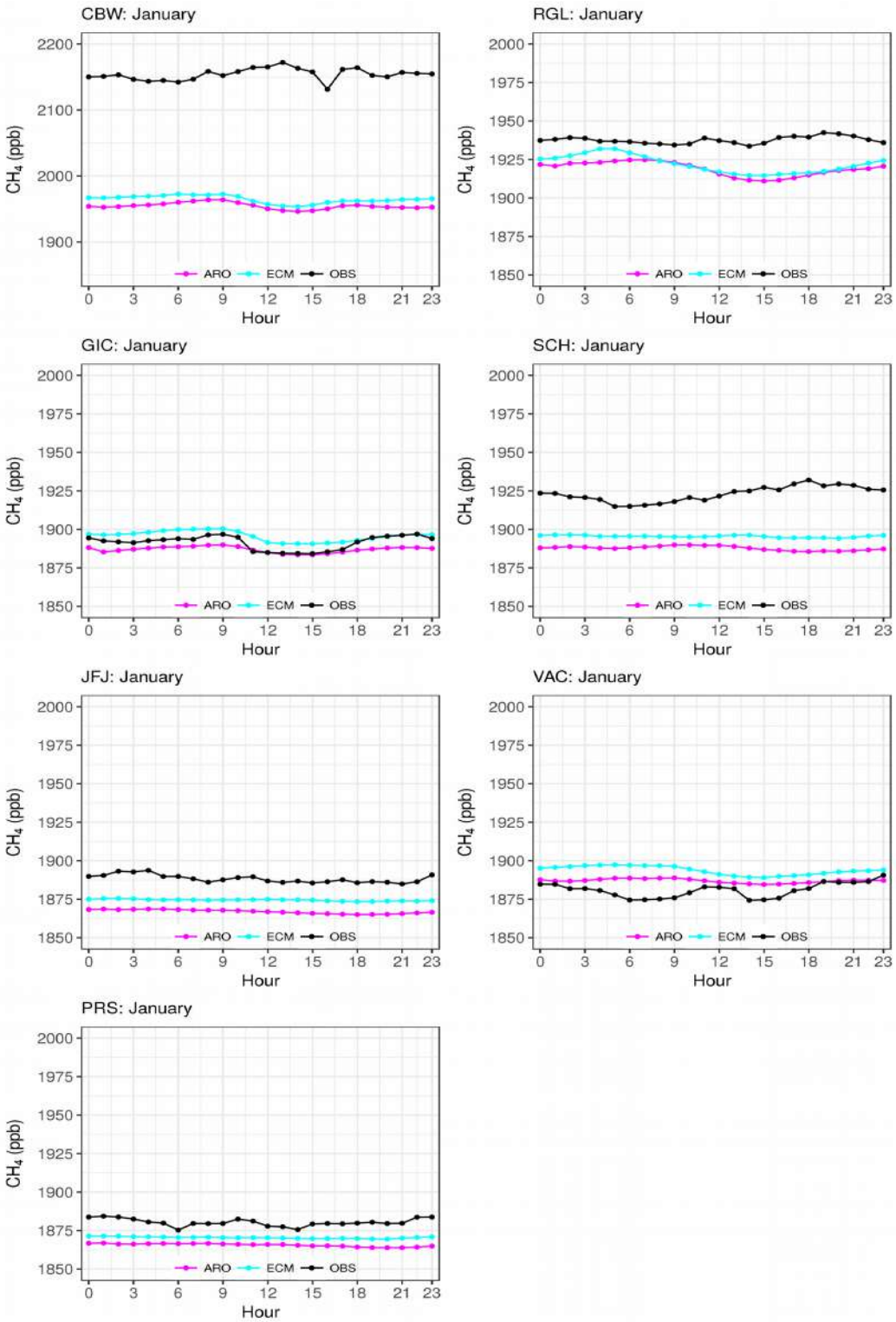

Figure SIII.6: CH_4 average diurnal cycle at CBW, GIC, JFJ, PRS, RGL, SCH, and VAC for the observed (black) and the simulated (red and blue for AROME and ECMWF respectivly) during January.

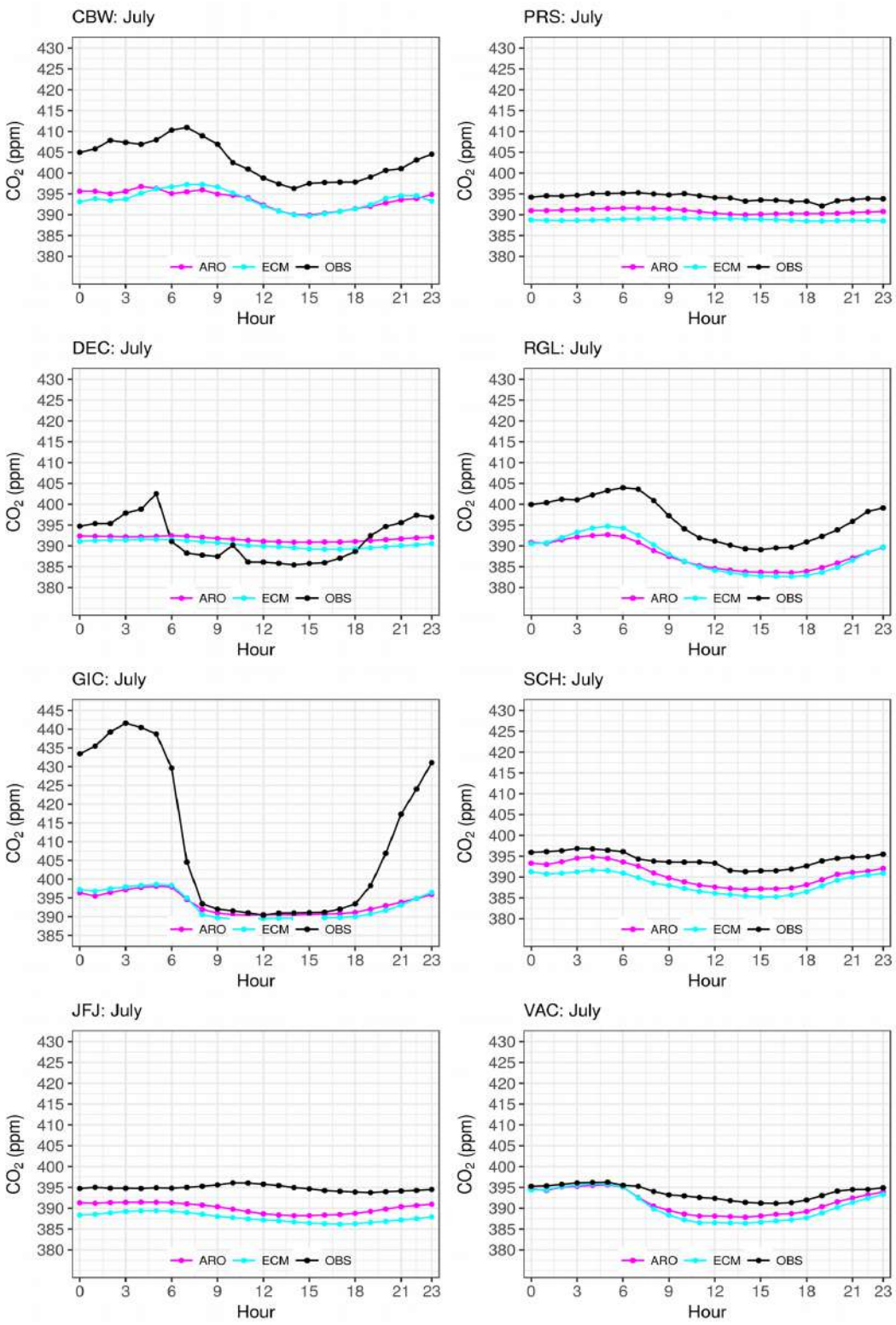

Figure SIII.7: CO_2 average diurnal cycle at CBW, DEC, GIC, JFJ, PRS, RGL, SCH, and VAC for the observed (black) and the simulated (red and blue for AROME and ECMWF respectivly) during July.

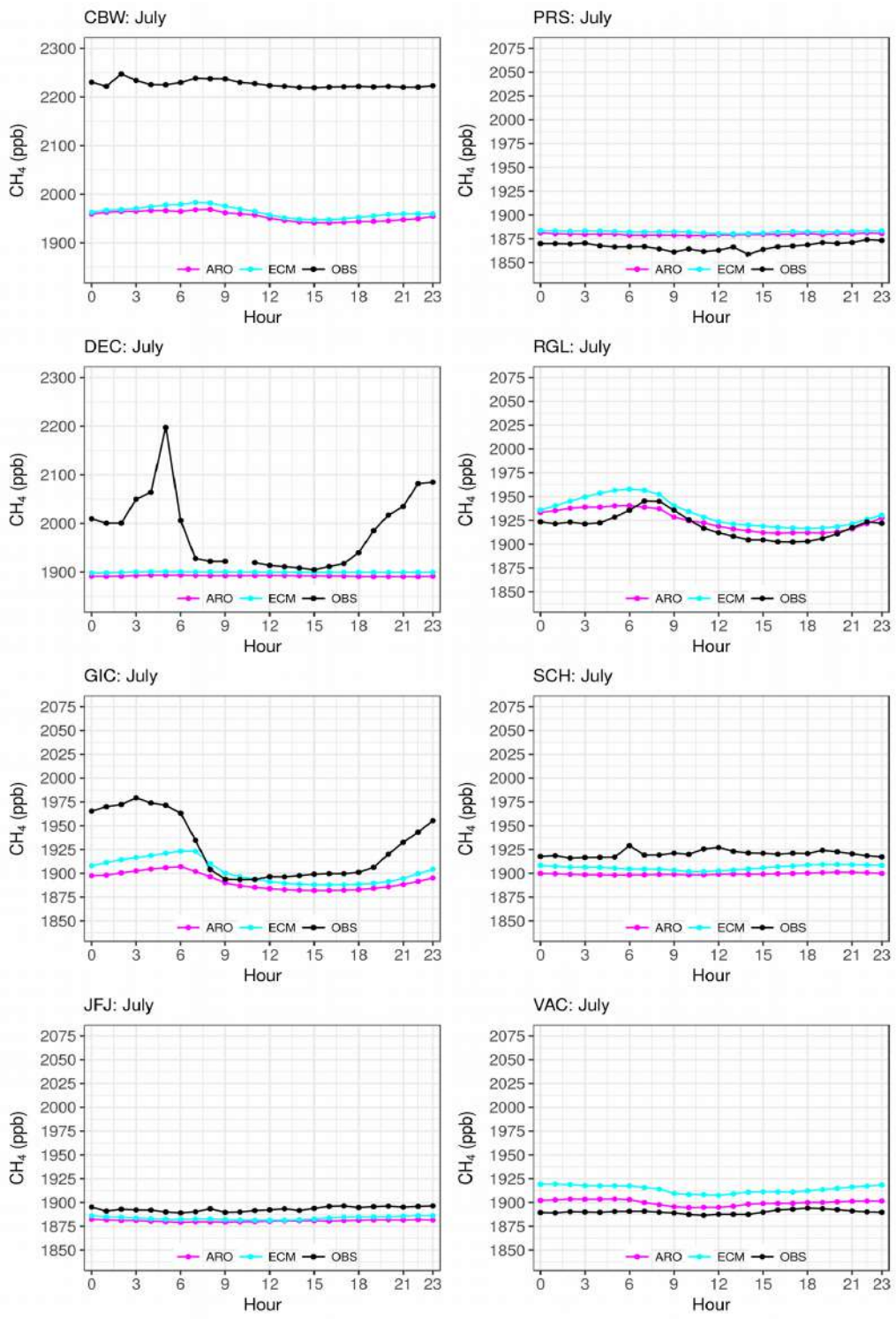

Figure SIII.8: CH_4 average diurnal cycle at CBW, DEC, GIC, JFJ, PRS, RGL, SCH, and VAC for the observed (black) and the simulated (red and blue for AROME and ECMWF respectivly) during July.

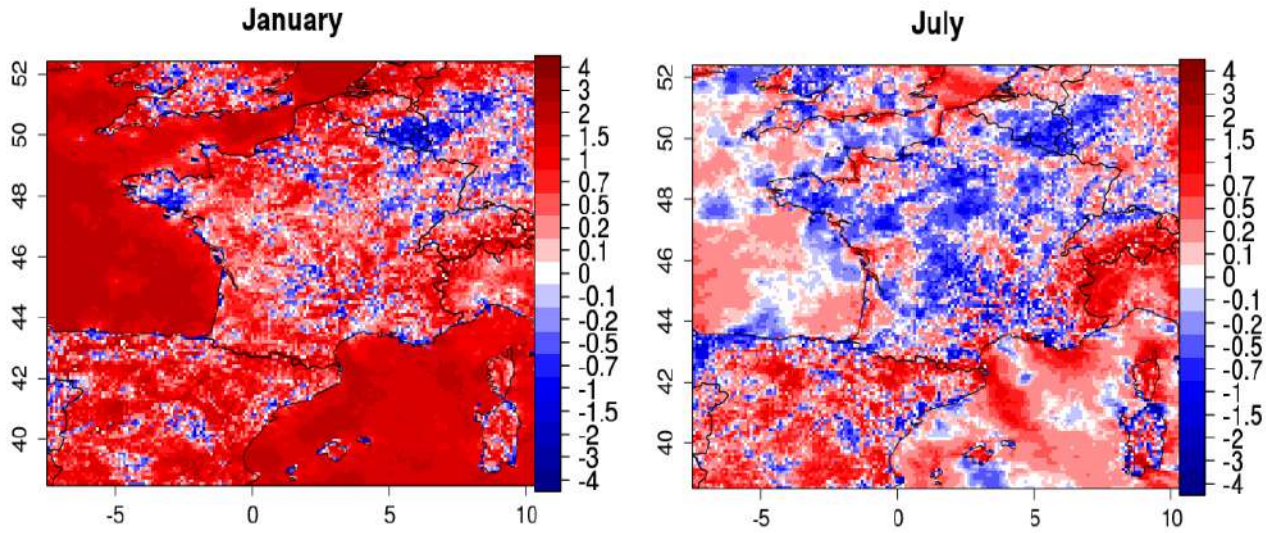

Figure SIII.9: Spatial distribution of the wind speed monthly differences (m/s) between the two meteorological models (AROME minus ECMWF) for January and July.

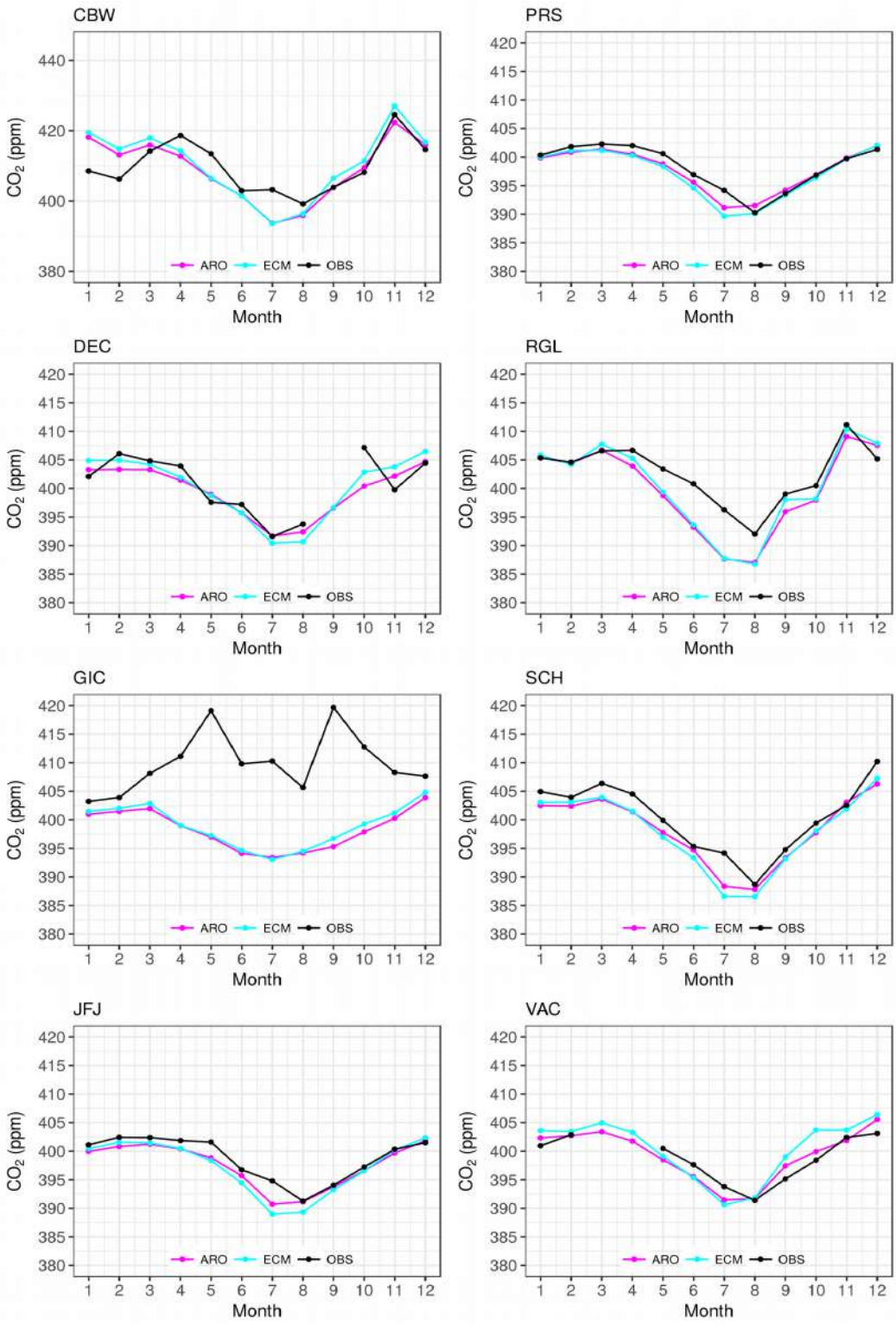

Figure SIII.10: CO_2 average seasonal cycle at CBW, DEC, GIC, JFJ, PRS, RGL, SCH, and VAC for the observed (black) and the simulated (red and blue for AROME and ECMWF respectivly).

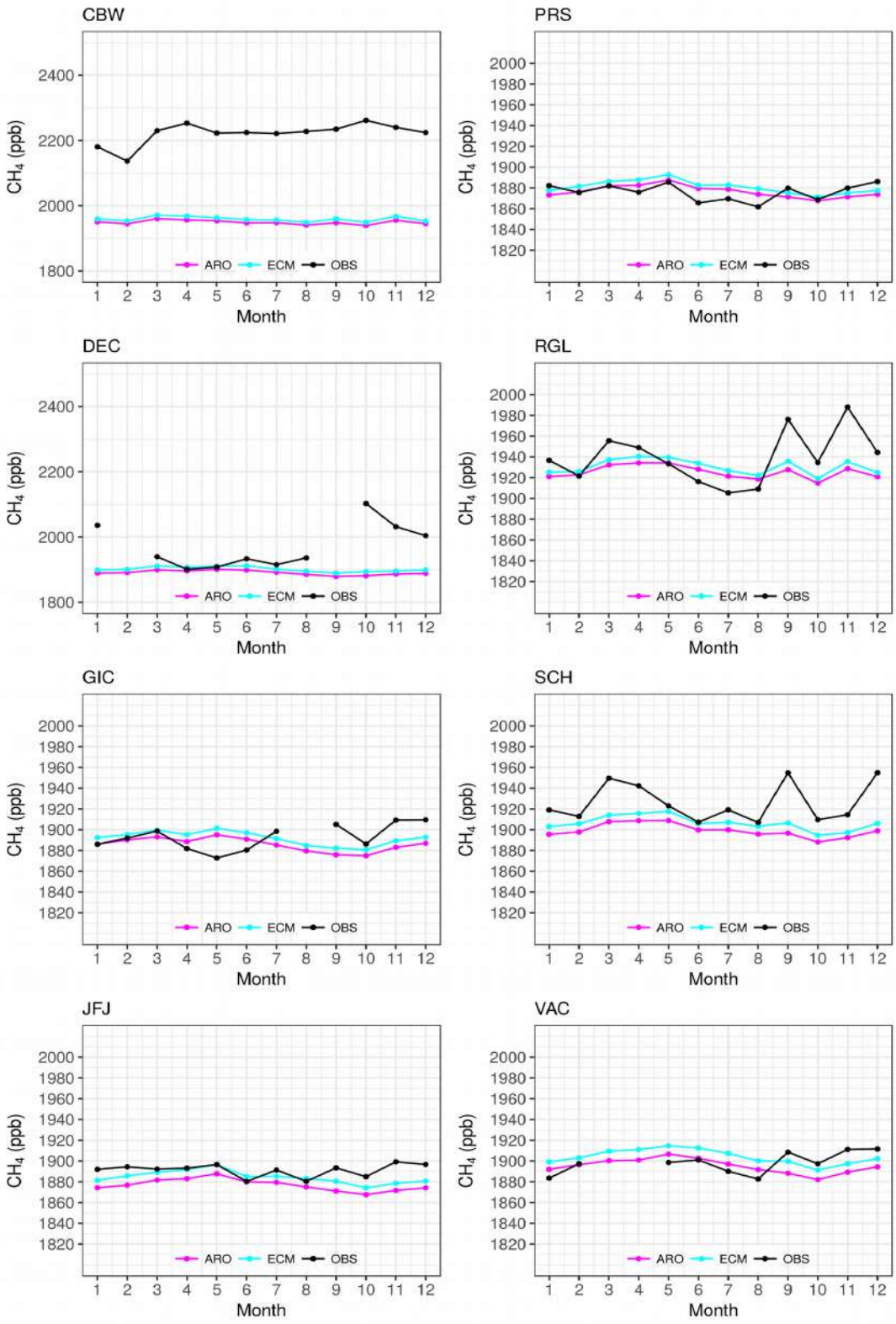

Figure SIII.11: CH_4 average seasonal cycle at CBW, DEC, GIC, JFJ, PRS, RGL, SCH, and VAC for the observed (black) and the simulated (red and blue for AROME and ECMWF respectivly).

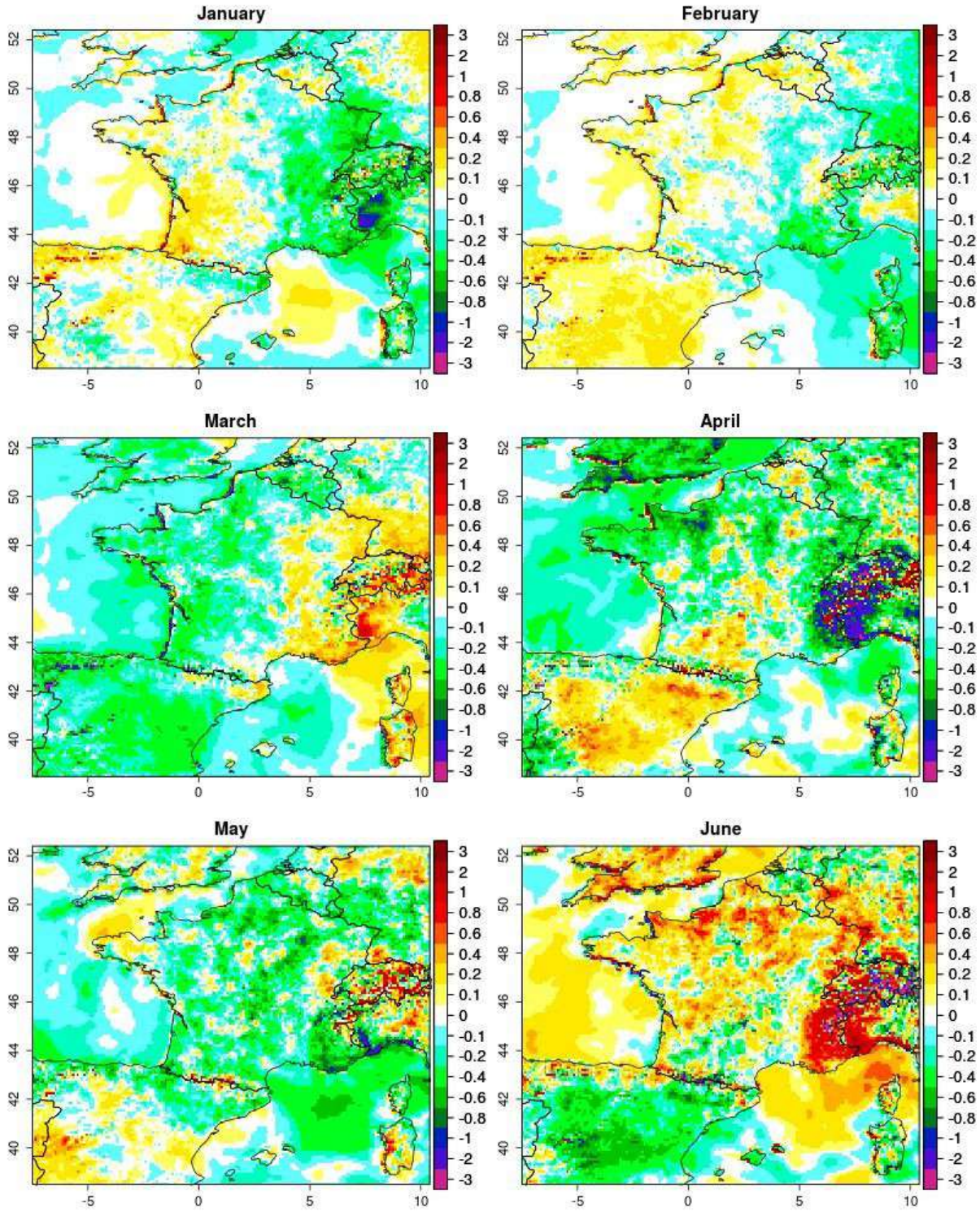

Figure SIII.12: Spatial distribution of CO_2 monthly differences (ppm) between the two meteorological models (AROME minus ECMWF), using the data from 12:00 to 18:00 at the first level of the model, from January to June.

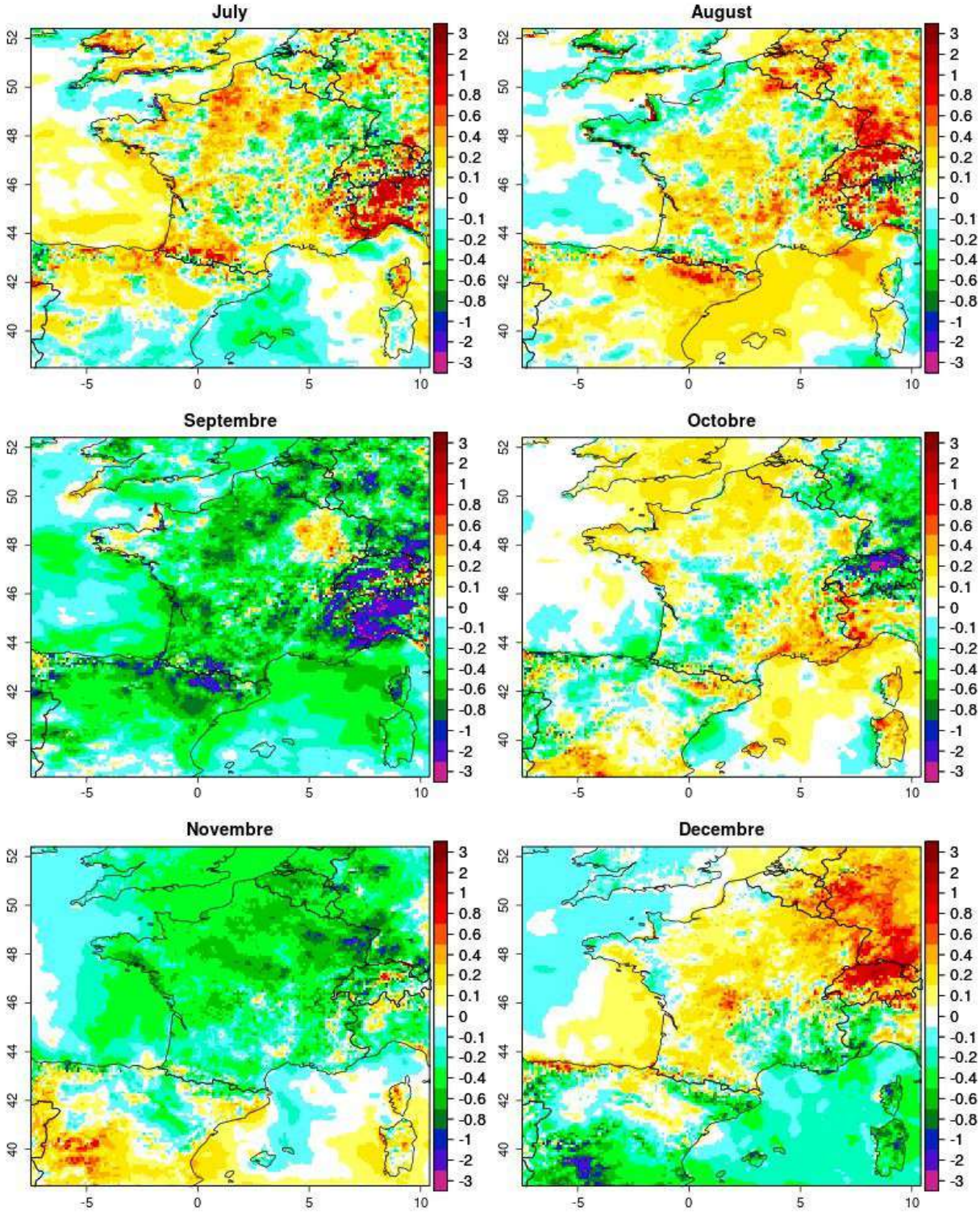

Figure SIII.13: Spatial distribution of CO_2 monthly differences (ppm) between the two meteorological models (AROME minus ECMWF), using the data from 12:00 to 18:00 at the first level of the model, from July to Decembre.

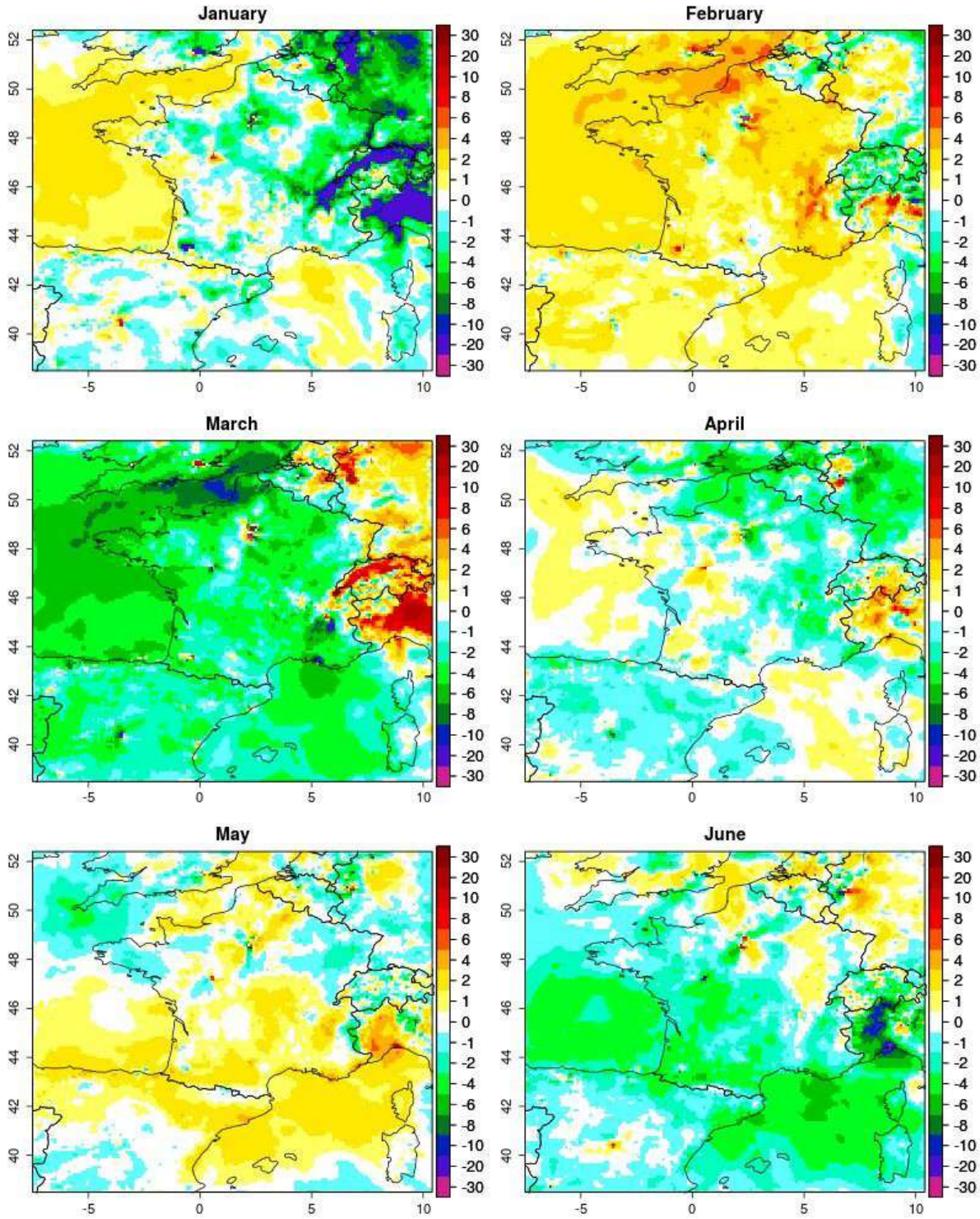

Figure SIII.14: Spatial distribution of the CH_4 monthly differences (ppb) between the two meteorological models (AROME minus ECMWF), using the data from 12:00 to 18:00 at the first level of the model, from January to June.

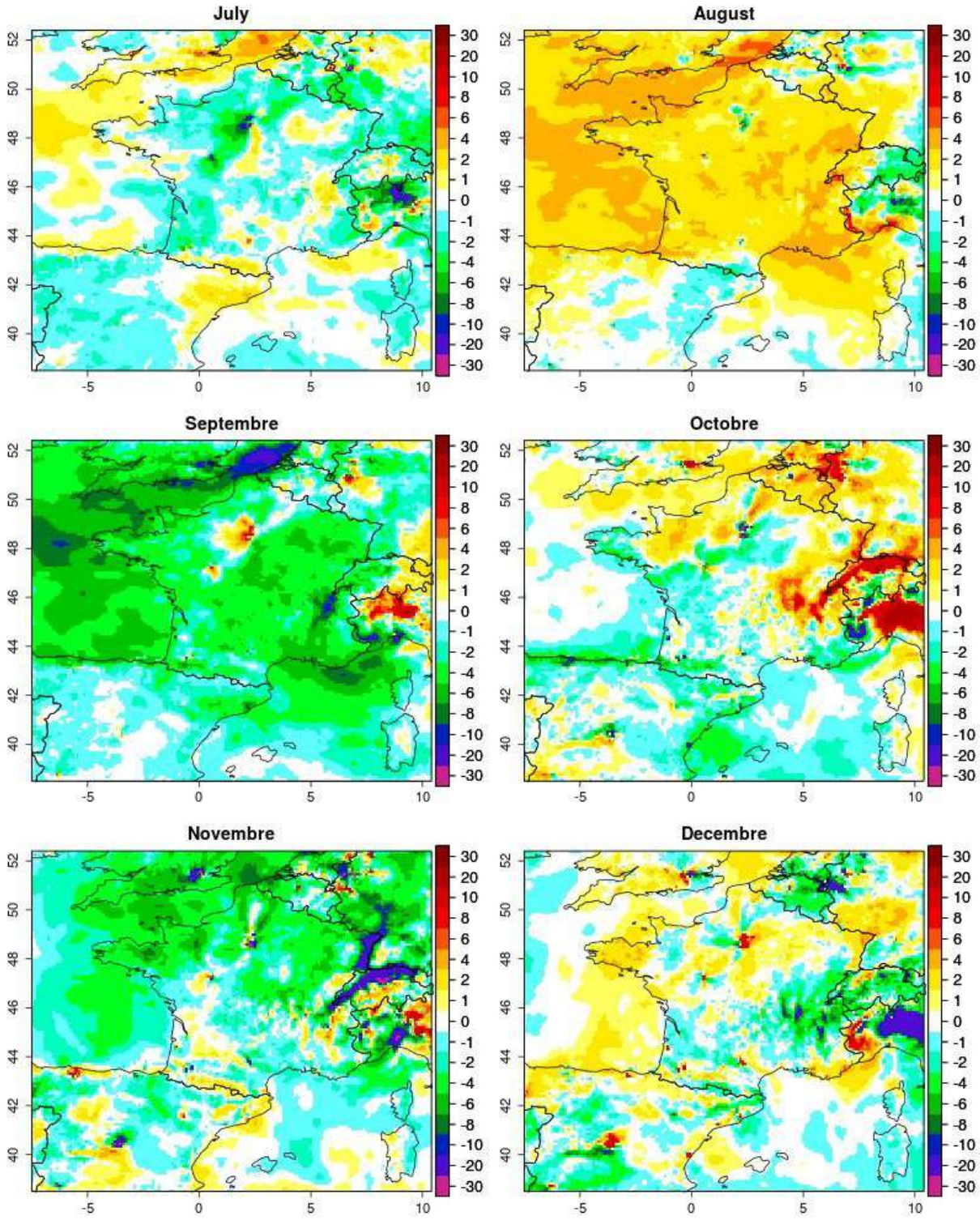

Figure SIII.15: Spatial distribution of the CH_4 monthly differences (ppb) between the two meteorological models (AROME minus ECMWF), using the data from 12:00 to 18:00 at the first level of the model, from July to Decembre.

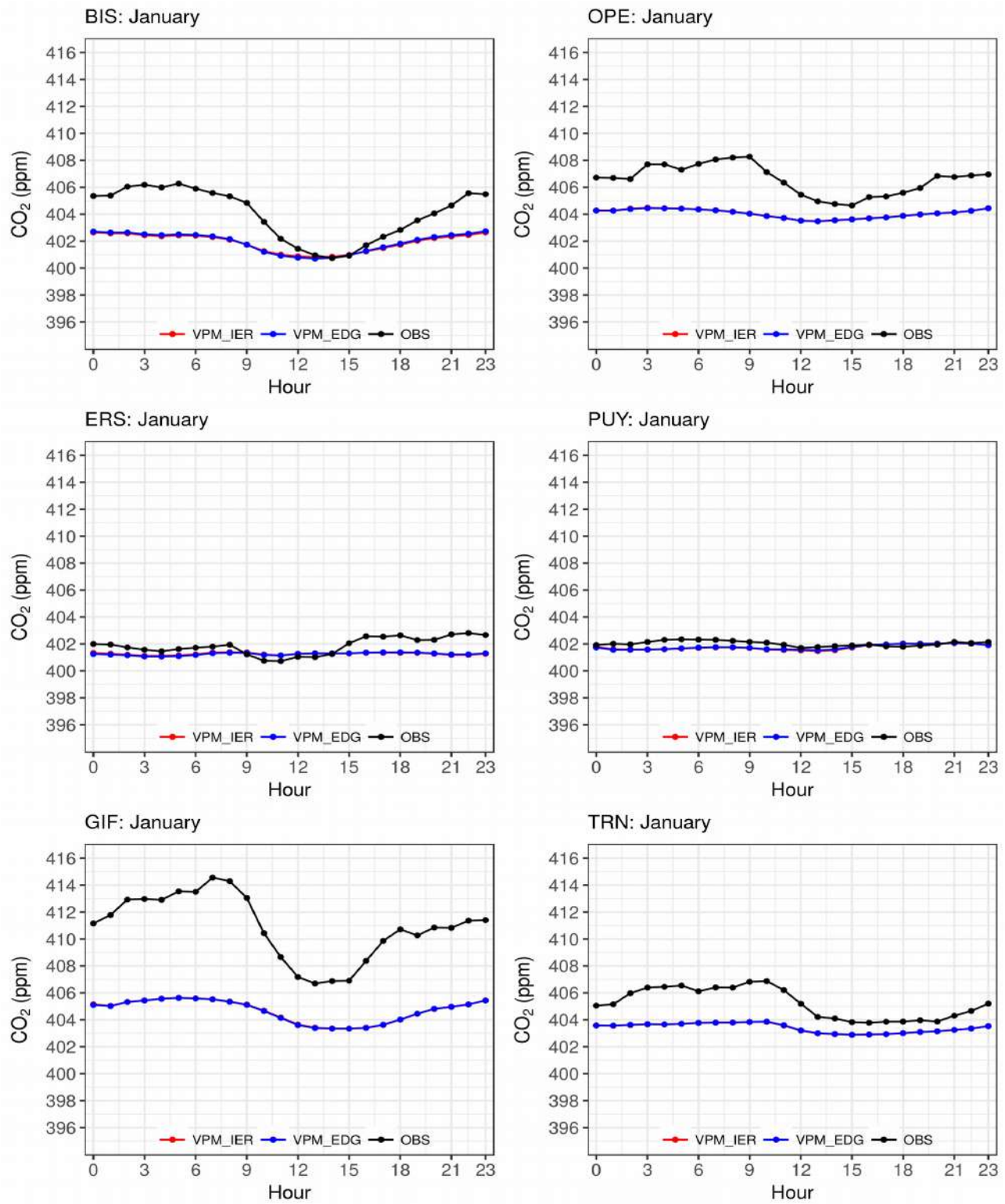

Figure SIII.16: CO_2 average diurnal cycle at the French sites for the observed (black) and the simulated (red and blue for IER and EDGAR respectivly) during January.

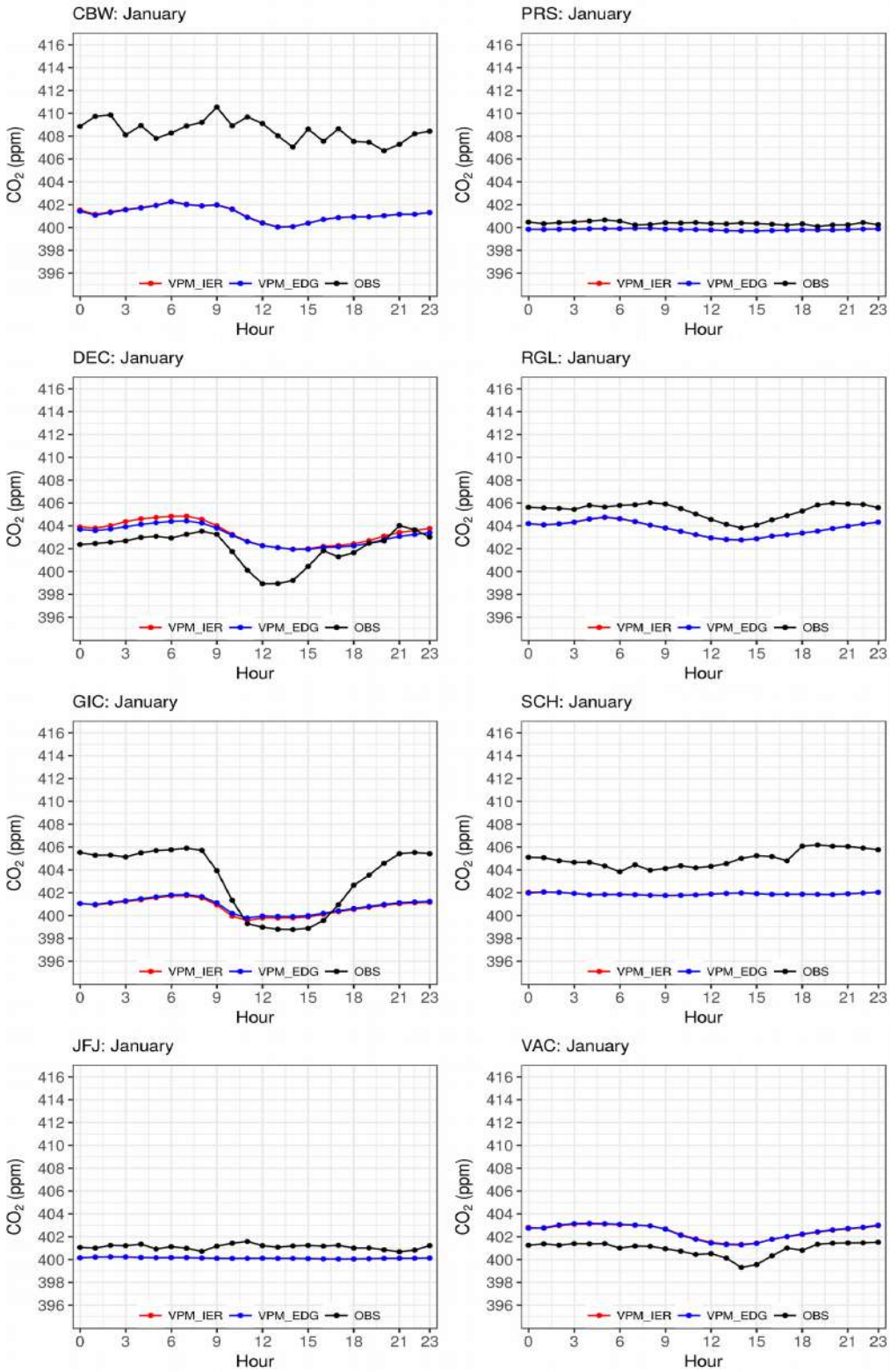

Figure SIII.17: CO_2 average diurnal cycle at the sites outside of France for the observed (black) and the simulated (red and blue for IER and EDGAR respectivly) during January.

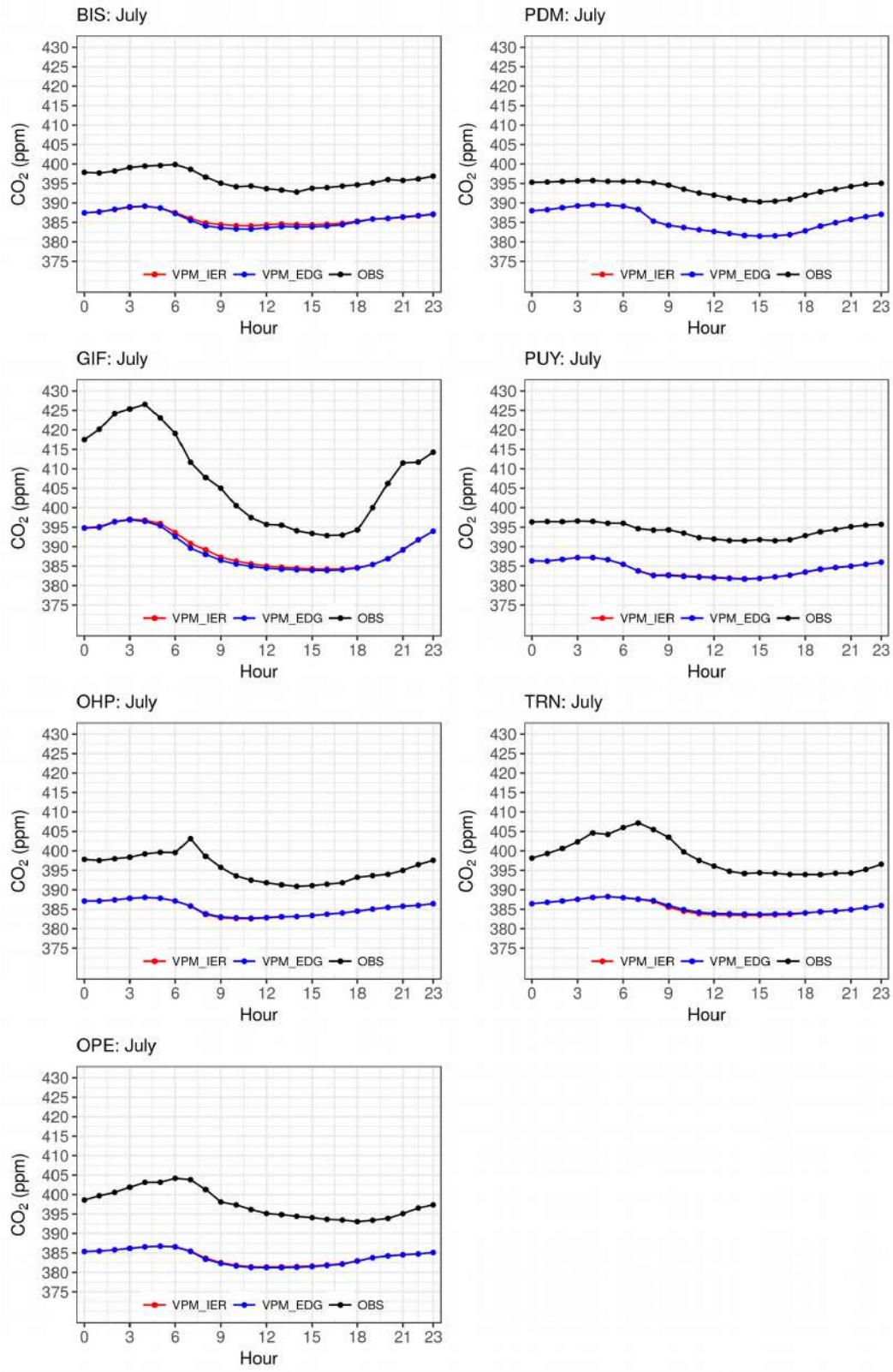

Figure SIII.18: CO_2 average diurnal cycle at the French sites for the observed (black) and the simulated (red and blue for IER and EDGAR respectivly) during July.

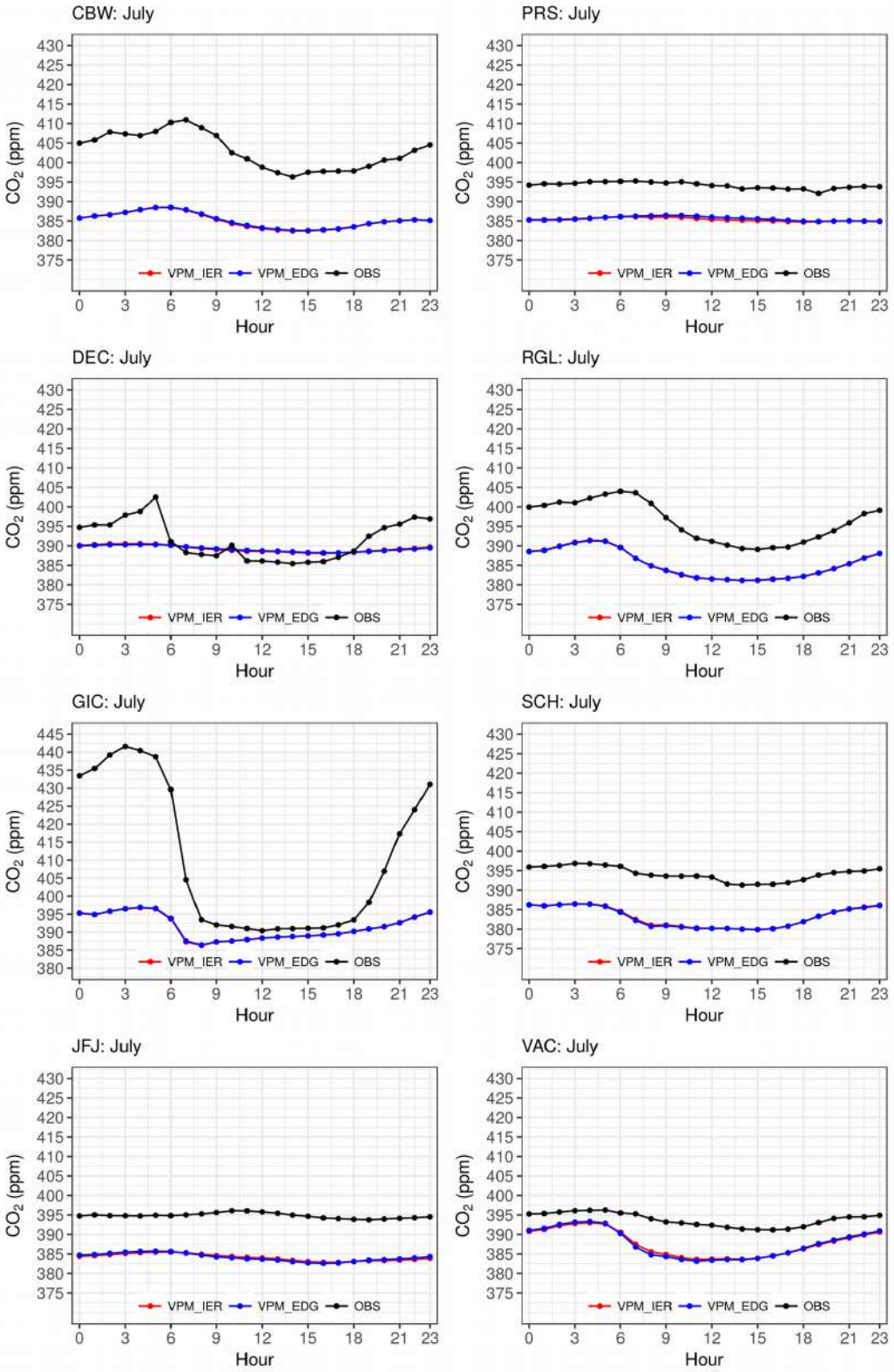

Figure SIII.19: CO_2 average diurnal cycle at the sites outside of France for the observed (black) and the simulated (red and blue for IER and EDGAR respectivly) during July.

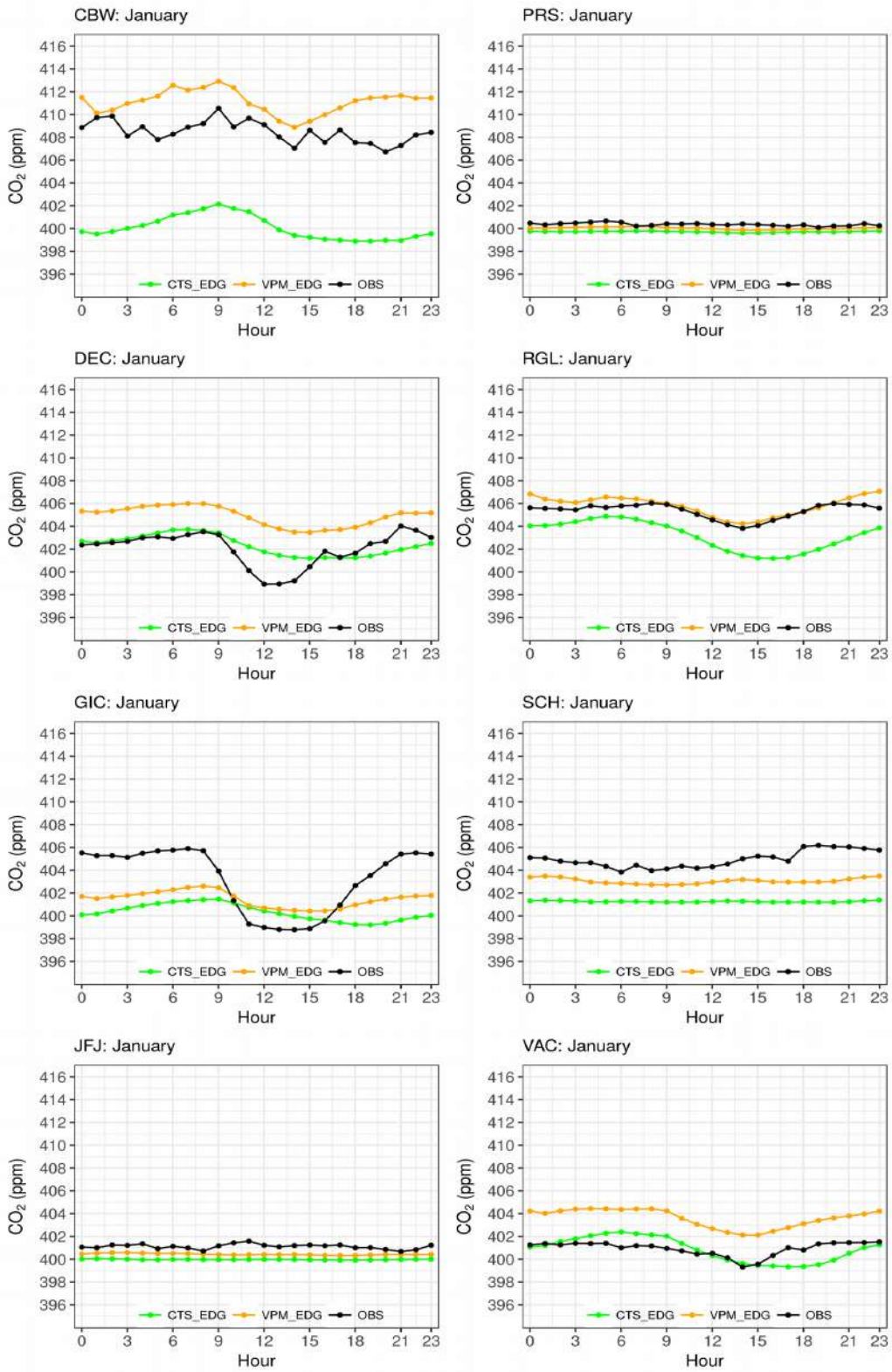

Figure SIII.20: CO_2 diurnal average cycle at CBW, DEC, GIC, JFJ, PRS, RGL, SCH, and VAC for the observed (black) and the simulated (green and orange for CTESSEL and VPRM respectivly) during January.

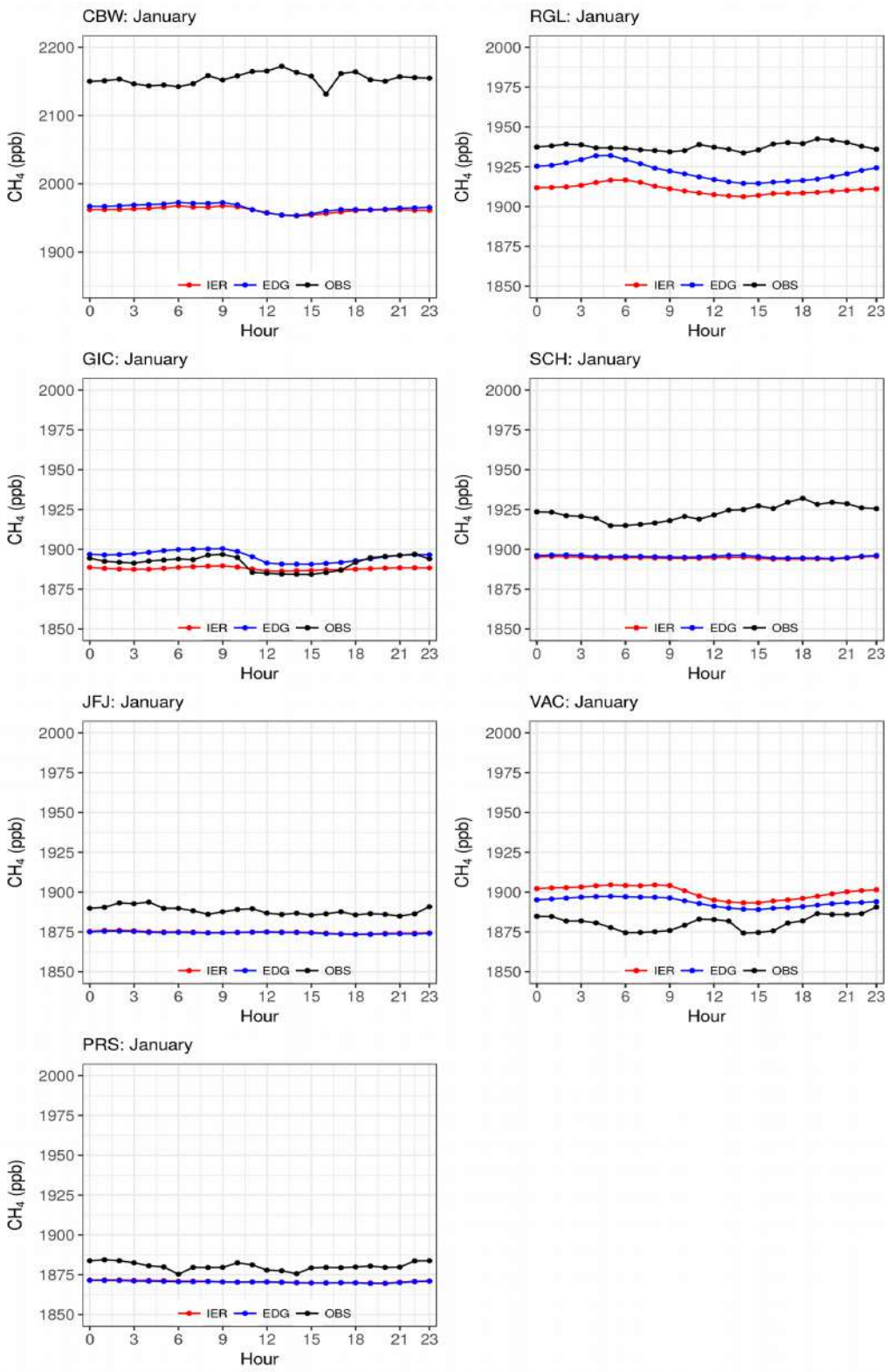

Figure SIII.21: CH_4 average diurnal cycle at CBW, GIC, JFJ, PRS, RGL, SCH, and VAC for the observed (black) and the simulated (red and blue for IER and EDGAR respectivly) during January.

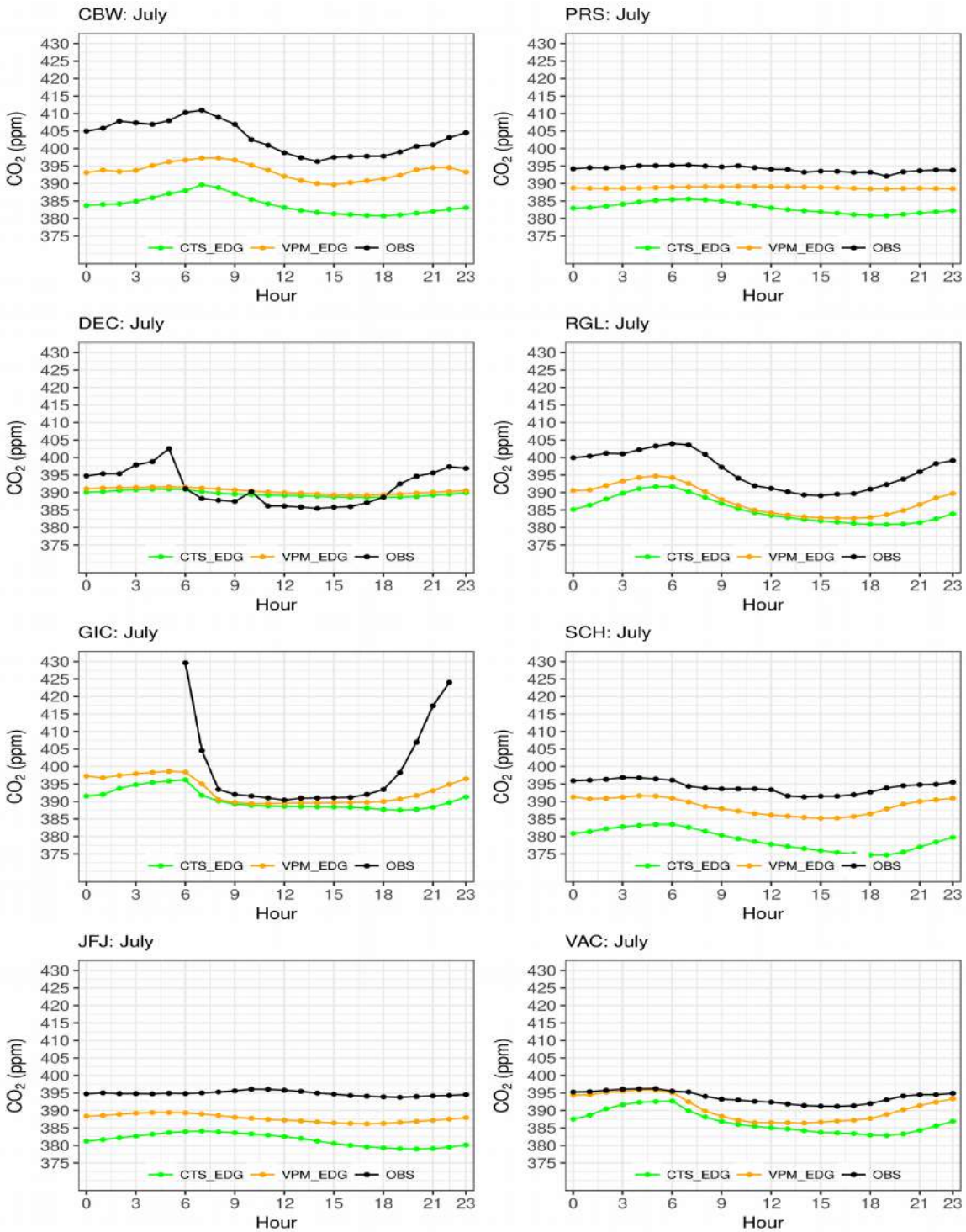

Figure SIII.22: CO_2 diurnal average cycle at CBW, DEC, GIC, JFJ, PRS, RGL, SCH, and VAC for the observed (black) and the simulated (green and orange for CTESSEL and VPRM respectivly) during July.

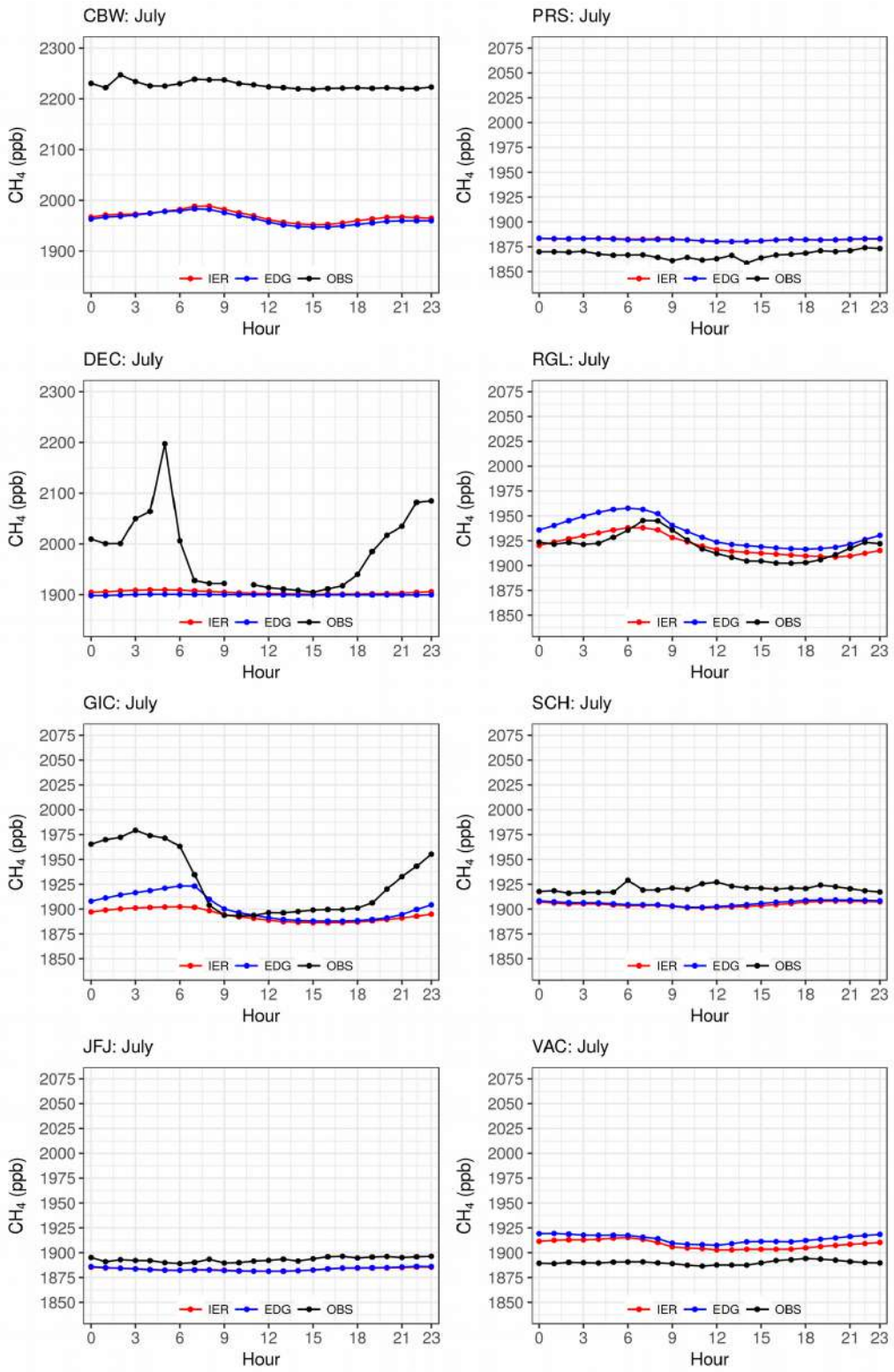

Figure SIII.23: CH_4 average diurnal cycle at CBW, DEC, GIC, JFJ, PRS, RGL, SCH, and VAC for the observed (black) and the simulated (red and blue for IER and EDGAR respectivly) during July.

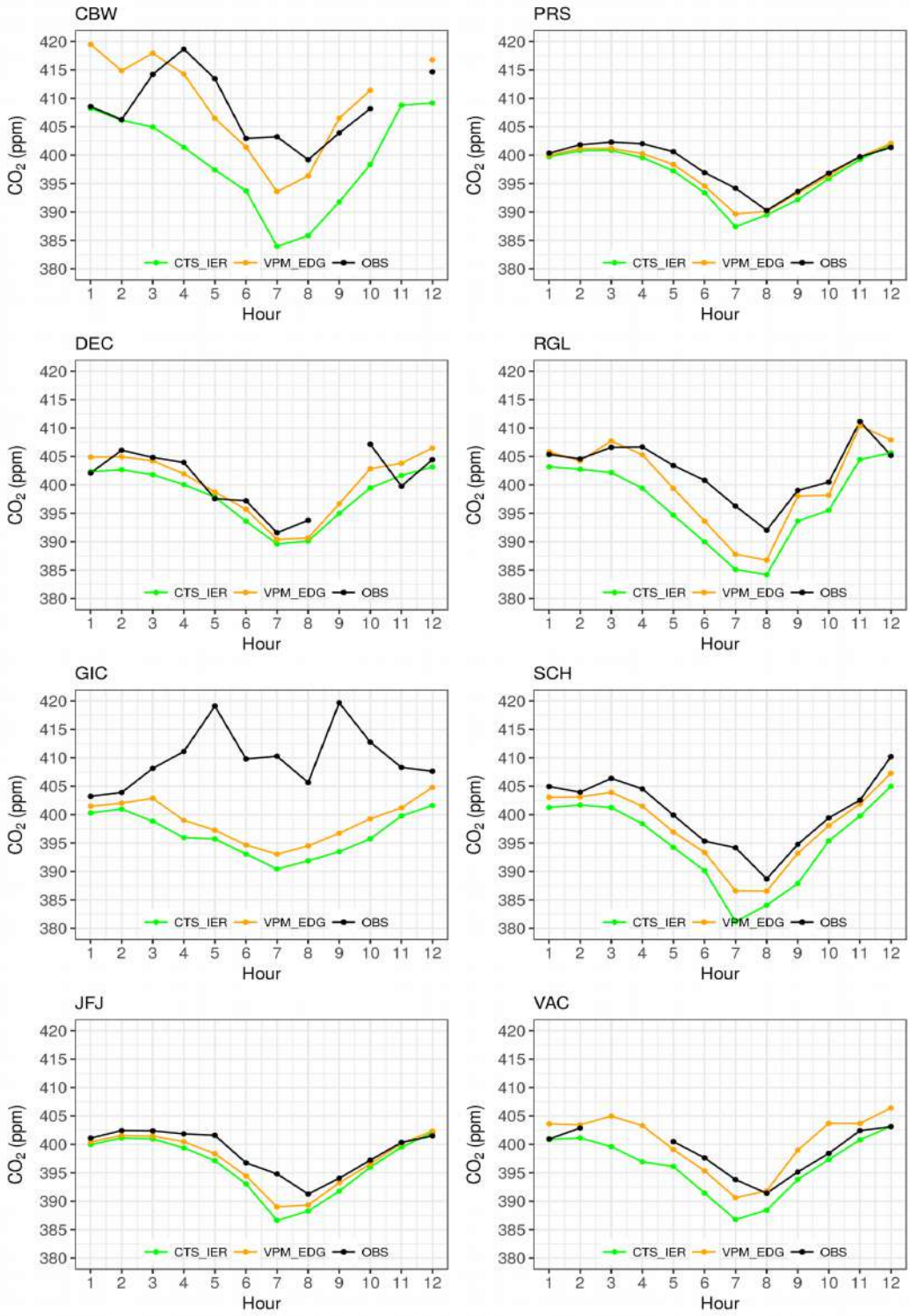

Figure SIII.24: CO_2 average seasonal cycle at CBW, DEC, GIC, JFJ, PRS, RGL, SCH, and VAC for the observed (black) and the simulated (green and orange for CTESSEL and VPRM respectivly).

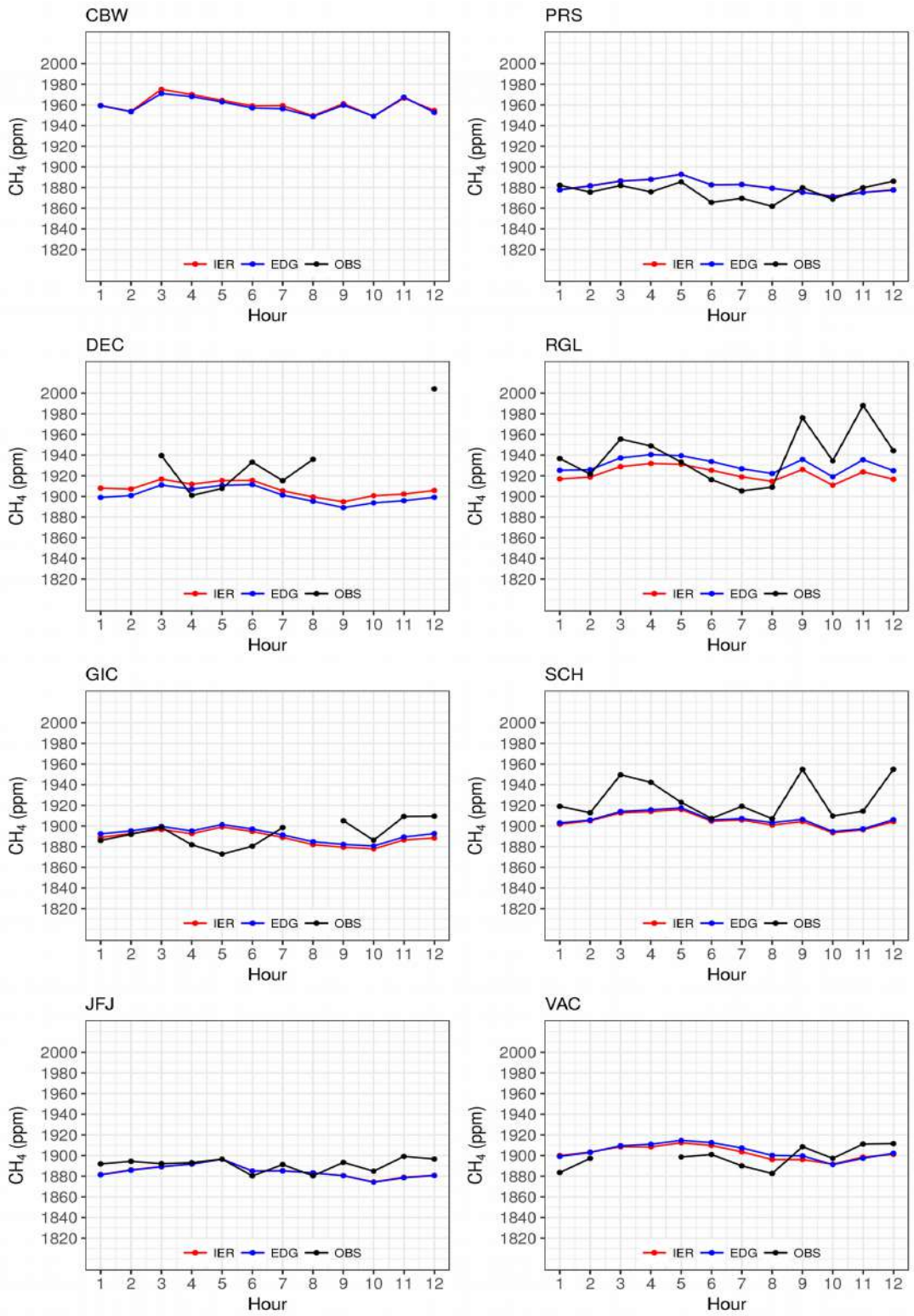

Figure SIII.25: CH_4 average seasonal cycle at CBW, DEC, GIC, JFJ, PRS, RGL, SCH, and VAC for the observed (black) and the simulated (red and blue for IER and EDGAR respectivly).

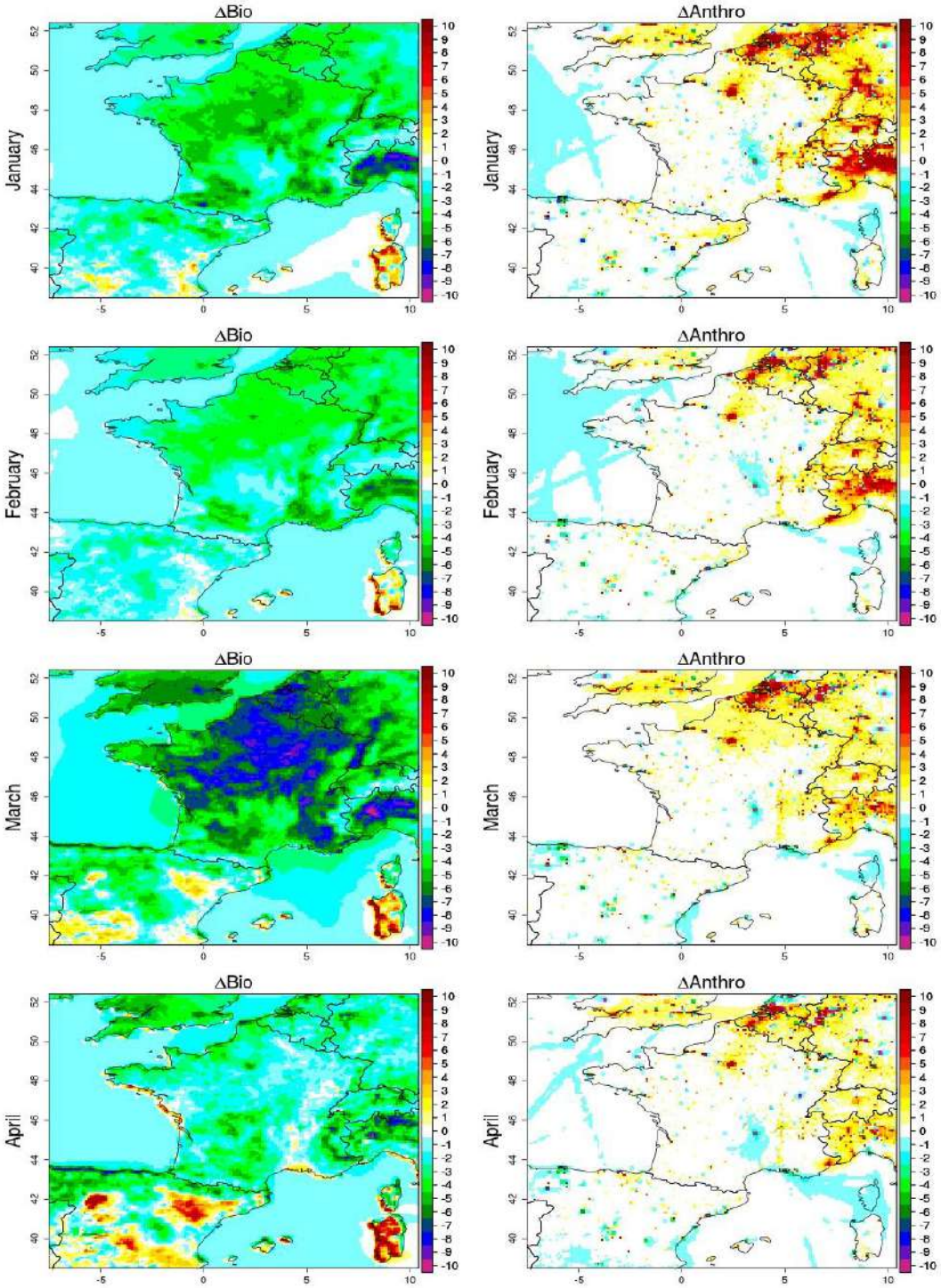

Figure SIII.26: Spatial distribution of the CO_2 monthly differences (ppm) between the two biogenic models (CTESSEL minus VPRM) panel ΔBio, and between the two anthropogenic inventories (IER minus EDGAR) panel ΔAnthro, using the data from 12:00 to 18:00 at the first level of the model, from January to April.

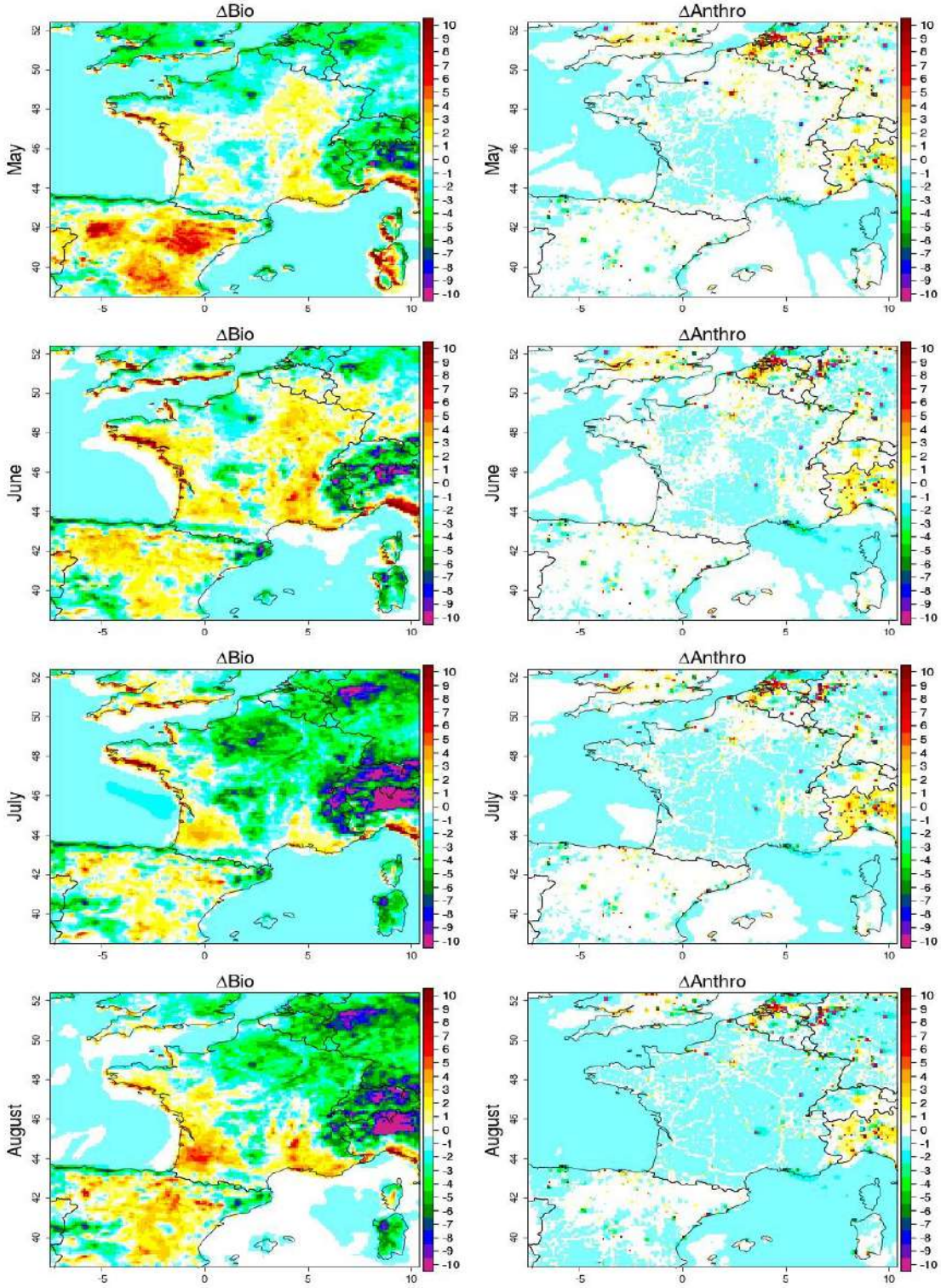

Figure SIII.27: Spatial distribution of the CO_2 monthly differences (ppm) between the two biogenic models (CTESSEL minus VPRM) panel ΔBio, and between the two anthropogenic inventories (IER minus EDGAR) panel ΔAnthro, using the data from 12:00 to 18:00 at the first level of the model, from May and August.

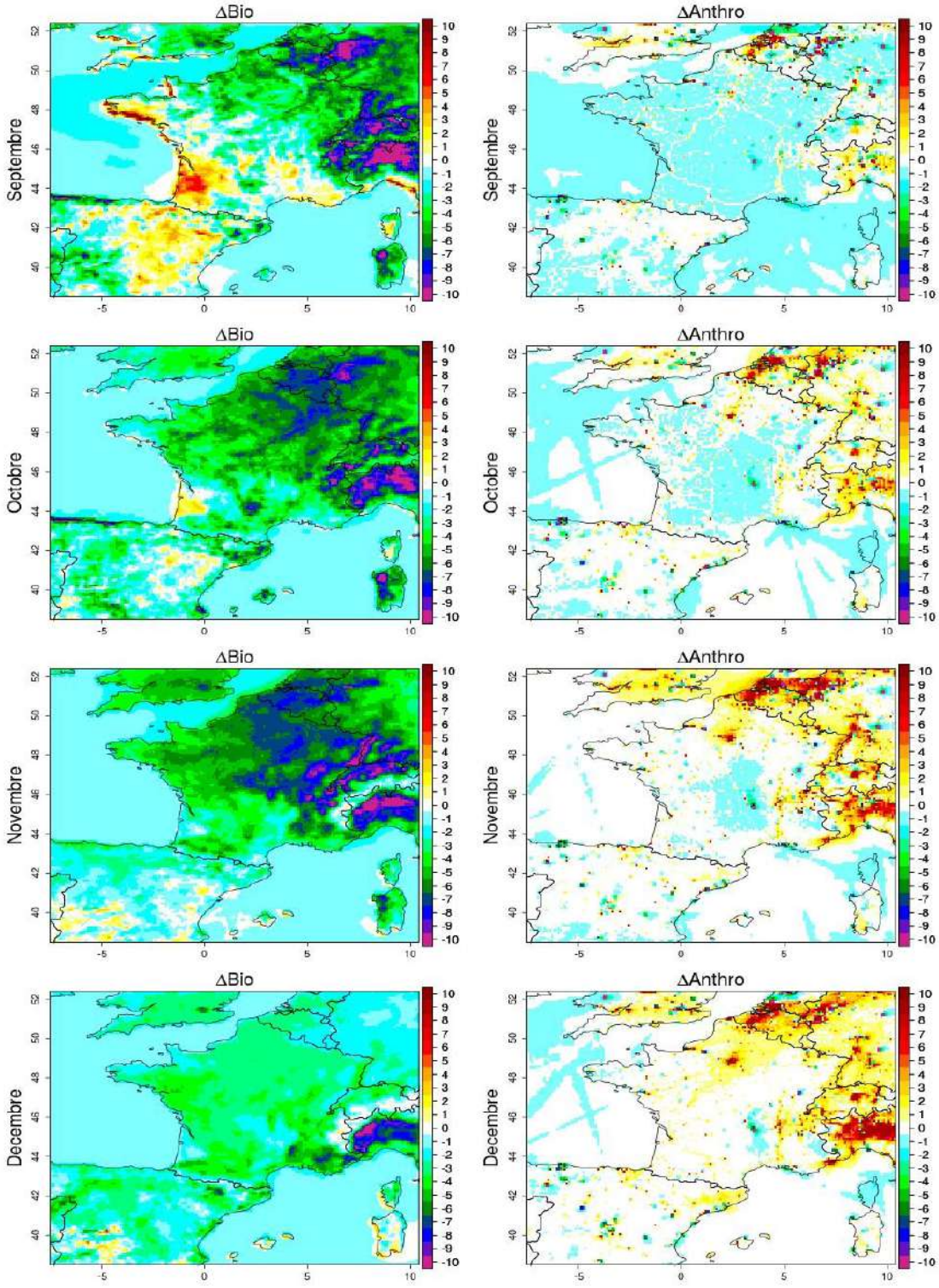

Figure SIII.28: Spatial distribution of the CO_2 monthly differences (ppm) between the two biogenic models (CTESSEL minus VPRM) panel ΔBio, and between the two anthropogenic inventories (IER minus EDGAR) panel ΔAnthro, using the data from 12:00 to 18:00 at the first level of the model, from Septembre and Decembre.

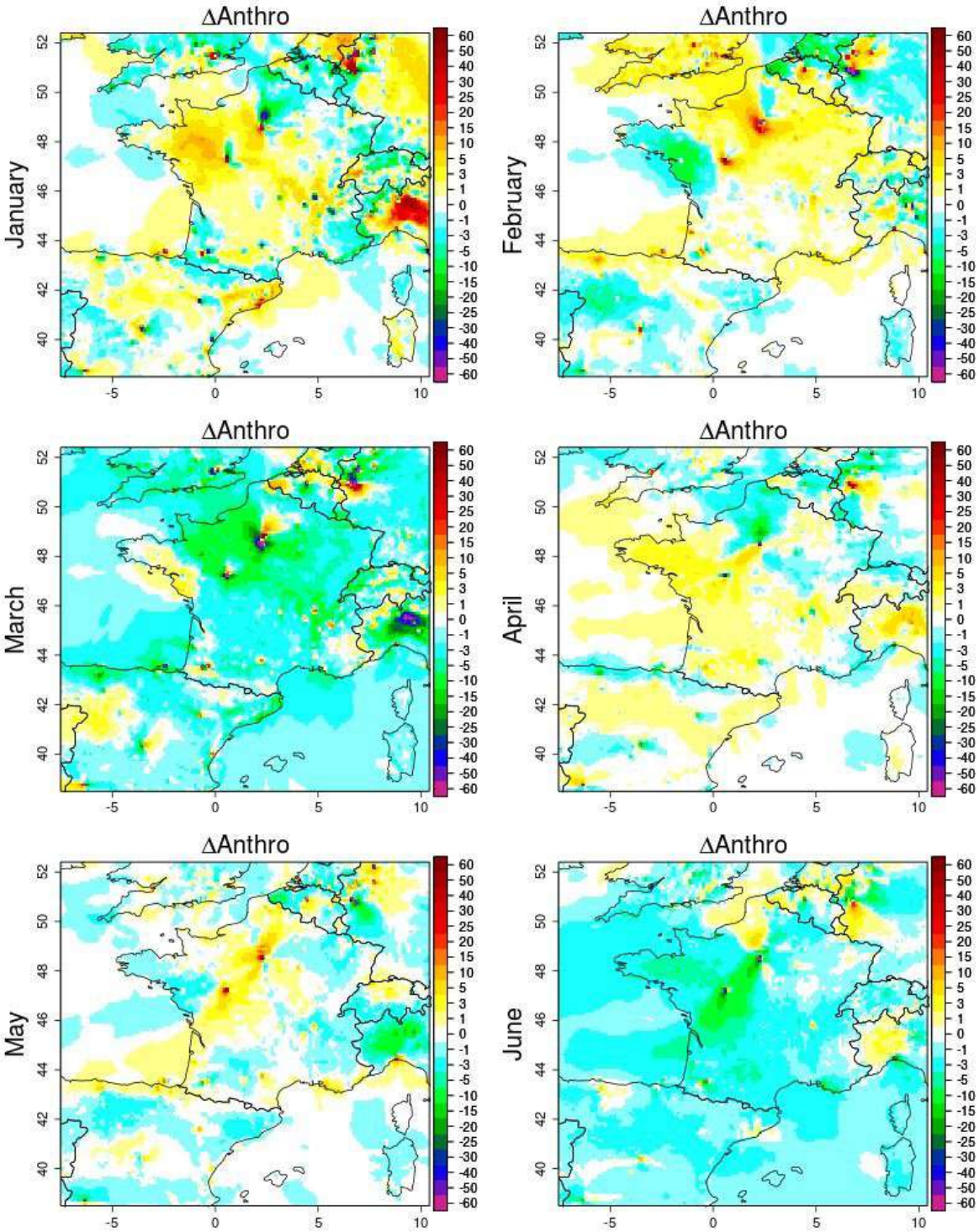

Figure SIII.29: Spatial distribution of the CH_4 monthly differences (ppb) between the two anthropogenic inventories (IER minus EDGAR) panel ΔAnthro, using the data from 12:00 to 18:00 at the first level of the model, between January and June.

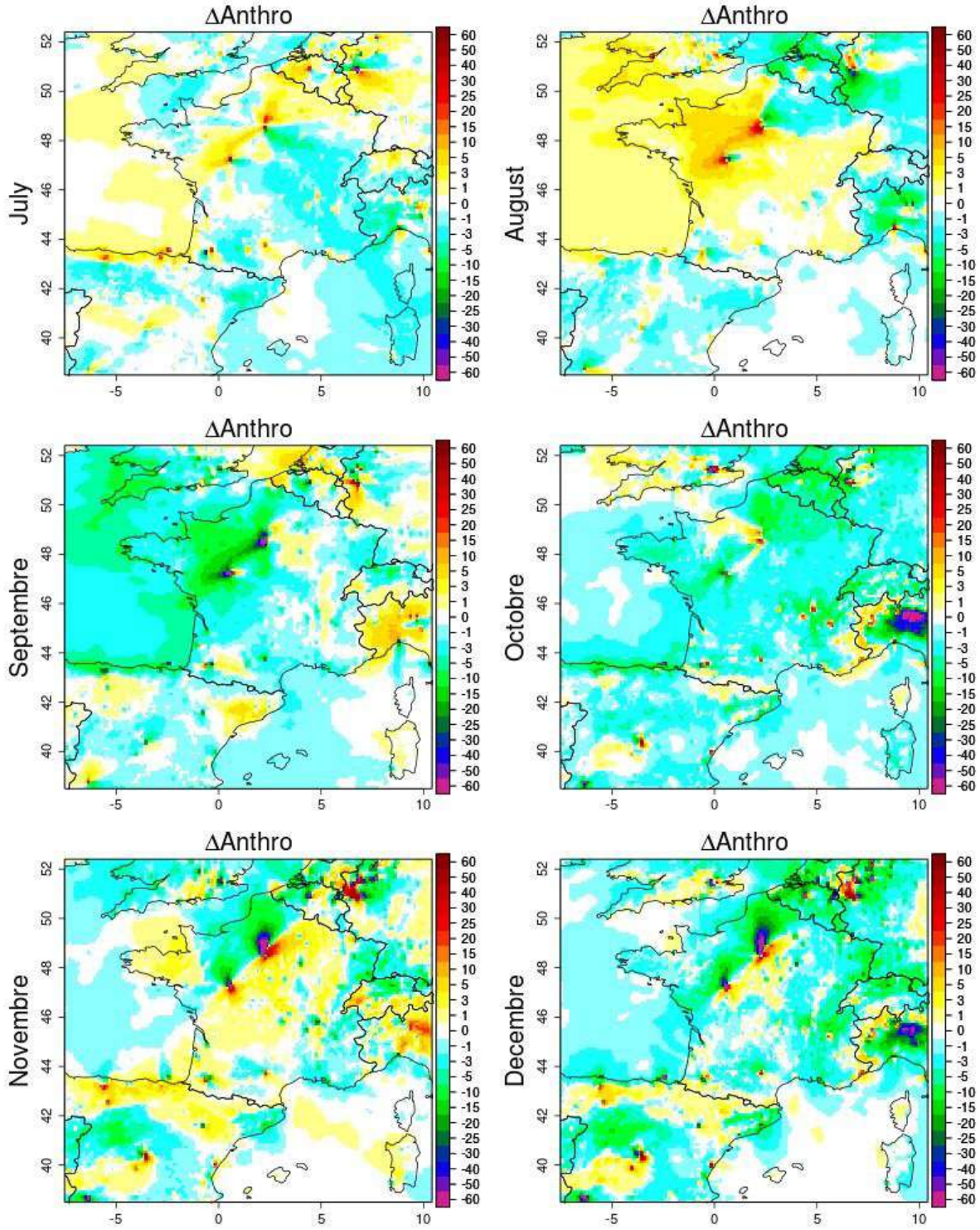

Figure SIII.30: Spatial distribution of the CH_4 monthly differences (ppb) between the two anthropogenic inventories (IER minus EDGAR) panel ΔAnthro, using the data from 12:00 to 18:00 at the first level of the model, between July and December.

VI.1.3 Chapter IV

	January			July		
Station	Number of the available data	Number of the selected data	Number of data used by the inversion system	Number of the available data	Number of the selected data	Number of data used by the inversion system
BIS	734	182	168 (22%)	670	144	134 (20 %)
OPE	711	180	164 (23%)	617	123	114 (18 %)
PUY	700	178	169 (24%)	673	168	140 (21 %)
TRN	600	150	144 (24%)	482	104	92 (19 %)
ERS	634	151	133 (21%)	0	0	0
GIF	588	151	136 (23%)	531	117	108 (20 %)
PDM	0	0	0	722	184	161 (22 %)
OHP	0	0	0	337	70	62 (19 %)
CBW	644	136	84 (13%)	633	117	75 (10 %)
RGL	672	162	152 (22%)	737	150	115 (16 %)
SCH	456	114	108 (24%)	729	178	172 (24 %)
JFJ	714	178	167 (23%)	706	179	144 (20 %)
PRS	415	108	102 (25%)	390	113	85 (22 %)
DEC	16	4	2 (13%)	381	80	66 (17 %)
GIC	741	185	179 (24%)	239	50	44 (18 %)
VAC	86	18	16 (19%)	741	153	145 (20 %)

Table SIV.1: Statistis of the observed CH_4 data used by the inversion system

	January			July		
Station	Number of the available data	Number of the selected data	Number of data used by the inversion system	Number of the available data	Number of the selected data	Number of data used by the inversion system
BIS	734	151 (21%)	139 (19%)	671	144 (21%)	131 (20%)
OPE	711	150 (21%)	137 (19%)	617	123 (20%)	112 (18%)
PUY	700	178 (25%)	168 (24%)	673	168 (25%)	148 (22%)
TRN	599	125 (21%)	115 (19%)	482	104 (22%)	97 (20%)
ERS	635	127 (20%)	112 (18%)	0	0	0
GIF	589	589 (21%)	109 (19%)	533	118 (22%)	106 (20%)
PDM	0	0	0	722	182 (25%)	180 (25%)
OHP	0	0	0	337	70 (20%)	65 (19%)
CBW	674	123 (18%)	103 (15%)	635	117 (18%)	105 (17%)
RGL	672	135 (20%)	127 (19%)	737	150 (20%)	137 (19%)
SCH	456	114 (25%)	106 (23%)	729	178 (24%)	164 (22%)
JFJ	714	178 (25%)	162 (23%)	706	179 (25%)	170 (24%)
PRS	681	172 (25%)	160 (23%)	433	116 (27%)	112 (26%)
DEC	382	78 (20%)	66 (17%)	381	80 (21%)	74 (19%)
GIC	741	154 (21%)	142 (19%)	239	50 (21%)	46 (19%)
VAC	86	15 (17%)	13 (15%)	741	153 (21%)	147 (20%)

Table SIV.2: Statistis of the observed CO_2 data used by the inversion system

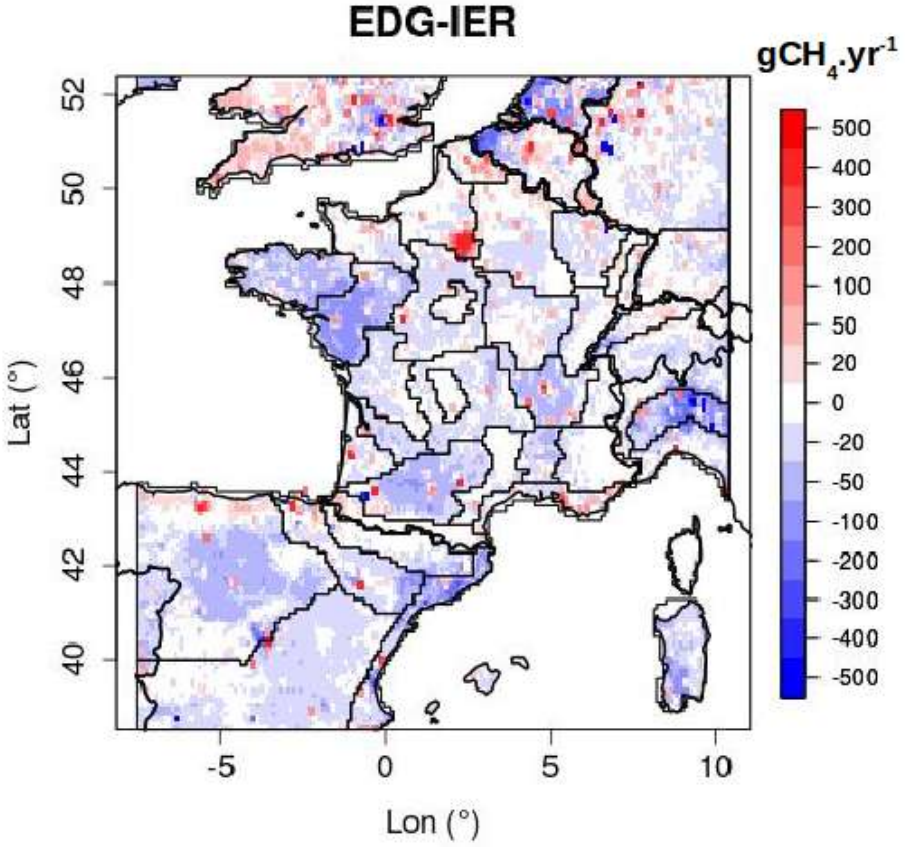

Figure SIV.1 Spatial distribution of the difference between EDGAR and IER inventories (see section III.3.4) for CH_4

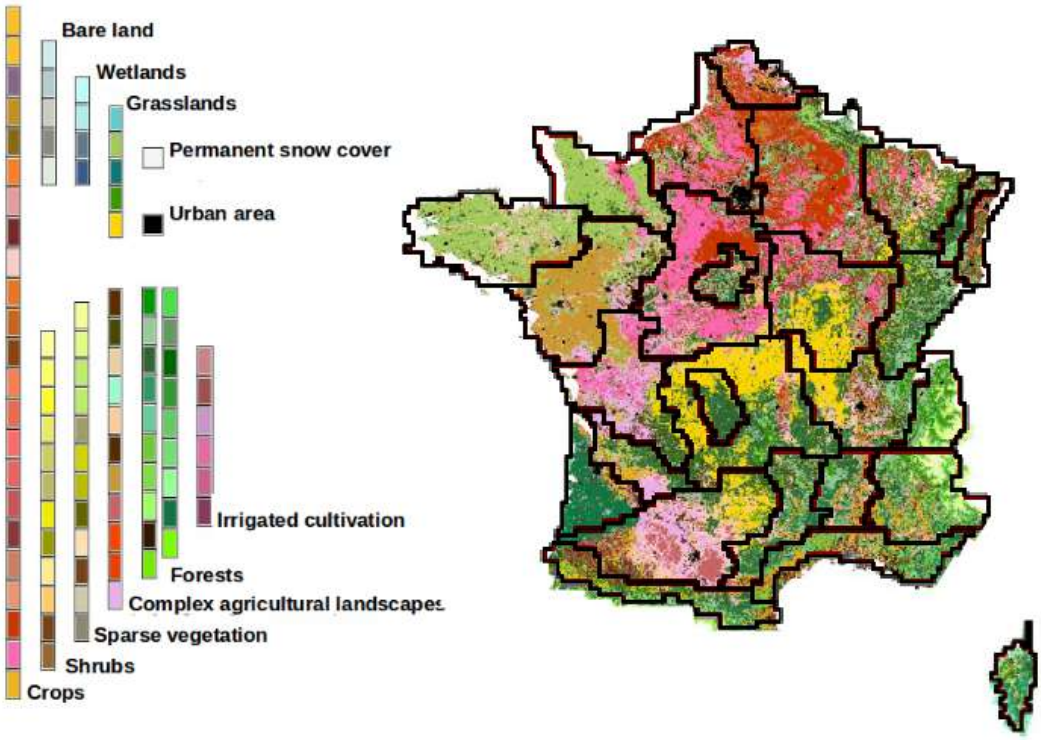

Figure SIV.2: Classification of the vegetation types in France using the ECOCLIMAP database (Champeaux et al., 2005). The black polygons in the figure represent the used regions in France. The figure is taken from the National Centre for Meteorological Research website (https://www.umr-cnrm.fr/spip.php?rubrique257&lang=fr).

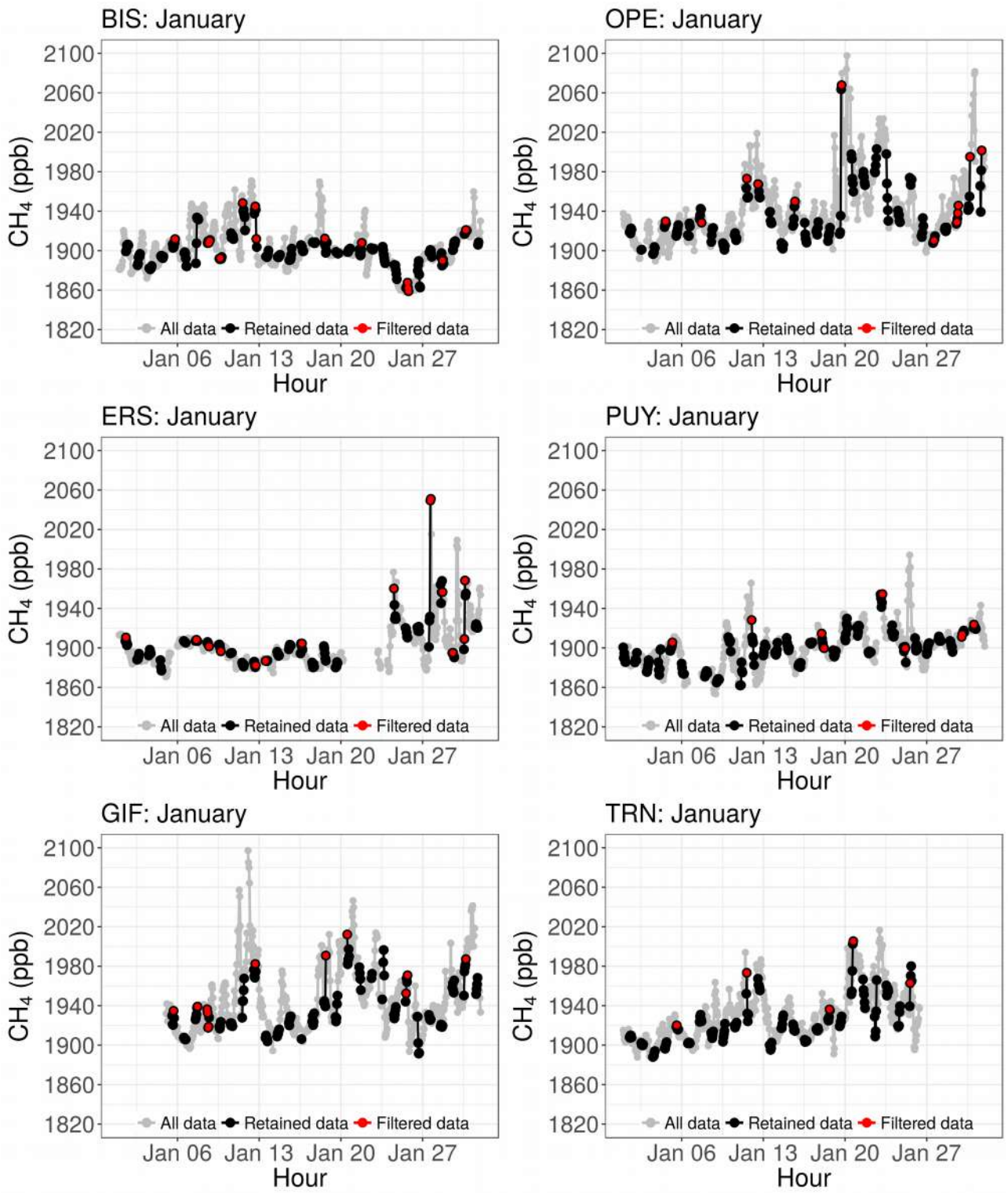

Figure SIV.3: CH_4 hourly data at BIS, OPE, ERS, PUY, GIF, and TRN during January. The grey color represents the available observations for each site. The back data points stand for the mid-afternoon data (data between 14:00 and 18:00) at low altitude sites, and the nighttime data (data between 00:00 and 06:00) at the mountain stations. The red data show the observations rejected by the inversion system (see section IV.2.3.1).

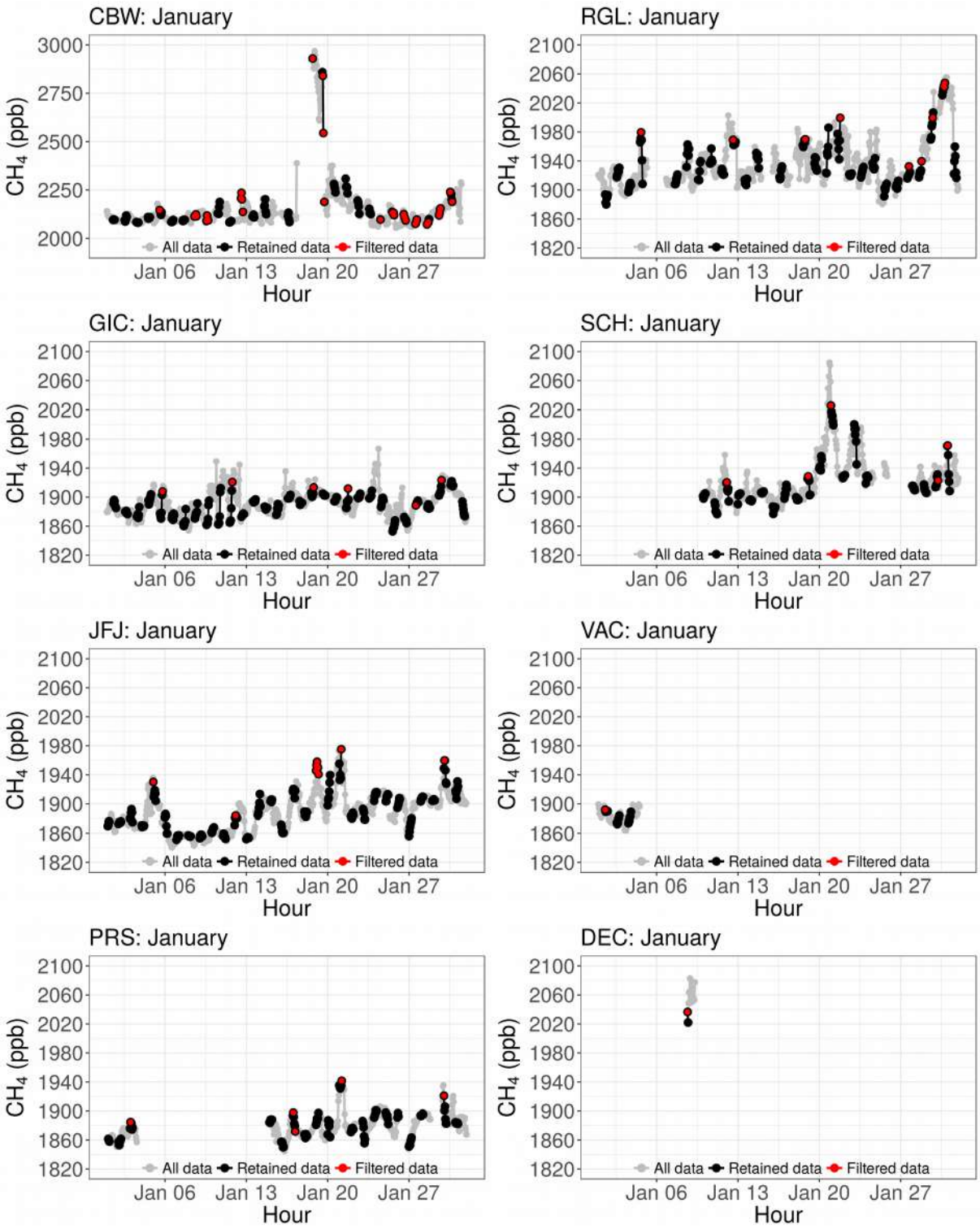

Figure SIV.4: CH_4 hourly data at CBW, DEC, GIC, JFJ, PRS, RGL, SCH, and VAC during January. The grey color represents the available observations for each site. The back data points stand for the mid-afternoon data (data between 14:00 and 18:00) at low altitude sites, and the nighttime data (data between 00:00 and 06:00) at the mountain stations. The red data show the observations rejected by the inversion system (see section IV.2.3.1).

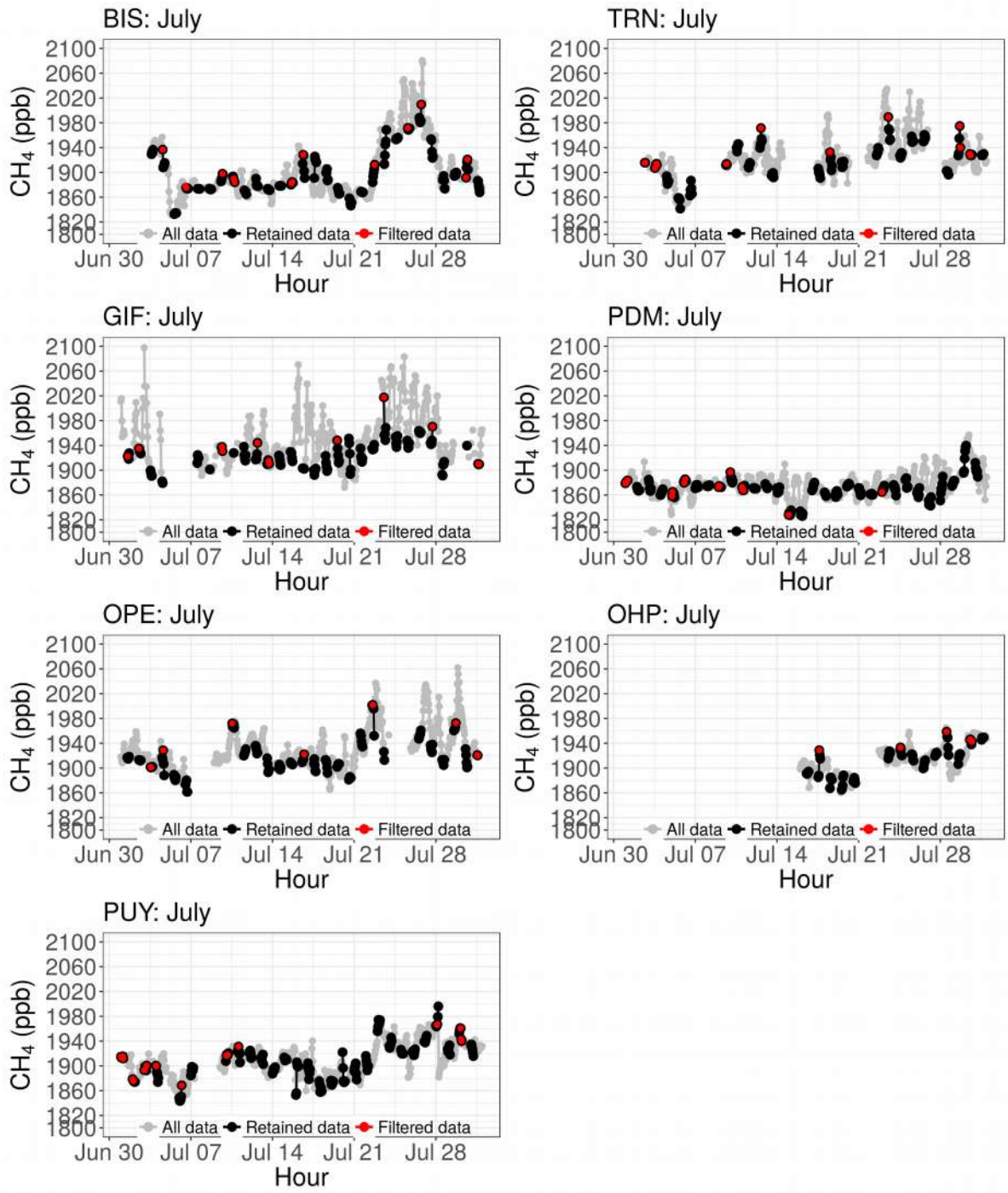

Figure SIV.5: CH_4 hourly data at BIS, OPE, GIF, PDM, PUY, OHP, and TRN during July. The grey color represents the available observations for each site. The back data points stand for the mid-afternoon data (data between 14:00 and 18:00) at low altitude sites, and the nighttime data (data between 00:00 and 06:00) at the mountain stations. The red data show the observations rejected by the inversion system (see section IV.2.3.1).

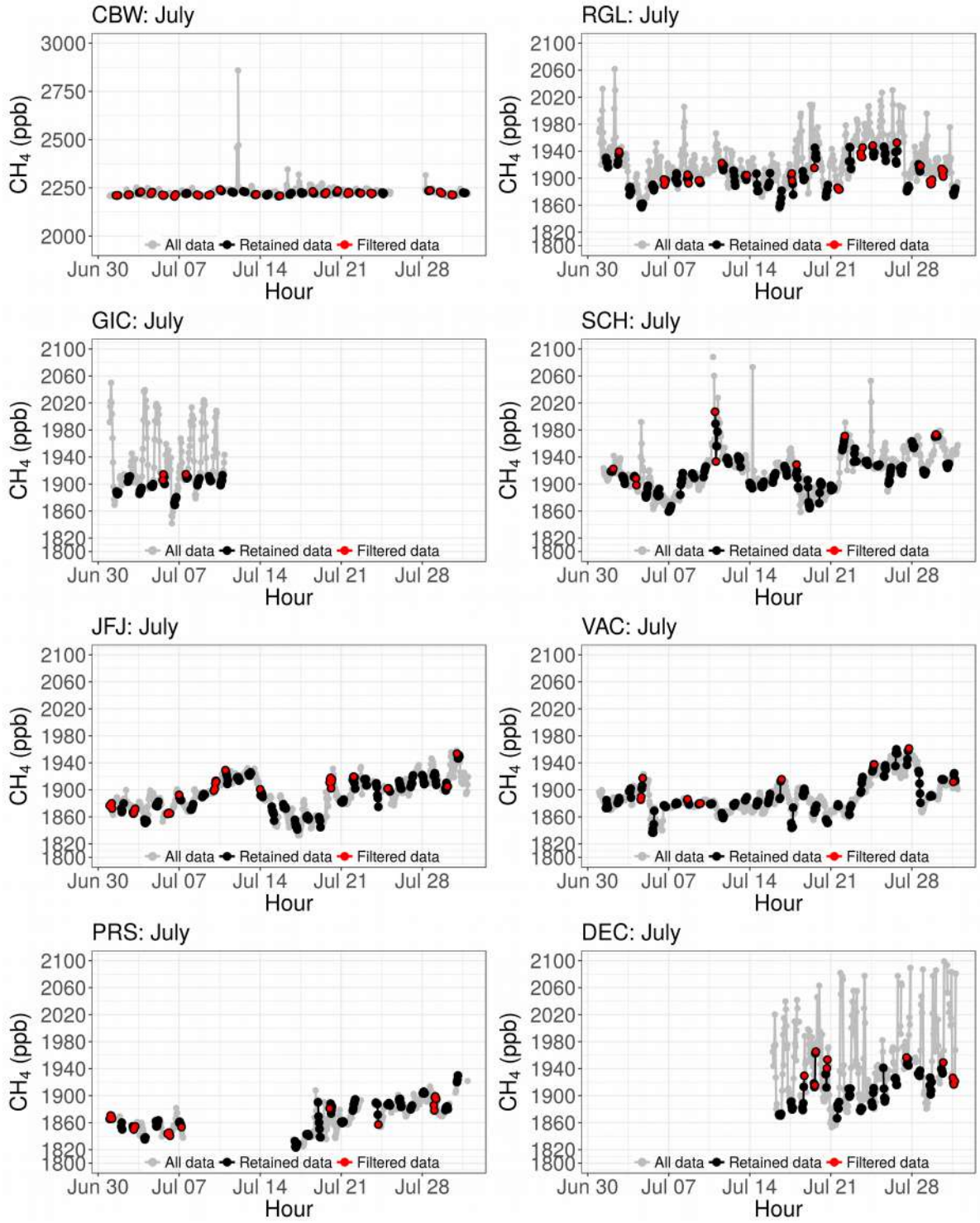

Figure SIV.6: CH_4 hourly data at CBW, DEC, GIC, JFJ, PRS, RGL, SCH, and VAC during July. The grey color represents the available observations for each site. The back data points stand for the mid-afternoon data (data between 14:00 and 18:00) at low altitude sites, and the nighttime data (data between 00:00 and 06:00) at the mountain stations. The red data show the observations rejected by the inversion system (see section IV.2.3.1).

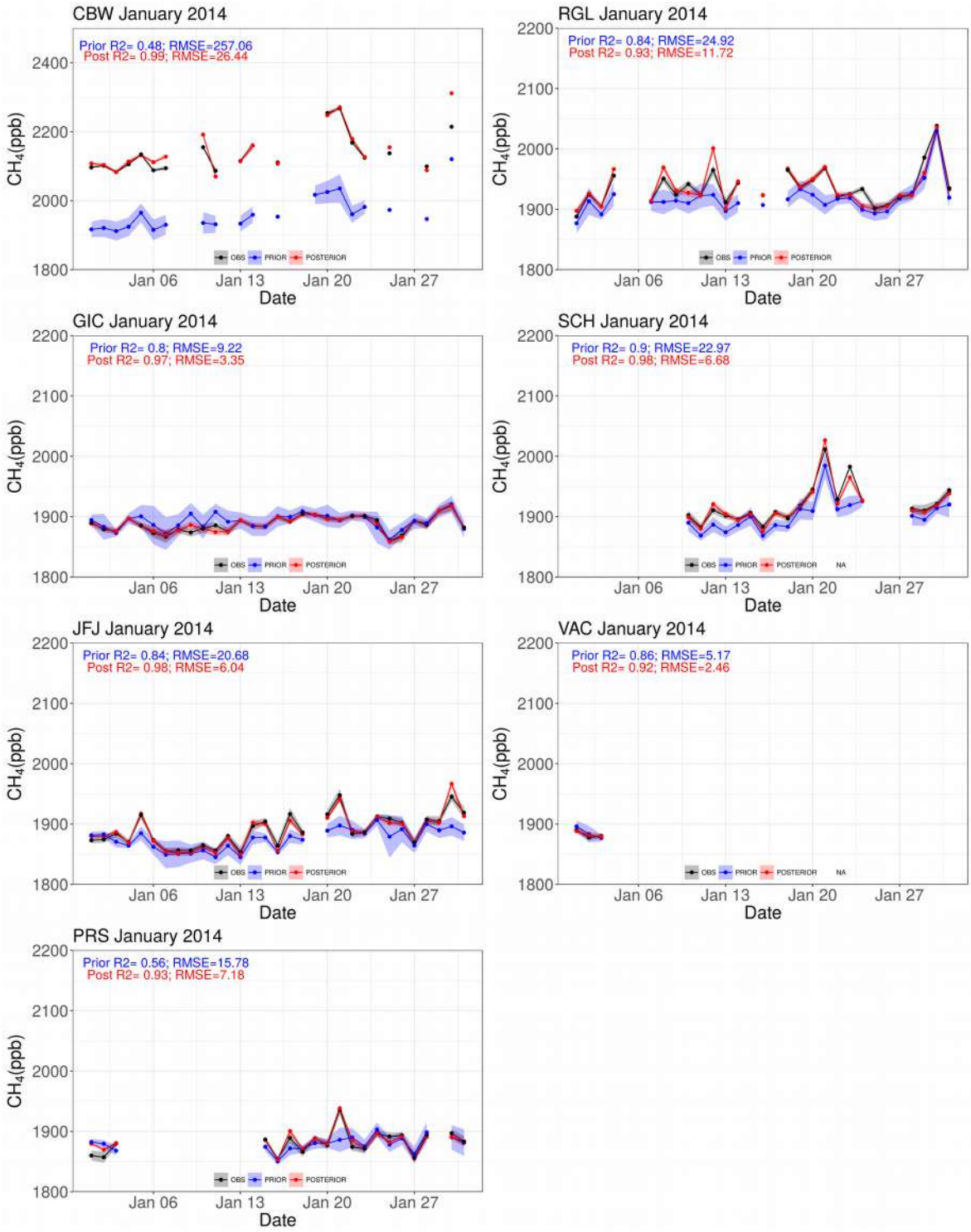

Figure SIV.7: Observed (black) and simulated prior (blue) and posterior (red) CH_4 daily averages for the French atmospheric sites (CBW, RGL, GIC, SCH, JFJ, VAC, and PRS) during January. The shaded areas represent the uncertainties of the observed (grey) and simulated prior (shaded blue) and posterior (shaded red) CH_4 concentrations. For each sites we calculate the root mean square error (RMSE) and the coefficient of correlation (R2) for the prior and the posterior concentration.

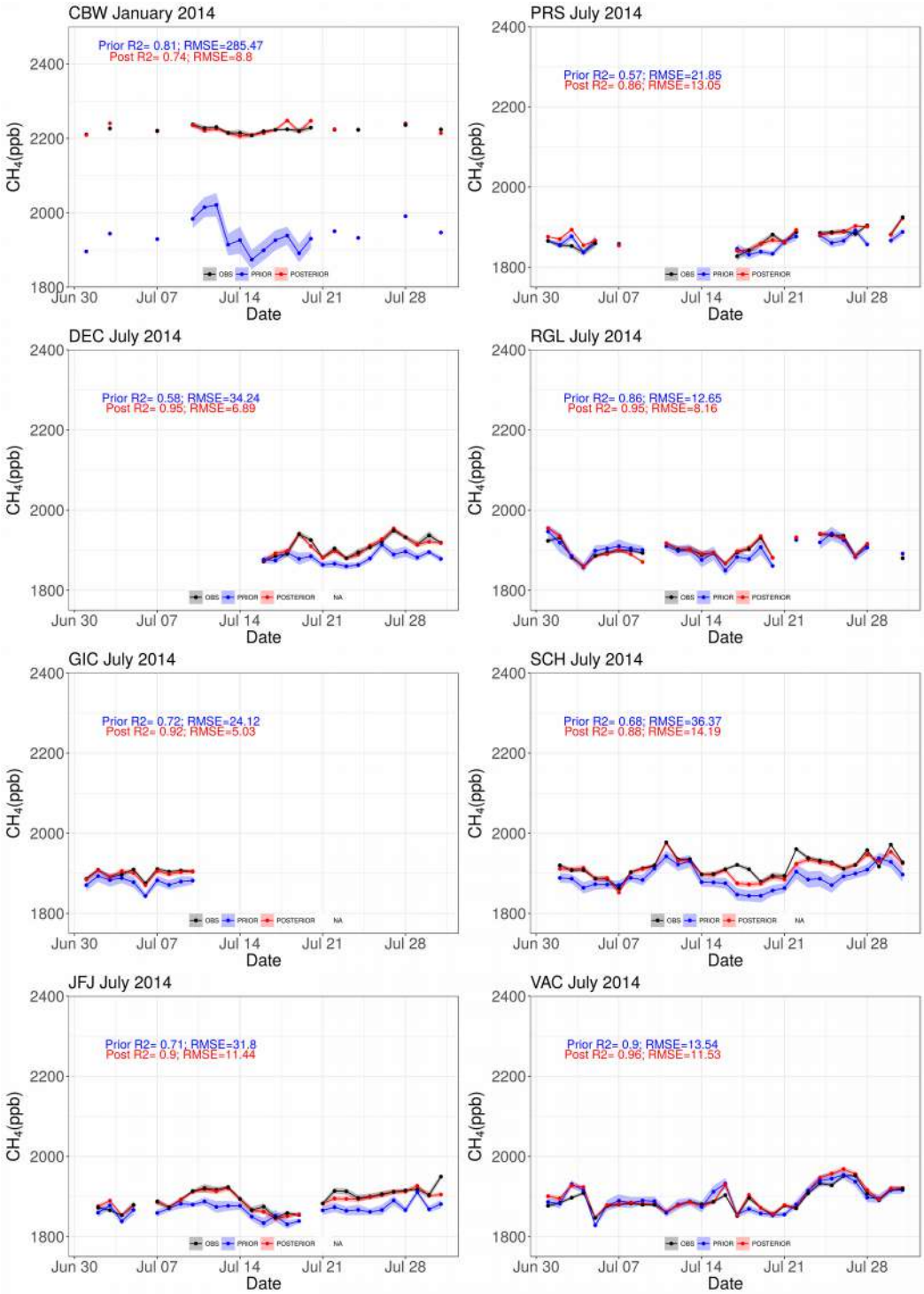

Figure SIV.8: Observed (black) and simulated prior (blue) and posterior (red) CH_4 daily averages for the French atmospheric sites (CBW, RGL, GIC, SCH, JFJ, DEC, VAC, and PRS) during July. The shaded areas represent the uncertainties of the observed (grey) and simulated prior (shaded blue) and posterior (shaded red) CH_4 concentrations. For each sites we calculate the root mean square error (RMSE) and the coefficient of correlation (R2) for the prior and the posterior concentration.

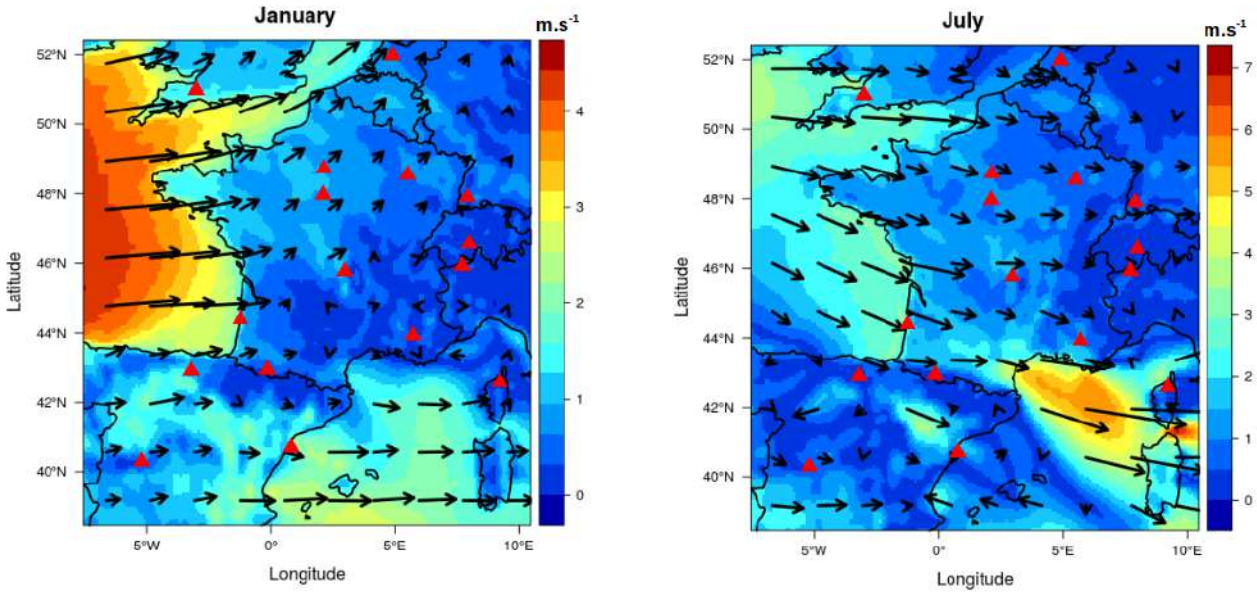

Figure SIV.9: Monthly mean wind field modeled by the ECMWF during January (left) and July (right). The arrows stand for the wind direction, whereas the wind speed is represented by the color level in m/s.

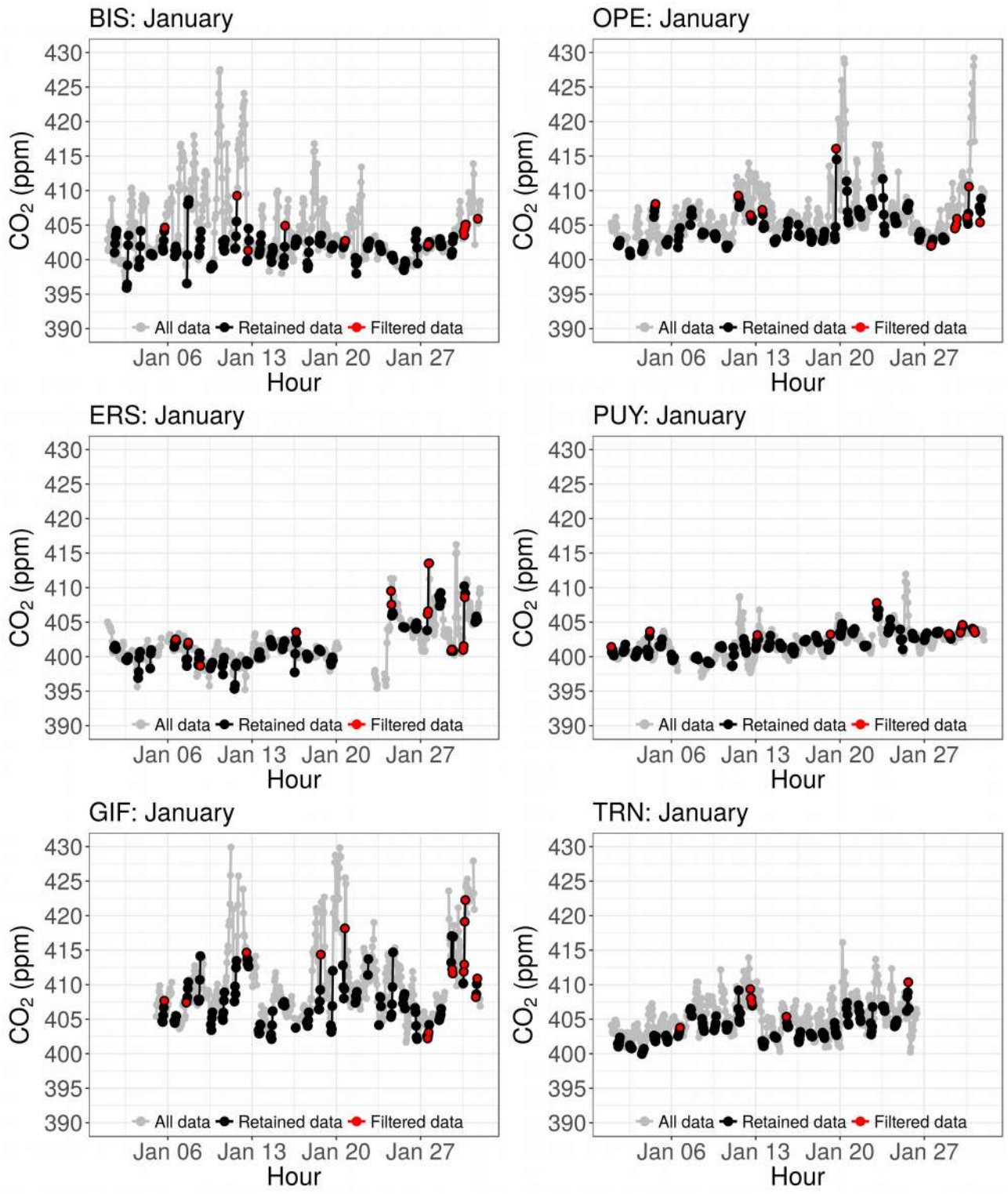

Figure SIV.10: CO_2 hourly data at BIS, OPE, ERS, PUY, GIF, and TRN during January. The grey color represents the available observations for each site. The back data points stand for the mid-afternoon data (data between14:00 and 18:00) at low altitude sites, and the nighttime data (data between 00:00 and 06:00) at the mountainstations. The red data show the observations rejected by the inversion system (see section IV.2.3.1).

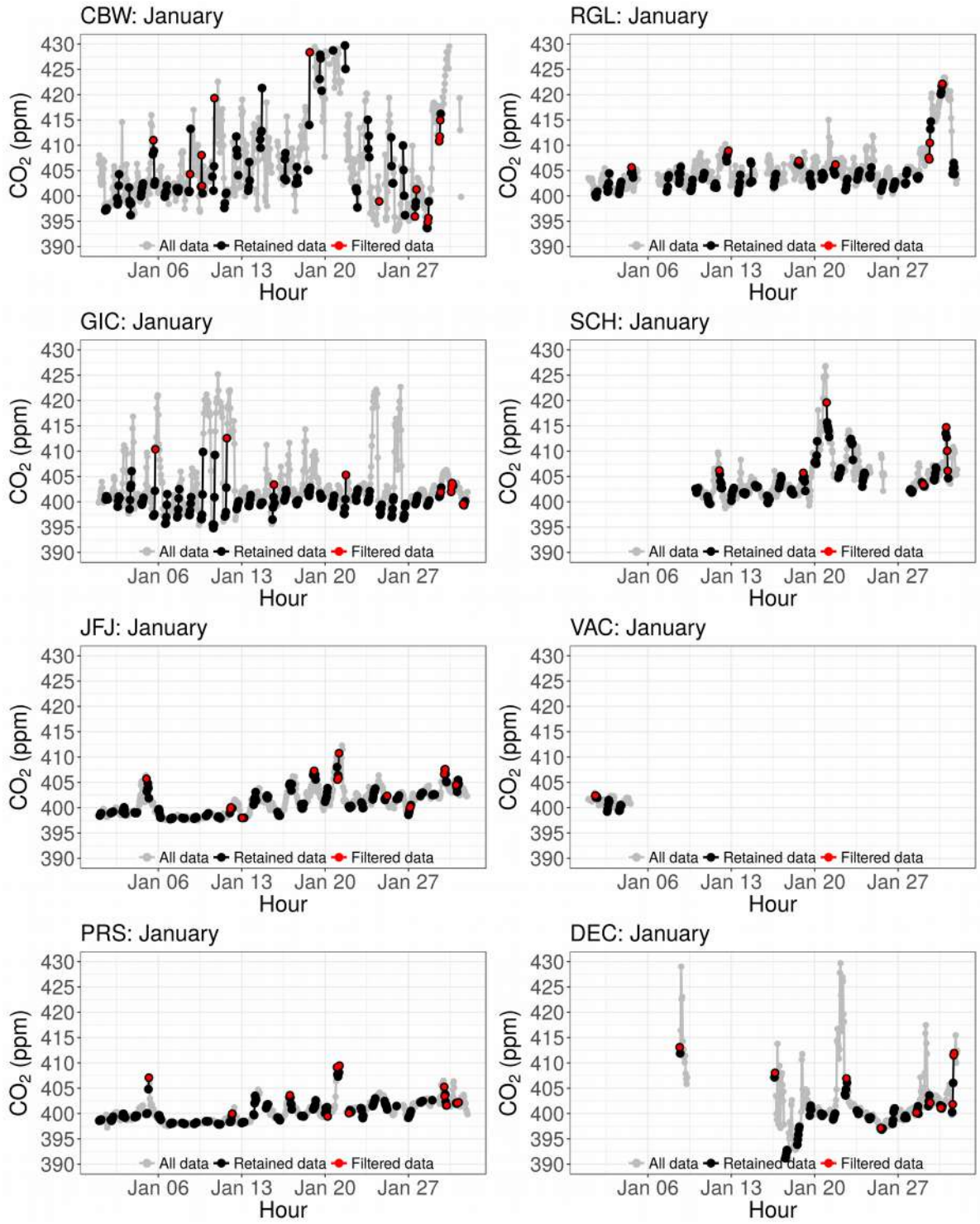

Figure SIV.11: CO_2 hourly data at CBW, DEC, GIC, JFJ, PRS, RGL, SCH, and VAC during January. The grey colorrepresents the available observations for each site. The back data points stand for the mid-afternoon data (databetween 14:00 and 18:00) at low altitude sites, and the nighttime data (data between 00:00 and 06:00) at the mountainstations. The red data show the observations rejected by the inversion system (see section IV.2.3.1).

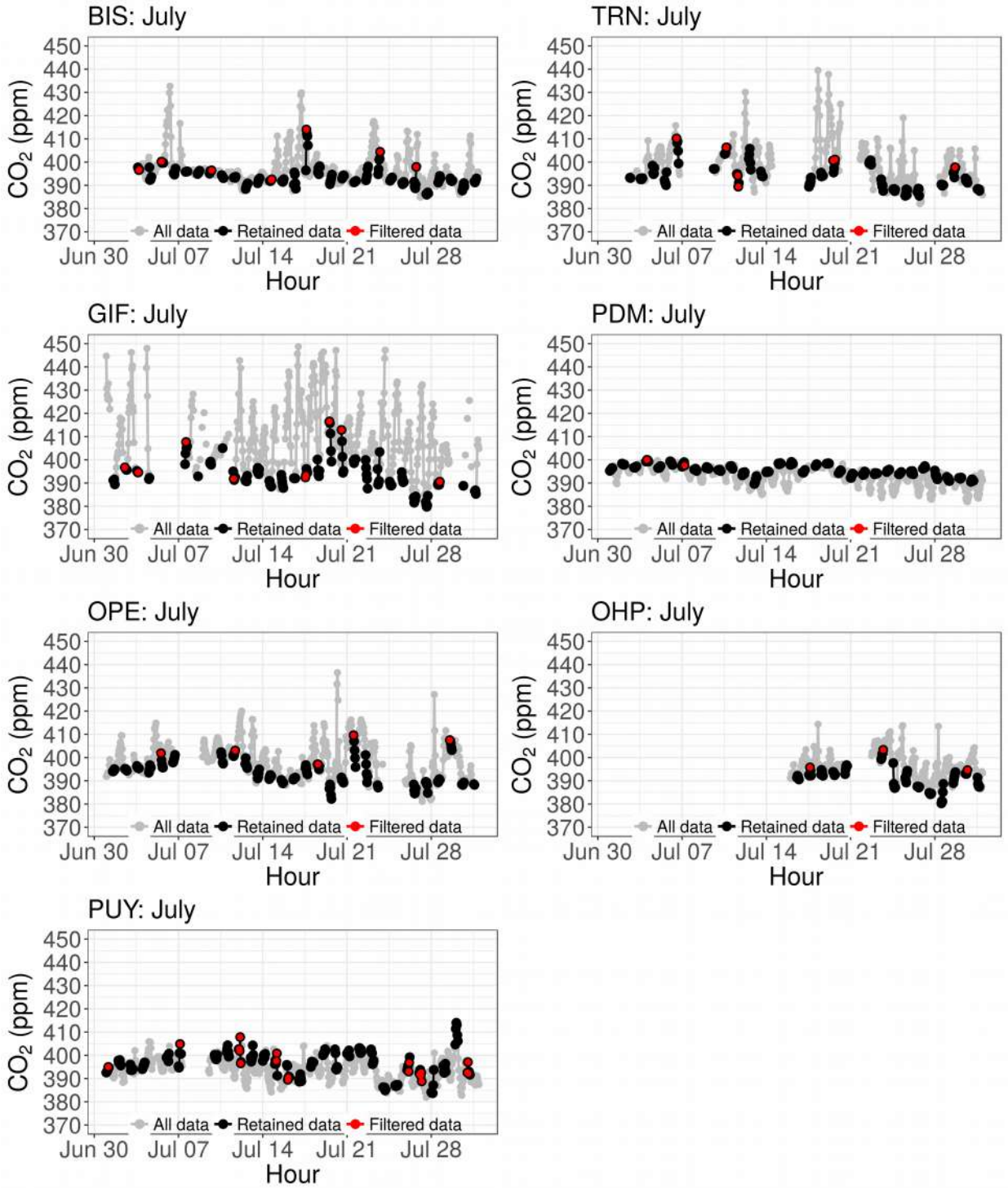

Figure SIV.12: CO_2 hourly data at BIS, OPE, GIF, PDM, PUY, OHP, and TRN during July. The grey color represents theavailable observations for each site. The back data points stand for the mid-afternoon data (data between 14:00 and18:00) at low altitude sites, and the nighttime data (data between 00:00 and 06:00) at the mountain stations. The reddata show the observations rejected by the inversion system (see section IV.2.3.1).

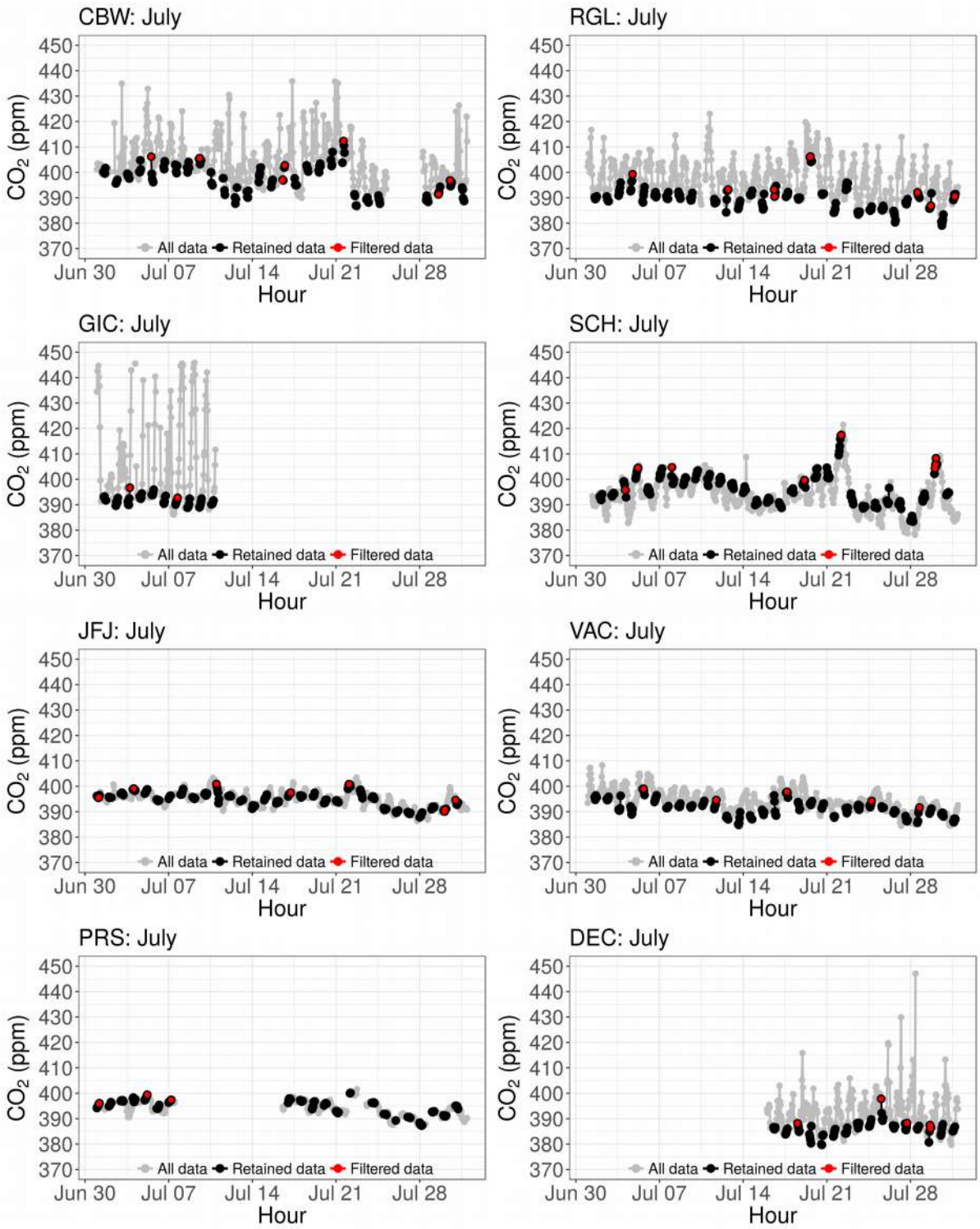

Figure SIV.13: CO_2 hourly data at CBW, DEC, GIC, JFJ, PRS, RGL, SCH, and VAC during July. The grey colorrepresents the available observations for each site. The back data points stand for the mid-afternoon data (databetween 14:00 and 18:00) at low altitude sites, and the nighttime data (data between 00:00 and 06:00) at the mountainstations. The red data show the observations rejected by the inversion system (see section IV.2.3.1).

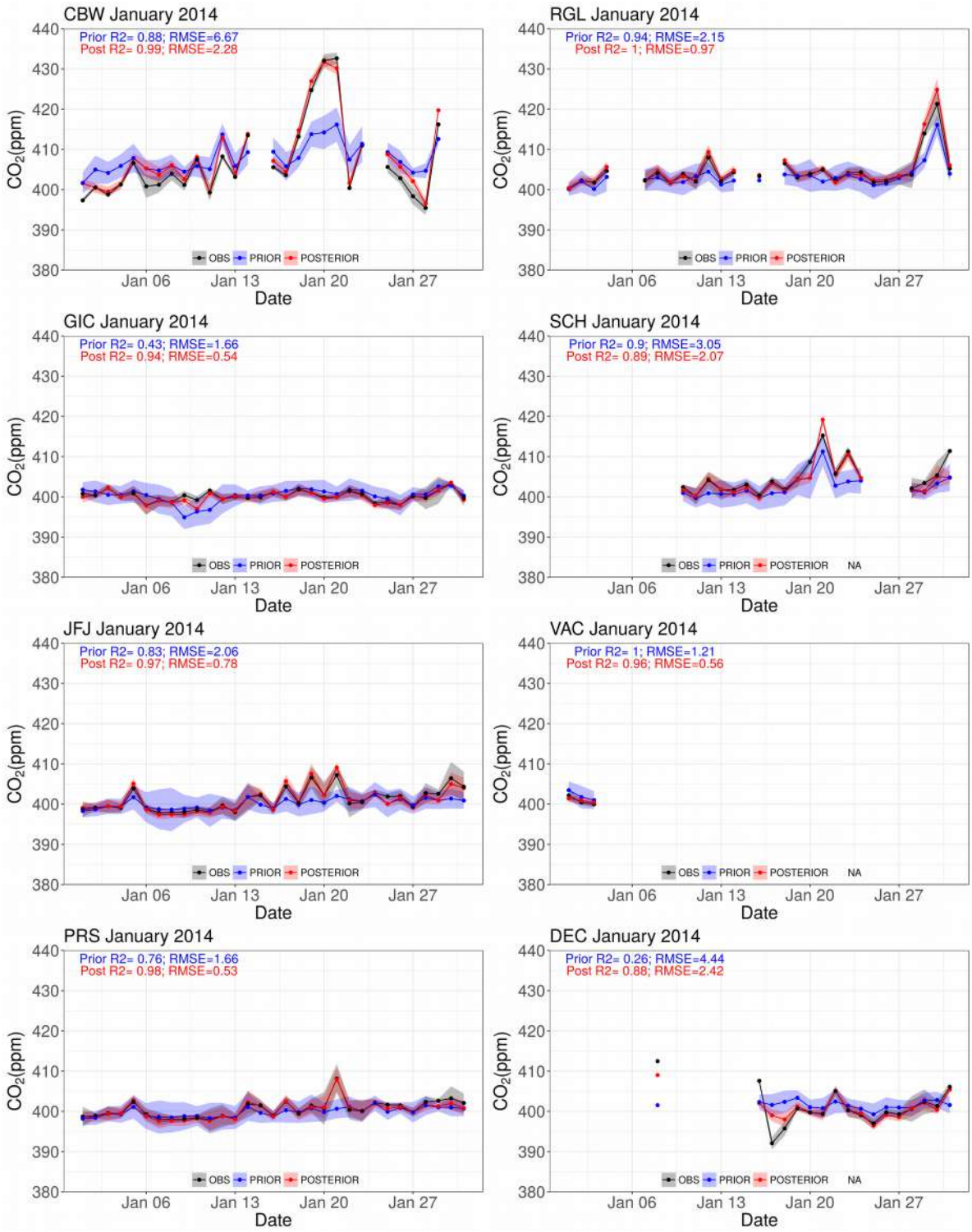

Figure SIV.14: Observed (black) and simulated prior (blue) and posterior (red) CO_2 daily averages for theFrench atmospheric sites (CBW, RGL, GIC, SCH, JFJ, VAC, and PRS) during January. The shaded areasrepresent the uncertainties of the observed (grey) and simulated prior (shaded blue) and posterior (shadedred) CO_2 concentrations. For each sites we calculate the root mean square error (RMSE) and thecoefficient of correlation (R2) for the prior and the posterior concentration.

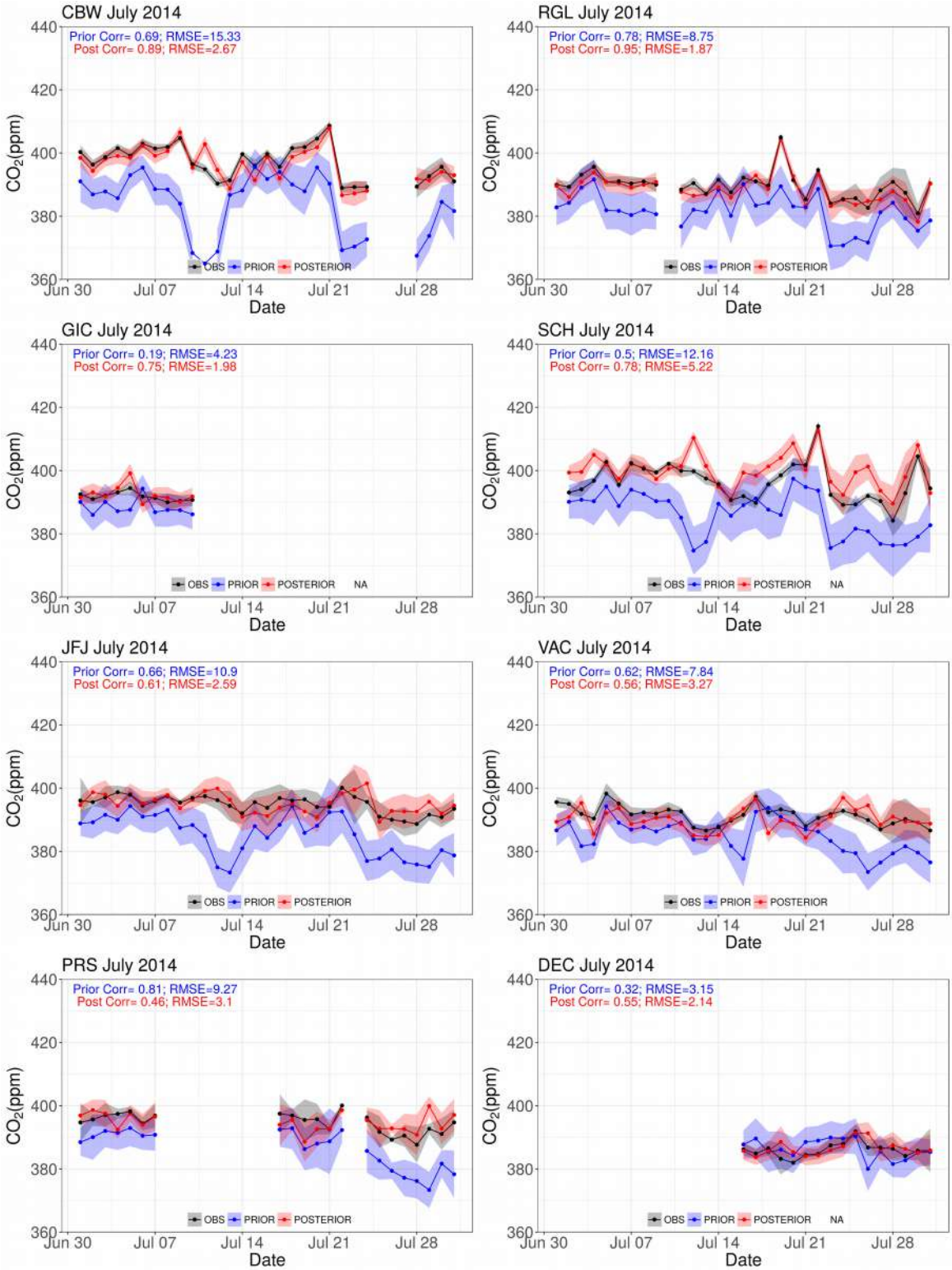

Figure SIV.15: Observed (black) and simulated prior (blue) and posterior (red) CO_2 daily averages for theFrench atmospheric sites (CBW, RGL,GIC, SCH, JFJ, DEC, VAC, and PRS) during July. The shaded areasrepresent the uncertainties of the observed (grey) and simulated prior (shaded blue) and posterior (shadedred) CO_2 concentrations. For each sites we calculate the root mean square error (RMSE) and thecoefficient of correlation (R2) for the prior and the posterior concentration.